Computer Simulation Studies of Thiol Collectors Adsorption on Sulphide Minerals, for Flotation Process.

by

Masilu Godfrey Mulaudzi

THESIS

Submitted in fulfilment of the requirements for the degree of

Doctor of Philosophy

in

Physics

in the

FACULTY OF SCIENCES & AGRICULTURE

(School of Physical & Mineral Sciences)

at the

UNIVERSITY OF LIMPOPO

SUPERVISOR: Prof. P.E. Ngoepe

2020

Declaration

I declare that the thesis "Computer Simulation Studies of Thiol Collectors Adsorption on Sulphides Mineral, for Flotation Process" hereby submitted to the University of Limpopo for the degree of Doctor of Philosophy has not previously been submitted by me for a degree at this or any other university, that it is my work both in design and execution, and that all material contained herein has been duly acknowledged.

Mr M.G Mulaudzi _____

Date

Acknowledgements

I would like to thank:

- Above all, I give thanks to YHWH, my ***Tsur***, who trained my hands to fight and fingers to do the battle, my merciful one, my ***Metsuda***, my stronghold, and my saviour, my ***Magen***, the one in whom I take refuge. Without him, all this wouldn't have worked out.

- My Supervisor and advisor, Professor Phuti Ngoepe, who taught me the art of finding good research topics and how to handle the research.
- The Material Modelling Centre (MMC) members, who kept life interesting by providing numerous occasions to chat about science and life in general.
- My parents, who have always encouraged me to pursue my studies although things were tough.
- My friends from far away, who did not forget about me for these tough years.
- My Fiancee, Mokhithi, for her support and encouragements, for keeping me from turning into a mad scientist, and for basically everything else.
- The Material Modelling Centre administrator Dr Jacob Mothapo for the encouraging words that`s inspired me to work hard.
- University of Cape Town Centre for Minerals Research, in particular, Dr Belindah McFaedzean and Dr Jestos Taguta for the project advice, discussion and the experimental work.
- Sponsors of this project: South African Minerals to Metal Institute (SAMMRI), University of Limpopo (UL) and the National Research Foundation (NRF).

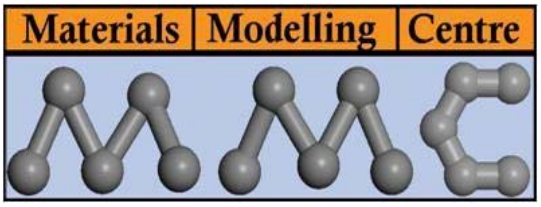

Dedications

This work is dedicated to:

My wonderful two daugher and son

Tebogo Abigail, Anzani Matsheba and Fhulufhelo Godfrey

My wonderful Wife

Mokhithi

My wonderful siblings

Mbulaheni, Phophi, Thabelo and Rofhiwa

My wonderful mother

Matshiba

Ndi a livhuwa!!

Abstract

Surface properties of pyrite (FeS_2), chalcopyrite ($CuFeS_2$), galena (PbS) and sphalerite (ZnS) most thermodynamically stable surfaces have been studied using first priniciples density functional theory. The most stable surfaces showed the highest surface exposure as it covered a higher percentage of the surface area on morphologies. The interaction of water with such sulphide surfaces was also investigated; the structures of sulphide minerals surfaces were changed in the presence H_2O molecules. The surfaces of FeS_2 and ZnS relax most while those of $CuFeS_2$ and PbS surfaces change slightly in the presence of H_2O molecules.

The results on the effect of chain length of DTPs and DTCs on the enthalpies of adsorption on pyrite, galena, chalcopyrite and sphalerite have shown that an increase in chain length of the DTPs resulted in an increase in the enthalpies of adsorption trend for pyrite, galena and sphalerite. This is an important observation since the ligand is the same in all cases and therefore the effect is due to the role of the alkyl group Moreover, we noted a decrease of enthalpies of adsorption with an increase of DTCs chain lengths on pyrite, galena, chalcopyrite and sphalerite.

The effect of the branching of the hydrocarbon chain length of the dithiocarbamates on the enthalpy of adsorption of pyrite was investigated. The results show that the configuration of the alkyl chain length of the same carbon number has an influence on the enthalpy of adsorption. Furthermore, the results indicate that there was minimal enthalpy of adsorption when DeDTP was dosed to galena, chalcopyrite and sphalerite minerals as compared to DeDTC and ethyl xanthate. On the other hand, the enthalpies of adsorption of DeDTP on pyrite were very high which represented a greater exothermic reaction than for any of the DeDTC and ethyl xanthate. The bond distance between thiol collector and the surface is consistent with the corresponding calculated adsorption energies.

The Mulliken population of S-Fe/S-Pb/S-Zn bond for the adsorption of eX on $CuFeS_2$ surface are high compared to PbS and ZnS surfaces, which indicated that there is a strong covalent bond between S and Fe atoms as compared to S-Pb and Pb-Zn bonds. Such observations are consistent with results of other thiol collectors. It was seen that the Mulliken atomic charges populations of $CuFeS_2$, PbS and ZnS surface layers are different before and after DTPs adsorption. The charges of Fe atom reduce, which indicates that the Zn and Pb atoms become more positive and the Fe atom becomes more negative. In addition, there are changes in the charges of S atoms

in ZnS and PbS surface layers before and after H_2O absorption, suggesting that the presence of water would affect the adsorption of thiol collector.

The densities of states (DOS) of the thiol collectors on surfaces of sulphide minerals have shown a strong hybridisation between the S *3p*-orbital HOMO, metals (Fe, Pb, Zn) *3d*-orbital for pyrite and chalcopyrite, *6p*-orbital for galena and (*3d and 4s)*-orbitals for sphalerite. The collector S *3p*-orbital reduces to zero states on the surfaces of Fe, Pb and Zn atoms. The Fe-S bond population for DeDTP is lower than that of DispDTP and DbDTP in pyrite, respectively. For chalcopyrite the DeDTP Fe-S population is higher than both DispDTP and DbDTP: similar trends were observed for Pb-S and Zn-S, however, the Pb-S bonding was less covalent as compared to the Fe-S in chalcopyrite. The DTPs Fe-S bond population is generally higher in chalcopyrite than in pyrite. Mulliken charges analysis indicated that the DTPs S atoms lost charges and the metals gained with a decreasing DTPs chain length for pyrite: a similar trend was observed for chalcopyrite. The DTPs gained electrons from galena and sphalerite surface. For DTCs pyrite and chalcopyrite surface Fe atoms gain more electrons in the presence of DeDTP than other DTPs, while galena and sphalerite lost most electrons in the presence of DbDTC than other DTCs. As for xanthate, the Mulliken bond charges indicated that the S atoms and the metals lost charges, suggesting that some charges reside at the internuclear region between the metals and sulphurs (M–S). These show that electron charges are collector and mineral dependent; collector would be an electron acceptor or donor depending on the mineral makeup.

A comparison of the computational results, isothermal titration calorimetry (ITC) and microfloatation experiments for the interaction of DeDTP, DeDTC and eX with pyrite and galena was made. The calculated adsorption energies between thiol collectors and mineral surfaces were always more exothermic than the experimentally determined ones. In computational calulations, water adsorption was found to reduce the reactivity of Fe and Pb atom for the interaction with thiol collectors and bring the adsorption energies closer to the magnitude of the experimental values. FeS_2 (100) surface heat of adsorption depict similar trends to experimental recoveries from microfloation for DeDTP, DeDTC and eX, while FeS_2 (111) heats of adsorptions for DeDTP and DeDTC are consistent with ITC experimental results. Lastly, calculated DeDTP and DeDTC adsorptions on the PbS (100) are also consistent with experimental recoveries.

List of abbreviations and acronyms

MAR	Mid-Atlantic Ridge
PGEs	Platinum Group Elements
PGMs	Platinum Group Minerals
BMS	Base Metal Sulphides
XPS	X-ray Photoelectron Spectroscopy
AES	Auger Electron Spectroscopy
CEMS	Conversion Electron Mossbauer Spectroscopy
DFT	Density Functional Theory
GGA	Generalised Gradient Approximations
GGA-PBE	Generalised Gradient Approximations Perdew-Burke-Ernzerhof
GGA-PW91	Generalised Gradient Approximations Perdew–Wang 1991
ITC	Isothermal Titration Calorimetry
LDA	Local Density Approximation
VASP	Vienna Ab-initio Simulation Package
CASTEP	CAmbridge Serial Total Energy Package
METADISE	Minimum Energy Techniques Applied to Dislocation Interface and Surface Energy
PW	Plane-Wave
H-K	Hohenberg-Kohn
K-S	Kohn-Sham
SCF	Self-Consistent Functional
MD	Molecular Dynamics
eX	Ethyl Xanthate
DTP	Dithiophosphate
DeDTP	Diethyl Dithiophosphate
DispDTP	Diisopropyl Dithiophosphate
DbDTP	Dibutyl Dithiophosphate
DTC	Dithiocarbamate
DeDTC	Diethyl Dithiocarbamate
nbDTC	n-butyl Dithiocarbamate

DbDTC	Dibutyl Dithiocarbamate
DOS	Density of States
LDOS	Local Density of States
PDOS	Partial Density of States
TDOS	Total Density of States
VB	Valence Band
CB	Conduction Band
HOMO	Highest Occupied Molecular Orbital
LUMO	Lowest Un-Occupied Molecular Orbital
SOMO	Second Occupied Molecular Orbital
E_F	Fermi Energy
eV	Electron Volte
Å	Angstrom

List of minerals

FeS_2	Pyrite
$CuFeS_2$	Chalcopyrite
PbS	Galena
ZnS	Sphalerite

Table of Contents

List of Figures

List of Tables

Chapter 1

Introduction

Non-ferrous metals are in high demand due to technological advancement. Some of the metals are found as base-metal (Cu, Zn, Pb) sulphides. Base metals serve many purposes, such as construction, parts of stainless steel, galvanising steel, electronics, metallurgy, transport and energy generation. The platinum-group elements (PGEs) are used in jewellery, investment commodity, catalytic convertor and alloys; however, the concentrations of some PGEs in their respective applications have not yet been determined in base metal sulphide (BMS).

Mineral extraction (mining) is a major resource extraction activity that provides raw materials to support our economic infrastructure. The extraction of sulphides-containing minerals may be achieved through the flotation method, which is the most important unit operation in mineral benefaction process. The flotation method is used in several processing industries and historically this was first used in the mining industries. This method is one of the most versatile and flexible of all mineral separation processes because reasonable outcomes are fairly easy to obtain.

Given the general decrease in rich ore bodies, extractive metallurgists are faced with the challenge of processing complex and low-grade ores, to overcome the ever-growing demand for BMS and PGEs. Today, with the existence of computational modelling, it is possible to create enhanced alternatives. This will help in reducing the loss of revenue and unnecessary waste of the world's valuable minerals/metals and decline in mineral reserves. Basic understanding of the interaction between sulphides minerals with the collector will help to remedy the loss of valuable material through computational modelling. In this study, we report on the effect of hydration on the structural and surfaces properties of pyrite (FeS_2), chalcopyrite ($CuFeS_2$), galena (PbS) and sphalerite (ZnS). Furthermore, the effect of ligands on the mineral most stable surfaces is investigated. These properties have been investigated using *ab-initio* methods employing density functional theory (DFT).

In chapter 1, we review from the literature, the previous theoretical and experimental studies and related methods that were used to study the minerals. Furthermore, the flotation process necessary for mineral extraction is discussed. The crystal structures of FeS_2, $CuFeS_2$, PbS and ZnS are reviewed. Finally, we present the rationale and objectives of this study.

1.1 Flotation principle

Froth flotation is one of the most significant processes commonly used to separate valuable minerals from gangue minerals [1]. The principle of flotation is simple and easy to execute. Firstly, the ore is milled, and then water is added to form a pulp. Fine bubbles of air are pumped through the pulp while it is being subjected to mechanical mixing. Valuable minerals such as PbS, ZnS and $CuFeS_2$ are separated from gangue (siliceous matter and iron sulphides) according to the differences in their wetting properties [2]. The success of flotation essentially lies in the efficient chemical and electrochemical control of the system, for which a variety of chemical reagents are employed, including collectors, frothers, depressants, and activators [3, 4]. Several chemicals, such as activators, depressants and collectors, are added to the pulp to increase the efficiency of the flotation process. Collectors are surface-active chemicals containing a polar head group and one or more hydrocarbon chains. These chemicals can attach themselves selectively to the precious ore and increase the hydrophobicity of the particle; hence, it will float more easily.

The most commonly used thiol collectors are xanthates, which are alkali metal (e.g. Na^+, K^+) salts of monoalkyl esters of dithiocarbonic acid (e.g. Potassium Ethyl Xanthate: RCOSSK) [5]. The birth of xanthate in the flotation industry took place in 1925, which led to the development of other collectors [6]. They represent the largest volume of any sulphide mineral collector, mainly due to being easy and inexpensive to manufacture [6]. The floatation process generally occurs according to the following two reactions (this just an example of what you can write to explain the equations)

$$ROH + KOH = ROK + H_2O,$$

$$ROK + CS_2 = ROCS_2K,$$

where R denotes an arbitrary hydrocarbon chain. The precipitated potassium xanthate salt, $ROCS_2K$, has good storage properties. The salt is then dissolved in water (yielding $ROCS_2^-$) before it can be introduced as a collector into the flotation process. Another important chemical used as a flotation collector is dibutyl dithiophosphate, $(OC_4H_9)_2PS_2^-$.

A typical flotation cell and the processes that occur in it are presented in Figure 1.1.

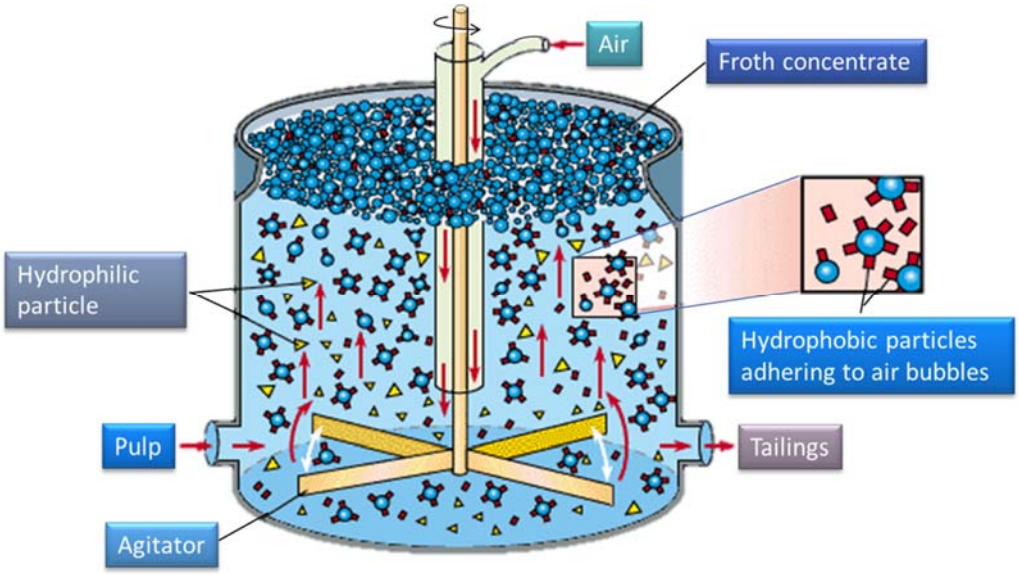

Figure 1.1: Flotation cell displaying the processes of froth floatation [5].

The continued use of xanthate, however, has raised ever-increasing environmental concern as carbon disulphide is readily emitted from xanthate decomposition, thus engineers and scientists have embarked on looking for the replacement of xanthate collectors [7]. The attempt to partially and completely replace the xanthate collector by dithiocarbamate has been performed and it was found that the mixture of xanthate and dithiocarbamate yield high recoveries. However, it was observed that pure xanthate is more efficient than pure dithiocarbamate alone, thus dithiocarbamate may not be able to fully replace xanthate. Moreover, the dithiocarbamates are economically problematic as they are more expensive than xanthates [8]. Furthermore, the dithiophosphate was also found not suitable to replace the xanthate on the flotation of sulphide minerals [9].

1.2 Factors affecting the flotation process

The froth flotation system is a complex system with many interrelated variables such as equipment, operation and chemistry variables. The variables are depicted

diagrammatically in Figure 1.2. While it is acknowledged that, many parameters influence the flotation process; this work focused on the chemistry component, specifically collector chemistry highlighted in Figure 1.2.

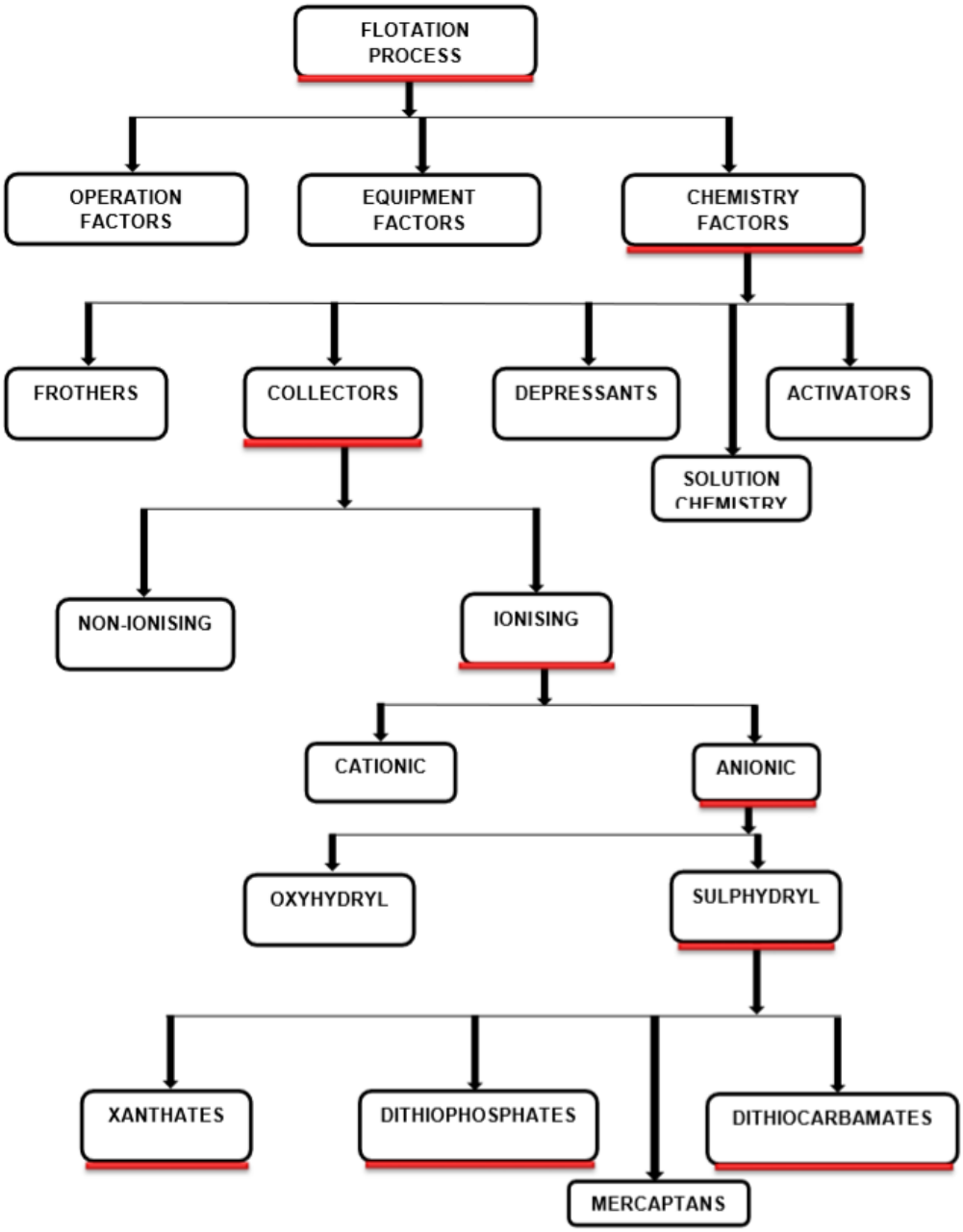

Figure 1.2: Variables affecting the flotation process and classification of flotation collectors [10]

1.3 Subprocesses of flotation

The overall froth flotation process is a combination of different sub-processes. Among them are:

1. Collector-mineral interactions,
2. Bubble particle interaction,
3. Particle recovery in the froth phase.

This investigation focused on the first sub-processes which take place in the pulp zone.

1.4 Mineral-collector interactions

This is one of the central sub-processes in flotation. Most minerals are naturally hydrophilic and do not have an affinity for air bubbles. For a bubble to attach to a mineral surface, a hydrophobic mineral surface is required. In mineral processing, the required hydrophobicity is usually achieved by the addition of a surfactant called a collector. The sub-process of collector mineral interaction is driven by the collector chemistry, mineral surface chemistry and the solution chemistry.

1.4.1 Collectors

A collector is a hetero-polar reagent that consists of the non-polar hydrocarbon chain, which is hydrophobic and belongs to the hydrophilic polar head group. The polar head group reacts with the mineral surface while the non-polar hydrocarbon chain induces hydrophobicity onto the mineral surface by extending into the liquid phase in the flotation pulp. Collector adsorption onto a mineral surface is depicted diagrammatically in Figure1.3.

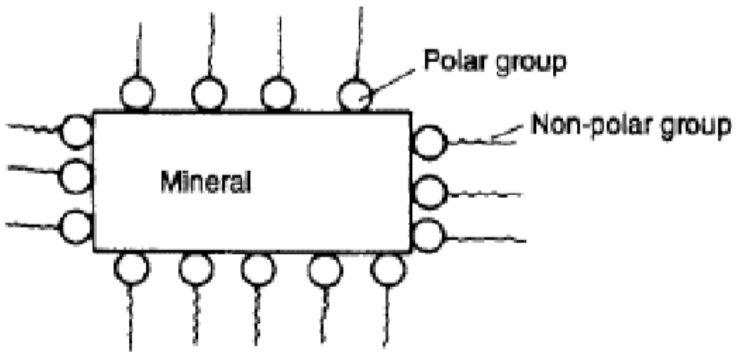

Figure 1.3: Schematic diagram of collector adsorption on a mineral surface [11].

The reaction between thiol collectors and sulphide minerals takes place because the 3*p* electrons of sulphur atoms of thiol collectors and the *d*-electrons of metal ions of

the sulphide minerals are located at the same energy level; hence, the orbitals overlap easily [12].

Collectors significantly increase the contact angle thereby enhancing the bubble-particle interaction. As shown in Figure 1.2, there are different classes of collectors but this work focusses on sulfhydryl collectors, specifically the xanthates, the dithiocarbamates and the dithiophosphates, since they are the most common collectors in the BMS and PGM flotation industry. Xanthates are used in bulk sulphide mineral flotation because they are relatively cheaper and more powerful collectors, however, they are not selective [13, 14]. The dithiophosphates and dithiocarbamates are usually used in selective flotation because of their improved selectivity [15, 14].

1.4.1.1 Collector Chemistry

Collector chemistry depends on the hydrocarbon chain length and the chemistry of the head group. It is also reported that the effectiveness of a collector is a function of both the hydrocarbon chain length and the polar group [16]. Generic structures of thiol collectors used in this work where R and R' represent the hydrocarbon chains of the thiol collectors are presented in Table 1.1.

Table 1.1: Generic structures of thiol collectors used in this work where R and R' represent the hydrocarbon chains of the thiol collectors [16].

Collector	Structure	Preparation
Xanthate	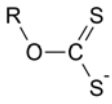	Xanthates are formed when an alkali hydroxide is reacted with an alcohol and carbon bisulphide
Dithiophosphate	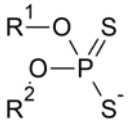	They are produced by neutralising dithiophosphoric acid with an organic or organic base like sodium hydroxide or zinc oxide
Dithiocarbamate	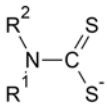	Dithiocarbamates are synthesised then an amine is reacted with carbon bisulphide and sodium hydroxide

1.4.1.2 The effect of the alkyl chain length on collector chemistry

The length of the carbon chain affects the hydrophobicity imparted to the mineral particle – the longer the hydrocarbon chain, the greater the hydrophobicity. Besides, the electron releasing or withdrawing behaviour of the organic group affects the electron densities around the donor atoms. In thiol collectors, the electron densities on the sulphur atoms depend on the inductive effects in the molecules [17]. A longer hydrocarbon chain makes the collector more reactive due to a stronger positive inductive effect, which increases the electron density around the polar head group [18]. Longer chain collectors are readily oxidised compared to shorter chain collectors [19, 16].The nature of the alkyl chain length also affects the chemistry of the collector. For collectors with the same number of carbon atoms, the straight alkyl chain length has a stronger inductive effect towards the functional group as compared to the branched-chain.

1.4.1.3 The effect of donor atoms in the collector head group

The differences in the electronegativity of the O, C, P or N atoms in the collector polar head groups affect the reactivity of the collectors [17]. According to Somasundaran and Nagaraj [17], the electronegativity decrease in the following order:

O	N	S	P
3.5	**3.07**	**2.44**	**2.06**

Oxygen is the most electronegative in the above series. Thus, DTP is less reactive than the xanthate because of the two RO groups that are electron-withdrawing, thus reducing electron density around the donor sulphur atoms. The electron density on the sulphur atoms in xanthate is higher than in DTP due to the presence of only one RO group in xanthates. The N in the DTC is less electronegative than the O in either atoms, rendering DTC more reactive [12]. Thus, the reactivity decreases in the following order: DTC > X > DTP [17].

1.4.2 Sulphide minerals

Table 1.2: Summary of the crystalline structure of sulphide minerals [20]

Sulphide	Chemical Formula	Crystalline Structure	Shortest S-S distance (A°)
Galena	PbS	Cubic, has a rock-salt type structure with Pb^{2+} and S^{2-} ions in the place of Na and Cl^- ions respectively. The coordination number of 6.	4.194
Pyrite	FeS_2	Cubic structure made up of Fe^{2+} and S_2^{2-} ions with a modified rock-salt structure.Fe^{2+} ions are surrounded by 6 sulphur atoms in an octahedral fashion and each sulphur is surrounded by sulphur and 3 Fe^{2+} ions in a distorted tetrahedral configuration.	2.177
Chalcopyrite	$CuFeS_2$	Crystallises in a tetragonal structure where half of the cations are replaced by Cu and the other half by Fe. Cu(I), iron(III) and sulphide ions arranged in such a way that each Cu(I) and iron(III) is tetrahedrally surrounded by 4 sulphide ions and the sulphide ions are tetrahedrally surrounded by 2 Cu(I) and 2 iron(III) ions.	3.685

sphalerite,	ZnS	Zincblende is characterized as a cubic closet packing (ccp), also known as face-centred cubic. It has a tetrahedral ion arrangement and four nearest neighbours from standard crystal structure prediction tables. Therefore, four sulfur atoms surround each zinc atom and four zinc atoms surround each sulfur atom. The coordination number, the number of electron pairs donated to metal by its ligands, for both zinc sulfur is four.	3.390

1.4.3 Interactions of thiol collectors with sulphide minerals

The interaction of sulphide minerals with thiol collectors has been widely studied using different surface science techniques, e.g. XPS, UV-VIS, computation, ToF-SIMS while extraction and identification have been studied using infrared spectroscopy. Electrochemical methods, rest potential measurements and cyclic voltammetry, have also been used to identify the collector species on mineral surfaces. Despite more than a century of research, the mechanisms whereby sulphide minerals interact with thiol collectors are still widely researched. The proposed mechanisms of interaction between the thiol collectors and sulphide minerals concerned with this work are discussed in the review of the related work.

1.5 Review of related work

This review begins with previous studies performed on thiol collectors such as xanthate, dithiophosphate and dithiocabarmate, and their adsorption on sulphide surfaces. Finally, some other work is considered that, while not being directly associated with the main subject matter, is still important. The modelling of minerals and even mineral surfaces is not new, particularly as a field to assist crystallographers in calculating solid-state structures.

Thiols collectors and their adsorption on mineral surfaces are the subjects for many experimental studies. For example, infrared absorption techniques have been used to study the interaction between xanthates and sulphide surfaces [21, 22]. Adsorption of ethyl and octyl xanthates on other surfaces such as sulphidised copper, silver and germanium has also been studied with infrared techniques [23, 24].

The PGEs occurs as either discrete with platinum group minerals (PGMs) or in solid solution in the base metal sulphides (BMS), such as pentlandite, chalcopyrite, pyrrhotite and pyrite [25]. Palladium and rhodium are the PGEs contained mostly in pentlandite [26]. The PGEs are found in platreef, which is one of the ore bodies of platinum-group elements and base metal enriched mafic and ultramafic layers situated along the base of the northern limb (Mokopane previously known as Potgietersrus) of the bushveld igneous complex [25]. The reef is enriched with palladium 6 with a maximum content of 20000 ppmw in pentlandite [26]. According to Manyeruke's there are three platreef horizons (i.e. lower, middle and upper platreef) on the farm townlands, which consist predominantly of pyrrhotite and chalcopyrite with a minor amount of pentlandite and pyrite. The pentlandite found in the reef is associated with pyrrhotite or pyrite. It was mentioned that when pentlandite is associated with pyrite, it has a well-developed cleavage, resulting in the formation of triangular pits when polished [27].

Investigation of the $CuFeS_2$ anisotropy through DFT calculation that was done by Wei *et al*. [28] demonstrated that the $CuFeS_2$ (112) surface was the preferential cleavage surface rather than the commonly recommended (001) surfaces, suggesting that the (112) surface should be preferentially considered for investigation of $CuFeS_2$ surface properties. The S_2^{2-} and S_n^{2-} species formed on the S-terminated $CuFeS_2$ surfaces during relaxation processes may hinder the contact between lixiviant and the inner metal atoms, negatively impacting on the leaching of $CuFeS_2$.

Several research groups are currently engaged in studying interactions between collector reagents and mineral (or metal) species using molecular modelling tools. The geometrical structure and vibrational modes of ethyl and heptyl xanthates in metal xanthate complexes were studied by Hellstrom *et al*. [29] using Hartree–Fock and DFT methods. They reported that vibrational frequencies calculated using DFT are in good agreement with the experimental results. Hellstrom *et al*. [30] further studied the interaction between ethyl xanthate on clean and hydroxylated Ge (III) surfaces using DFT. They showed a bidentate bridging confirmation on a clean Ge (III) surface and a

monodentate binding when the surface is saturated with hydrogen atoms [31]. Hung *et al*. studied the adsorption of xanthate on pyrite surfaces using DFT and showed that xanthate undergoes chemisorption at defect sites on real pyrite surfaces. More recently, [32] Chen *et al*. utilised DFT methods to study the adsorption of xanthate, dithiophosphate, and dithiocarbamate collectors on galena and pyrite mineral surfaces, and reported better selectivity offered by dithiophosphate and dithiocarbamate in galena-pyrite separation compared to xanthate.

Yekeler *et al*. [33] studied the reactivity and interaction of different thiol collectors with Ag^+ ions in the vacuum phase. Based on the calculated highest occupied molecular orbital (HOMO) and interaction energies, dithiocarbamate was predicted to possess the strongest collecting power, followed by xanthate, trithiocarbonate and dithiophosphate, respectively. Same authors used the concepts of HOMO localisation and HOMO energy along with Mulliken charges and electrostatic potential to predict the reactivity of different 2-mercaptobenzothiazole (MBT) derivatives from DFT calculations at the B3LYP level [4]. The same methodology was used to predict the reactive behaviour of 2-mercaptobenzoxazole (MBO) and its derivatives [4]. Bag e*t al.* [34] studied the effect of structure and length of the hydrocarbon chain in xanthate collector on its reactivity and interaction with Cu (I) ion. Pradip *et al.* studied interactions of alkyl hydroxamates and oleate molecules with calcium minerals and rare earth minerals [35] by using semi-empirical methods. Liu *et al.* [36] studied the effect of nature of substituent group present on N-atom on the performance of thionocarbamates and thiourea collectors by DFT methods. Studies on activation of sphalerite through adsorption of Pb, Cu and Fe ions on the ZnS surface have also been reported [37].

Li *et al*. [38] studied the DFT Simulation on Interaction of H_2O Molecules with ZnS and Cu-Activated Surfaces, they found that the adsorption adsorption of water molecules on ZnS surface is stronger than that on Cu-activated ZnS surface, suggesting the ZnS surface is more hydrophilic than Cu-activated surface. Thier Dynamics simulations suggest that the water molecules close to the mineral surfaces are arranged in order, suggesting that the solid surface affects the properties of the interfacial water. The activation of Cu changed the structure and properties of the ZnS surface. The Cu-activated surface has a stronger π bonding character and a greater covalency, which

leads to weaker adsorption of water molecules on the Cu-activated surface. The interaction of surface with water is related to the surface structure and bonding characters(σ-bondandπ-bond) between atoms. It is found that the Cu−S bond is mainly formed by π bond, whereas the Zn−S bond is mainly formed by σ-bond due to the weak participation of d electrons in the bonding.

Mkhonto in his PhD thesis [39] investigated the interaction of thiol collectors (ligands) with the three surfaces of pentlandite and found that all thiol collectors adsorb strongly on Fe atoms compared to Ni atoms. Their findings indicated that the DeDTP collector adsorbs stronger on Fe than Ni atoms on (100) and (110) surfaces, while a strong interaction for DeDTP bridge on Fe and Ni atoms was observed on the (111) surface. Furthermore, Chowdhry in his thesis [40] observed that sulphide collectors should be based on sulphur binding centres to ensure selectivity against gangue minerals. To ensure maximum chelating ability, the functional group of the collector should be designed in such a manner that five or six-membered chelates could be formed with the metal atoms. Also, careful consideration should be given to the atoms attached to the main binding group as they are capable of increasing or decreasing the chelating ability of the binding group through inductive and/or mesomeric effects.

Jordaan in his Masters thesis [41] found that neither SEDTP nor SEX improved the flotation of pyrite at pH 9 and only a slight improvement in recovery was achieved at pH 4. Thus, although various measures were taken to prevent and remove surface oxidation, it is safe to assume that the pyrite (and galena) was oxidized. Therefore, the SEDTP-frother synergy could have a major application in the flotation of oxidized PGM ores.

Cui *et al* [42] in their research of comparative study on surface structure, electronic properties of ulfide and oxide minerals showed that the surface atoms of the sulphide minerals are more susceptible and more easily affected by the fracture bonds. The sulfide surfaces possess higher chemical potential than the corresponding oxide surfaces, and are more likely to be electron donors in reactions. The S 3p states are the mainly contributing states in the sulfide surface, while that in the oxide surface are O 2p states. The bonds of the sulphide surface have more covalent features and that of the oxide surface are ionic interactions. The O–M (M represents Fe, Pb or Zn) bonds are more stable, as the DOS of the oxide surfaces distribute in the lower energy range.

1.6 Rationale and objectives

1.6.1 Rationale

Froth flotation is a bulk sulphide-recovery process, which is used to separate the BMS minerals containing the PGE from the gangue minerals. It is required to optimise the recovery of the BMS minerals to maximise the recovery of the PGEs. The flotation process largely depends on differences in hydrophobicity of the various mineral surfaces [43]. Chemical variables that include collectors, frothers and modifiers are vital for effective separation as they are responsible for inducing hydrophobicity, increasing froth stability and creating favourable pulp conditions. Also, they are the easiest variables to control and optimise [43, 44]. Part of flotation such as mineral-collector interaction depends mainly on the mineral surface makeup atoms and the molecular structure of the collector's head functional group. Experimentally driven parameters, such as contact angle, flotation recovery, etc. are not very capable means of extracting this information, and the recent technology of computation algorithms offers hope in investigating the complex surfaces with low cost and efficiency. The first principle calculations can give some better reactive properties of this mineral surface that experiments might not easily accomplish. For example, the hydration and influence of ligand on surfaces.

The current study focuses on fundamental interactions between FeS_2, $CuFeS_2$, PbS and ZnS with the DTPs, DTCs homologues and eX using the first principles method. Although novel collectors may be available, patent ownership limits their application and restricts open research on their optimal use. There are several mechanisms for the adsorption of some thiol collectors on sulphide minerals that have been reported [44, 45, 46]. The collaboration with the experimentalist focuses on the interaction between FeS_2 and PbS with DeDTP, DeDTC and eX, mainly owing to the availability of good samples.

The study investigates only pure sulphides minerals and no attempt is made to investigate a real ore. Therefore, the study focus on the most stable surfaces properties of FeS_2, $CuFeS_2$, PbS and ZnS, their interaction with water, and the influence of ligands. The surface interaction is investigated from the surface and adsorption energies on different minerals. More importantly, the electronic signature and behaviour of DOS, Mulliken charges and Mulliken bond population are determined.

1.6.2 Research objectives

The objectives are to:

i. determine the suitable cut-off energy and k-point mesh parameters for FeS_2, $CuFeS_2$, PbS and ZnS systems (or any other general noun will do)

ii. perform full geometry optimisation of bulk and surface structures to determine their respective ground state energies,

iii. determine morphologies of FeS_2, $CuFeS_2$, PbS and ZnS surface energy calculations and identify dominant surfaces.

iv. investigate the oxidation state of FeS_2, $CuFeS_2$, PbS and ZnS surfaces by H_2O,

v. investigate the adsorption of DTC, DTP and eX on dry surfaces,

vi. connect the flotability of the sulphide minerals with type and concentration of species present on their surface,

vii. compare the computational work with experimental determination of the enthalpy of adsorption of DeDTP, DeDTC and eX collector molecule with FeS_2 and PbS surface, as well as actual micro flotation recoveries,

viii. extend the concept of a computational approach to PGMs.

1.7 Structure of the thesis

This thesis reports on the study of surfaces and electronic properties of the sulphides minerals, using the *ab-initio* method of the DFT. The thesis is partitioned into seven chapters: in the first chapter, we present the introductory background and literature review based on the theory and different techniques that have been used previously on the studies of these groups of transition metal sulphides. We also review the crystal structure analysis of the pyrite, chalcopyrite, galena and sphalerite mineral and thiol collectors. Finally, the rationale and objectives of this work are stated.

Chapter 2 is a methodology section mainly about describing the methods and techniques used in this study.

Chapter 3 is concerned with the bulk and surface relaxation. Cut-off and k-points mesh variations are discussed along with the effect of water of the structure of the surfaces.

Chapter 4 presents the theoretical studies on thiol collector geometry and total energies.

Chapter 5, deals with the results and discussions for all our calculations on the surface studies i.e. the adsorption of ligands on the surface. The results are compared with available experimental and theoretical data.

In Chapter 6 we present the effect of water and ITC comparison on pyrite and galena.

Finally, Chapter 7 will present the major conclusions and recommendations drawn from this study.

Chapter 2

Methodology

This chapter is concerned with the methods of calculations employed in this study. Computational simulations offer alternative means of investigating various structural, electronic and surface properties of materials alongside experiment and theory. This approach has been widely used in solid-state physics, chemistry and materials science, to predict the real situation by presenting physical systems as models.

The newly developed computer algorithm of high-performance computers has made modelling of surface chemistry studies possible. There are three types of computational approaches that can be used to study surfaces properties of materials. Firstly, the quantum mechanical methods, which take into account the motions and the interactions of electrons in a material. Secondly, the empirical potential methods (atomistic method), consider the interactions of atoms in Quasi-classical form and avoids the electronic interactions. Lastly, semi-empirical methods, these act as a bridge between quantum and atomistic methods. This method incorporates both quantum mechanical and the atomistic methods, where the electron and atom interaction in quasi-classical can be obtained.

In this study we have used *ab initio* quantum mechanical density functional theory [50, 51], to study surface properties of sulphides minerals. The theory solves the Schrödinger equation and applies the plane-wave (PW) pseudopotential method. The plane-wave pseudopotential method is necessary for performing full geometry optimisation of the structures. In the next section, we discuss the DFT for describing the many-body problem by approximation methods, using electron density (n).

2.1 Density functional theory

Density functional theory is a quantum mechanical based method used in physics and chemistry to investigate the electronic structure of many-body systems, in particular atoms, molecules, and the condensed phases [47]. Within the DFT, the properties of a many-electron system can be determined by using functional, i.e. function of another function, which in this case is the spatially dependent electron density. DFT is among the most popular and versatile methods available in condensed-matter physics, computational physics, and computational chemistry. It is used for calculations in solid-state physics. Although DFT has its theoretical

backgrounds in the Thomas-Fermi model, the theoretical basis was confirmed by the two Hohenberg-Kohn (H-K) theorems [48]. The first H-K theorem demonstrates that the ground state properties of a many-electron system are uniquely determined by an electron density that depends on only three spatial coordinates. This gives the possibility for reducing the many-body problem of N electrons with 3N spatial coordinates to 3 spatial coordinates, through the use of functionals of the electron density. This theorem can be extended to the time-independent domain to develop time-dependent density functional theory, which can be used to describe excited states [48].

The second H-K theorem defines energy functional for the system and proves that the correct ground-state electron density minimizes this energy functional. Within the framework of Kohn-Sham (K-S) DFT, the intractable many-body problem of interacting electrons in static potentials is reduced to a tractable problem of non-interacting electrons moving in an effective potential [49]. The effective potential includes the external potential and the effects of the Coulomb interactions between the electrons, that is the exchange and correlation interactions. Modelling the latter two interactions is impossible within K-S DFT. The LDA is based upon exact energy for a uniform electron gas, which can be obtained from the Thomas-Fermi model, and form fits the correlation energy for a uniform electron gas. Non-interacting systems are relatively easy to solve as the wave function can be represented as a Slater determinant of orbitals [50]. Further, the kinetic energy functional of such a system is known exactly. The exchange-correlation part of the total-energy functional remains unknown and must be approximated. The Kohn-Sham total energy functional for a set of doubly occupied electronic states can be written as:

$$\mathrm{E} = \{\psi_\mathrm{i}\} = 2\sum_\mathrm{i}\left(\frac{-\hbar}{2\mathrm{m}}\right)\nabla^2\psi_\mathrm{i}\mathrm{d}^3\mathrm{r} + \int \mathrm{V_{ion}}(\mathrm{r})\mathrm{n}(\mathrm{r})\mathrm{d}^3\mathrm{r} + \frac{\mathrm{e}^2}{2}\int \frac{\mathrm{n}(\mathrm{r})\mathrm{n}(\mathrm{r}')}{|\mathrm{r}-\mathrm{r}'|}\mathrm{d}^3\mathrm{r}\mathrm{d}^3\mathrm{r}' + \mathrm{E_{xc}}[\mathrm{n}(\mathrm{r})] + \mathrm{E_{ion}}(\{\mathrm{R_I}\}), \quad 2.1$$

where E_{ion} is the Coulomb energy associated with interactions among the nuclei (or ions) at positions $\{R_I\}$, V_{ion} is the static total electron-ion potential, n(r) is the electronic density given by

$$\mathrm{n}(\mathrm{r}) = 2\sum_\mathrm{i}|\psi_\mathrm{i}(\mathrm{r})|^2, \quad 2.2$$

and E_{XC} [n(r)] is the exchange-correlation functional. Only the minimum value of the Kohn-Sham energy functional has physical meaning. At the minimum, the Kohn-Sham energy functional is equal to the ground-state energy of the system of electrons with the ions in positions $\{R_I\}$. It is necessary to determine the set of wave functions ψ_i that minimizes the Kohn-Sham energy functional. These are given by the self-consistent solutions to the Kohn-Sham equations:

$$\left[\frac{-\hbar}{2m}\nabla^2 + V_{ion}(r) + V_H(r) + V_{xc}(r)\right]\psi_i(r) = \varepsilon_i\psi_i(r), \qquad 2.3$$

where ψ_i is the wave function of electronic state i, ε_i is the Kohn-Sham eigenvalue and V_H is the Hartree potential of the electrons [51]. DFT calculations are normally used to solve K-S equations self consistently. Within the framework of Kohn and Sham DFT, the intractable electrons in a static external potential are reduced to tractable of non-interacting electrons moving in an interacting effective potential. The effective potential includes the external potential and the effects of the Coulomb interactions between electrons. K-S DFT shows that only exchange-correlation as a function of the electron spin (up and down) density n(r) must be approximated [48].

2.1.1 Local density approximation

The Hohenberg-Kohn theorem provides some motivation for using approximate methods to describe the exchange-correlation energy as a function of the electron density. The simplest method of describing the exchange-correlation energy of an electronic system is to use the LDA [51]. In local density approximation the exchange-correlation energy of an electronic system is constructed by assuming that the exchange-correlation energy per electron at a point r in the electron gas, $\varepsilon_{XC}(r)$, is equal to the exchange-correlation energy per electron in a homogeneous electron gas that has the same density as the electron gas at point r, thus

$$E_{xc}[n(r)] = \int \varepsilon_{xc}(r)n(r)d^3r, \qquad 2.4$$

The local density approximation assumes that the exchange-correlation energy functional is purely local. The local density approximation, in principle, ignores correction to the exchange-correlation energy at a point r due to nearby inhomogeneities in the electron density. The LDA is a first principle approach in the sense that the quantum mechanical problem is solved without any adjustable, arbitrary or system-dependent parameters [52]. For any many-electron system, the function for

total energy has a minimum equal to the ground state energy at the ground state density.

2.1.2 Generalized gradient approximation

The generalized gradient approximation is still local but it also takes into account the gradient of the density at the same coordinates as follows;

$$E_{xc}[n_{\uparrow}, n_{\downarrow}] = \int \varepsilon_{xc}(n_{\uparrow}, n_{\downarrow}, \nabla n_{\uparrow}, \nabla n_{\downarrow})\rho(r)d^3r, \qquad 2.5$$

GGA for the exchange-correlation energy improves upon the local spin density approximations (LSDA) description of atoms and solids. It tends to improve total energies and structural energy differences and it expands and weakens the bonds, an effect that corrects the LSDA prediction [53]. The GGA functions are accurate and give very good results for molecular geometries and ground-state energies and are expressed in terms of Perdew-Wang, however potentially more accurate than the GGA functional and meta-GGA functions [54]. These functionals include further terms in expansion depending on the density, the gradient of the density and the Laplacian second derivatives of the density. There are other important functionals of DFT such as hybrid Meta GGA, hybrid and double functional. There are different GGA exchange-correlation functionals important for calculating solids, such as GGA-Am05, GGA-PBE, GGA-PBEsol, GGA-rPBE and GGA-BLYP.

2.1.3 Projector augmented wave method

This work employs the project augmented wave (PAW) method within the framework of DFT as implemented in the CASTEP code that has been shown to yield reliable results for the electronic and structural properties of various solids. The PAW method is successful and has been used effectively, and in many ways functions like pseudopotentials. The method has a strong relationship with the ultrasoft pseudopotentials, but it also allows the full-wave functions including the core electron wave functions to be calculated. In this method, the full wavefunctions are transformed onto auxiliary wavefunctions. The auxiliary functions can be expanded relatively easily in a plane wave basis, while the full wavefunctions are augmented with atomic wavefunctions. It assumes the frozen-core approximation but is significantly more transferable than pseudopotentials [55].

2.2 Plane-wave pseudopotential method

The plane-wave pseudopotential technique is a good method used to calculate with accuracy the variational self-consistent solution to the density functional theory. It is applicable in large systems that are subject to 3D periodic boundary condition. In this method the wave function is expressed in terms of plane-wave basis and a good pseudopotential representation of the ions in the crystal is given.

2.2.1 Plane-wave basis

An infinite plane-wave basis set is required to expand the electronic wave functions of the system. The Plane-wave pseudopotential method is a powerful and reliable tool to study the properties of materials. This method is designed for periodic solids but again is used for problems such as atoms and surfaces. The key of this method is Bloch's theorem which allows the electronic wave functions to be expanded in terms of a discrete set of plane waves as follows:

$$\psi_i(\mathrm{r}) = \mathrm{e}^{[\mathrm{ik.r}]}\mathrm{F_i}(\mathrm{r}) \tag{2.6}$$

This expression has a wavelike and cell periodic part where,

$$\mathrm{F_i}(\mathrm{r}) = \sum_{\vec{\mathrm{G}}} \mathrm{C_{i,G}}\mathrm{e}^{[\mathrm{iG.r}]}, \tag{2.7}$$

where G is the reciprocal lattice vectors of the periodic cell. Thus each electronic wave function can be written as follows:

$$\psi\mathrm{k_i}(\mathrm{r}) = \sum_{\mathrm{G}} \mathrm{C_{i,K+G}}\ \mathrm{e}^{[\mathrm{i(k+g).r}]}, \tag{2.8}$$

where $C_{i,K+G}$ are the coefficients of plane waves and depend entirely on the specific kinetic energy,

$$\left(\frac{\hbar^2}{2\mathrm{m}}\right)|\mathrm{K} + \mathrm{G_c}|^2. \tag{2.9}$$

The plane wave's basis set is limited by including all plane waves whose kinetic energies are less than some particular cut-off energy (E_{cut}) as follows:

$$\left(\frac{\hbar^2}{2\mathrm{m}}\right)|\mathrm{K} + \mathrm{G_c}|^2 \ < \ \mathrm{E_{cut}} \tag{2.10}$$

The cut-off energy is chosen by increasing its magnitude until the total energy is converged to require accuracy [53]. However, when the number of a plane wave is increased one can describe more rapidly varying features and an infinitely large number of basis set could be achieved. Thus finite bases set are obtained when finite cut-off energy is introduced to the discrete plane-wave basis set. This may lead to some errors in the computation of the total energy; cut-off energy should be increased until the calculated energy has converged. Also one needs to use a much denser set of k-points to reduce errors and ensure good convergence.

2.2.2 Pseudopotentials

Although Bloch's theorem states that the electronic wave functions can be expanded using a discrete set of plane waves, a plane-wave basis set is usually very poorly suited to expanding electronic wave functions because a very large number of plane waves are needed to expand the tightly bound core orbitals and to follow the rapid oscillations of the wave functions the valence electrons in the core region. It is well known that most physical properties of solids are dependent on the valence electrons to a much greater extent than on the core electrons. The pseudopotential approximation exploits this by removing the core electrons and by replacing them and the strong ionic potential by a weaker pseudopotential that acts on a set of pseudo wave functions. Anionic potential, valence wave function and the corresponding pseudopotential and pseudo wave function are illustrated schematically in Figure 2.1.

The valence wave functions oscillate rapidly in the region occupied by the core electrons due to the strong ionic potential in this region. These oscillations maintain the orthogonality between the core wave functions and the valence wave functions, which is required by the exclusion principle. The pseudopotential is constructed ideally so that its scattering properties or phase shifts for the pseudo wave functions are identical to the scattering properties of the ion and the core electrons for the valence wave functions, but in such a way that the pseudo wave functions have no radial nodes in the core region. In the core region, the total phase shift produced by the ion and the core electrons will be greater by π, for each node that the valence functions had in the core region than the phase shift produced by the ion and the valence electrons. Outside the core region, the two potentials are identical, and the scattering from the two potentials is indistinguishable. The phase shift produced by the ion core is different for each angular momentum component of the valence wave function, and so the

scattering from the pseudopotential must be angular momentum dependent. The most general form for pseudopotential is:

$$V_{NL} = \sum_{lm} |lm > V_i < lm| \qquad 2.11$$

where |lm> is the spherical harmonics and V_i is the pseudopotential for angular momentum l, acting on the electronic wave function with this operator decomposes the wave function into spherical harmonics, each of which is then multiplied by the relevant pseudopotential V_i.

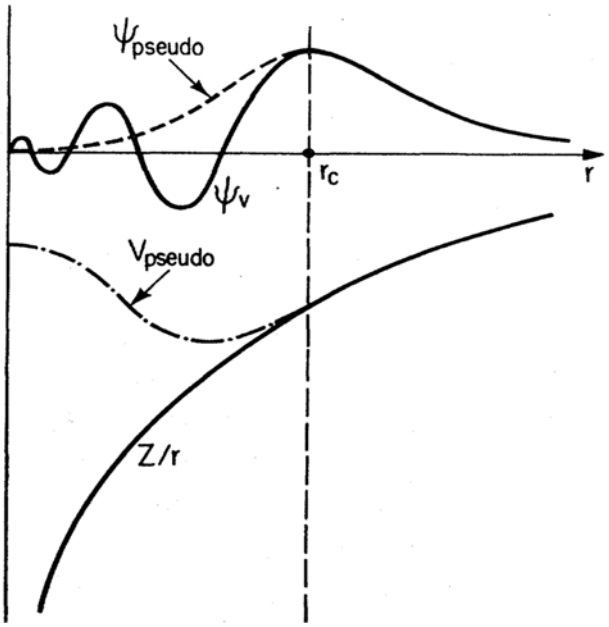

Figure 2. 1: The all-electron potential (solid lines) and pseudopotential (dashed lines) with the corresponding valence wave function and pseudo-wave functions [56].

The one-electron Schrodinger equation is replaced by the pseudopotential equation as follows:

$$\frac{P^2}{2m} + V_{pseudo}(r)\psi_{pseudo}(r) = \varepsilon\psi_{pseudo}(r), \qquad 2.12$$

where $\psi_{pseudo}(r)$ is the pseudo wave function and $V_{pseudo}(r)$ is the exact pseudopotential.

2.3 CASTEP code

CASTEP is a software package which uses density functional theory with a plane wave basis set to calculate electronic properties of solids from first principles. The CASTEP program is a first principle quantum mechanical (*ab initio*) code for performing

electronic structure calculations. Within the density functional formalism, it can be used to simulate a wide range of materials including crystalline solids, surfaces, molecules, liquids and amorphous materials; the properties of any material that can be thought of as an assembly of nuclei and electrons can be calculated with the only limitation being the finite speed and memory of the computers being used.

CASTEP is a fully-featured first principles code and as such its capabilities are numerous. Aiming to calculate any physical property of the system from first principles, the basic quantity is the total energy from which many other quantities are derived. For example, the derivative of total energy concerning atomic positions results in the forces and the derivative concerning cell parameters give stresses. These are then used to perform full geometry optimizations and possibly finite temperature molecular dynamics. Furthermore, symmetry and constraints (both internal and external to the cell) can be imposed in the calculations, either as defined by the user, or automatically using in-built symmetry detection.

The total-energy code used, CASTEP, performs a variational solution to the Kohn-Sham equations by using a density mixing scheme [57] to minimise the total energy and also conjugate gradients to relax the ions under the influence of the Hellmann-Feynman forces.

CASTEP uses fast Fourier transforms (FFT) to provide an efficient way of transforming various entities (wavefunctions, potentials) from real to reciprocal space and back as well as to reduce the computational cost and memory requirement for operating with the Hamiltonian on the electronic wavefunctions, a plane-wave basis for the expansion of the wavefunctions. The convergence of this expansion is controlled by a single parameter, namely the highest frequency at which the series is terminated (conventionally defined as the highest kinetic energy of a plane-wave).

2.4 Energy calculations

We have employed the CASTEP code [57] to describe the total energy of the Minerals surfaces. The cleaving of surfaces releases some excess energy per unit area and this is defined as surface energy. This was then used to determine the most stable surface; as such the most stable surface is the one with the lowest positive value. This was obtained using equation 2.13 with units of eV/Å^2:

$$E_{surface} = \left(\frac{1}{2A}\right)[E_{slab} - (n_{slab})(E_{bulk})], \quad 2.13$$

where $E_{(slab)}$ is the energy of the surface, $E_{(bulk)}$/atom is the energy of the bulk per total number of atoms in the bulk and $n_{(slab)}$ is the number of atoms of the surface and A is the surface area. This formula is used to account for the number of atoms in the surface and normalize it to the bulk.

The adsorption energies for oxidation, hydrations, organic collectors (ligands) on the surface are defined as the mean adsorption energy or energy per molecule on the surface and are calculated using this formula in (eV):

$$E_{adsorption} = [E_{system} - (E_{surface} + nE_{adsorbate})]/n\,, \quad 2.14$$

where E_{system} is the energy of the surface slab and the adsorbate/s, $E_{surface}$ is the energy of the clean surface slab and $E_{adsorbate}$ is the energy of the isolated adsorbate and n is the number of adsorbates on the surface. Within this calculation, negative adsorption energy corresponds to an exothermic adsorption process and a positive adsorption energy corresponding to an endothermic process. The adsorption energy was also calculated in (KJ/mol), a multiplication of 96.485 (KJ/mol)/eV where adsorption of multi water molecules on the surface was considered. For complete oxidation and hydration, the surface coverage (Φ) is defined as:

$$\Phi = \frac{\text{Number of occupied adsorption site (metal)}}{\text{Number of adsorption site (metal) present}} \quad 2.15$$

2.5 Density of states

The density of states (DOS) of a system describes the number of states per interval of energy at each energy level that is available. The DOS indicates how densely packed quantum states are in a system. Integration of DOS over a range of energy yields a number of states;

$$N(E) = \int_{E}^{\Delta E} g(E)dE \quad 2.16$$

where N(E) denotes the carrier density and g(E)dE represents the number of states between E and dE. The density of states permits integration to be done with respect to the electron energy instead of the integration over the Brillouin zone. It is often used for quick visual analysis of the electronic structure. Characteristics such as the width of the valence band, the energy gap in insulators and the number of intensity of the main features help interpret experimental spectroscopic data. The most accurate

methods used are based on linear or quadratic interpolations of band energies between the reference points in the Brillouin zone. The most popular and reliable technique is based on the tetrahedron interpolation. However, it is not well suited to the Monkhorst-Pack grid of special points [58].

In the study of complex minerals, there can be a formation of the pseudogap in the electronic density of states at the Fermi energy (E_F) and the relation of this feature to the stability of the particular structure. Pierce *et al.* [59] and Matsuda *et al*. [60] have suggested the role of the pseudogap in the structural stability by the experimental observation of very high resistivity in structurally well-ordered stable quasicrystals. Several contexts have proposed the direct relations between the formation of a pseudogap and stability of the structure. Literature reveals that densities of states are also essential in determining the stability trend of structures with the same composition with respect to the E_F. The theory suggests that the element with the highest density of states around the E_F is considered the least stable, while the element with the lowest density of states is most stable. Moreover, the element with a greater contribution at the E_F is the most active or reactive element.

2.6 Mulliken charges and population

The attribution of charge to a specific atom within DFT calculations is always somewhat arbitrary and one must remember that pseudo charge can only be calculated which is based on Kohn-Sham electronic density. There are no real atoms; there are only nuclei and a wavefunction and a charge density of electrons in the field of those nuclei. From the obtained spatial charge density, there are several different schemes of partitioning this charge density into sites or ”atoms” (see e.g. [61]) for a more complete overview) and it is worth comparing the results from different methods in order to better understand what ”really happens” in the system and to get some idea on the accuracy that can be achieved when willing to make charge analysis per sites (and possibly orbitals) with DFT.

The properties of chemicals and materials are often described in terms of charge transfer between atoms and the presence of ionic charges or electric multipoles on atoms or molecules. Theoretical calculations producing estimates of the electronic charge distribution in the system can, in principle, provide this type of information but

it is not clear how to extract it. The atomic charges in molecules or solids are not observables and therefore not defined by quantum mechanical theory. The output of quantum mechanical calculations is a continuous electronic charge density and it is not clear how one should partition electrons amongst fragments of the system such as atoms or molecules. Many different schemes have been proposed, some are based on electronic orbitals (such as Mulliken Population Analysis) and others based on only the charge density such as Bader's atoms in molecules method.

The Mulliken analysis is the most commonly used orbital based method. It can be applied when basis functions centred on atoms are used in the calculation of the electronic wavefunction of the system. The charge associated with the basis functions centred on a particular atom is then assigned to that atom. This can be a fast and useful way of determining partial charges on atoms but it has the major drawback that the analysis is sensitive to the choice of basis set.

In practice, the corresponding matrix elements of density and overlap matrices are multiplied to form the population matrix in such a way, that electronic density from the overlap matrix is partitioned equally between atoms. This method has the great advantage of simplicity and efficiency. Since it requires the use of an atom centred basis, the main drawback of this method will be its high sensitivity to the choice and optimization of that basis. It works best for small basis sets and in order to allow for charge comparisons the same basis sets must be used for all calculations.

2.7 Experimental part

The experimental part was done by our experimental collaborators from centre for minerals research at UCT and part of the work has already been published in the Master of Science in Chemical Engineering [10]**.**

2.7.1 Microflotation.

Miniaturised flotation experiments can be useful in proving direct applicability of trial ligands to the real-world flotation system. Whilst the method does not provide direct validation of computational work per se (being orders of magnitude more complex) it was deemed worth pursuing to put the modelling work in context. The 'theory'

underpinning micro flotation is the same as that for flotation, simply on a smaller scale, so a separate theoretical consideration of micro flotation is unrequired.

2.7.2 Mineral Preparation

Pure sulphide minerals of interest in this study are pyrite and galena, These were received from the Ward's Natural Science Establishment NY as chunks of up to 150 mm diameter. The chunks were hammered manually and then pulverised for 15 seconds in a laboratory disk mill (*Siebtechnik)* to 100% passing -106 µm. The material was then dry sieved into two fractions: - 38 µm for microcalorimetry and + 38 µm to -106 µm for micro flotation. The material was split using a rotary splitter into 10 samples. All the samples were stored under nitrogen at - 30°C to minimise oxidation of the samples.

2.7.3 Mineralogical analysis of the sulphide minerals

X-ray diffraction (XRD) was used to determine the mineralogical compositions or phases of the sulphide minerals. Powder XRD spectra were obtained using a Bruker D8 Advance powder diffractometer with Vantec detector and fixed divergence and receiving slits with Co-Ka radiation. The phases were identified using Bruker Topas 4.1 software [62] and the relative phase amounts (weight %) were estimated using the Rietveld method.

Pure sulphide minerals were desirable for this work as impurities would lead to complex interactions and interference with the targeted sulphide mineral-collector interactions. The mineralogical analysis is shown in Table 2.1.

Galena and pyrite were relatively pure, being 100% and 95% of the desired mineral type. In addition, 3.6% of the pyrite contaminant was quartz, an inert mineral.

Table 2.1: X-ray diffraction results for pyrite and galena

	XRD results		
Expected mineral	**Mineral**	**Composition %**	**Chemical Formula**
	Pyrite	94.9	FeS_2
	Chalcopyrite	1.5	$CuFeS_2$
Pyrite	Quartz	3.6	SiO_2
Galena	Galena	100	PbS

2.7.4 Reagents

Thiol collectors used in this study were supplied by Senmin (Pty) Limited. Different xanthate homologues were supplied in powder form while DeDTP and dithiocarbamates were supplied in solution form at basic pH to stabilise them. All the collectors used in this study are shown in Table 2.2. It must be emphasised that all collector dosages were calculated based on active content.

Table 2.2: List of collectors used in this work

Collector	Abbreviation	Molecular Mass (g/mol)	Purity, % (w/w)
Sodium Ethyl Xanthate	SEX	144	100
Sodium Diethyl Dithiophosphate	DeDTP	208	43.5
Sodium Diethyl Dithiocarbamate	DeDTC	171	24.6

2.7.5 Collector dosage calculations

The Brunauer–Emmett–Teller (BET) method was used to determine the surface areas of all the mineral samples, both the – 38 µm and the + 38–106 µm size fractions. The BET method is premised on the physical adsorption of gas molecules on a solid surface as a basis to approximate the specific surface area of a given material. The results are as shown in Table 2.3.

Collector dosages for both microcalorimetry and microflotation were calculated using the BET surface areas and the cross-sectional area of the head-group of the collector molecule, 28.8 A° [63]. In these calculations, it was assumed that all the minerals were 100% pure for simplicity. It is assumed that the xanthate, dithiocarbamate and the dithiophosphate molecules have the same cross-sectional area of the thiol head-group. It must be noted that the total molar dosage was maintained constant for the collector mixtures.

Table 2.3: Surface area of the -38 μm and the +38-106 μm size fractions of all minerals

Mineral	BET Surface Area(m^2/g)	
	-38μm	-106μm/+38μm
Galena	0.3477	0.1142
pyrite	0.6213	0.3946

2.7.6 Microcalorimeter

A TAM III isothermal titration microcalorimeter manufactured by TA instruments was used in the heat flow mode to measure heats of adsorption at 25 °C. Details of the equipment, calibration and reproducibility are described elsewhere [64]. The output of the TAM III microcalorimeter is in the form of a power versus time curve which appears as peaks where each peak corresponds to the addition of an aliquot of the titrant. The specific heats of adsorption per injection were calculated by integrating the area under each peak and dividing it by the number of moles of collector contained in each injection. A pH of 9.2 was chosen as a typical BMS-processing pH and sodium hydroxide was used as a pH modifier throughout the investigations. Blank experiments were performed in which all the collectors were diluted into a solution with no mineral present. The heat of dilution was then subtracted from the total heat of interaction to give the heat of interaction between mineral and collector. It was observed that the DeDTP had the greatest heat of dilution.

0.2 ± 0.0005 g of the mineral samples were weighed into the sample and reference ampoules. 0.7 mL of pH 9.2 water was added to each ampoule and sonicated for 30 s to disperse the slurry before being loaded into the microcalorimeter. The collector solution was loaded into the titration syringe and 2 μL, a volume equivalent to 0.25 monolayer coverage, was injected every hour. 20–25 injections were performed, which are equivalent to 5–6 monolayers, although only the heat of adsorption corresponding to 50% pseudo-monolayer coverage is reported in this paper. Half a monolayer was chosen since, at this concentration, collector molecules are interacting directly with the mineral surface and not with each other, as they would at dosages above one monolayer. 50% of pseudo-monolayer surface coverage was also chosen as the collector dosage for microflotation experiments to allow direct comparison between

the calorimetric results and the microflotation results. To calculate the molar enthalpy of adsorption, the heat of interaction was divided by the number of moles of collector that were added. This assumes that all of the collectors interact with the mineral surface. This has been shown to be the case in a number of experiments performed in our laboratories and this data has been added as supplementary material. Due to the fact that each experiment took around 25 h to be completed, only one run was conducted for each investigation reported in this work.

2.7.7 Procedure for microflotation tests

A UCT microflotation rig was used to measure the relative hydrophobicity of different mineral surfaces [65]. 3 g of the sulphide mineral was weighed out into a beaker; 50 mL of pH 9.2 solution was added and sonicated for 5 min to disperse the slurry, destroy agglomerates and to remove ultra-fines from the mineral surfaces. The slurry was then transferred to the microflotation cell and the cell was topped up with pH 9.2 water to the mark. Collector solution equivalent to 50% theoretical surface coverage (2.88×10^{-6} mol/m^2 of the mineral surface area) was dosed using an auto pipette. Air at a flow rate of 10 ml/min was introduced from the bottom of the cell after 6 min conditioning time. Concentrates were collected at 2, 6, 12 and 20 min. Experiments were done in duplicates and averages were then calculated and reported in this work.

Chapter 3

Bulk, Surface structure relaxation and theoretical Studies of Reagents.

While the choice of the exchange-correlation functional determines the accuracy that can in principle be reached with the DFT calculation, several other technical parameters influence the accuracy from the numerical side. All the latter parameters need to be tested in detail to ensure numerical convergence of the calculations.

3.1 The convergence of cut-off energy and k-points sampling

Each numerical calculation can depend on various parameters, which do not describe the physical system but only influence the algorithm and precision used for the simulation. To obtain physically correct, converged results, one has to make sure that the influence of these parameters on the result is sufficiently reduced. One also has to keep in mind that the computational complexity (and with that the runtime required for the calculation) increases with the precision. Typical convergence parameters for plane-wave DFT include the choice of the kinetic cut-off energy and k-points.

3.1.1 Cut-off energies

To determine the appropriate cut-off energy for FeS_2, $CuFeS_2$, PbS and ZnS, single-point calculations were performed for different kinetic energy cut-offs at a default number of k-points for each system within GGA-PW91 for FeS_2, $CuFeS_2$ and PbS, GGA-PBE for ZnS using CASTEP CODE. We used ultrasoft pseudopotentials [66], which require significantly less computational resources than the norm-conserving potentials [67]. The interactions between valence electrons and ionic core were represented with ultrasoft pseudopotentials. Valence electrons configuration considered in this study included Fe $3d^6\ 4s^2$, S $3s^2\ 3p^4$, Cu $3d^{10}\ 4s^1$, and Fe $3d^6\ 4s^2$, Pb $5d^{10}\ 6s^2\ 6p^2$ and Zn $3d^{10}\ 4s^2$ states. A plane wave cut-off energy of 550 eV was sufficient to converge the total energy of PbS while the energy of 450 was sufficient for FeS_2, $CuFeS_2$ and ZnS systems. The thicknesses of the vacuum layer for all four crystals structures are 20 Å. beyond these values energy differences of less than 1meV/atom are obtained. We choose this cut-off energy to reduce computational cost.

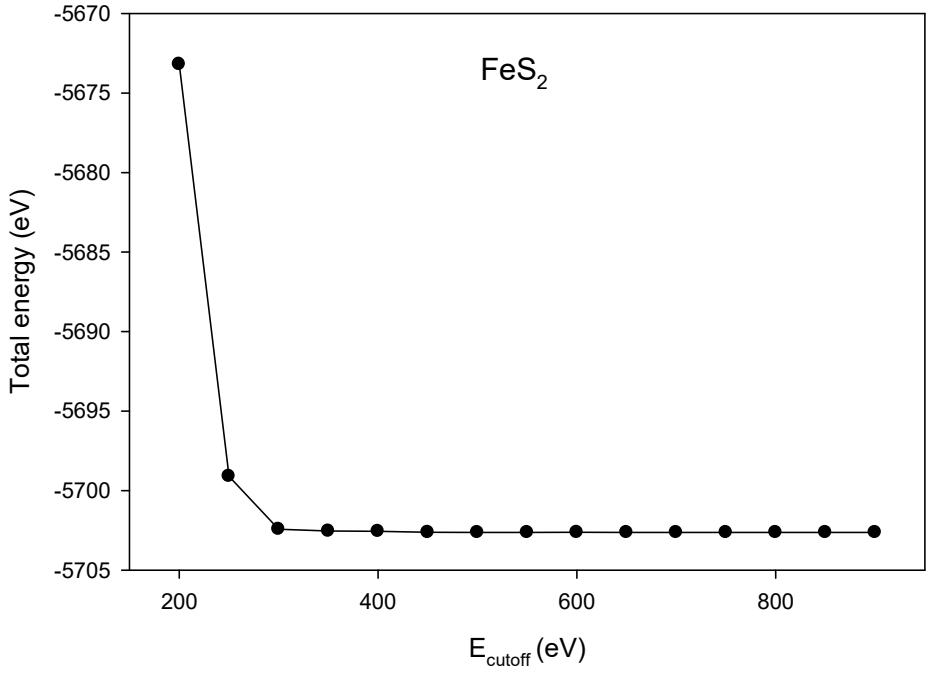

Figure 3.1: Total energy against kinetic energy cut-off for FeS_2 structure.

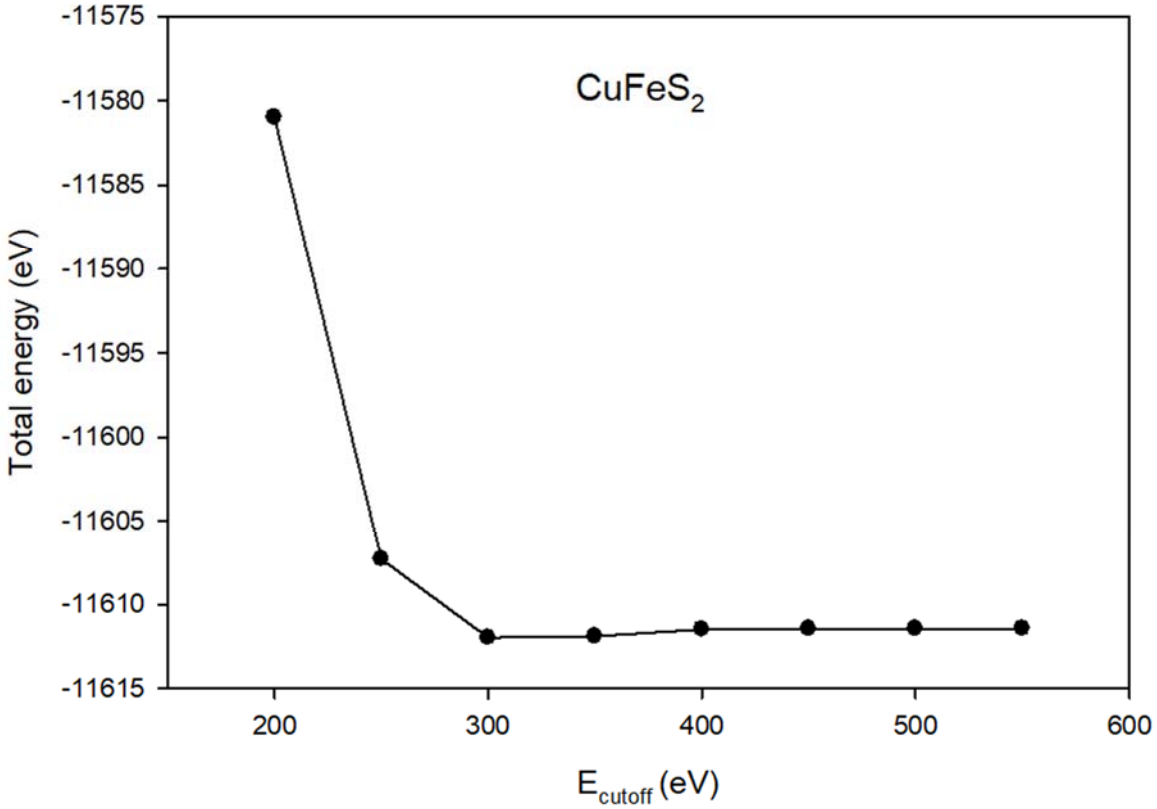

Figure 3.2: Total energy against kinetic energy cut-off for $CuFeS_2$ structure

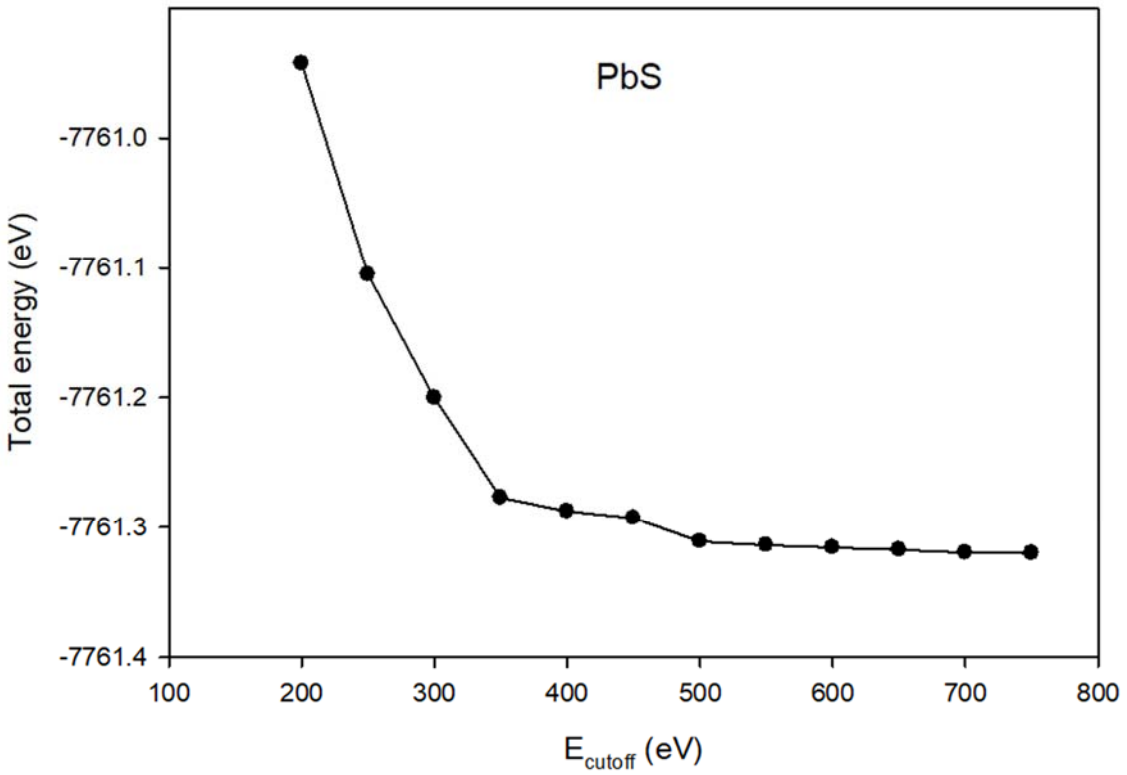

Figure 3.3: Total energy against kinetic energy cut-off for PbS structure.

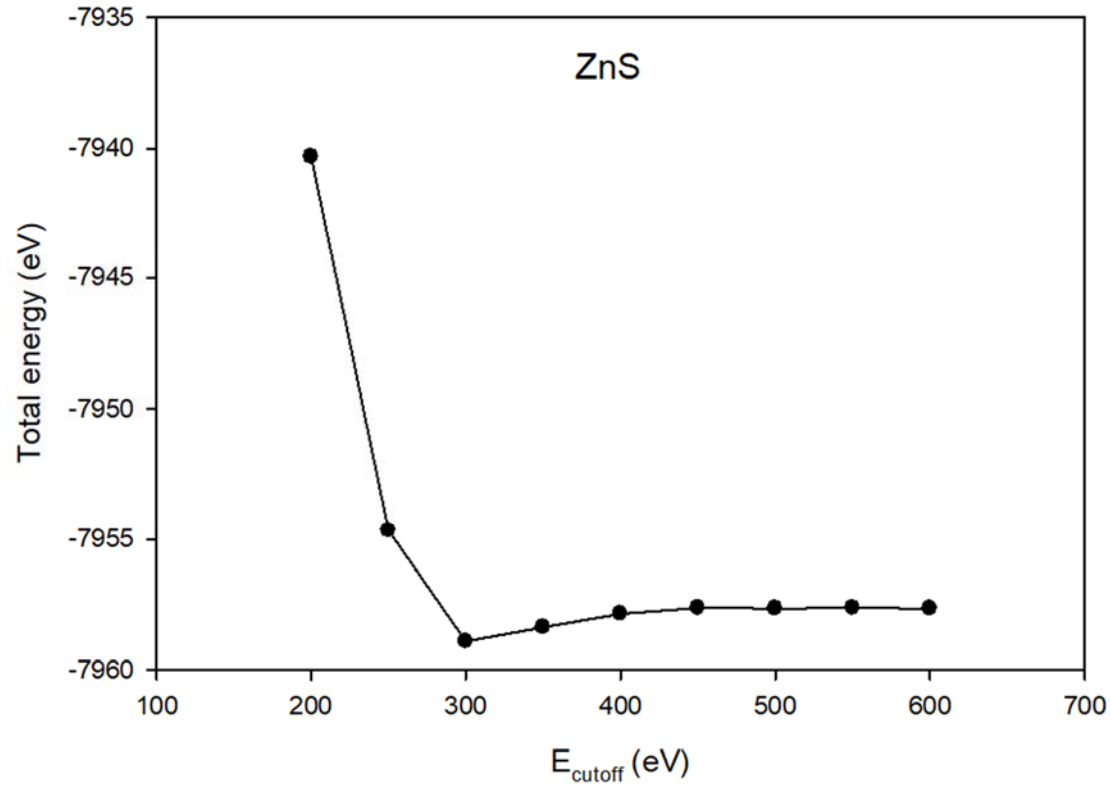

Figure 3.4: Total energy against kinetic energy cut-off for ZnS structure.

3.1.2 K-points

After suitable kinetic cut-off energies were obtained, it is crucial to also determine the appropriate number of k-points to use in plane-wave pseudopotential calculations. Several methods have been suggested for special k-points sampling in the Brillouin zone. Such methods help in obtaining an accurate approximation for the total energy by calculating the electronic state at a very small number of k-points. The Monkhorst-Pack scheme [58] of the k-points sampling was used to select an optimal set of special k-points of the Brillouin zone such that the greatest possible accuracy was achieved from the number of k-points used. Different values of k-points mesh parameters were for different structures. Appropriate k-points mesh parameters were found to be 7x7x7 for FeS_2, 8x8x1 for $CuFeS_2$, 5x5x5 for PbS and 6x6x6 for ZnS. At this point, it was observed that the total energy between two consecutive points converged to within 1 meV.

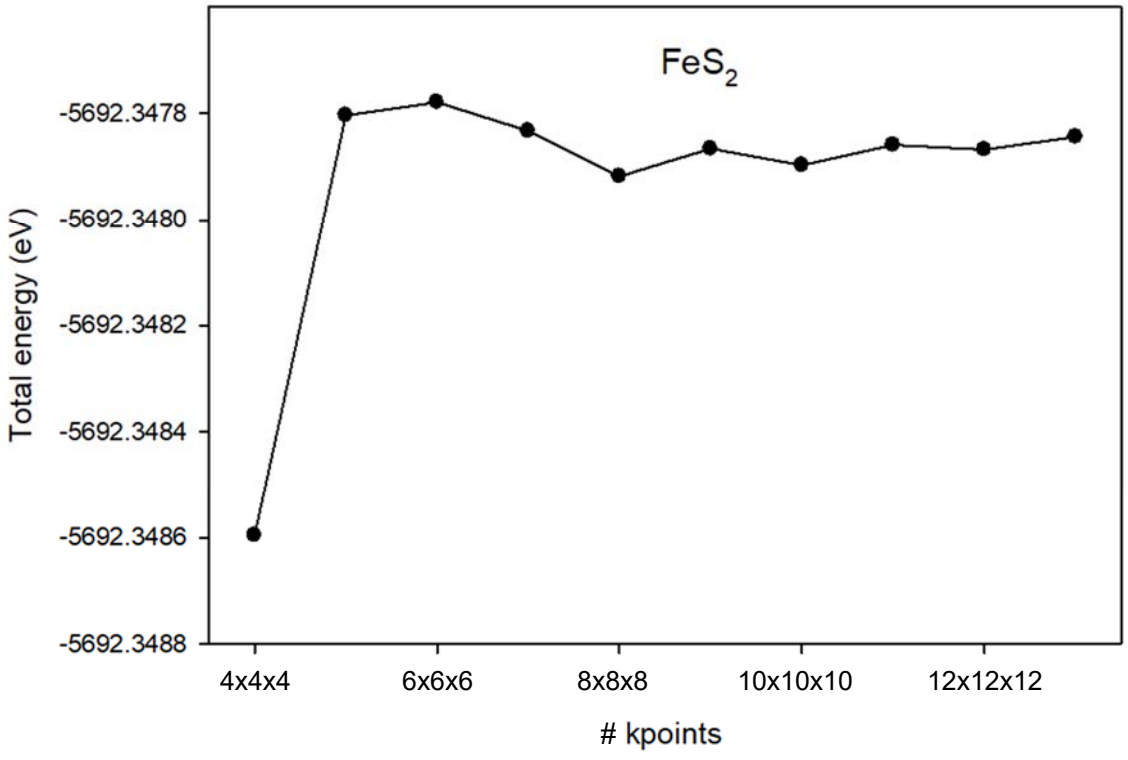

Figure 3.5: Total energy against k-points mesh for FeS_2 structure.

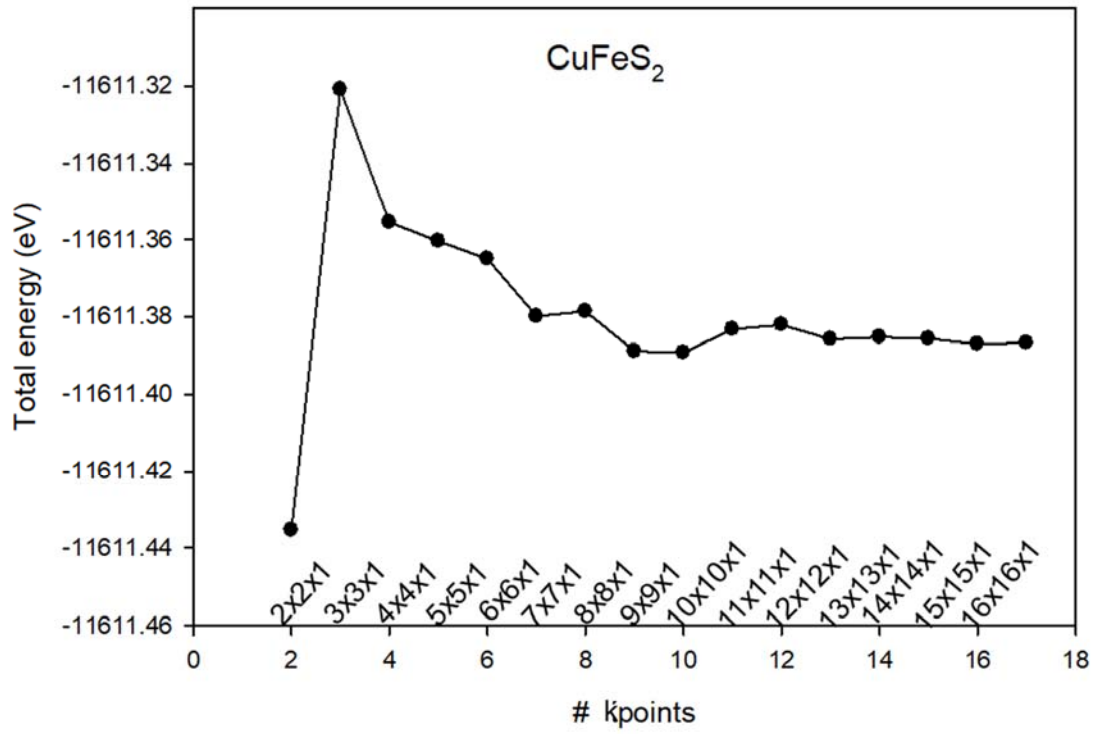

Figure 3.6: Total energy against k-points mesh for $CuFeS_2$ structure

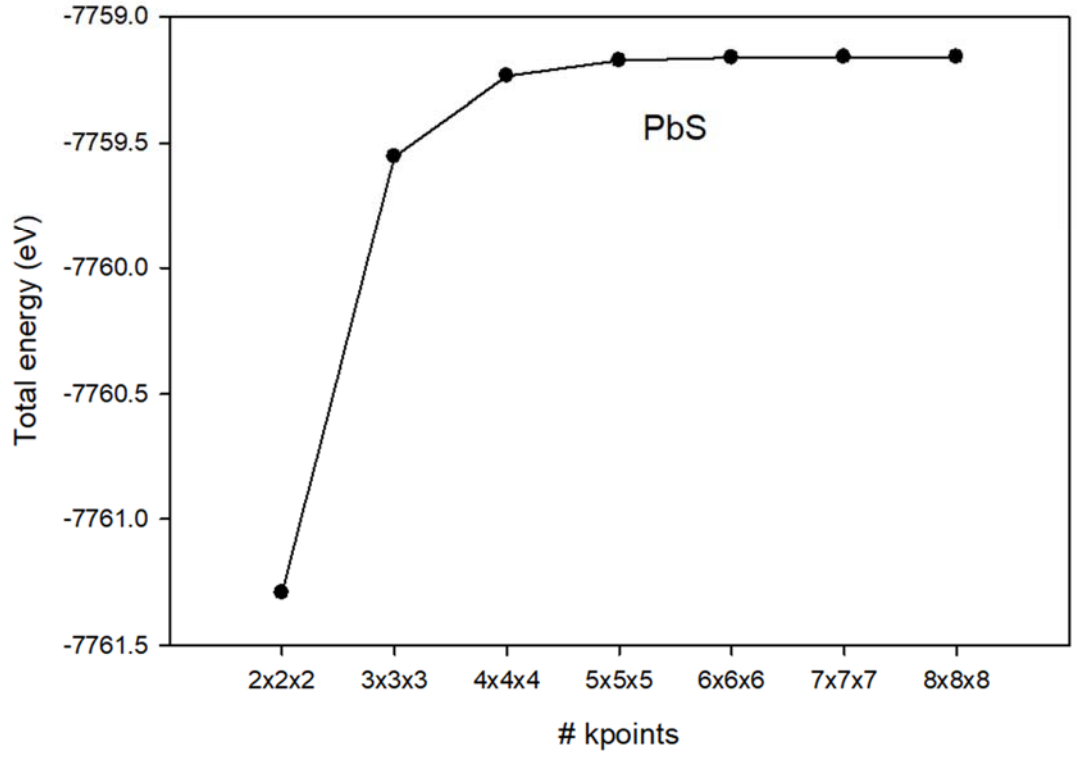

Figure 3.7: Total energy against k-points mesh for PbS structure.

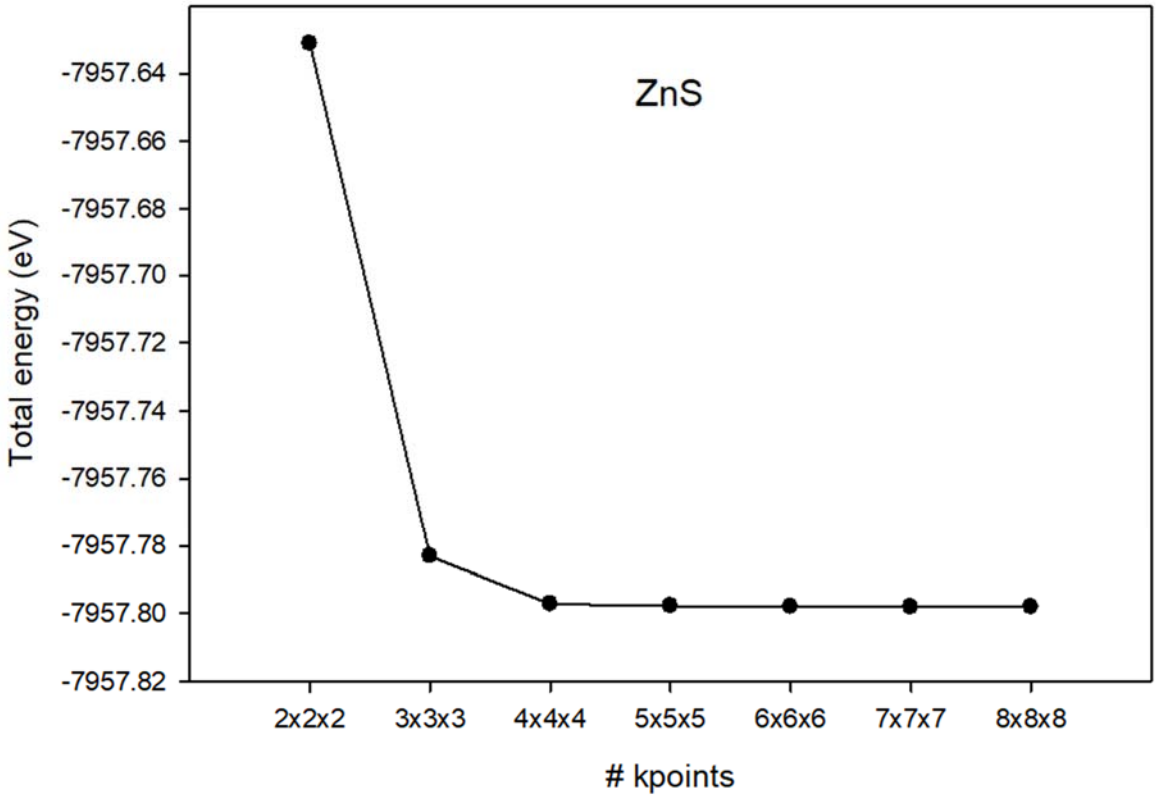

Figure 3.8: Total energy against k-points mesh for ZnS structure.

3.2 Structural optimisation and working surfaces

To study the reactivity of the mineral surface using electronic structure calculations, it is necessary to define a suitable model for the calculation. The first step is a study of bulk structure to determine an optimal set of parameters for the proposed model that best reproduces the properties of the real material. After this inevitable first step, it is necessary to choose a proper surface for the adsorption and effect of water studies (see Chapters 4 and 5). In this chapter, the reasoning behind the selection of the surface is presented. Before any more complex simulations with surfaces can be done, one first has to know the structure of the bulk. Hence the lattice constants were determined by employing DFT calculations.

3.2.1 Pyrite

Determination of the working surface

In Figure 3.9 and Table 3.1, we present the crystallographic data for the pyrite system. Previous experimental data is also given where available. A k-point grid mesh of 7x7x7 and 2x2x1 were used for the bulk and surface slab models, respectively.

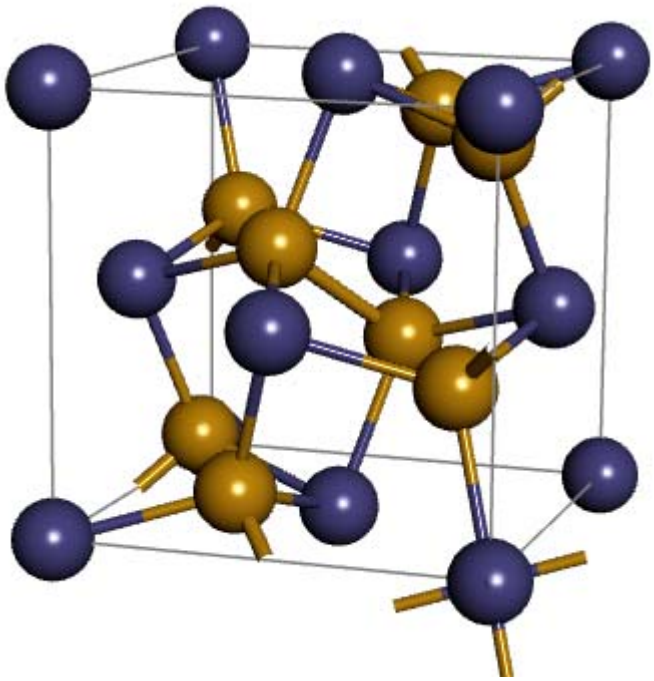

Figure 3.9: Bulk unit cell of FeS_2

Table 3.1: Structural parameters of optimised bulk FeS_2 compared with experimental values.

Property	Value (Å)	Population	Literature (Å)
Unit cell length(a=b=c)	5.414		5.406[a]
Fe–S bond	2.560	0.35	2.23–2.30[a]
Fe-Fe bond	3.827	-	3.808
S–S bond	2.196	0.22	2.14–2.17[a]

a [68],

The Pyrite (FeS_2) structure crystallises in the cubic system with space group Pa3, as shown in Figure 3.9. It possesses a lattice constant of 5.414 Å and one cell contains four FeS_2 units. The cation Fe^{2+} is in octahedral coordination with six dianions (S_2^{2-}) while each anion is tetrahedrally coordinated to three Fe ions and one other anion.

We note that our calculated results are consistent with the experimental values (<1% difference), suggesting the reliability of the approach employed in this study. Fe-S coordination has equivalent six bonds with the lengths of 2.560 Å, while S–S and Fe-Fe have lengths of 2.196 Å and 3.827 Å, respectively. Moreover, we noted that the octahedral Fe-Fe share a common corner. Goodenough [69] reported that the interactions between two octahedral cations will be cation-anion-cation interactions if

the two octahedra share a common corner but cation-cation interactions if the two octahedra share a common edge. The Mulliken bond population result shows values of 0.22 and 0.34 for the S–S interactions and Fe–S, respectively. The population in the Fe–S region is greater than that in the S–S region, indicating stronger covalent interaction between Fe and S atoms

Table 3.2: Calculated and experimental surface energies (J/m^2) for pyrite mineral.

MI	**Value (J/m^2)**	**Literature (J/m^2)** [70]
100	1.04	1.06
110	1.68	1.68
111	1.40	1.40
210	1.66	1.50

In Table 3.2 we present the calculated and experimental surface energies for the pyrite mineral. The surface energy we calculated according to equation 2.13. Similarly, to the lattice constant and population value, we note a good agreement between our calculated and experimental results. The lower the surface energy, the more stable is the surface. We note that the (100) terminated surface is the most stable, followed by the (111), (210) and (110), respectively. Furthermore, we note that the order of stability obtained in this work matches with the data in the literature. It is worth noting that the DFT treatment of surfaces in this study is more rigorous, and the predicted surface energies are more stable. This was also based on the report that during the first stage of flotation where mineral particles are crushed, the minerals will mainly cleave along surfaces that have large inter-planar spacing and few inter-planar bonds, usually low-index surfaces with low surface energies under dry conditions [71].

Since the surface free energy of FeS_2 can be expressed as a function of the Wulff-constructions facets, the obtained construction should also be related to the three-dimensional equilibrium shapes of FeS_2. The exposed surfaces are labelled accordingly. In Figure 3.12 we show that the shape of the FeS_2 crystal is a truncated octahedron, covered by the (100) and (111) surfaces. Furthermore, the (100) terminating the apices of the octahedron has higher surface ratio than (111) at the

surface of the octahedron. There is no significant change in structure for the most stable surface before and after optimisation (see Figure 3.11). There is no visible appearance of other surfaces. On this basis, the (100) terminated surface will be used as the pyrite working surface. A side-on view of a 15-layer, 2x2 supercell of the pyrite working surface and a top-down-net of the same are shown in Figure 3.11.

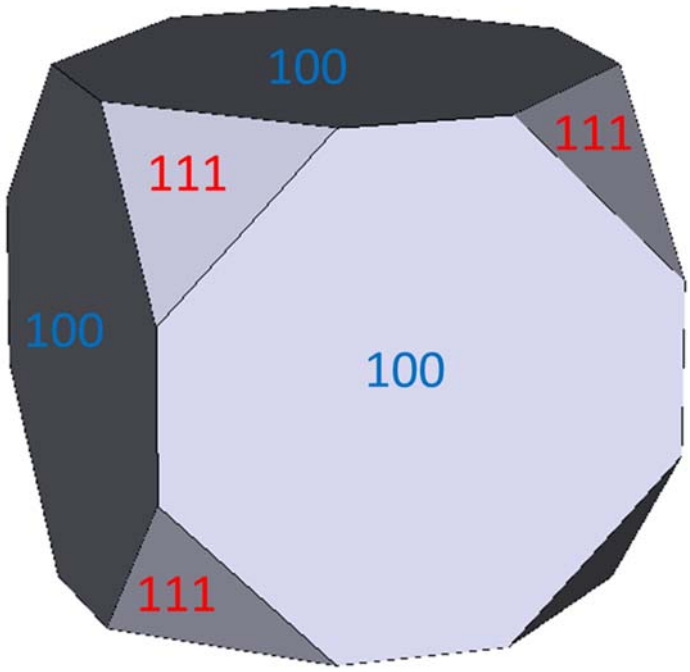

Figure 3.10: Wulff construction of FeS_2 surfaces

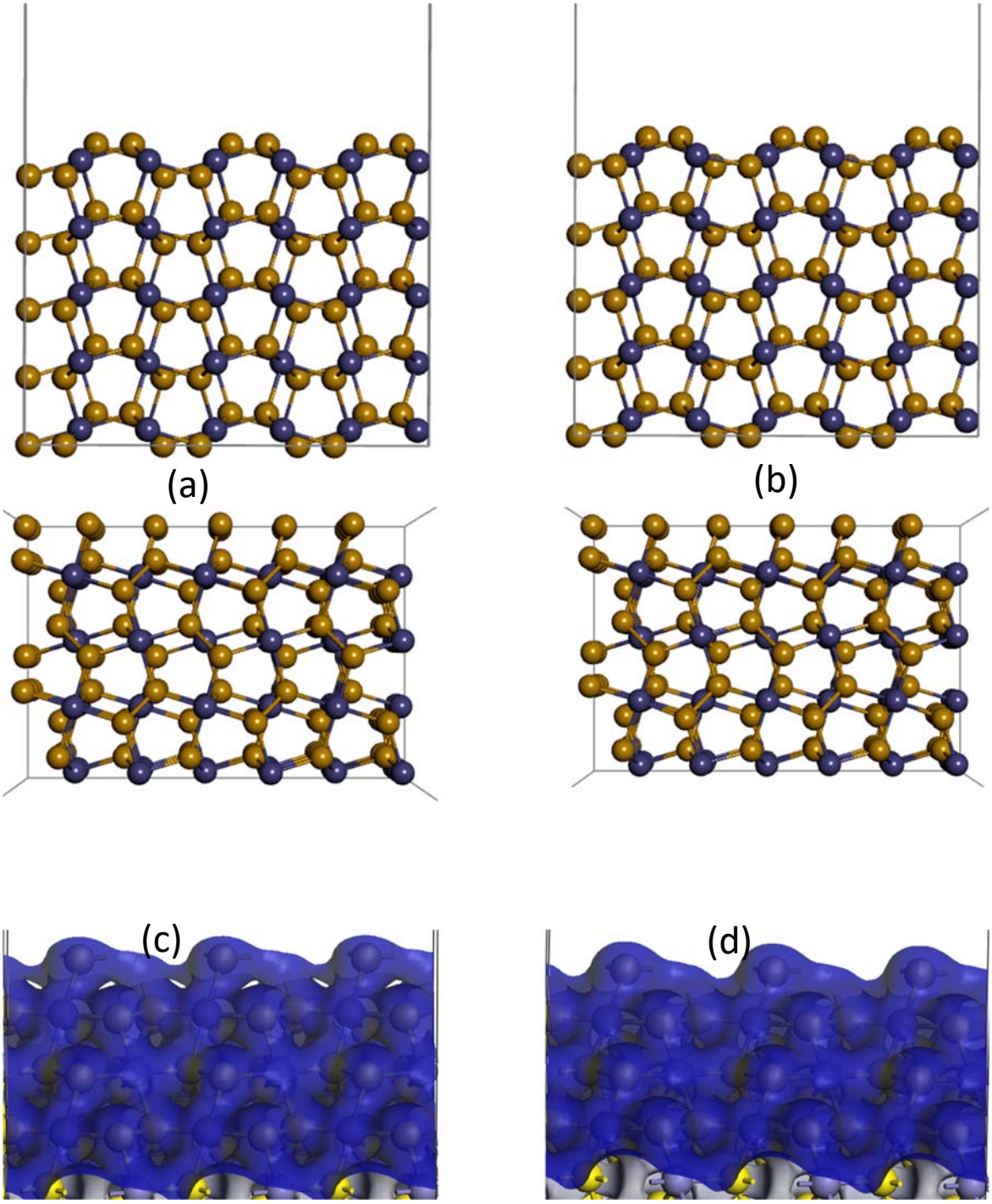

Figure 3.11: Pyrite FeS_2 (100) surface: (a) Before being relaxed and (b) Fully being relaxed. The electron density of pyrite (100) surfaces: (c) unrelaxed and (d) relaxed.

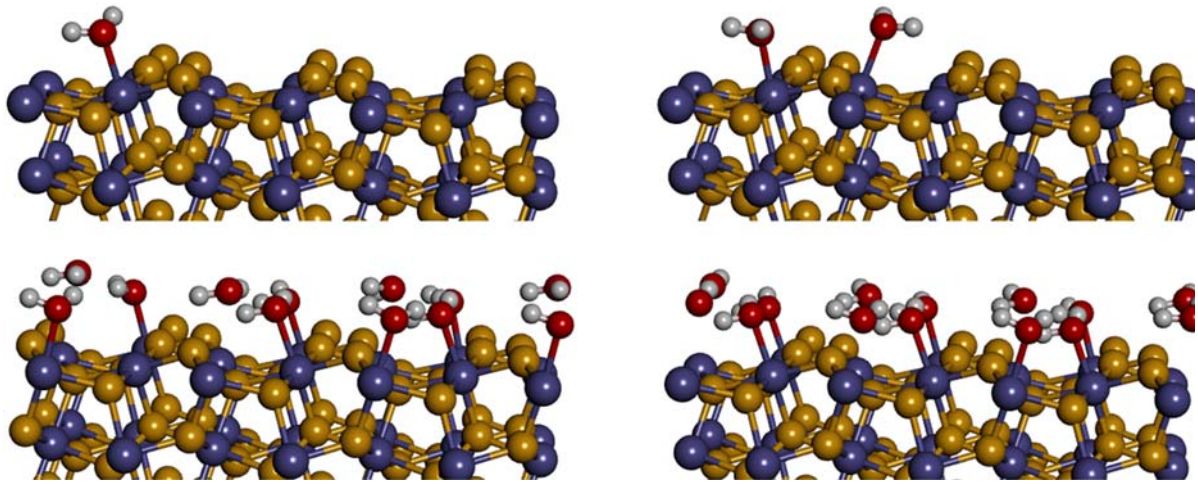

Figure 3.12: Water adsorbed on the FeS_2 (100) surface

Before the reagent adsorption, water molecules were placed on the FeS_2 (100) surfaces to investigate the effect of water on the surface properties. The optimised geometry configurations are shown in Figure 3.12. To discuss the influence of water adsorption on the surface properties of FeS_2, the bond populations and lengths and Mulliken charges between FeS_2 atoms are listed in Table 3.3 to Table 3.4.

Table 3.3: Pyrite Mulliken bonding population of atoms in the absence and in the presence of H_2O molecule(s) on the surface.

		Bond	**Population**	**length**
FeS_2(100)	In the absence of water molecule	S3 - Fe1	0.48	2.176
		S4 – Fe1	0.51	2.219
		S3 - Fe2	0.52	2.221
		S5 - Fe2	0.49	2.164
	In the presence of water molecule	S3 - Fe1	0.54	2.244
		S4 – Fe1	0.49	2.181
		S3 - Fe2	0.45	2.201
		S5 - Fe2	0.44	2.241

We note that the Mulliken atomic charges populations on the FeS_2 surfaces layers before and after H_2O absorption are different. The charge of Fe1 atom increases from 0.07e to 0.15e, while the charge of Fe2 reduces from 0.07e to 0.02e, indicating Fe1 becomes more positive and Fe2 more negative. On the other hand, we note that the charges of S1 and S2 become more negative. This shows that the Fe atoms lose electrons while S atoms gain more after the adsorption of the water molecule.

Table 3.4: Mulliken charge populations before and after H_2O adsorption on the pyrite surface (s, p and d are the orbitals).

			s	p	d	total	q/e
FeS_2(100)	In the absence of water molecule	**Fe1**	0.34	0.44	7.14	7.93	0.07
		S1	1.86	4.25	0	6.1	-0.1
		S2	1.82	4.2	0	6.02	-0.02
		Fe2	0.35	0.44	7.14	7.93	0.07
		S1	1.82	4.2	0	6.02	-0.02
		S2	1.86	4.25	0	6.1	-0.1
	In the presence of water molecule	**Fe1**	0.33	0.43	7.09	7.85	0.15
		S1	1.85	4.29	0	6.15	-0.15
		S2	1.84	4.32	0	6.16	-0.16
		Fe2	0.35	0.49	7.14	7.98	0.02
		S1	1.81	4.17	0	5.98	0.02
		S2	1.84	4.3	0	6.15	-0.15

For FeS_2, the atomic relaxation on the top layer of the surface is not very remarkable. However, it is worth noting that the displacement of surface atoms is greater after the surface atoms were reacted with the H_2O molecule, i.e., Fe1, Fe2, S1 and S2, is much greater than that of the other surface atoms.

We note that the S4 – Fe1, S3 - Fe2 and S5 - Fe2 bond population decrease after water adsorption, while it increases between the S3 - Fe1 bond. This indicates that

water adsorption generally reduces the covalent bonding between Fe and S atoms in FeS_2.

3.2.2 Chalcopyrite

Determination of the working surface

Crystallographic data for chalcopyrite is presented in Table 3.12. A k-point grid of 8x8x1 was used for bulk model and 2x2x1 for surface slab models.

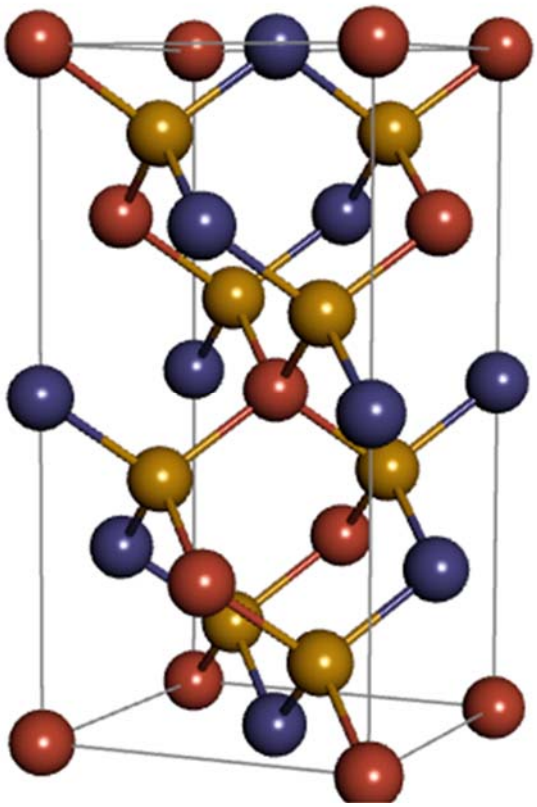

Figure 3.13: Bulk unit cell of $CuFeS_2$

The lattice parameters of the bulk chalcopyrite after geometric optimization agree highly with the experimental values obtained by Hall and Stewart [72], i.e., a value of 5.135 vs. 5.289 Å and c value of 9.978 vs. 10.423 Å, indicating that the computational setting of this study is highly reliable. In addition, the distances of Fe–S and Cu–S bonds in this work are 2.225 and 2.303 Å, respectively, which are within a very minor difference as compared to that experimentally identified—i.e., a 0.032 and 0.001 Å difference from the related experimental values [72].

Table 3.5: Structural parameters of optimised bulk $CuFeS_2$ compared with experimental values.

Parameter	Value(Å)	population	Literature(Å)
a=b	5.1347		5.289[a]
c	9.978		10.423 [b]
Fe–S	2.124	0.50	2.257
Cu-S	2.286	0.36	2.302
Fe-Fe	3.580		3.713
Cu-Cu	3.580		3.713
Fe-Cu	3.580		3.740
S–S	3.484	0.22	3.685

The bond lengths of Fe–Fe, Cu–Cu and Fe–Cu are calculated as 3.580, 3.580 and 3.580 Å, respectively, consistent with that both measured and calculated using other software, such as PWscf Quantum Espresso package and Siesta [73], as shown in Table 3.5. Moreover, the S–S bond is calculated as 3.484 Å, which is within a 5% variation compared to the experimental result of 3.685 Å. These calculations indicate that the optimization process is well performed.

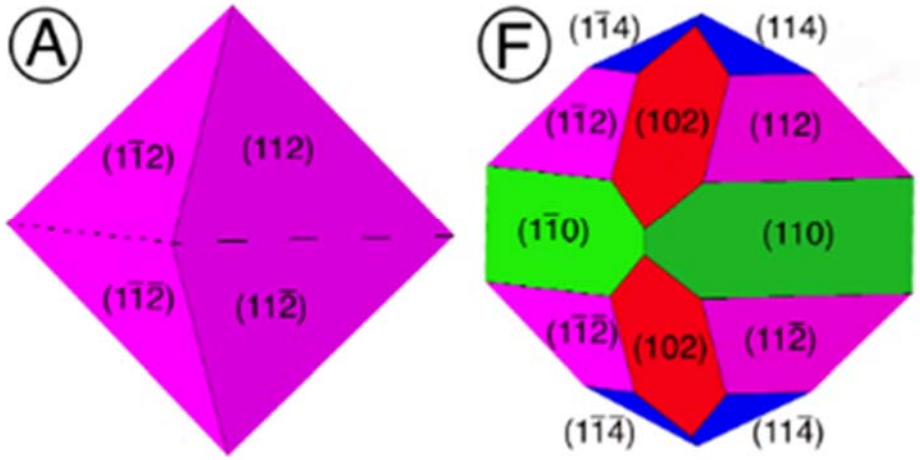

Figure 3.14: Wulff constructions of $CuFeS_2$ under growth conditions A (Cu-poor) and F (Cu-rich) defined in Table II. Due to symmetry, (hkl) is equivalent to (hkl),(hkl) and (hkl). Taken from surface morphology of $CuFeS_2$: The stability of the polar (112)/(112) surface pair by V. H.-Y. Chen et al [74].

As shown in Figure 3.13. The optimization performed using Materials Studio indicates that the developed pseudopotential and numerical basis sets are capable of simulating

bulk chalcopyrite. From the Wulff constructions and other theoretical studies, (112) surface would be our working surface to investigate.

Table 3.6: Surface energies (J/m^2) for chalcopyrite mineral surfaces computed using computational molecular modelling techniques.

MI	**Value (J/m^2)**	**Literature (J/m^2)** [74]
102	0.62	0.61[b]
110	0.59	0.58
112	0.63 (0.21)	0.61 (0.22)
114	0.68	0.66

The calculations show that the (110) surface is the most stable non-polar surface with a surface energy of 0.59 J/m^2, while the (102) and (114) surfaces are also low in energy (0.62 and 0.68 J/m^2 respectively). The relaxed polar defect-free (112)/(112) surface pair was also found to be thermodynamically stable with a surface formation energy similar to the non-polar (110), (102) and (114) surfaces. The surface pair was stabilised during geometry relaxation due to a combination of electronic and geometric mechanisms that combine to suppress the electrostatic dipole perpendicular to the surface. Specifically, the (112) surface was stabilised via the transfer of charge to the (112) surface, while the (112) surface was additionally stabilised by a combination of geometric and electronic rearrangement. Where the surface energy ended being 0.21 J/m^2. The surface energies are within 3% different from the other theoretical work as indicated in Table 3.6.

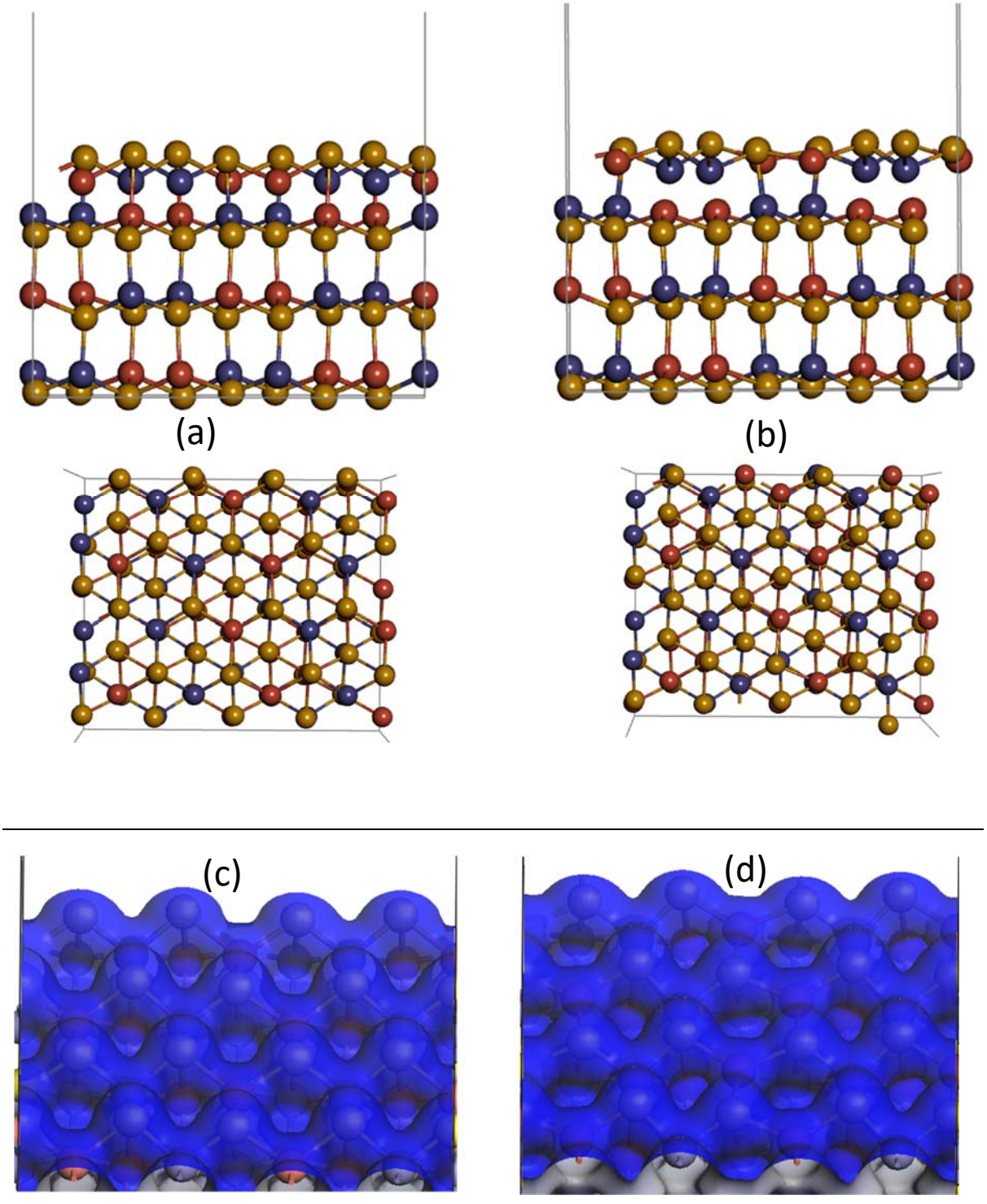

Figure 3.15: $CuFeS_2$ (112) surface: (a) Before being relaxed and (b) Fully being relaxed. The electron density of (100) surfaces: (c) unrelaxed and (d) relaxed.

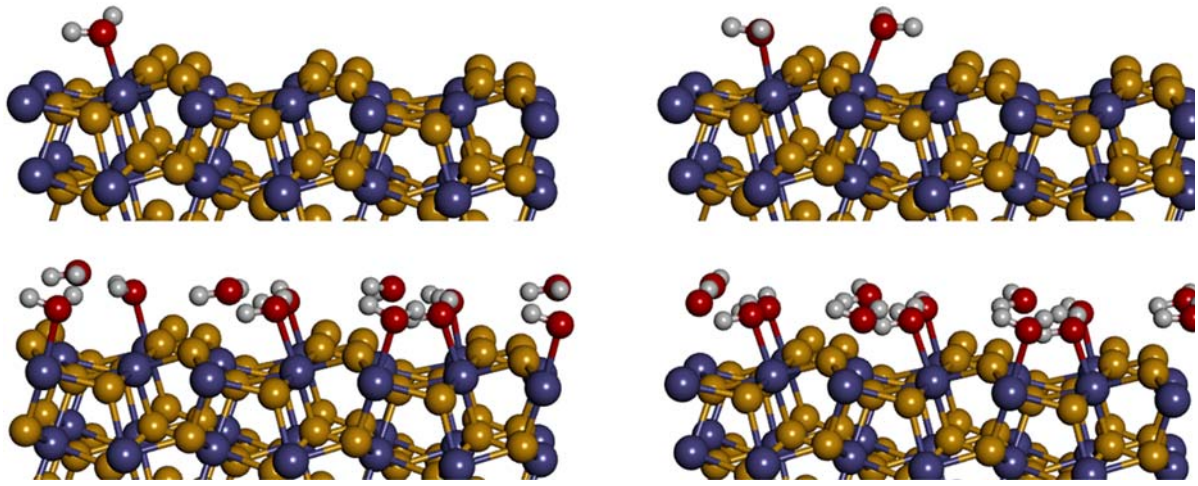

Figure 3.16: Water adsorbed on the $CuFeS_2$ (100) surface.

Table 3.7: Mulliken charge populations of H_2O adsorption on the chalcopyrite surface (s, p and d represent s orbitals, p orbitals and d orbitals, respectively) before and after adsorption.

			s	p	d	total	q/e
$CuFeS_2$(112)	In the absence of water molecule	Fe1	0.33	0.41	6.94	7.68	0.32
		Fe1	0.33	0.41	6.94	7.69	0.31
		Cu1	0.61	0.42	9.73	10.76	0.24
		Cu2	0.61	0.42	9.73	10.76	0.24
		S3	1.85	4.29	0	6.14	-0.14
		S4	1.86	4.3	0	6.15	-0.15
	In the presence of water molecule	Fe1	0.37	0.44	6.94	7.75	0.25
		Fe1	0.37	0.43	6.94	7.73	0.27
		Cu1	0.60	0.45	9.74	10.79	0.21
		Cu2	0.60	0.42	9.75	10.76	0.24
		S3	1.84	4.3	0	6.15	-0.15
		S4	1.86	4.3	0	6.15	-0.15

Table 3.8: chalcopyrite Mulliken bonding population of atoms in the absence and in the presence of H_2O molecule(s) on the surface.

		Bond	Population	length
$CuFeS_2$(112)	In the absence of water molecule	S3–Fe1	0.56	2.127
		S4–Fe2	0.56	2.127
		S3 –Cu1	0.45	2.273
		S4 –Cu2	0.45	2.272
	In the presence of water molecule	S3–Fe1	0.53	2.183
		S4–Fe2	0.57	2.147
		S3 –Cu1	0.42	2.292
		S4 –Cu2	0.42	2.275

3.2.3 Galena

Determination of the working surface

Crystallographic data for galena is presented in Table 3. 9. A k-point grid of 6x6x6 was used for all bulk models and 5x5x2 for all surface slab models.

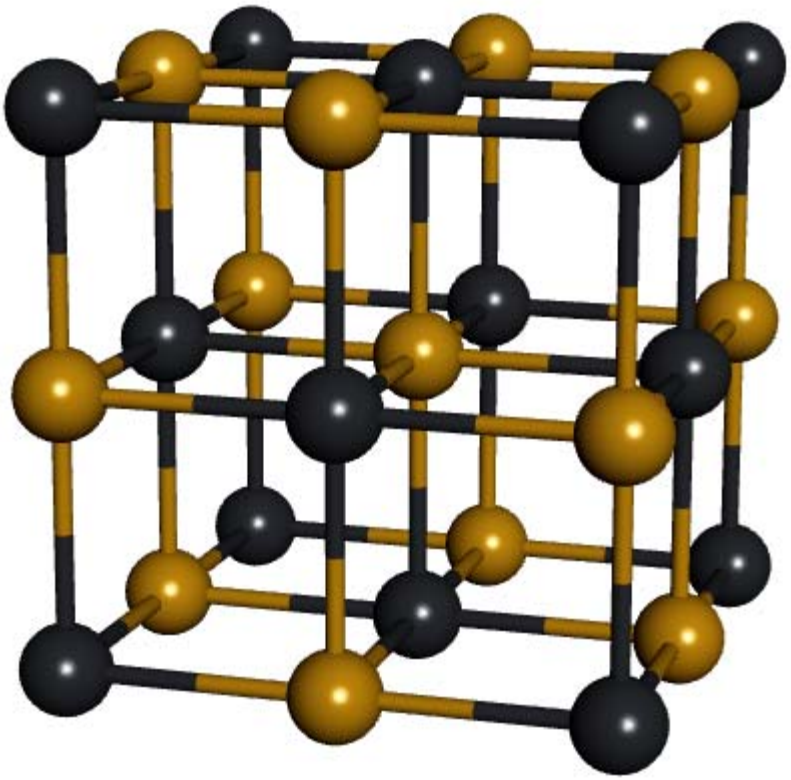

Figure 3.17: The bulk unit cell of PbS [75]

The cell parameter and interatomic distances calculated for PbS bulk are presented in Table 3.9 in comparison to available experimental values. The differences between lattice parameters did not exceed 0.022 Å. The calculation results for interatomic distances show a greater similarity to the experimental data with a maximum of 2% difference, which is more recent and refers to a sample rich in As. The average Pb–S distance calculated is 2.203 Å, about 0.028 Å less than the average experimental value, as expected. The average Pb–S distance of 2.999 Å is longer than the experimental value, and the S–S distance of 3.484 Å longer.

Table 3.9: Structural parameters of optimised bulk PbS compared with experimental values.

Parameter	**Value(Å)**	**Population**	**Literature(Å)** [75]
a=b=c	5.999		5.936
Pb–S	2.999	0.22	2.257
Pb-Pb	2.286		2.302
S–S	3.484		3.685

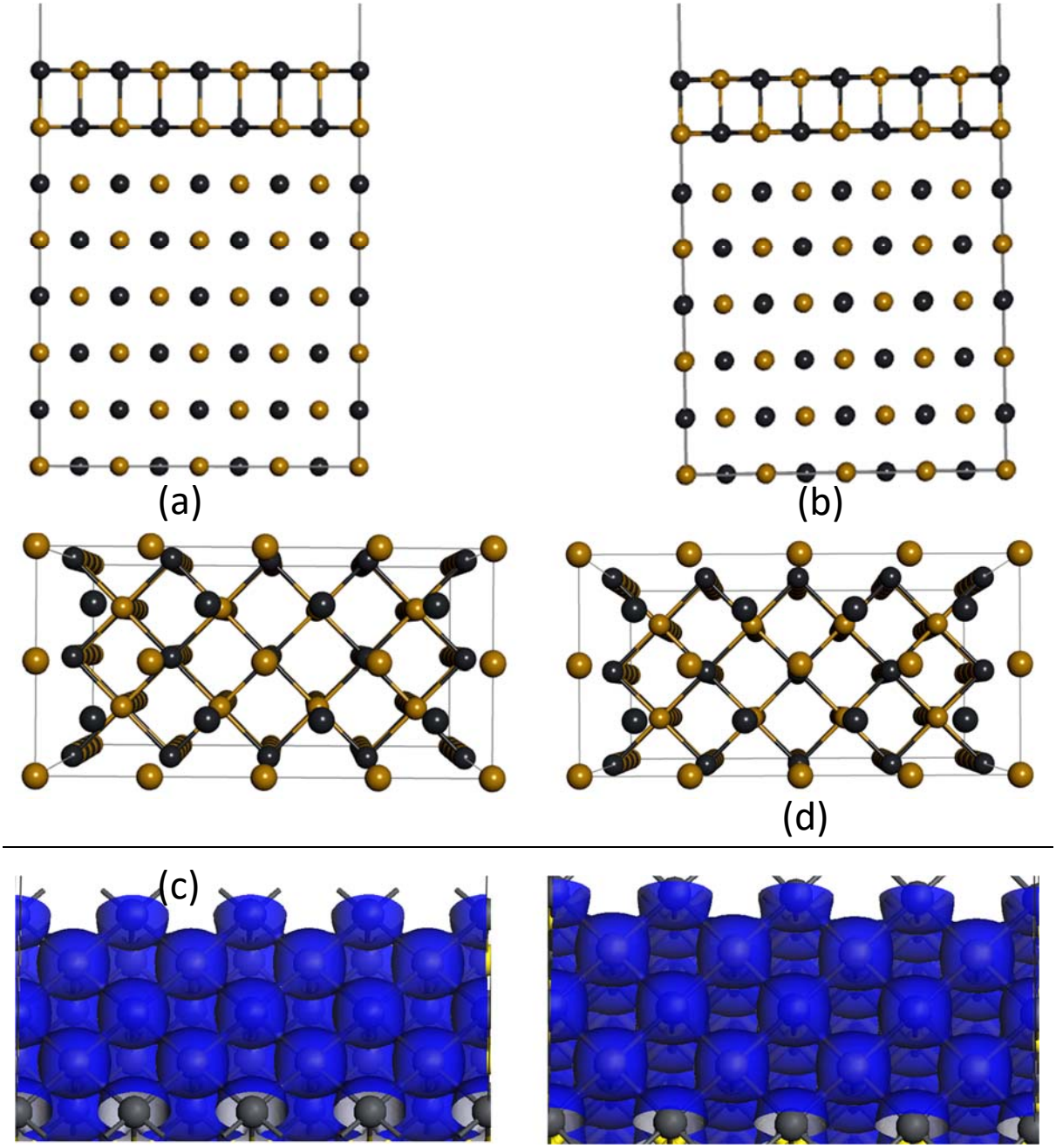

Figure 3.18: PbS (100) surface: (a) Before being relaxed and (b) Fully being relaxed. The electron density of (100) surfaces: (c) unrelaxed and (d) relaxed.

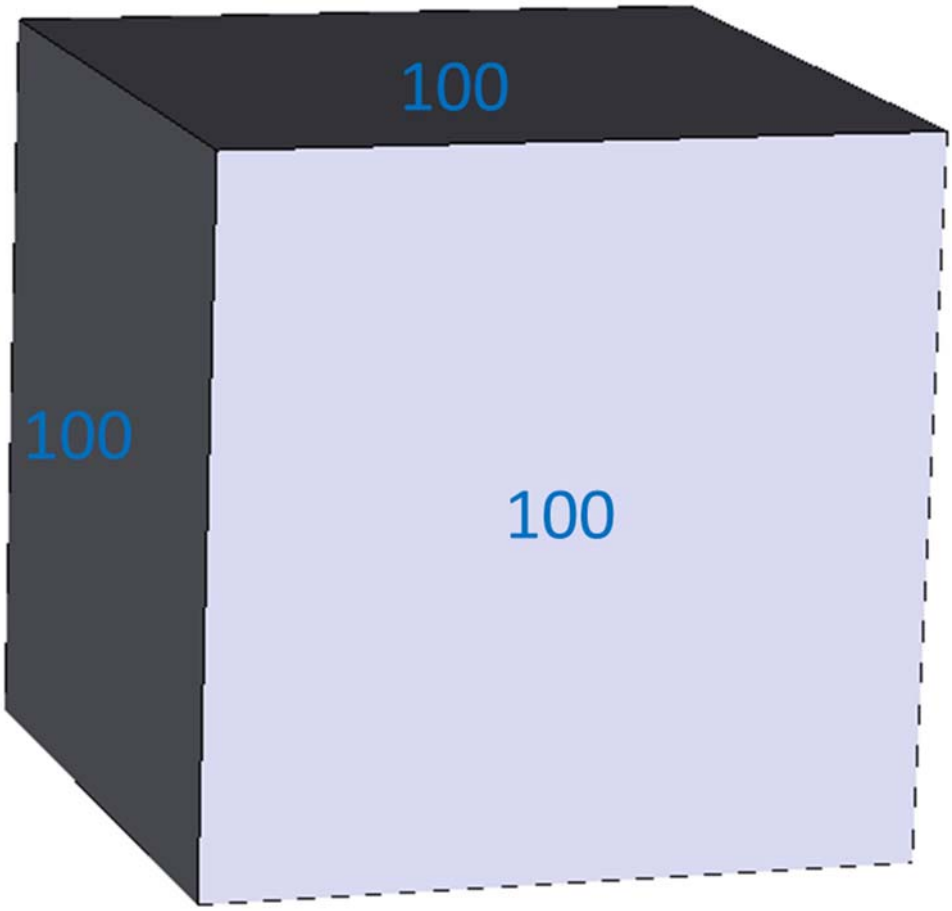

Figure 3.19: Wulff constructions of PbS surfaces

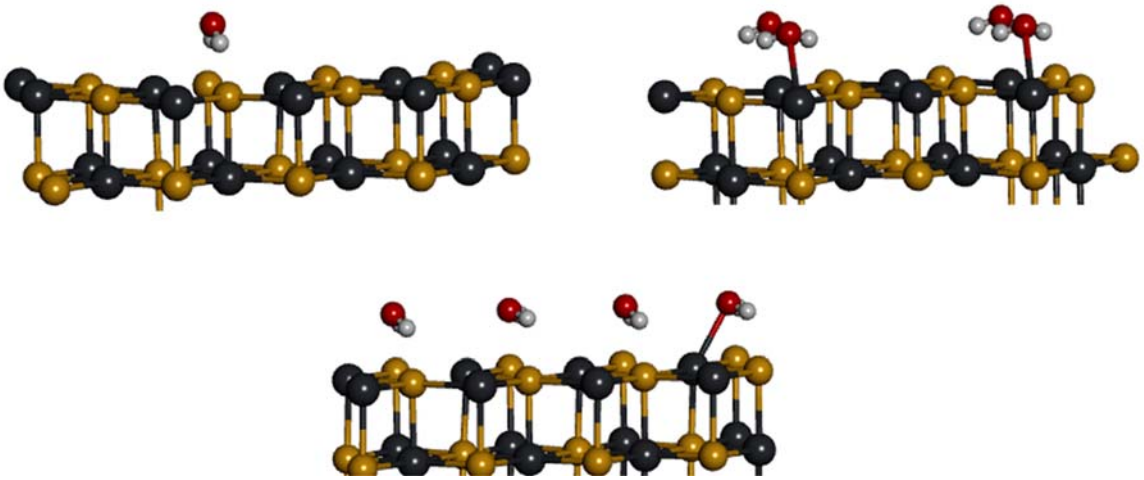

Figure 3.20: Water adsorbed on the PbS (100) surface.

Table 3.10: Mulliken charge populations of H_2O adsorption on the galena surface (s, p and d represent s orbitals, p orbitals and d orbitals, respectively) before and after adsorption.

			s	p	d	total	q/e
PbS(100)	In the absence of water molecule	Pb1	1.98	1.41	10	13.4	0.60
		Pb2	1.98	1.41	10	13.4	0.60
		S3	1.93	4.75	0	6.68	-0.68
		S4	1.93	4.75	0	6.68	-0.68
	in the presence of water molecule	Pb1	1.95	1.4	10	13.35	0.65
		Pb2	1.97	1.36	10	13.33	0.67
		S3	1.92	4.77	0	6.7	-0.70
		S4	1.92	4.78	0	6.7	-0.70

Table 3.11: galena Mulliken bonding population of atoms in the absence and in the presence of H_2O molecule(s) on the surface.

		Bond	Population	length
PbS(100)	In the absence of water molecule	S3 – Pb1	0.06	2.995
		S4—Pb2	0.06	2.995
		S3—Pb2	0.06	2.995
	In the presence of water molecule	S3 – Pb1	0.10	2.892
		S4—Pb2	0.11	2.873
		S3—Pb2	0.10	2.903

S atom for PbS, there is a sharp change at the Mulliken bonds populations and length. we discover that the bond populations of Pb1—S5 connected between the layers, namely the interlayer bonds, change from 0.21 to 0.11 before and after H_2O absorption and the length increases Hence, this manifests that the Pb1—S5 bond becomes more ionic and the interaction between layers becomes more greatly

enhanced. Meanwhile, the bonds on the same plane layer have no significant changes in the presence of H_2O.

As for the preferential cleavage of PbS, there is a definitive conclusion in the literature, and the surfaces (100) was identified as the most favourable for cleavage by different authors. It is important to note that in some works the unit cell used to define the Miller indices was not indicated, which may lead to misinterpretations. Table 3.12 shows the correspondence between the cleavage planes in cells C21/d and P21/c.

3.2.4 Sphalerite

Determination of the working surface

Crystallographic data for sphalerite is presented in Table 3.12. A k-point grid of 6x6x6 was used for bulk model and 5x5x2 for all surface slab models.

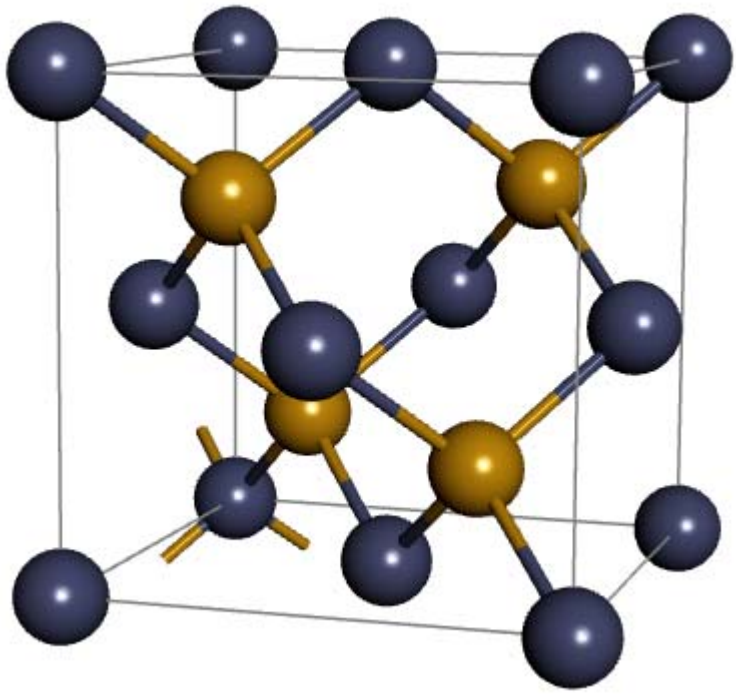

Figure 3.21: Bulk unit cell of ZnS.

Table 3.12: Structural parameters of optimised bulk ZnS compared with experimental values.

parameter	Value(Å)	population	Literature(Å) [76]
a=b	5.999		5.409
c	9.978		10.423
Zn–S	2.357	0.46	2.360
S–S	3.484	0.22	3.685

The equilibrium unit-cell length and population for sphalerite models are listed, together with measured data taken from the literature, in Table 3.13 on the facing page. There is no provision in crystal to include either temperature or the zero-point energy (zpe), and so where possible the measured data used to validate the models in this project have been taken from experiments carried out at low temperatures.

Table 3.13: Surface energies (J/m^2) for sphalerite mineral surfaces computed using computational molecular modelling techniques.

MI		Value (J/m^2)	Literature (J/m^2) [77]
110		0.43	0.53
100	Zn	2.03	1.12
100	S	2.03	1.30
111	Zn	0.80	0.87
111	S	1.04	1.01

The surface energies of all the surfaces modelled for the cubic phase ZnS surfaces are summarized in Table 3.14. The most stable surface is (110), with a surface energy of 0.43 J/m^2, in good agreement with the value obtained from other calculations, 0.53 J/m^2. The next most stable surfaces are the (111) polar surface, Zn terminated, 0.80 J/m^2. The higher stability of the (110) surface, compared with any other polar or nonpolar surfaces, has also been observed experimentally [77].

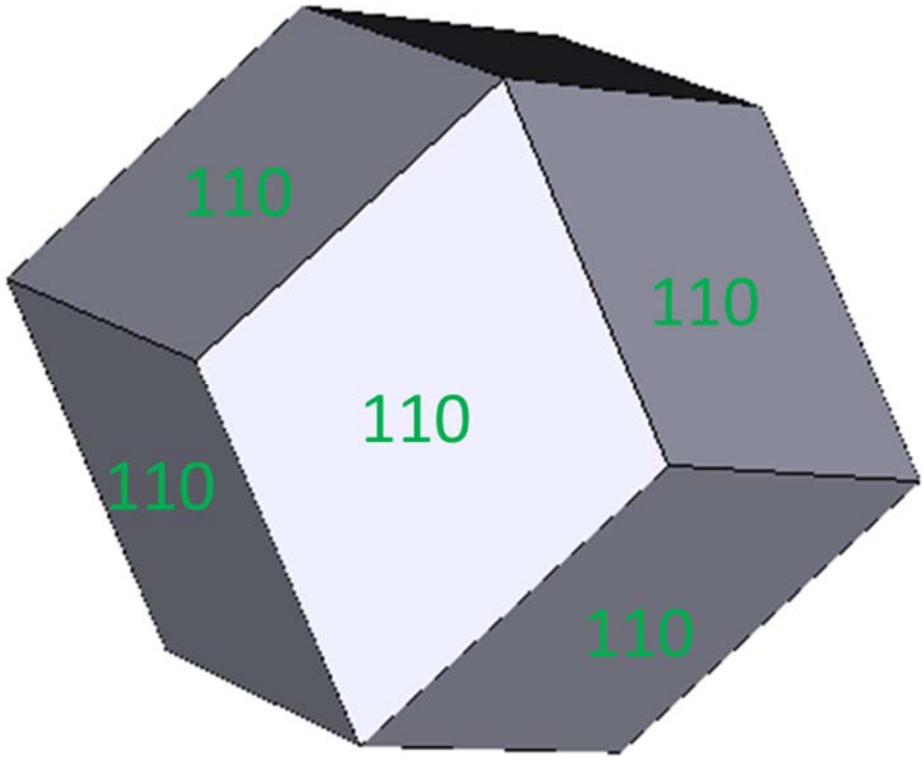

Figure 3.22: Calculated morphology of the cubic phase of ZnS, obtained by using relaxed surface energies. The only surface to appear is the (110).

The nonpolar (110) surface is the most stable in this phase and entirely dominates the crystal morphology, which is a dodecahedron showing only the (110) surface and its equivalent.

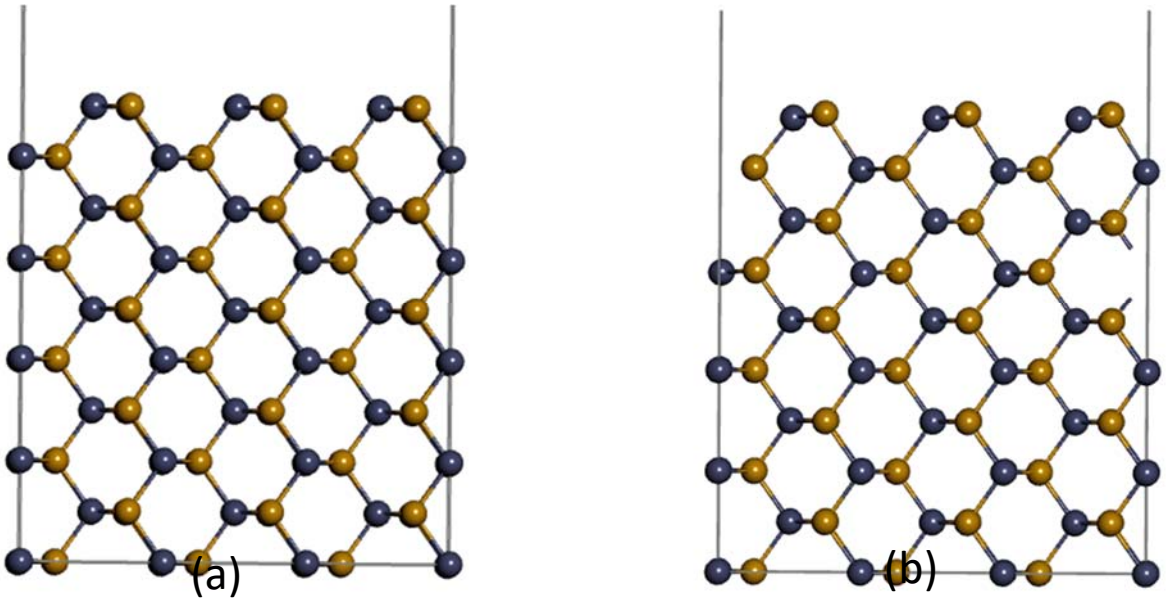

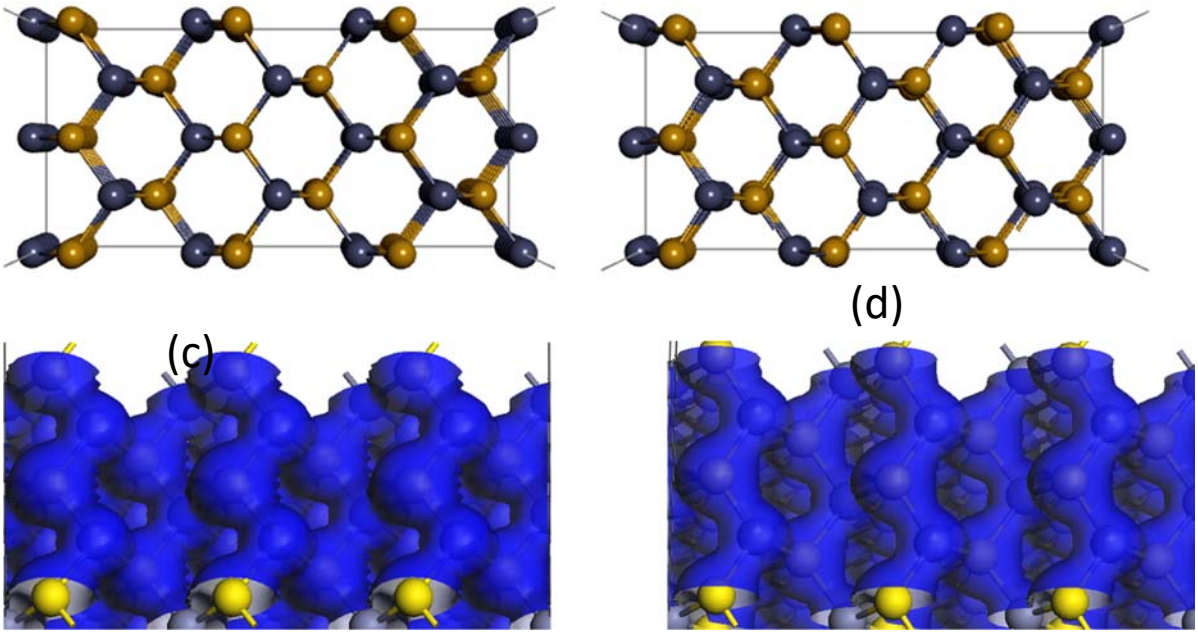

Figure 3.23: ZnS (110) surface: (a) Before being relaxed and (b) Fully being relaxed, The electron density of ZnS (110) surfaces: (c) unrelaxed and (d) relaxed.

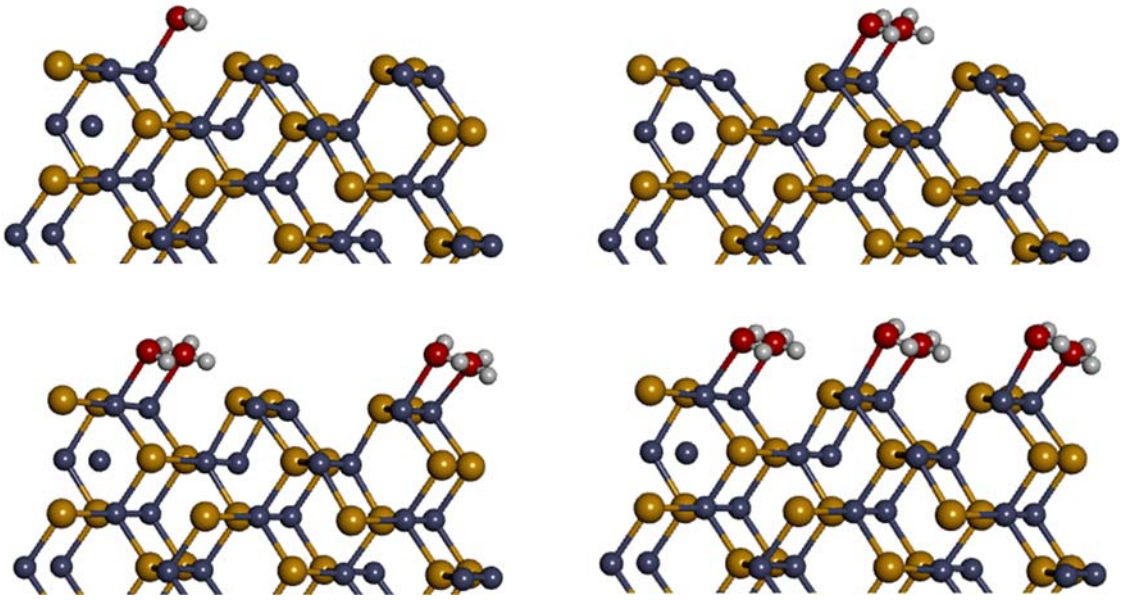

Figure 3.24: water adsorbed on the ZnS (110) surface

Table 3.14: Mulliken charge populations of H_2O adsorption on the sphalerite surface (s, p and d represent s orbitals, p orbitals and d orbitals, respectively) before and after adsorption.

		Atom	s	p	d	Total	q/e
ZnS (110)	In the absence of water	Zn1	0.91	0.76	9.98	11.66	0.34
		S3	1.86	4.67	0	6.53	-0.53
		S4	1.86	4.67	0	6.53	-0.53
	In the presence of water molecule	Zn1	0.85	0.79	9.99	11.62	0.38
		S3	1.86	4.69	0	6.55	-0.55
		S4	1.86	4.69	0	6.55	-0.55

The charges of Zn1 atoms increase from +0.34e to +0.38e which indicates that the Zn1 atom becomes more positive. In addition, there are changes in the charges of S atoms on ZnS surface layers before and after H_2O absorption, that is, the charge of S atom on the surface layers of ZnS becomes more negative, such as S1 (from −0.530e to −0.55e) and S2 (from −0.53e to −0.55e).

Table 3.15: Sphalerite Mulliken bonding population of atoms before and after H_2O adsorption to the surface.

		Bond	Population	length
ZnS (110)	In the absence of water	S3 – Zn1	0.70	2.282
		S4 – Zn2	0.70	2.282
		S5 – Zn1	0.48	2.405
	in the presence of water molecule	S3 – Zn1	0.68	2.271
		S4 – Zn2	0.68	2.271
		S5 – Zn1	0.41	2.473

According to Table 3.15, it can been seen that the Mulliken bonds populations on the first layer are almost reduced, i.e., the populations of Zn1—S2, Zn1—S3 and Zn1—S4 decrease from 0.70 to 0.68, 0.70 to 0.68 and 0.48 to 0.41, respectively, which suggests that the bonds become more ionic. Meanwhile, the lengths of bonds on the surface decrease for Zn1—S1, Zn1—S2, thus these bonds become more covalent in

the presence of H_2O. On the contrary, we find that the bond length increases only for Zn1—S3 which manifests the interaction between bonds gradually weakened.

3.3 Summary

We have determined the cut-off energy suitable to converge the total energy of the system to be 550 eV for PbS and 450 eV for FeS_2, $CuFeS_2$ and ZnS. We choose this cut-off energy to reduce the computational cost, while the number of k-points of 7x7x7, 8x8x1, 5x5x5 and 6x6x6 for FeS_2, $CuFeS_2$, for PbS and ZnS respectively were sufficient to converge the bulk.

In this chapter, we have constructed the sulphides and performed bulk and surface structural relaxations. Pyrite (FeS_2) possesses a cubic crystal structure and has a space group of Pa3(T). 6 h Common cleavage plane is (100) face along with Fe-S bond. Each Fe atom of the surface coordinates with adjacent five S atoms, while each S atom coordinates with adjacent two Fe atoms and one S atom. Galena (PbS) also belongs to the cubic crystal structure with a space group of Fm3m. Common cleavage plane is (100) face along with Pb-S bond. Each Pb atom of the surface coordinates with adjacent five S atoms, and each S atom coordinates with five Pb atoms. Chalcopyrite crystallizes in the tetragonal group (space group $I\bar{4}2d$) with four formulas ($CuFeS_2$) we focused on (112) surface, the (112) surface reconstructs, forming S−S bonds. One S−S bond is formed between sulphur atoms in the same supercell and another between sulphur atoms in different supercells. Sphalerite (ZnS) has a cubic crystal structure, whose space group is F43m with (110) surface. Each Zn atom of the surface coordinates with three S atoms, while each S atom coordinates with two Zn atoms and one S atom. The most stable surfaces were also the ones with the highest surface exposure as it covered about a higher percentage of the surface area.

The structures of sulphide minerals surfaces have been changed by the presence of the H_2O molecule. The surfaces of FeS_2 and ZnS relax obviously and those of $CuFeS_2$ and (PbS) surfaces change slightly by presence of H_2O molecule.

The Mulliken atomic charges and bonds populations of FeS_2, ZnS and PbS surfaces affect evidently after adsorbing H_2O, whereas those of $CuFeS_2$ surface changes little.

The adsorption of the flotation reagent at the interface of mineral-water would be different from that of the mineral surface due to the changes of surface structures and electronic properties caused by H_2O molecule. Hence, the influence of the H_2O molecule on the reaction of flotation reagent with the mineral surface will attract more attention.

Chapter 4

Theoretical studies on Collectors

Collectors are molecules with the ability to change the surface characteristics of particles. In the flotation process collectors are added to the pulp to make metal particles hydrophobic and, thereby making them float with relative ease. The more common ones are anionic surfactants and their surface activity at the mineral surface leading to the formation of the hydrophobic film follows chemical or electrochemical interactions, some of the sulphide mineral collectors are xanthates, dithiophosphate, dithiocarbamate, dixanthogens, alkyl thionocarbamate and alkyl thioether amine [78]. some of these collectors are studied using computational methods. in addition to the studies of collectors themselves, the validation of the main surface modelling method, namely DFT in combination with pseudopotentials is also investigated. The thiol collectors are important during the flotation process for enhancing the extraction of the concentrated mineral [78]. We began by examining the molecular geometries of the isolated thiol collectors to gain an understanding of how these collectors might react before adsorption.

4.1 Isolated organic collectors

Thiol collectors are generally used to enhance ore recovery in the mining industry since this render hydrophobicity to the desired minerals. To investigate the process of ore recovery, we have considered adsorption of the DTPs, xanthate and DTCs organic collectors on the most stable surfaces, the thiol collectors considered for the study are DeDTP, DispDTP, DbDTP, eX, DeDTC, nbDTC and DbDTC. The use of these surfactants will also give an understanding of the effect of the thiol collector chain length and ligand type when adsorbing on FeS_2, $CuFeS_2$, PbS and ZnS minerals.
The seven collectors were first optimized employing PAW potential, cut-off energy and other precision parameters as in the surface system, with k-points parameters at Gama point (1x1x1). Each molecule was placed in a cell of (25x25x25). The optimized organic collector geometries are shown in Figure 4.2 to 4.10 and their geometric parameters are given in Table 4.1 to 4.3 for comparison with theoretical/experimental studies.

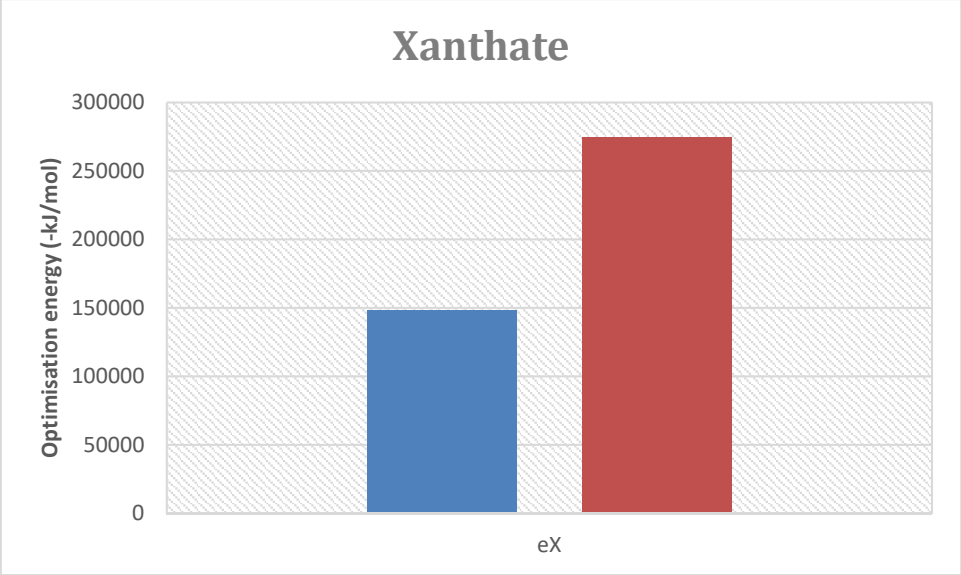

Figure 4.1: Effect of Na on the total energy eX.

Table 4.1: Calculated bond lengths (*R*, in Å), bond angles (θ, in deg.) and torsion/dihedral angle (ϕ, in deg.) for ethyl xanthate anion and its sodium salts. The theoretical/experimental values are shown in parenthesis for comparison.

	eX	
	In the absence of Na	**In the presence of Na**
R(C1-S1)	1.674(1.670)[a]	1.700(1.670)[a]
R(C1=S2)	1.675(1.700)[a]	1.710(1.700)[a]
R(C1–O)	1.326 (1.350)[a]	1.354(1.350)[a]
θ(S1=C1–S2)	112.13(124.0)[a]	127.36(124.0)[a]
ϕ(S1=C1–S2–O1)	-179.94(179.93)[b]	-179.87(179.93)[b]
HOMO	-5.026	-1.842
LUMO	-5.863	-4.905

a – Experimental values of ethyl xanthate (Ex^-) by Winter (1980) [79].
b– Calculated ethyl xanthate (Ex) from Mkhonto *et al.* (2016) [39]

Table 4.1 above shows the results of the geometrical optimization of eX with and without Na. The metal ion is placed in the S-C-S plane at a fairly large and symmetrical distance from the two sulphur atoms, as shown in Figure 4.2. We note that the S-C-S bond angle is affected slightly by 14.37° in the presence of the alkali metal ion. Moreover, the torsion/dihedral angle increases insignificantly by 0.07 ° in the presence of Na. the red colour on the collector's total energies Figures indicated the presence of Na, while Blue colour indicate the absence of Na.

.

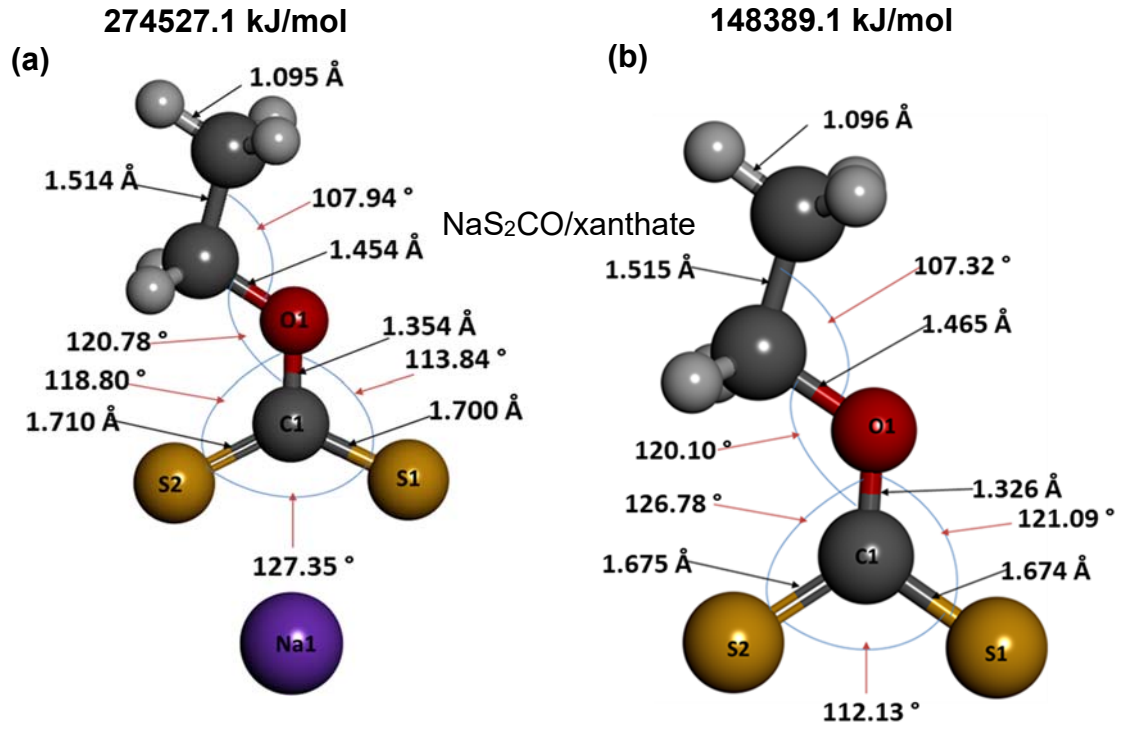

Figure 4.2: Relaxed molecular geometries of organic collectors: (a) $C_2H_5OCS_2Na$ and (b) $C_2H_5OCS_2^-$.

The main usage for the ionic salts of DTP is as a collector in the froth flotation of sulphide minerals [80]. The versatility of applications of DTPs, as well as their ability to combine with metal ions into a variety of coordination complexes, have led to a large interest in their structure and the factors governing the properties of the DTP complexes. The crystal structure of a wide range of Metal DTPs has been determined by single-crystal X-ray diffraction, and also studied with various other spectroscopic techniques [81].

In Figures 4.4 to 4.6, the three conformations of the DTPs salts and anions are shown. The torsion angles of the S1=P1–S2–O1 plane are 115.69° and -129.44°, 113.63° and 127.82°, -115.03° and -129.54° whereas the torsion angles of the S1=P1–S2–O2 left and right conformation -116.19° and -130.03°, 113.88° and 128.98°, -115.33° and -129.09° for DeDTP, DispDTP and DbDTP (salts and anions) conformations respectively. The DTPs conformations with Na were found to have the lowest total energy in contrast to the DTPs anion, where the DbDTP conformations have the lowest total energies both anion and Na containing DTPs. There exist several low energy conformations due to the small energy differences between the various conformations of the hydrocarbon chain. Here, only the three conformations with different torsion angles of the O-C bonds with respect to the O-P-O plane are

presented. A distorted tetrahedral environment around phosphorus can be seen with two sulfurs and two oxygens bonded to phosphorus.

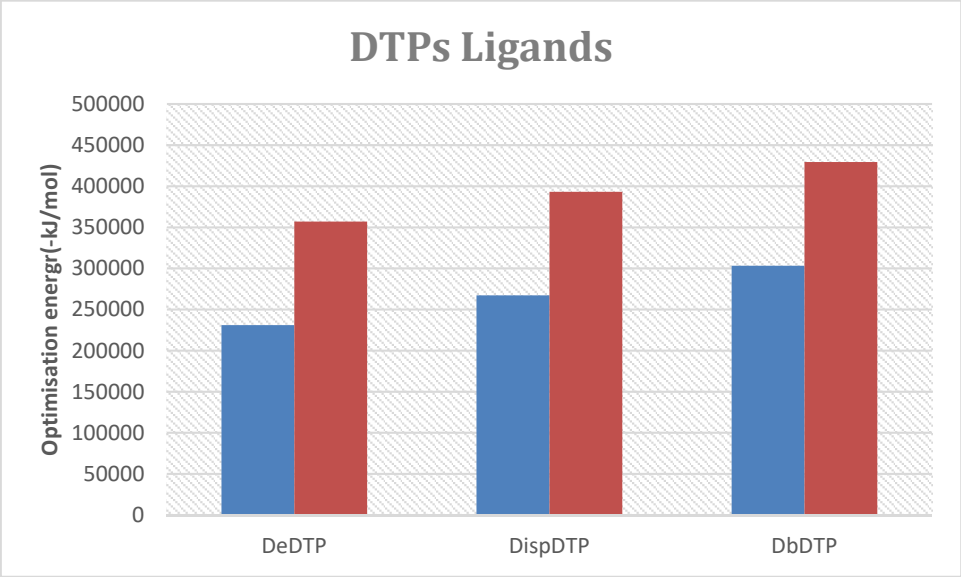

Figure 4.3: Effect of Na on the total energies DTPs.

Table 4.2: Calculated bond lengths (*R*, in Å), bond angles (θ, in deg.) and torsion/dihedral angle (ϕ, in deg.). The theoretical/experimental values are shown in parenthesis for comparison.

	DeDTP		**DibDTP**		**DbDTP**	
	In the absence of Na	In the presence of Na	In the absence of Na	In the presence of Na	In the absence of Na	In the presence of Na
R(P1-S1)	1.974(1.985)[a]	2.001	1.969	1.991	1.966(2.013)[b]	1.989
R(P1=S2)	1.972(1.988)[a]	1.995	1.966	1.990	1.965(2.013)[b]	1.986
R(P1–O1)	1.578(1.595)[a]	1.598	1.460	1.600	1.578(1.641)[b]	1.596
R(P1–O2)	1.572(1.595)[a]	1.590	1.464	1.593	1.579(1.641)[b]	1.599
θ(S1=P1–S2)	100.36(99.68 [a]	115.41	101.57	116.16	102.54(116.74)[b]	117.61
ϕ(S1=P1–S2–O1)	115.69(124.87)[a]	129.44(	113.63	127.82	115.03(128.62)[b]	129.54
ϕ(S1=P1–S2–O2)	116.19(124.36)[a]	130.03	113.88	128.98	115.33(128.65)[b]	129.09
HOMO	-5.258	-0.406	-5.427	-0.311	-5.404	-0.375
LUMO	-6.073	-5.282	-6.157	-5.346	-6.120	-5.441

a Calculated ethyl diethyl dithiophosphate (DeDTP) from Mkhonto *et al.* (2016) [39]

b– Calculated values in diisobutyl dithiophosphate (DisbDTP) from Liu *et al.* (2012) [82].

On the other hand, the torsion/dihedral angle of O–P1(=S1)–S2^{-} group in DTP molecule is about ±124.8°, which infers that the O–P1(=S1)–S2^{-} group of DTP is difficult to form a conjugated π– or π^{*}–bond [82].

The frontier orbitals of highest occupied molecular orbital energy (HOMO) and lowest unoccupied molecular orbital energy (LUMO) are related to the activity of a molecule. The formation of a transition state is due to an interaction between the frontier orbitals (HOMO and LUMO) of reactants according to the frontier molecular orbital theory [82]. It is well established that the higher HOMO energy value or less negative HOMO reflects that the molecule more easily releases the electrons to the unoccupied orbitals of the metal and stronger chemisorbed band efficiency, thus the molecule has the strongest interaction with metal and the best collector ability.

The decreasing order of E_{HOMO} of the studied DTPs in the absence and present of Na metal is DeDTP > DbDTC >DispDTP /DispDTP > DbDTC >DeDTP which implies that the DeDTP has the highest tendency to donate its most energetic electron to a suitable orbital of an acceptor molecule, in the E_{LUMO} is a measure of the tendency of a molecule to accept electrons from the appropriate orbital of a donor species. The lower the E_{LUMO} the better the chance of electron acceptance by the molecule. The values of the E_{LUMO} listed in Table 4.4 for the studied complexes are in the order in DeDTP > DispDTP > DbDTP > which implies that the DeDTP has the highest tendency to accept electrons from the appropriately occupied orbitals of an electron-donating species.

(a)

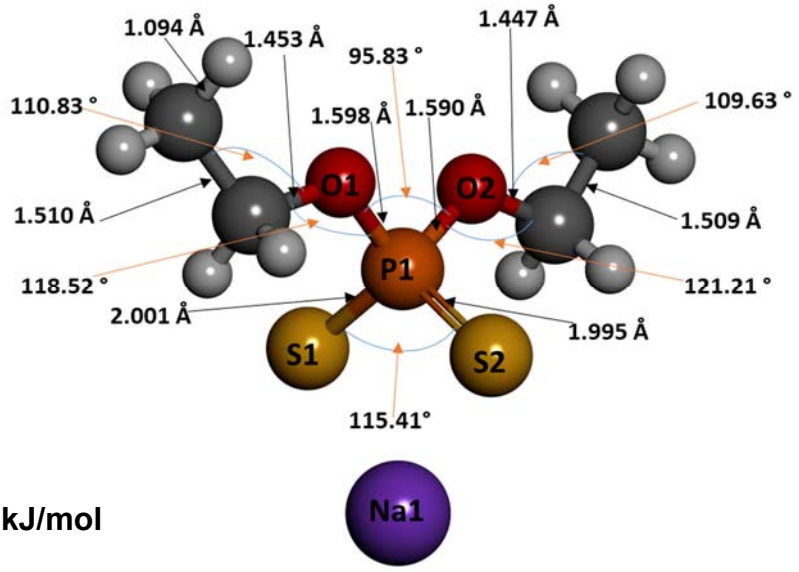

357116.0 kJ/mol

(b)

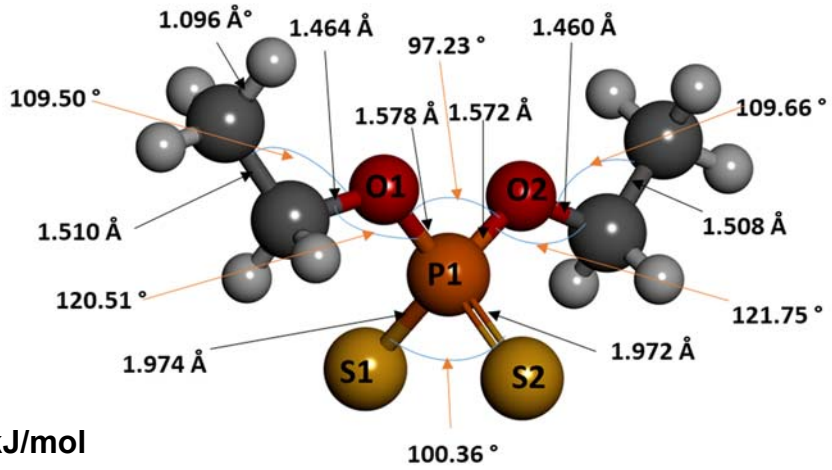

230955.2 kJ/mol

Figure 4.4: Relaxed molecular geometries of organic collectors: (a) $(C_2H_5O)_2PS_2Na$ and (b) $(C_2H_5O)_2PS_2^-$.

(a)

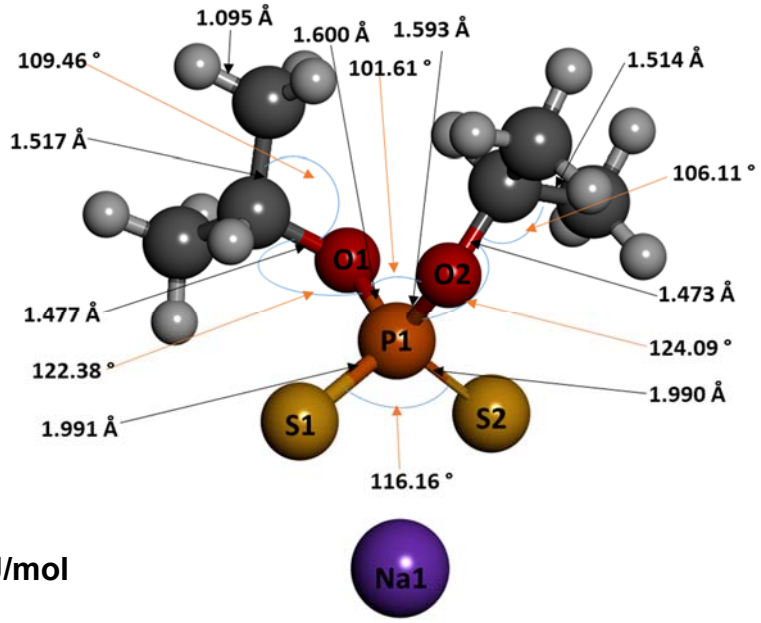

393318.0 kJ/mol

(b)

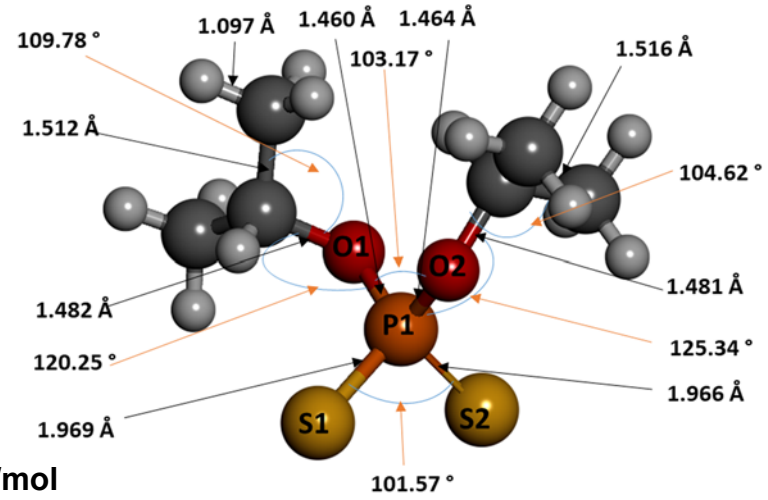

267162.1 kJ/mol

Figure 4.5: Relaxed molecular geometries of organic collectors: (a) $(C_3H_7O)_2PS_2Na$ and (b) $(C_3H_7O)_2PS_2^-$.

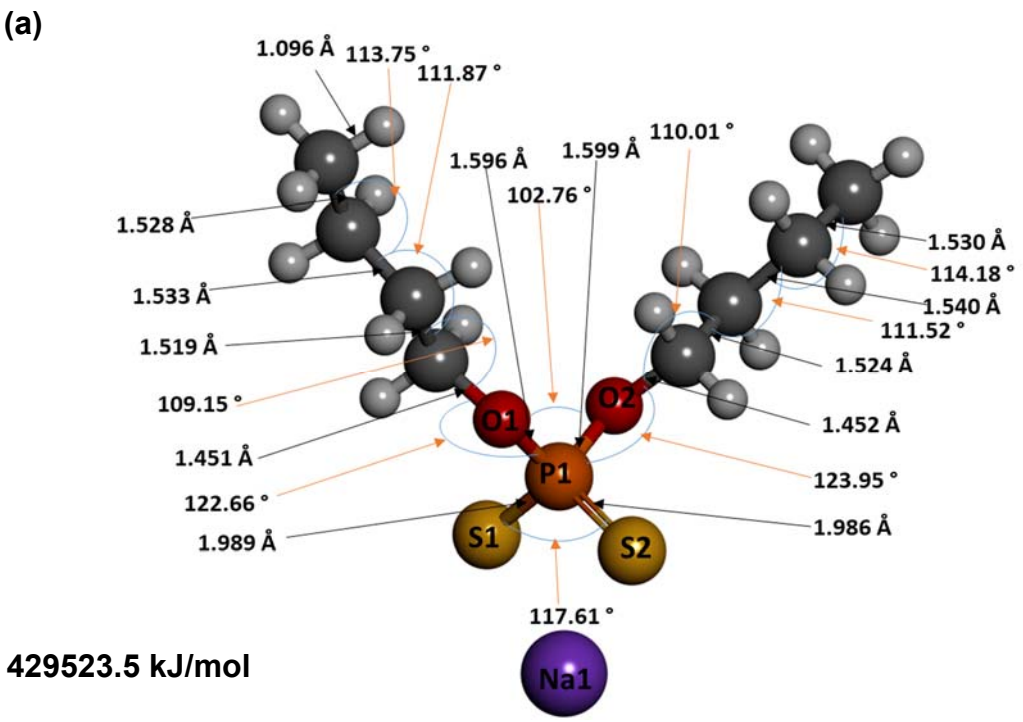

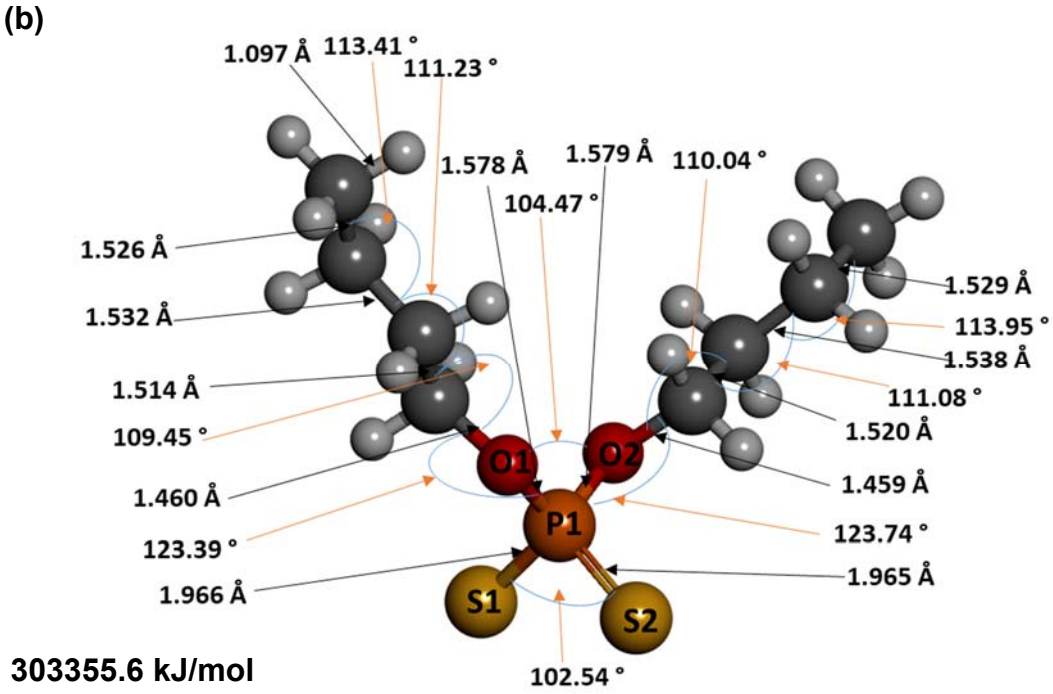

Figure 4.6: Relaxed molecular geometries of organic collectors: (a) $(C_4H_9O)_2PS_2Na$ and (b) $(C_4H_9O)_2PS_2^-$.

Carbamate and dithiocarbamate are organic compounds are also used in a variety of agriculture and household application as herbicides, fungicides, anthelmintics, pest repellent, and bacteriostatic agent. The carbamate is represented by a general structure of R-NH(CO)O and the dithiocarbamate are Characterized by R-NH(CS)S^- with R representing an alkyl group.

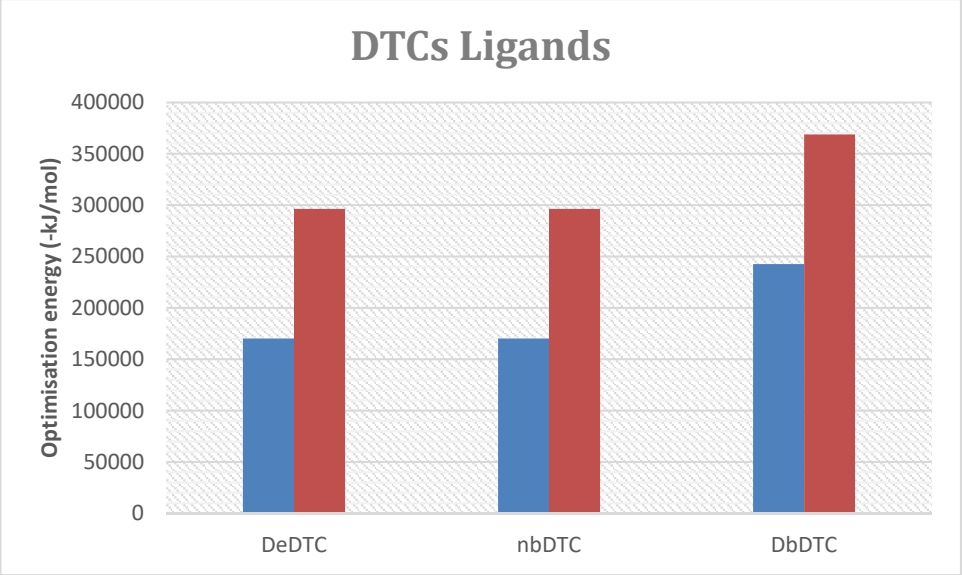

Figure 4.7: Effect of Na on the total energies of DTCs.

Table 4.3: Calculated bond lengths (*R*, in Å), bond angles (θ, in deg.) and torsion/dihedral angle (ϕ, in deg.). The theoretical/experimental values are shown in parenthesis for comparison.

	DeDTC		**nbDTC**		**DbDTC**	
	In the absence of Na	In the presence of Na	In the absence of Na	In the presence of Na	In the absence of Na	In the presence of Na
R(C1-S1)	1.691(1.728)[a]	1.725	1.690	1.723	1.691	1.731
R(C1=S2)	1.691(1.728)[a]	1.730	1.685	1.723	1.694	1.730
R(C1–N1)	1.345(1.389)[a]	1.369	1.343	1.356	1.347	1.366
θ(S1=C1–S2)	108.29 (124)[a]	122.66	109.27	125.79	107.59	122.66
ϕ(S1=C1–S2–N1)	-178.92	-179.21	178.24	179.74	-179.82	-179.76
HOMO	-4.586	-1.295	-4.729	-1.370	-4.607	-1.309
LUMO	-5.393	-4.521	-5.550	-4.757	-5.412	-4.535

a Calculated trans diethyl dithiocarbamate (transEt2dtc) Georgieva (2007) [83]

Table 4.3 shows that the C–S group bond distance (*R*) for DeDTC, nbDTC and DbDTC ranges at about the same bond length of 1.691 - 1.694 Å without Na and 1.730 -1.730 Å with Na for double bond and ≈ 1.691 Å and 1.723 -1.731 Å for a single bond. However, the C–S group bond length on nBDTC on average appears to be shorter

which infers that is more stable than the other DTCs collectors. Note that the double bond on these collectors is on S2 (C1=S1). The DeDTP head group bond lengths are also comparable to those of DeDTC by Georgieva [83], where bond length and angles of C–N = 1.389 Å, C–S1 = 1.728 Å, C–S2 = 1.728 Å and S1–C–S2 = 124° were obtained.

Table 4.3 indicates that the selected torsion/dihedral bond angles in DTCs molecules and are nearly 180º or 0º, which means that the atoms in –O1–C3(=S1)–S_2^- group of DeDTC, nBDTC and DbDTC lie almost in the same plane.
The decreasing order of E_{HOMO} of DTCs is DeDTC > DbDTC > nBDTC which implies that the nBDTC has the highest tendency to donate its most energetic electron to a suitable orbital of an acceptor molecule. The E_{LUMO} is a measure of the tendency of a molecule to accept electrons from the appropriate orbital of a donor species. The lower the E_{LUMO} the better the chance of electron acceptance by the molecule. The values of the E_{LUMO} listed in Table 4.4 for the studied complexes are in the order DeDTC > DbDTC > nBDTC which implies that the nBDTC has the highest tendency to accept electrons from the appropriately occupied orbitals of an electron-donating species.

Calculated values for thiol collectors are in good agreement with their reported experimental or calculated values Nearly equal values for C-O, C-N or P-O bonds suggest strong electron delocalization over the CS_2^- (or PS_2^-) head group, and indicate bonding with a metal ion. This is further supported by the observation that the calculated values for various C-S bonds lie between the standard single and double r(C-S) bond lengths of 1.82 and 1.60 Å respectively. Similarly, P-S and C-O bond lengths (in PS_2^- head groups) are close to their standard double bond lengths of 1.94 and 1.21 Å respectively, thus indicating the strong presence of double bond character. In E–COS-, a shorter C-O bond length (more double bond character) and longer C-S bond length (more single bond character) than in E–CO_2^- and E– CS_2^- suggest that O competes more effectively than S for π-bond strength due to its higher electronegativity. What stands out in Table 4.2 to 4.6 is that the length of the hydrophobic chain has no significant effect on the bond lengths (dOC, dCS, and dCS^-)

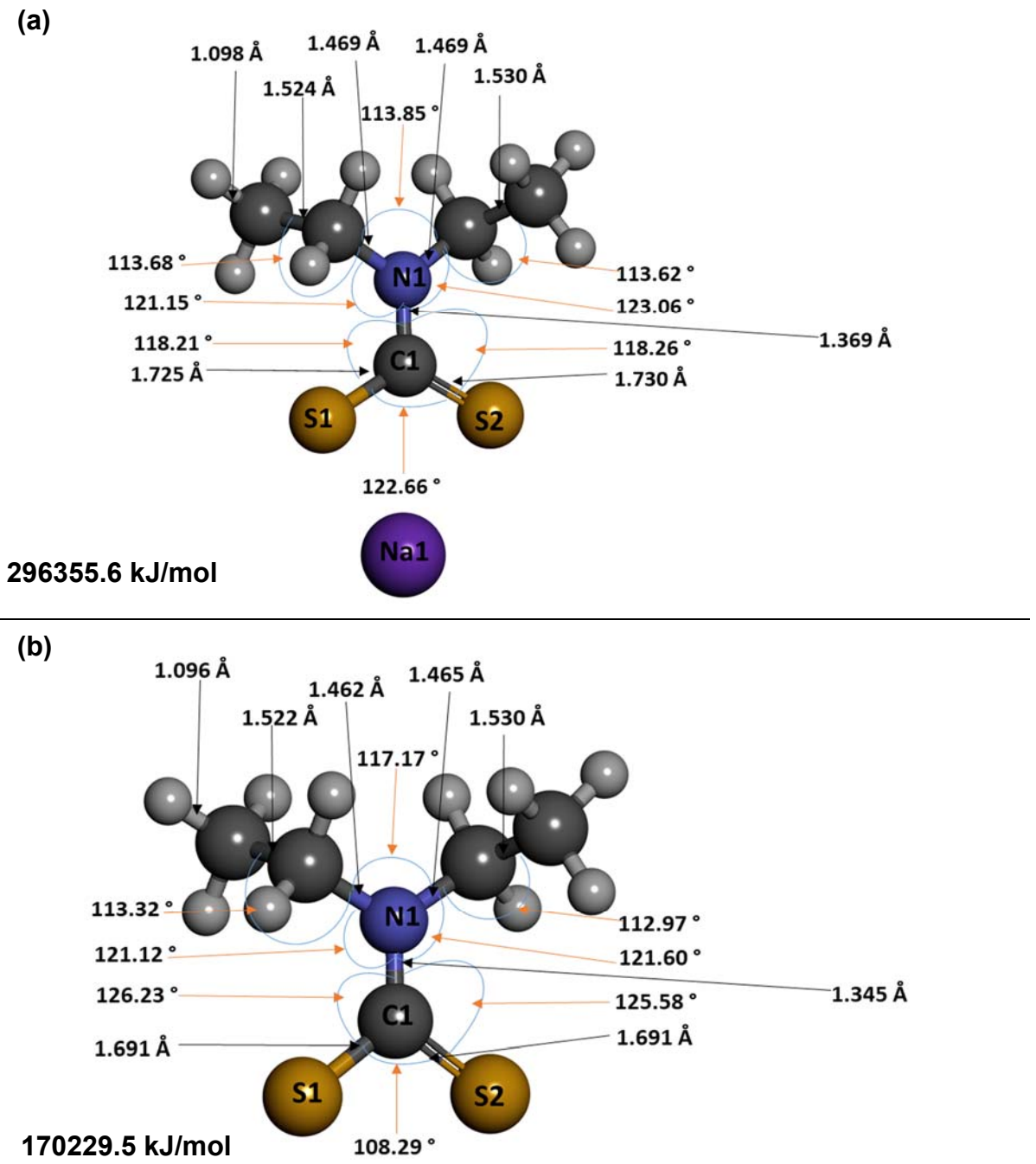

Figure 4.8: Relaxed molecular geometries of organic collectors: (a) $(C_2H_5)_2NCS_2Na$ and (b) $(C_2H_5)_2NCS_2^-$.

(a)

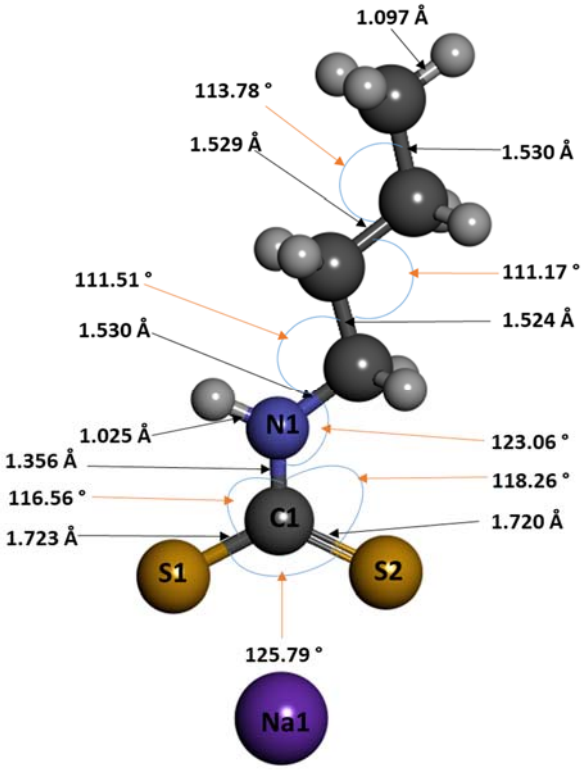

296369.7 kJ/mol

(b)

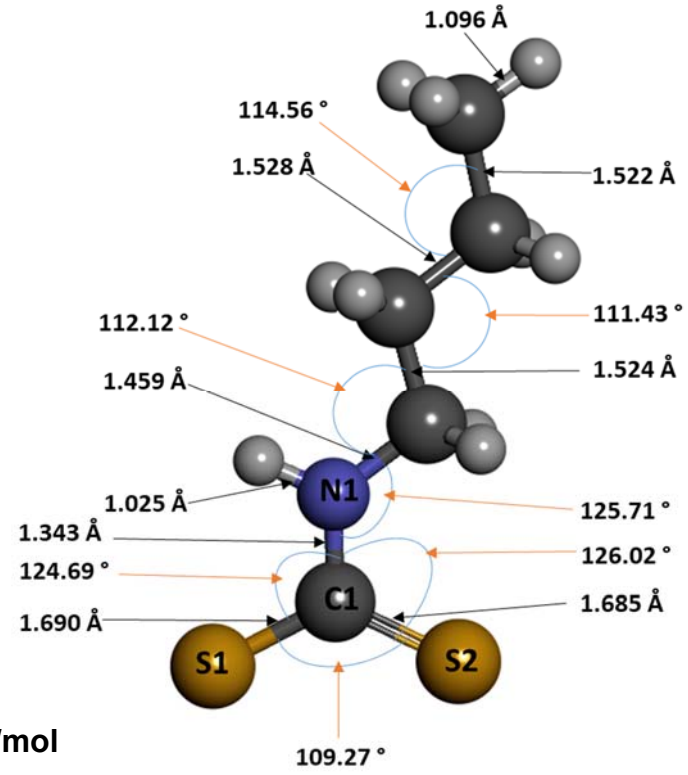

170238.1 kJ/mol

Figure 4.9: Relaxed molecular geometries of organic collectors: (a) $C_4H_9HNCS_2Na$ and (b) $C_4H_9HNCS_2^-$.

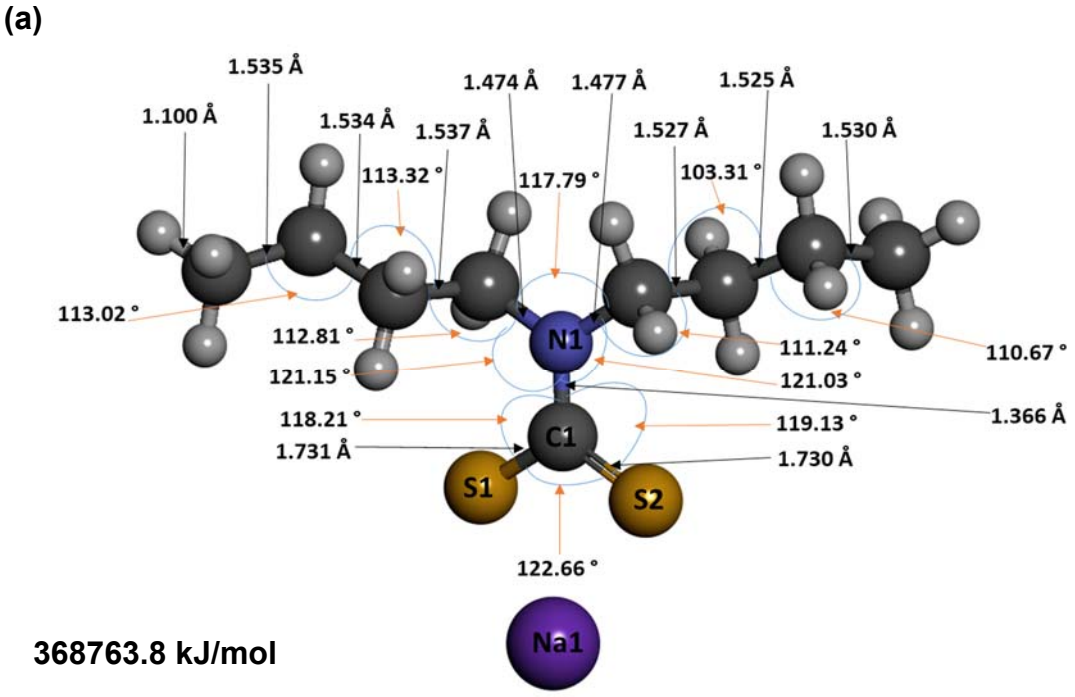

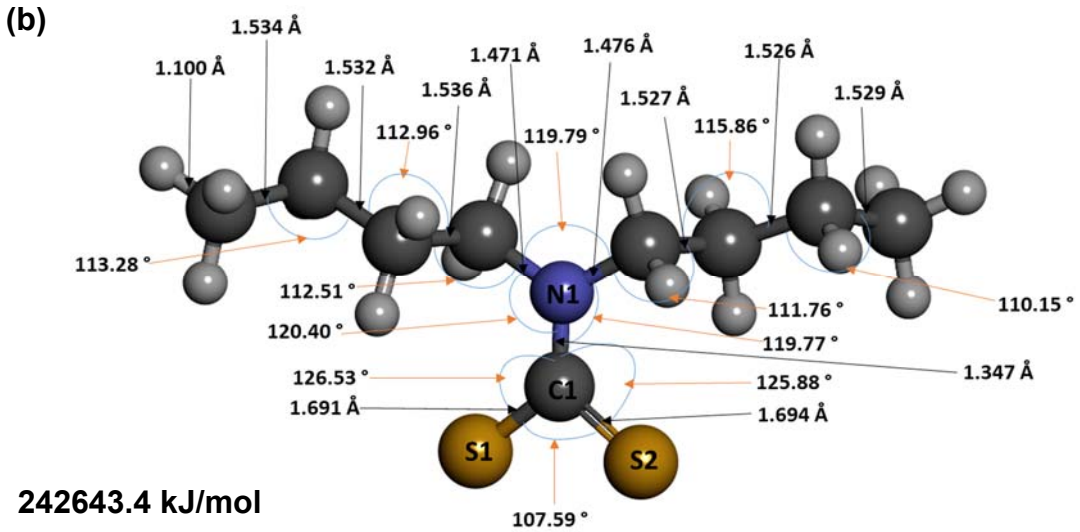

Figure 4.10: Relaxed molecular geometries of organic collectors: (a) $(C_4H_9)_2NCS_2Na$ and (b) $(C_4H_9)_2NCS_2^-$.

The parameters are in good agreement with the available theoretical values reported in previous studies sodium and potassium salts of thiol type reagents ionize in aqueous solutions owing to their ionic character [84] Selected optimized geometrical parameters for negatively charged ligand ions are listed in Table 4.1 to 4.6 As seen

from the data, bond lengths of C-O, C-N and P- bonds in $RO–CS_2^-$, $R_2N–CS_2^-$, and $RO_2–PS_2^-$ are similar while those of the other ligand ions are not. Authors of a previous study reported two equivalent P-S bonds in $(MeO)_2PS_2^-$ [85].

4.2 Mulliken charges of organic collectors

Table 4.4: Calculated bond lengths (*R*, in Å), bond angles (θ, in deg.) and torsion/dihedral angle (ϕ, in deg.). The theoretical/experimental values are shown in parenthesis for comparison. charge (in electron) of sulfur(S1) atom in thiol molecules.

	Mulliken Charges		**Hirshfeld**	
Thiol collectors	In the absence of Na	In the presence of Na	In the absence of Na	In the presence of Na
DeDTP	-0.41	-0.72	-0.14	-0.32
DibDTP	-0.38	-0.70	-0.13	-0.31
DbDTP	-0.38	-0.71	-0.13	-0.32
DeDTC	-0.02	-0.38	-0.09	-0.28
nbDTP	-0.01	-0.39	-0.11	-0.31
DbDTC	-0.02	-0.39	-0.08	-0.26
eX	0.08	-0.29	-0.06	-0.27

The atomic charge values are listed in Table 4.4 by Mulliken analysis. For the seven species investigated, it is observed that the S of the thiol molecule presents negative charges. The charges of sulfur (S) atom in thiol collectors' molecules with DFT calculations are given in Table 4.4. The results of absence of Na DFT calculations indicate that the Mulliken charge of sulfur atom is followed in this order: Ex > nbDTC > DbDTC=DeDTC > DibDTP=DbDTP> DeDTP. The electronic charge of the sulfur atom in S1 is more negative in the presence of Na. This means the thiol molecule may improve its electrostatic affinity in the presence of metal. Therefore, DTPs collectors' molecule are the more favourable reactive electron donor to the metal atom.

4.3 Summary

Our computational results on DeDTP, DispDTP, DbDTP, eX, DeDTC, nbDTC and DbDTC classes of flotation collectors show that exploring their molecular reactivity

through computational methods and modelling their interactions with metal ions is an efficient approach to relate the molecular structure of collector reagents to their binding affinity. Trends observed in the calculated geometry correlated well with the experimental findings cited in flotation literature. This implies that reactivity and selectivity of reagents can be qualitatively extended to minerals. The calculated values of interaction energies show that all collector reagents considered have a greater preference for binding with Na. Reactivity of sulfhydryl collectors is mainly determined by the electron flow around the reactive S centre(s). The length of the C-S bond (where S is the reactive centre) gives a fair approximation of collector's reactivity. Thus, the effect of remaining atoms or substituent groups that constitute the collector molecule on reactivity can be predicted by analysing how they affect the C-S bond length. Among the reagents studied, eX is the most powerful collectors, followed by DeDTC (collectors with CS_2^- head group). The primary function of substituent groups in collector molecules is to impart hydrophobicity. However, these substituent groups may also alter the reactivity and binding capability of collectors' head groups if they are capable of increasing or decreasing the C-S/P-S bond length (or electron density around reactive S atom) through inductive or resonance effect. Compared to groups, which show only inductive effect, the groups that exhibit resonance with C-S bond have a more significant effect on their reactivity of bonding to metal ions. The reactivity and binding ability of anionic sulfhydryl collectors follow the order: dithiocarbamate > xanthate > dithiophosphate. The reactivity order can be described in terms of C-S bond length of CS_2^- (PS_2^- in dithiophosphate) binding group. The resonance between lone pair electrons of O and N atoms, and pi-electrons of CS_2^- group in xanthate and dithiocarbamate results in longer C-S bonds. The reactivity of dithiophosphate is the least, as there is no resonance between lone pair electrons of heteroatoms and P-S bonds in PS_2^-. Two hetero oxygen atoms exhibit strong negative inductive effect which decreases the P-S bond length and thus, the molecular reactivity of the reagent.

Chapter 5

Adsorption of thiol collectors on sulphide surfaces.

In this chapter, we discuss the effect of alkyl chain length and ligand type of thiol collectors on the enthalpies, geometry and charges when adsorbed on the sulphides minerals most stable surfaces, i.e. pyrite (100), galena (110), chalcopyrite (112) and sphalerite (110). The relaxed geometries of the collectors on the surface, their reactivity and bonding mode will also be discussed. Thiol collectors (DTPs, DTCs and ethyl xanthate) were adsorbed to determine their effect on the mineral surface.

5.1 Effect of chain length on the adsorption of DTPs and DTCs on pyrite

Figure 5.1 below presents the effect of chain length on the heat of adsorption of different dithiophosphates homologues on pyrite. The dithiophosphate used, in order of decreasing alkyl chain length, were DbDTP (di-C4), DpDTP (diiso-C3), DeDTP (di-C2).

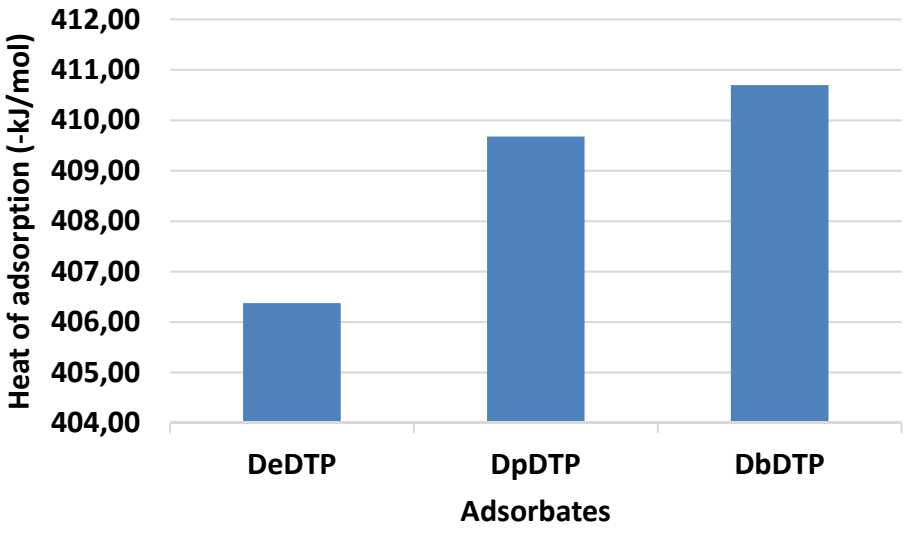

Figure 5.1: Effect of chain length (di-C2, diiso-C3, di-C4) on the enthalpy of adsorption of DTP homologues on pyrite.

It was assumed that all the thiol collectors used in this work have the same cross-sectional head area of 28.8 Å [63]. Since cross section is a function of the specific ligand type and the sodium cations play a role of spectator ions, then we only consider the anions for adsorptions.

The measured heats of adsorption ranged from 404 kJ/mol to 412 kJ/mol. The calculation show that the enthalpy of adsorption decreased in the order: DbDTP >DispDTP > DeDTP.

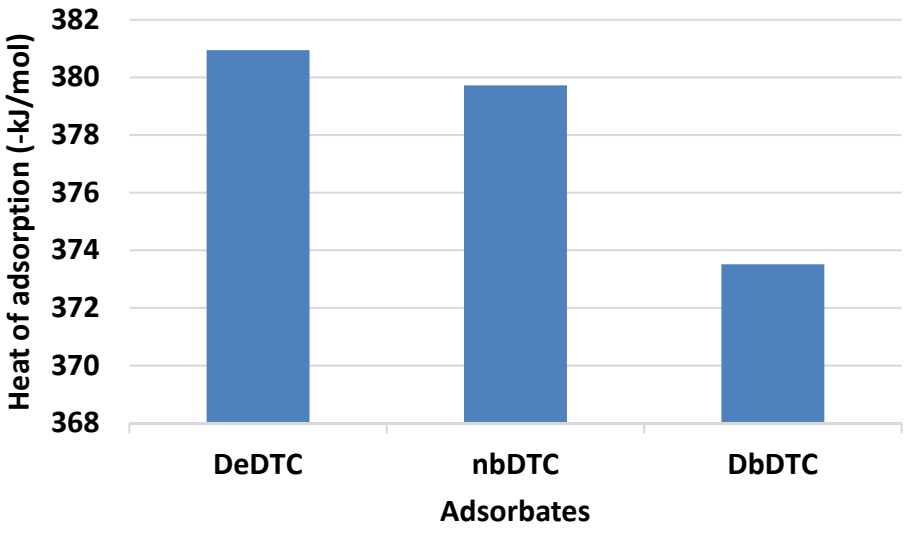

Figure 5.2: Effect of chain length (di-C2, diiso-C3, di-C4) on the enthalpies of adsorption of DTC homologues on pyrite.

Figure 5.2 shows the variation of the enthalpy of adsorption with alkyl chain length, from DeDTC through to DbDTC. The calculated heats of adsorption ranged between 368 kJ/mol and 382 kJ/mol. Our results show that the enthalpy of adsorption decreased in the order: DeDTC > nbDTC > DbDTC. Moreover, we note that the order of enthalpies of adsorption in pyrite DTC homologues are an opposite of the DTP homologues. Furthermore, the chain length in DTC homologues decreases the adsorption energies. As a result, all DTCs show adsorption energies that are lower than of their respective DTPs counterparts.

5.1.1 The geometries of DTPs, DTCs and ethyl xanthate collector on pyrite surface.

In Table 5.1, we present the relaxed calculated bond lengths and angles for DTPs collectors on the (100) pyrite surface. The calculations were performed with the collector single bond on S1 and double bond on the S2 atom. The radius (d_o) between Fe–S of 2.310 Å give the theoretical bond lengths and is shown for comparison. We note that our calculated Fe-S bond lengths are slightly longer than the reported radius values for all DTP collectors. It has been reported that bonds that are longer than the

radius reflect weak electron overlap [13]. Furthermore, longer bond lengths indicate that the adsorption of DTP collectors on the (100) pyrite surface is mainly via the bond formation between the DTP S and Fe atoms.

The P–S bonds of DeDTP, DispDTP and DbDTP on pyrite Fe atoms were observed to be longer but close to the isolated DeDTP (S1-P1 = 2.067 Å and S2–P1 = 2.063 Å), DispDTP (S1-P1 = 2.081 Å and S2–P1 = 2.087 Å) and DbDTP (S1-P1 = 2.068 Å and S2–P1 = 2.082 Å), suggesting weakening of the bonds. The weakening of the P–S bonds is an indication of electron transfer from the surface to the ion. DbDTP S atom with pyrite Fe has shortest bonds indicating that the adsorption is stronger compared to both DeDTP and DispDTP, which agrees well with the adsorption energies.

Table 5.1: Calculated bond lengths (*R*, in Å), bond angles (θ, in deg.) for DTP collectors on the (100) pyrite surface.

	DeDTP	**DispDTP**	**DbDTP**
Bonds	**Fe-top**		
d_o(Fe–S)	2.310	2.310	2.310
R(Fe1–S1)	2.455	2.414	2.369
R(Fe2–S2)	2.411	2.372	2.391
R(C3/P1–S1)	2.067	2.081	2.068
R(P1-O1)	1.575	1.585	1.603
R(C3/P1–S2)	2.063	2.087	2.082
R(P1-O2)	1.575	1.568	1.573
θ(S1–P1/C3–S2)	126.76	125.27	126.64

$d_o = r_o + r_{metal}$, is the theoretical value, r_o is the radius of S for the collector; r_{metal} is the atomic radius of metal (M) for sulphide.

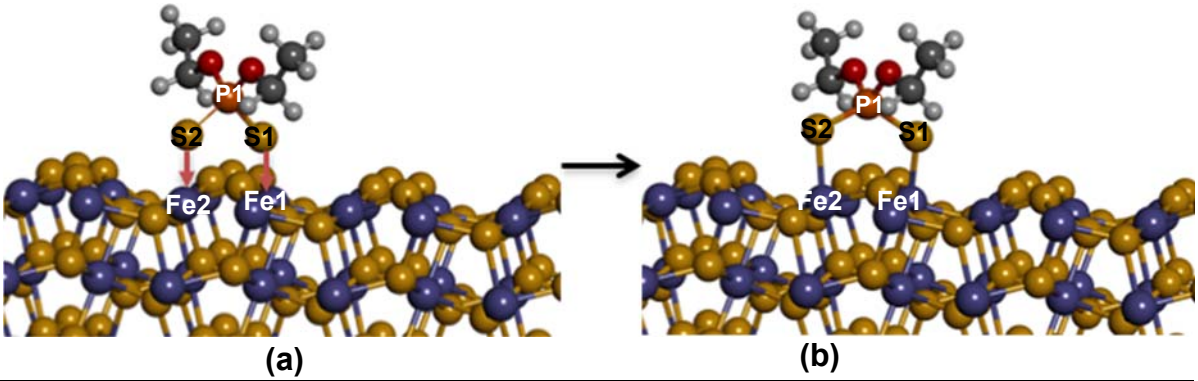

Figure 5.3: DeDTP collector adsorbed on the FeS_2 (100) surface: (a) before and (b) after adsorption.

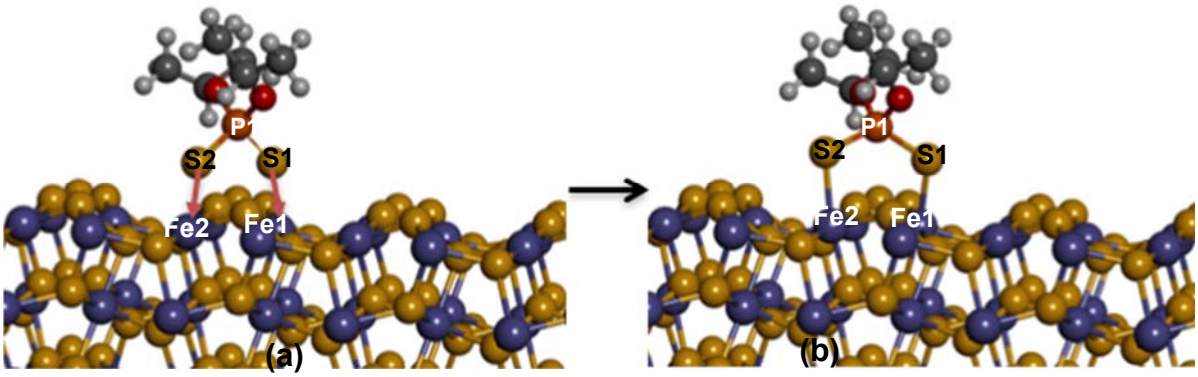

Figure 5.4:DispDTP collector adsorbed on the FeS_2 (100) surface: (a) before and (b) after adsorption.

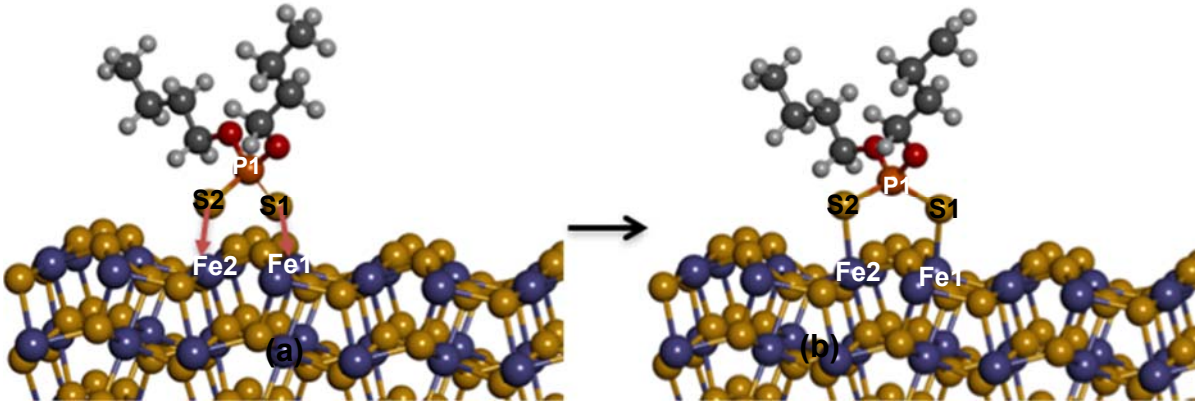

Figure 5.5: DbDTP collector adsorbed on the FeS_2 (100) surface: (a) before and (b) after adsorption.

The respective initial and final adsorption geometric orientations of the DTP collectors are shown in Figures 5.3, 5.4 and 5.5. We observed that the orientation of DTP collectors on pyrite formed a bridging geometry on Fe1 and Fe2 atoms. Furthermore, we observed a tetrapodal geometry, where S1 interacts with Fe1, while S2 interacted with Fe2 atoms.

Table 5.2: Calculated bond lengths (*R*, in Å), bond angles (θ, in deg.) for collectors on the (100) surface.

Bonds	DeDTC	nbDTP	DbDTC
	Fe-top		
d_o(Fe–S)	2.310	2.310	2.310
R(Fe1–S1)	2.349	2.377	2.392
R(Fe2–S2)	2.377	2.490	2.367

R(N1-C3)	1.354	1.359	1.364
R(C3-S1)	1.757	1.762	1.758
R(C3=S2)	1.778	1.759	1.772
θ(S1–P1/C3–S2)	130.56	131.391	130.13

$d_o = r_o + r_{metal}$, is the theoretical value, r_o is the radius of S for the collector; r_{metal} is the atomic radius of metal (M) for sulphide.

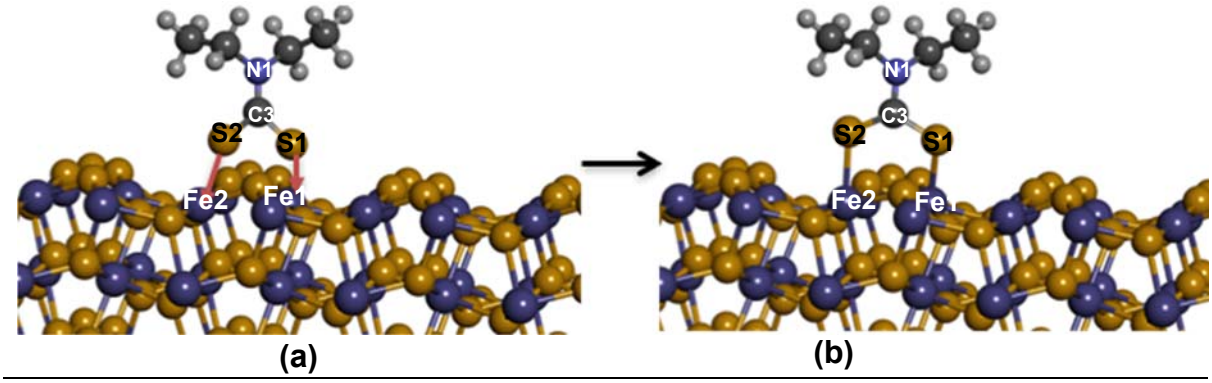

Figure 5.6: DeDTC collector adsorbed on the FeS_2 (100) surface: (a) before and (b) after adsorption.

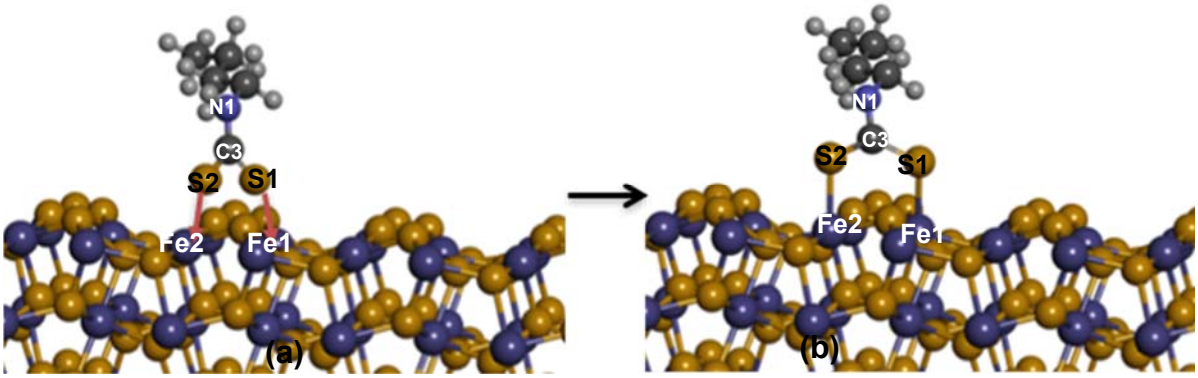

Figure 5.7: nbDTP collector adsorbed on the FeS_2 (100) surface: (a) before and (b) after adsorption.

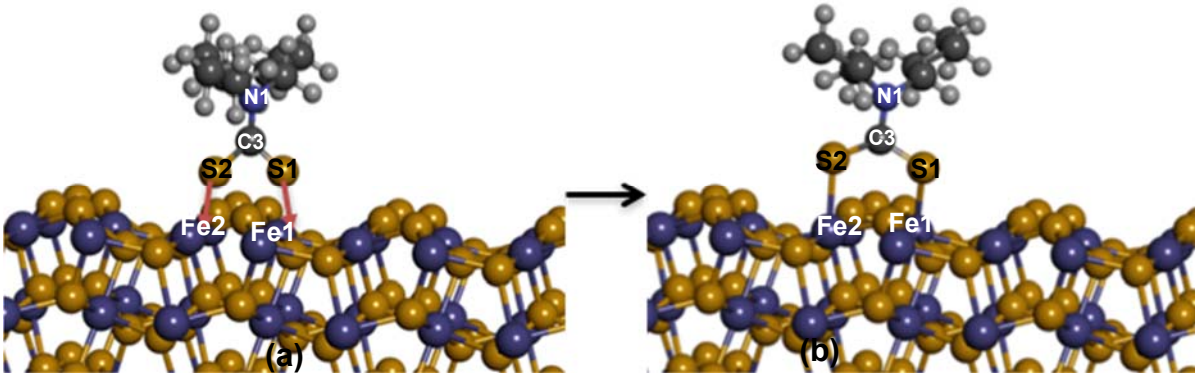

Figure 5.8: DbDTC collector adsorbed on the FeS_2 (100) surface: (a) before and (b) after adsorption.

The equilibrium distance between the sulphur atoms and Fe atoms amounts to 2.349 (Fe1–S1), 2.377 (Fe2–S2) for DeDTC, 2.377 (Fe1–S1), 2.490 (Fe2–S2) for nbDTC and 2.392 (Fe1–S1), 2.367 (Fe2–S2) for which is close to the theoretical Fe-S bond of 2.310 Å of the (100) face of FeS_2. The mean S-C bond length amounts to 1.757, 1.762 and 1.758 (C3-S1) and 1.778, 1.759, and 1.772Å (C3=S2) while the S-C-S bond angle is 130.56, 131.39 and 130.13 for DeDTC, nbDTC and DbDTC respectively. This calculated bond length corresponds to typical values for conjugated bonds between sulphur and carbon atoms as apparent in the systems (C-S bond length 1.71 Å) whereas the bond angle ideally matches the sp2-hybridization of the system.

Another important measure is given by the C-N bond length between the dithiolate carbon and the nitrogen atom, dC=N≈1.354, 1.359 and 1.364 Å, for DeDTC, nbDTC and DbDTC respectively, which is a fingerprint characteristic of dithiocarbamate compounds. The C-N bond can neither be regarded as a single bond of an amine compound (dC-N≈1.48 Å) nor as a double bond of imines (dC=N≈1.27 Å). Indeed, the calculated bond length corresponds well to the partial C-N double bond found for conjugated carbon-nitrogen systems like pyridine C=N≈1.34 Å and pyrrole C=N≈1.37 Å. The establishment of a carbon-nitrogen bond is always accompanied by a rather strong polarization towards the more electronegative nitrogen atom.

Table 5.3: Calculated bond lengths (*R*, in Å), bond angles (θ, in deg.) for collectors on the (100) surface.

	eX
Bonds	**Fe-top**
d_o(Fe–S)	2.281
R(Fe1–S1)	2.440
R(Fe2–S2)	2.360
R(C3–S1)	1.742
R(C3=S2)	1.734
R(C3–O1)	1.348
θ(S1–P1/C3–S2)	134.214

$d_o = r_o + r_{metal}$, is the theoretical value, r_o is the radius of S for the collector; r_{metal} is the atomic radius of metal (M) for sulphide.

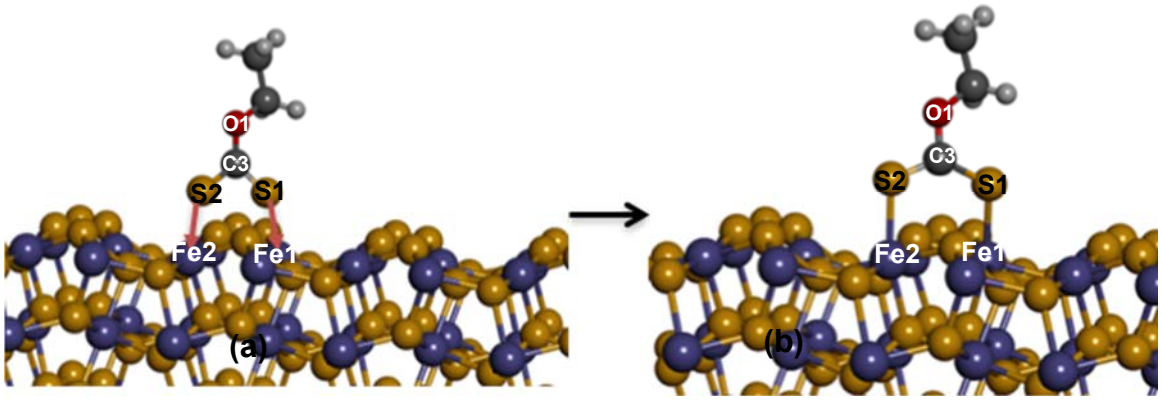

Figure 5.9: eX collector adsorbed on the FeS_2 (100) surface: (a) before and (b) after adsorption.

Figure 5.10 and Table 5.3 the distances between the xanthate S1 and the surface Fe1 is 2.440 Å, which is much larger to the radius between Fe–S of 2.310 Å, while that of the xanthate S2 and the surface Fe is 2.360 Å, which is closer to than 2.310 Å. It is indicating that the adsorption of xanthate on the FeS_2 surface is mainly via bond formation between the xanthate S1 and the surface Fe1 atom. Which indicate a strong electron overlap across S2–Fe2 and a weak electron overlap of S1–Fe2.

The C–S bonds of eX was noted to be elongated relative to the isolated eX (S1=C3 = 1.706 Å and S2–C3 = 1.704 Å). The weakening of the C–S bonds was an indication of electron transfer from the surface to the ion [70].

5.1.2 Electronic shift between S atoms of thiol molecules and surface atoms of pyrite

Mulliken atomic charge and population calculation have an important role in the application of quantum chemical calculation of molecular system because of their effect on dipole moment, molecular polarisability, electronic structure etc. The calculated atomic charge values shown in Table 5.4 were obtained by the Mulliken population analysis. Due to the nature of the charge scheme, the atomic charges are unlikely to match the formal charges of the atoms.

Table 5.4: Mulliken bond populations of the interaction between DeDTP, DispDTP and DbDTP and pyrite surfaces

	Adsorbate	Bond atoms	Population	Bondlength
FeS_2(100)	DeDTP	S1-Fe1	0.31	2.455
		S2-Fe2	0.34	2.411
	DispDTP	S1-Fe1	0.34	2.414
		S2-Fe2	0.36	2.372
	DbDTP	S1-Fe1	0.35	2.369
		S2-Fe2	0.34	2.391

The charge analysis shows that all sulphur atoms involved in the coordination of the metal ions have approximately the same charge; the variation between Sulphur atoms is very small for each of the charge decomposition schemes. The S1-Fe1 and S2-Fe2 Mulliken populations on the DeDTP are 0.31 and 0.34, which are similar to those of eX (Table 11). On the other hand, DispDTP (0.34) and DbDTP (0.36) show larger S1-Fe1 and S2-Fe2 bond population values.

The DeDTP S1 and S2 Mulliken charges are slightly negative. Thus, the Mulliken charges show that the atomic charges are slightly smaller for the DeDTP sulphur atoms than the corresponding to DpDTP and DbDTP sulphur atoms (Table A.1). The Mulliken population for S atoms of DTCs on Fe atoms are generally higher for DTCs than DTPs. in addition, on average the population for DeDTC and DbDTC are the same for S atoms. After adsorption, it is visible that the thiol collectors are gaining electrons from the surface.

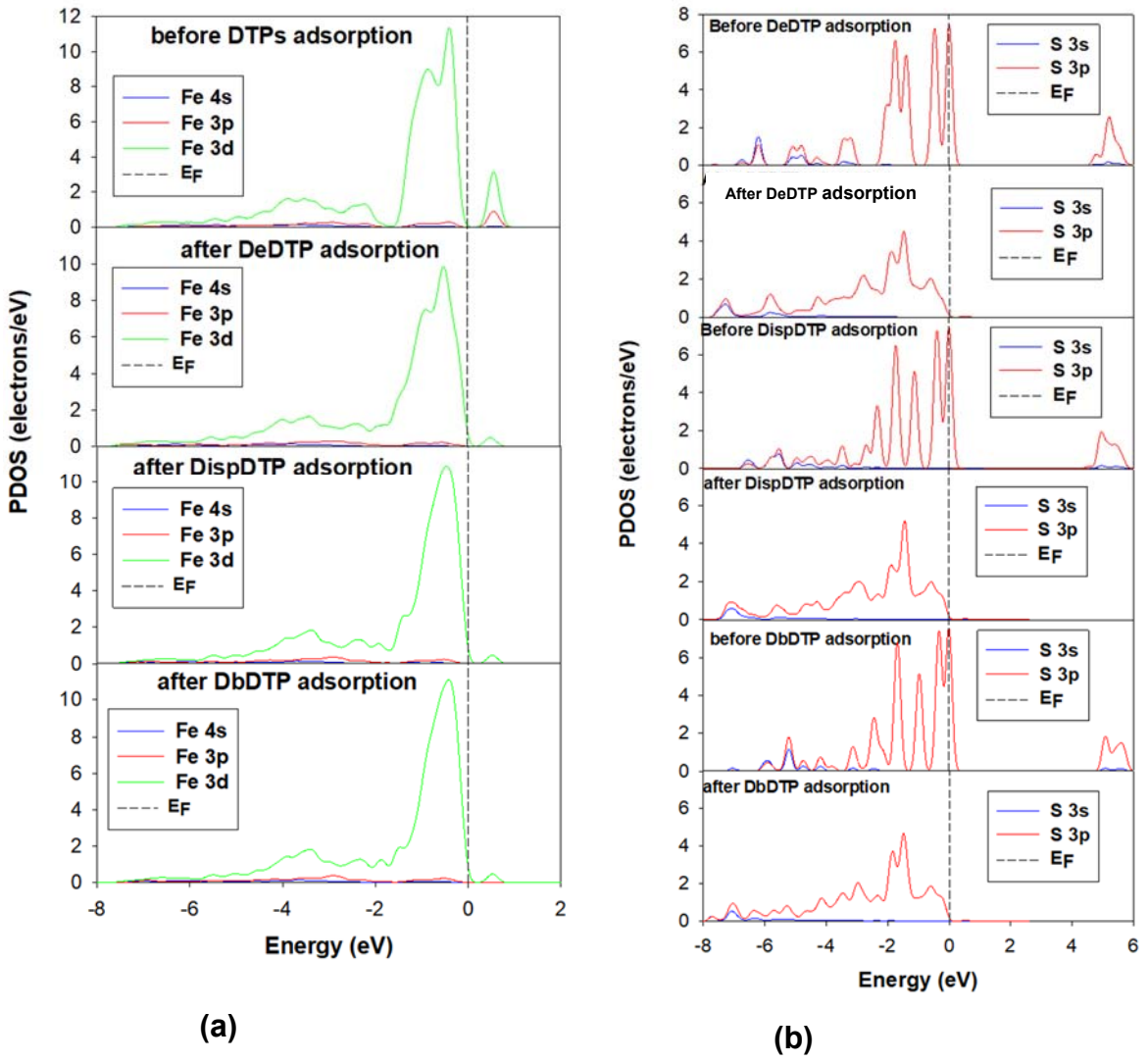

Figure 5.10: Orbital-projected partial densities of states for (a) Fe and (b) S atoms before and after DTPs adsorption. The Fermi energy is taken as the zero energy ($E-E_F=0$).

In Figure 5.10 we present the orbital-projected partial densities of states of Fe and S atoms before and DTP adsorptions. We note that Fe states around the Fermi (particularly in the valence band) are predominantly of 3*d* orbital, with minimal contribution from 3*s* and 4*s*, while the S states are principally of 3*p* character. This shows that Fe 3*d* and S 3*p* states are the valence states and hence active during bonding. Moreover, we observe two degenerate peaks on Fe before adsorption suggesting Fe^{2+} and Fe^{3+} oxidation states. It can also be observed that the introduction lowers Fe and S states population. The S 3*p* states around the Fermi vanish and shifts to lower energies after adsorption.

Table 5.5: Mulliken bonding population of atoms before and after thiol collector adsorption to the surface for DeDTP, DispDTP and DbDTP

		Bond	Population	length
FeS_2(100)	In the absence of thiol collector	S3 - Fe1	0.48	2.176
		S4 – Fe1	0.51	2.219
		S3 - Fe2	0.52	2.221
		S5 - Fe2	0.49	2.164
	DeDTP	S3 - Fe1	0.44	2.134
		S4 – Fe1	0.47	2.231
		S3 - Fe2	0.49	2.134
		S5 - Fe2	0.41	2.206
	DispDTP	S3 - Fe1	0.45	2.195
		S4 – Fe1	0.46	2.249
		S3 - Fe2	0.46	2.210
		S5 - Fe2	0.41	2.197
	DbDTP	S3 - Fe1	0.45	2.206
		S4 – Fe1	0.47	2.247
		S3 - Fe2	0.46	2.217
		S5 - Fe2	0.41	2.200

The population and length of the R(P1-S1) 0.72 and 1.974 Å, R(P1=S2) 0.72 and 1.972 Å for DeDTP, R(P1-S1) 0.74 and 1.969 Å, R(P1=S2) 0.72 and 1.966 for DispDTP, and R(P1-S1) 0.73 and 1.966 Å, R(P1=S2) 0.73 and 1.965 Å for DbDTP respectively; the population and length of (S3 - Fe1) 0.48 and 2.176, (S4 – Fe1) 0.51 and 2.219 Å, (S3 - Fe2) 0.52 and 2.221 Å, (S5 - Fe2) 0.49 and 2.164 Å before adsorption see Table 5.5 and for DTCs.

Meanwhile, population and length of the R(P1-S1) 0.70 and 2.063 Å, R(P1=S2) 0.70 and 2.055 Å; (S3 - Fe1) 0.44 and 2.131, (S4 – Fe1) 0.47 and 2.231 Å, (S3 - Fe2) 0.49 and 2.134 Å, (S5 - Fe2) 0.41 and 2.206 Å after DeDTP adsorption. Population and length of the R(P1-S1) 0.68 and 2.081 Å R(P1=S2) 0.66 and 2.087 Å; (S3 - Fe1) 0.45 and 2.195 Å, (S4 – Fe1) 0.46 and 2.249 Å, (S3 - Fe2) 0.46 and 2.210 Å and (S5 - Fe2) 0.41 and 2.197 Å for DispDTP after adsorption. The population and length R(P1-

S1) 0.70 and 2.068, R(P1=S2) 0.67 and 2.082; (S3 - Fe1) 0.45 and 2.206, (S4 – Fe1) 0.47 and 2.247, (S3 - Fe2) 0.46 and 2.217, (S5 - Fe2) 0.41 and 2.200 for DbDTP after adsorption. The Mulliken bond population analysis showed that when the bond length was shorter, and the population was also smaller, the covalence was decreased. Therefore, the covalency of P1-S decreased; the Fe–S bond length became longer, the population value decreased and covalency became lower.

The population values were 0.49-0.52 and 0.41-0.49 on the pyrite (100) surface before and after adsorption, respectively. Although the effect of the thiol collectors on surface S-Fe bond population and bond length is the same on average, there is a significant difference in the effect of surface on the population of DTPs (Table 5.5), DTCs (Table A.3) and eX (Table 5.10). DTCs R(C-N) and C-S, eX R(C-O) and (C-S) population increases showing that the covalency of DTCs and eX increases.

Table 5.6: Mulliken bonding population of atoms before and after adsorption to the surface. DeDTP, DispDTP and DbDTP

	Adsorbate	Adsorption status	Bond	Population	length
FeS_2(100)	DeDTP	Before	R(P1-S1)	0.72	1.974
			R(P1=S2)	0.72	1.972
		after	R(P1-S1)	0.70	2.063
			R(P1=S2)	0.70	2.055
	DispDTP	Before	R(P1-S1)	0.74	1.969
			R(P1=S2)	0.72	1.966
		after	R(P1-S1)	0.68	2.081
			R(P1=S2)	0.66	2.087
	DbDTP	Before	R(P1-S1)	0.73	1.966
			R(P1=S2)	0.73	1.965
		after	R(P1-S1)	0.70	2.068
			R(P1=S2)	0.67	2.082

Table 5.7: Mulliken charge populations of DTPs adsorption on the pyrite surface (s, p and d represent s orbitals, p orbitals and d orbitals, respectively) before and after adsorption.

	Adsorbate	Adsorption status	Atom	s	p	d	Total	q/e
FeS_2(100)	DeDTP	Before	S1	1.9	4.51	0.00	6.41	-0.41
			S2	1.9	4.5	0.00	6.41	-0.41
		After	s1	1.87	4.53	0.00	6.41	-0.41
			s2	1.86	4.54	0,00	6.40	-0.40
		Before	Fe1	0.35	0.44	7.14	7.93	0.07
			Fe2	0.34	0.44	7.14	7.93	0.07
		After	Fe1	0.35	0.54	7.11	8.00	0.00
			Fe2	0.35	0.55	7.11	8.00	0.00
	DispDTP	Before	S1	1.9	4.48	0.00	6.38	-0.38
			S2	1.9	4.47	0.00	6.37	-0.37
		After	S1	1.87	4.53	0.00	6.41	-0.41
			S2	1.87	4.47	0.00	6.35	-0.35
		Before	Fe1	0.35	0.44	7.14	7.93	0.07
			Fe2	0.34	0.44	7.14	7.93	0.07
		After	Fe1	0.35	0.53	7.10	7.98	0.02
			Fe2	0.35	0.53	7.10	7.98	0.02
	DbDTP	Before	S1	1.9	4.48	0.00	6.38	-0.38
			S2	1.9	4.48	0.00	6.38	-0.38
		After	S1	1.87	4.54	0.00	6.41	-0.41
			S2	1.87	4.47	0.00	6.34	-0.34
		Before	Fe1	0.35	0.44	7.14	7.93	0.07
			Fe2	0.34	0.44	7.14	7.93	0.07
		After	Fe1	0.35	0.54	7.10	7.99	0.01
			Fe2	0.35	0.54	7.10	7.99	0.01

The charge decomposition scheme shows a significant difference in atomic charges on the sulphur atoms of DeDTP S1 compared to the DpDTP and DbDTP sulphur atom, indicating a highly ionic bonding in the system. The ionicity of the bond was probed using Mulliken orbital populations, which were investigated for any populated d metal orbitals. The local covalency of Fe–S became smaller, which provides further evidence for the adsorption of DTPs on the pyrite (100) surface, as shown in the configuration analysis. The covalency of P1-S and Fe–S changed there were bonds between the each S atoms in DTPs and the Fe atoms in pyrite (100); therefore, there was chemical adsorption between them, which is in agreement with the adsorption configuration and calculation of adsorption energy. The effect of chain length and branch is not clear on the surface, for long the chains the bond between Fe-S of the surface became longer compare to DTP with fewer carbons as seen table 5.6. The covalency of Fe-S bonds on the surface is stronger the covalency of the bonding between DTPs and surface as seen in table 5.7. after adsorption the is an exchange of electrons for thiol collectors (Table 5.7, Table 5.8 and Table A.4) and the surface. Although, DTPs showed higher Mulliken charges than the DTCs and eX before adsorptions and after adsorption, the change in charge transfer is more for DTCs and eX than DTPs.

Table 5.8: Mulliken charge populations of Ex adsorption on the pyrite surface (s, p and d represent s orbitals, p orbitals and d orbitals, respectively) before and after adsorption.

Adsorbate		Adsorption status	Atom	s	p	d	total	q/e
FeS_2(100)	eX	before	S1	1.84	4.08	0.00	5.92	0.08
			S2	1.85	4.13	0.00	5.98	0.02
		after	S1	1.83	4.15	0.00	5.98	0.02
			S2	1.82	4.24	0.00	6.06	-0.06
		before	Fe1	0.35	0.44	7.14	7.93	0.07
			Fe2	0.34	0.44	7.14	7.93	0.07
		after	Fe1	0.35	0.52	7.10	7.98	0.02
			Fe2	0.35	0.53	7.11	7.99	0.01

The S2 in the DeDTP lost 0.01 and S1 remains the same, S1 for DispDTP gains 0.03 electrons and S2 lost 0.02 and S1 for DbDTP gained 0.03 electrons while S2 lost 0.04 electrons after adsorption, respectively table 5.7. while Surface Fe gains from 0.05 to 0.07 electrons. The electron gain and loss were conserved between DTPs and the pyrite (100) surface in terms of the atom number, which led to the partial more negative charge of the pyrite (100) surface and less negative charge of the DTPS and the change is very small.

Figure 5.11: Mulliken bond populations of the interaction between eX and pyrite surface.

	Adsorbate	Bond atoms	Population	Bond
FeS_2(100)	eX	S1—Fe1	0.31	2.360
		S2 – Fe2	0.34	2.440

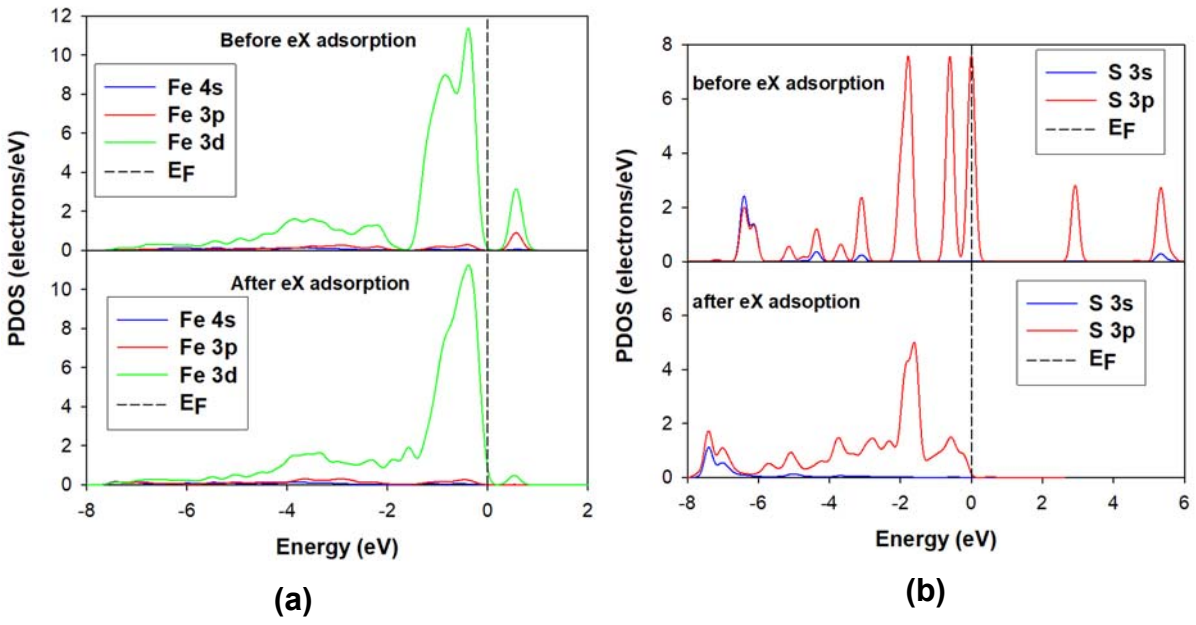

Figure 5.12: Bonding Fe–S atoms before and after eX adsorption. The zero of energy has been set at the Fermi level EF. (a) Surface Fe and (b) S of eX atom.

In Figure 5.13, we present the partial densities of states of pyrite Fe atoms and Xanthates S before and after eX adsorption. Similarly, to DTPs adsorption, we note that eX slightly enhances metallic behaviour of Fe atoms, since the Fermi level shifts to valence band after adsorption. Furthermore, S 3s and 3p states are largely reduced from 7.8 1/eV and 2.3 1/eV to 5.0 1/eV and 1.0 1/eV, respectively after adsorption. Moreover, the Fermi level moves to the edge of the valence band, suggesting insulator behaviour characteristics.

Table 5.9: Mulliken bonding population of atoms before and after thiol collector adsorption to the surface eX.

Adsorbate			Bond	Population	length
FeS_2(100)	eX	In the absence of eX collector	S3 - Fe1	0.48	2.176
			S4 – Fe1	0.51	2.219
			S3 - Fe2	0.52	2.221
			S5 - Fe2	0.49	2.164
		In the present of eX collector	S3 - Fe1	0.44	2.188
			S4 – Fe1	0.46	2.230
			S3 - Fe2	0.46	2.206
			S5 - Fe2	0.40	2.224

Table 5.10: Mulliken bonding population of atoms before and after adsorption to the surface. eX.

	Adsorbate	Adsorption status	Bond	Population	length
FeS_2(100)	eX	Before	R(C1–O1)	0.67	1.326
			R(C1-S1)	0.73	1.674
			R(C1=S2)	0.77	1.675
		after	R(C1–O1)	0.98	1.354
			R(C1-S1)	0.81	1.757
			R(C1=S2)	0.74	1.778

Figure A.1 show the PDOS of bonding Fe–S atoms before and after DTCs adsorption. For the (100) surface, the upper parts of the valence band and conduction band had significant contributions from the surface Fe 3d states, and a significant band gap existed between the valence band and conduction band. The DTCs S 3p state was occupied in the vicinity of the Fermi level (EF), thereby forming six apparent DOS peaks. After DTPs adsorption, the DOS peak of S 3p was lowered, and the non-locality of the 3p electrons was enhanced. The Fe 3d states at the upper valence band, however, were decreased, and the two DOS peaks formed one peak. In addition, the

bandgap between the valence band and conduction band was significantly lowered, and significant hybridisation occurred between the S 3p and Fe 3d states.

5.2 Effect of chain length on the adsorption of DTPs and DTCs on Galena, chalcopyrite and sphalerite.

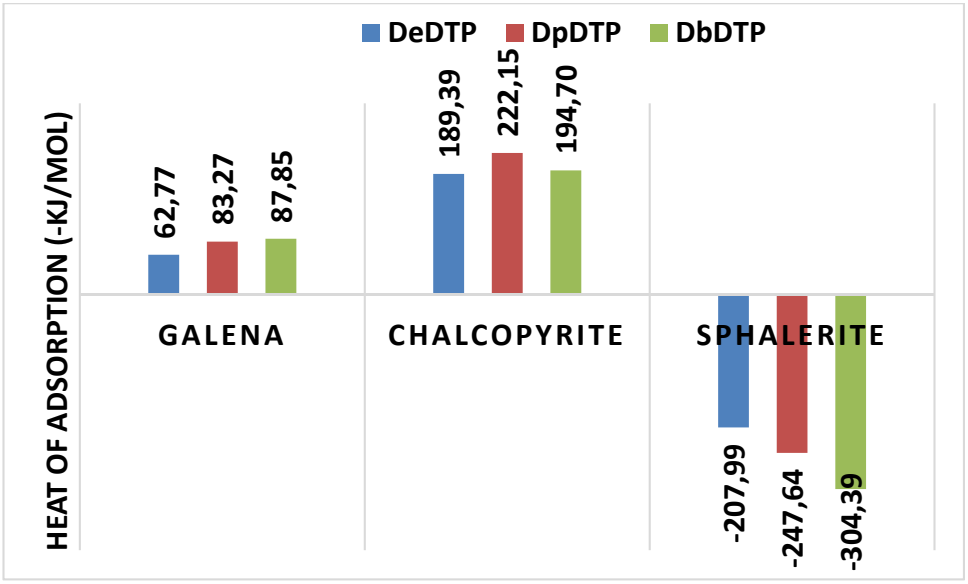

Figure 5.13: Effect of chain length (di-C2, diiso-C3, di-C4) on the enthalpy of adsorption of DTC homologues galena, chalcopyrite, and sphalerite.

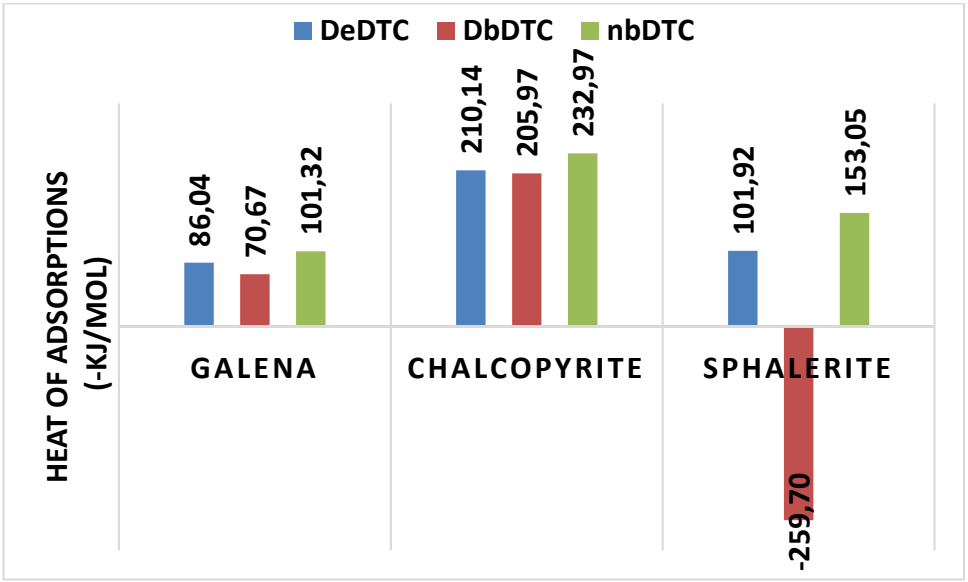

Figure 5.14: Effect of chain length (di-C2, n-C4, di-C4) on the enthalpy of adsorption of DTC homologues on galena, chalcopyrite, and sphalerite.

The results of the effect of chain length of DTPs and DTCs on the enthalpies of adsorption on pyrite, galena, chalcopyrite and sphalerite (Figure 5.1, 5.2, 5.13 and 5.14) have shown that an increase in chain length of the DTPs resulted in an increase in the enthalpies of adsorption for pyrite and galena. This is an important observation since the ligand is the same in all cases and therefore the effect is due to the role of the alkyl group. This has not been shown previously through the use of directly measured enthalpies of adsorption. The increase of the enthalpies of adsorption with increasing alkyl chain length is intuitive to be expected since longer alkyl chain lengths are associated with a stronger positive inductive effect, releasing electrons towards the head/ligand/functional group and thereby increasing the electron density around the functional group rendering the collector more reactive [18]. Thus the collectors with a longer chain length will result in a more exothermic reaction than those with shorter chain lengths.

The enthalpy of adsorption results are also consistent with decreasing trends of the pKa with the increasing alkyl chain lengths for the DTPs. The electron-donating or withdrawing effects of the substituent groups in a collector molecule not only affects the electron density around the donor atom but also the pKa of the collector [17].

Collectors with a larger pKa should have greater electron-donating capacity and have stronger bonds with the mineral surface and hence a more negative enthalpy of adsorption. The assumption here is that the collector anion reacts with the metal cations on the mineral surface.

The effect of the branching of the hydrocarbon chain length of the dithiocarbamates on the enthalpy of adsorption of pyrite was investigated. The collectors investigated were DeDTC and n-butyl DTC. The collectors have alkyl chain lengths with equivalent carbon numbers, viz. 4, though the two collectors have different chemical structures in the case of DeDTC and n-butyl DTC. Thus this investigation provides an opportunity to investigate the effect of branching of the alkyl chain length on the enthalpy of adsorption where the carbon number of each alkyl group was the same. Figure 5.2 shows that the DeDTC produced a higher enthalpy of adsorption than n-butyl DTC on the pyrite surface. The results show that the configuration of the alkyl chain length of the same carbon number has got an influence on the enthalpy of adsorption.

5.2.1 The geometry of DTPs, DTCs and eX collector on chalcopyrite, galena and sphalerite

The effect of chain length of DTPs and DTCs on the heat of adsorption on chalcopyrite, galena and ZnS was investigated. This was conducted to investigate to what extent the results were mineral specific. DeDTP and DbDTP, DeDTC and DbDTC were chosen since they represent the two extreme samples in terms of alkyl chain length of those investigated in this work. The heat of adsorption results are shown in Figure 5.13 and 5.14.

The adsorption configurations of DTPs on the $CuFeS_2$/PbS/ZnS surfaces are presented in. It is found from figure 5.13 that the distances between DTPs S atom and the chalcopyrite Fe atom (are around 2.135–2.149 Å) which less to the sum of atomic radius of Fe and S of 2.310 Å, galena Pb atom (2.869-2.936) which are close to the sum of atomic radius of Pb and S of 2.840 Å and sphalerite Zn atom are around 2.520–2.664 Å, which are far to the sum of atomic radius of Zn and S of 2.37 Å. This implies that there is a relatively strong interaction between these DTPs reagents and $CuFeS_2$ surface, and very weak or no interaction between DTPs and ZnS, which agrees well with the corresponding calculated adsorption energies, respectively, which are supposed as the chemisorption. It could conclude from the calculated results that DTPs could float $CuFeS_2$ and Galena and no float sphalerite, which corresponds with the flotation result. It is well known that the unactivated sphalerite responds very poorly [86, 87]

We have calculated the relaxed bond distances and bond angles between the S atoms of DeDTP, DispDTP, DbDTP, DeDTC, nbDTC, DbDTC and DbDTC collectors' and metals atoms on sulphide surfaces, as shown in Table 5.11 to Table 5.10. The results were compared with the radius (d_o) between Fe–S (2.310 Å) in Table 6.4. The geometric bonding of DeDTP, DispDTP and DbDTP on Fe sites are shown in Figure 6.15. We observed that adsorption of DeDTP, DispDTP and DbDTP on chalcopyrite surface preferred to chemisorb, thus forming a bridging geometry with Fe1 and Fe2 atoms and are coordinated to S1 and S2 atom, respectively (Figure 6.15a).

The P-O bonds in dithiophosphate do not participate in conjugation as the -PS_2 and -PO_2 groups lie in different planes. This observation is well reflected in the calculated P-O bond lengths (1.6173, 1.6285 Å) which are very close to the standard single P-O bond length of 1.63 Å. The extent of conjugation between the lone pair orbital of the heteroatom and -CS_2- (-PS_2-) head group is also reflected in trend observed for C-Y bond lengths

Table 5.11: Calculated bond lengths (*R*, in Å), bond angles (θ, in deg.) for collectors on the (112) surface.

Bonds	DeDTP	DispDTP	DbDTP
	Fe-top		
d_o(Fe–S)	2.310	2.310	2.310
R(Fe1–S1)	2.138	2.160	2.137
R(Fe2–S2)	2.135	2.138	2.149
R(C3/P1–S1)	2.043	2.037	2.043
R(P1-O1)	1.570	1.584	1.584
R(C3/P1–S2)	2.041	2.030	2.015
R(P1-O2)	1.570	1.566	1.567
θ(S1–P1/C3–S2)	123.99	123.03	125.128

$d_o = r_o + r_{metal}$, is the theoretical value, r_o is the radius of S for the collector; r_{metal} is the atomic radius of metal (M) for sulphide.

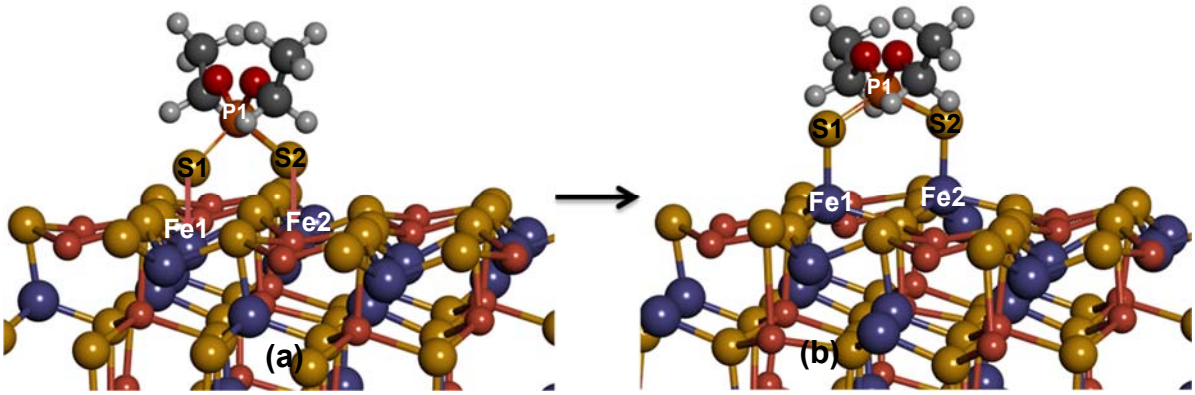

Figure 5.15: DeDTP collector adsorbed on the $CuFeS_2$ (112) surface: (a) before and (b) after adsorption.

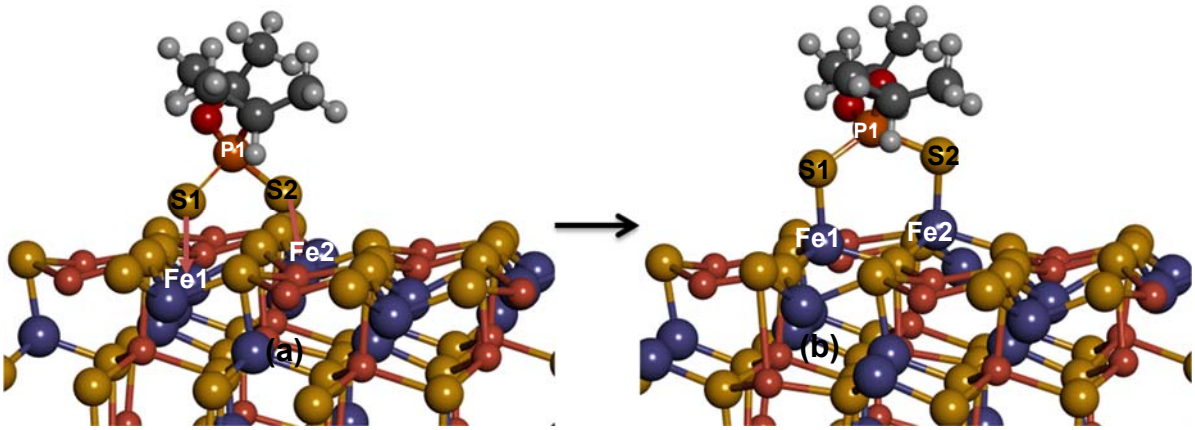

Figure 5.16: DispDTP collector adsorbed on the $CuFeS_2$ (112) surface: (a) before and (b) after adsorption.

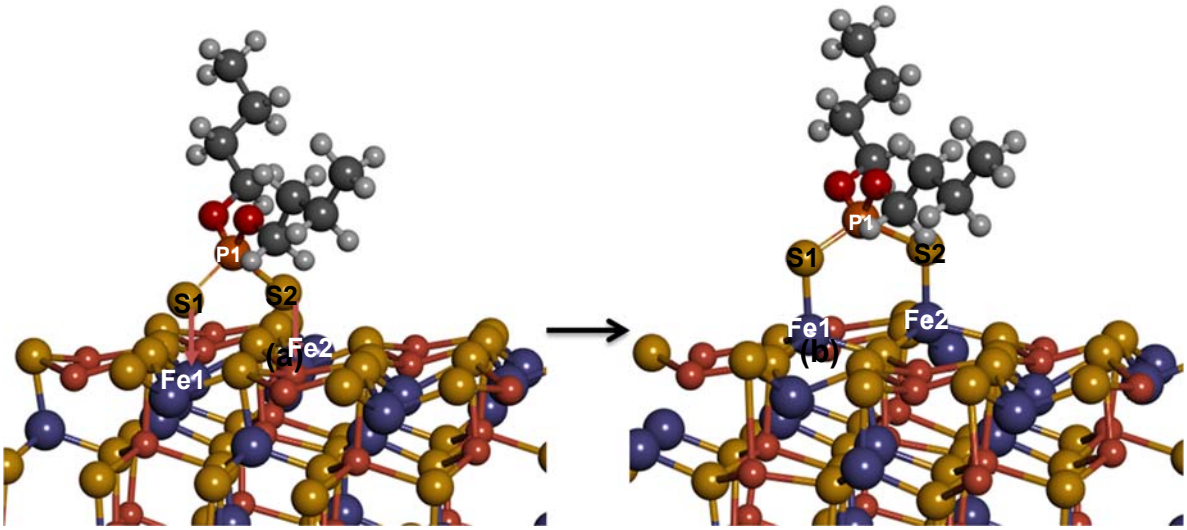

Figure 5.17: DbDTP collector adsorbed on the $CuFeS_2$ (112) surface: (a) before and (b) after adsorption.

The S complexes have a hemi directed or distorted square pyramid structure around the Pb atom. Each of the complexes is of non-planar asymmetric, although each coordinating sub-branch is almost planar except alkyl dithiophosphate, owing to tetrahedral geometry at P atom. The S atoms of three DTPs ligands in are symmetrically placed bridging geometry across the Pb atoms except in $Pb(ENH–CS_2)_2$ and $Pb(EHO_2–PS_2^-)_2$ which bind to the Pb atom in a bidentate fashion, with two different M-Y bond lengths which differ by ~0.15-0.20 Å.

Table 5.12: Calculated bond lengths (*R*, in Å), bond angles (θ, in deg.) for collectors on the Galena (100) surface.

Bonds	DeDTP	DispDTP	DbDTP
	Pb-top		
d_o(Pb–S)	2.281	2.840	2.840
R(Pb1–S1)	2.936	2.913	2.873
R(Pb2–S2)	2.869	2.910	2.897
R(C3/P1–S1)	1.998	2.011	2.002
R(P1-O1)	1.563	1.569	1.596
R(C3/P1–S2)	2.000	2.001	1.984
R(P1-O2)	1.591	1.592	1.589
θ(S1–P1/C3–S2)	121.12	121.12	119.95

$d_o = r_o + r_{metal}$, is the theoretical value, r_o is the radius of S for the collector; r_{metal} is the atomic radius of metal (M) for sulphide.

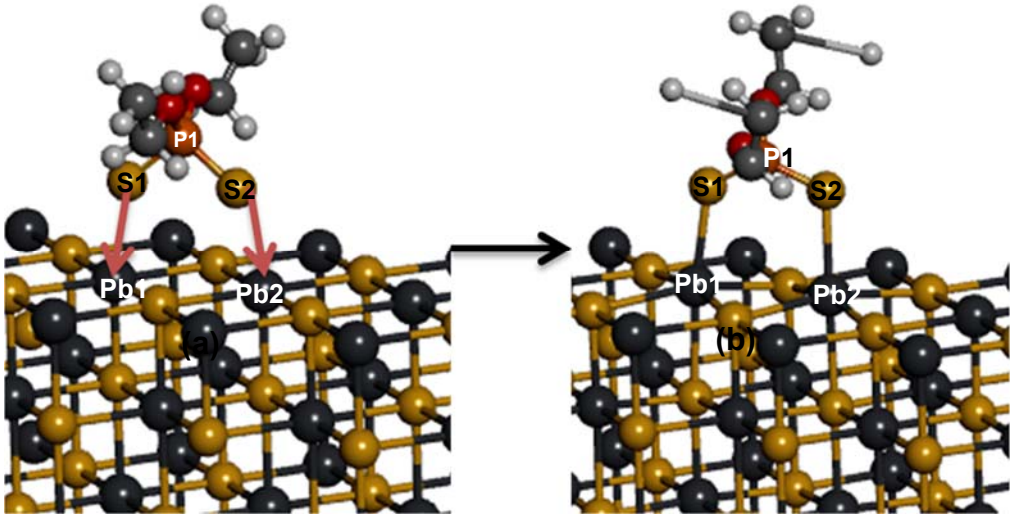

Figure 5.18: DeDTP collector adsorbed on the PbS (100) surface: (a) before and (b) after adsorption.

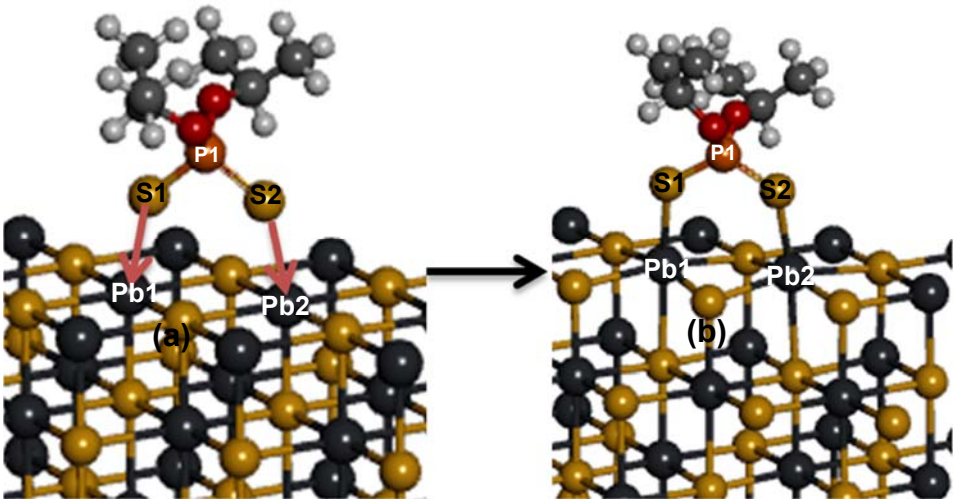

Figure 5.19: DeDTP collector adsorbed on the PbS (100) surface: (a) before and (b) after adsorption.

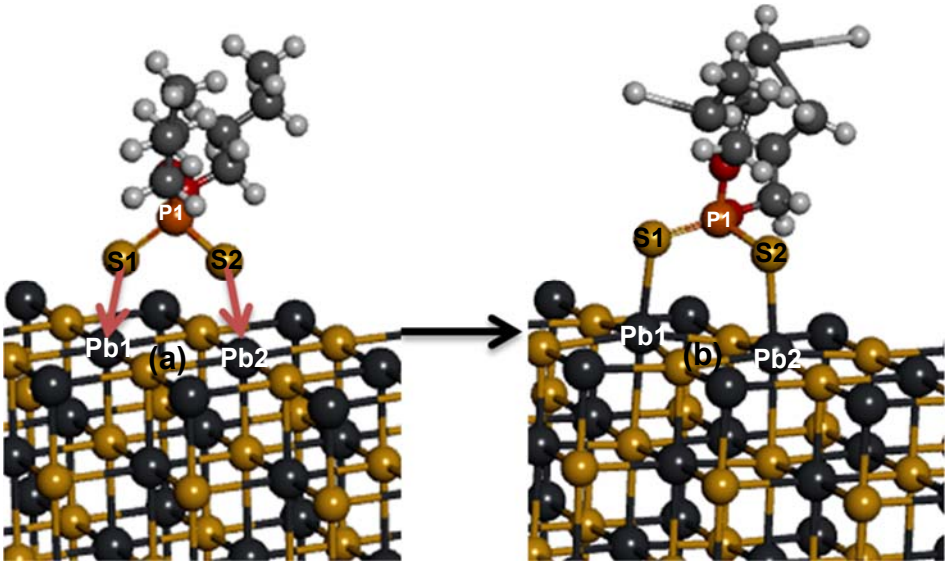

Figure 5.20: DbDTP collector adsorbed on the PbS (100) surface: (a) before and (b) after adsorption.

Table 5.13: Calculated bond lengths (*R*, in Å), bond angles (θ, in deg.) for collectors on the sphalerite (110) surface.

Bonds	DeDTP	DispDTP	DbDTP
	Fe-top		
d_o(Zn–S)	2.281	2.281	2.281
R(Zn1–S1)	2.520	2.664	2.597
R(Zn2–S2)	2.576	2.620	2.513
R(C3/P1–S1)	2.013	1.996	2.019
R(P1-O1)	1.586	1.582	1.597
R(C3/P1–S2)	2.009	2.025	2.005
R(P1-O2)	1.592	1.590	1.591
θ(S1–P1/C3–S2)	117.76	112.45	118.54

$d_o = r_o + r_{metal}$, is the theoretical value, r_o is the radius of S for the collector; r_{metal} is the atomic radius of metal (M) for sulphide.

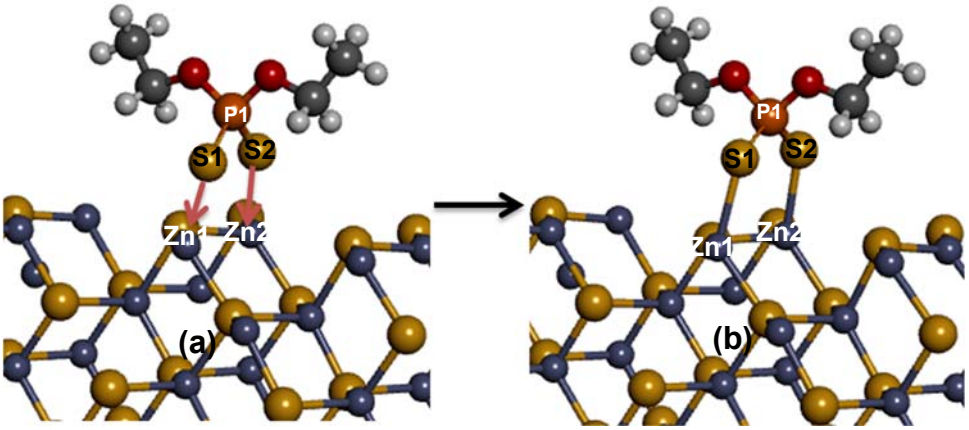

Figure 5.21: DeDTP collector adsorbed on the ZnS (110) surface: (a) before and (b) after adsorption.

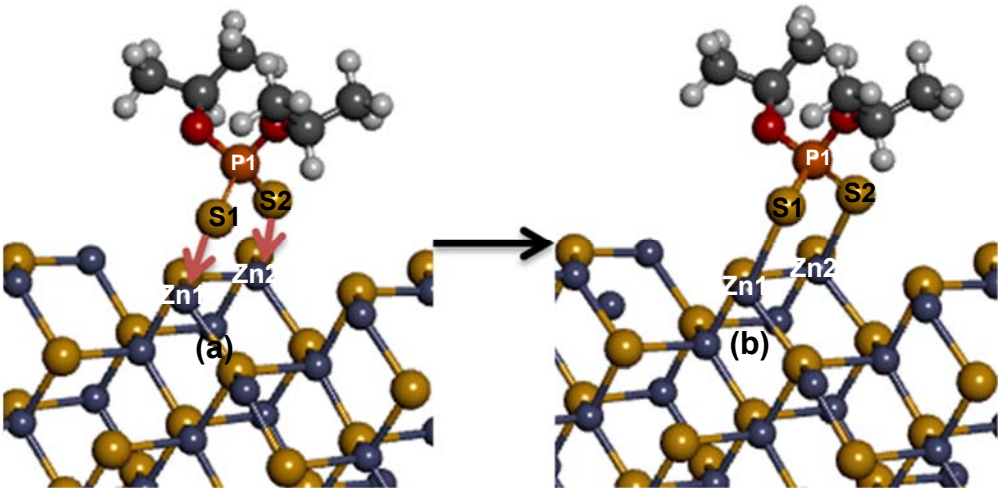

Figure 5.22: DispDTP collector adsorbed on the ZnS (110) surface: (a) before and (b) after adsorption.

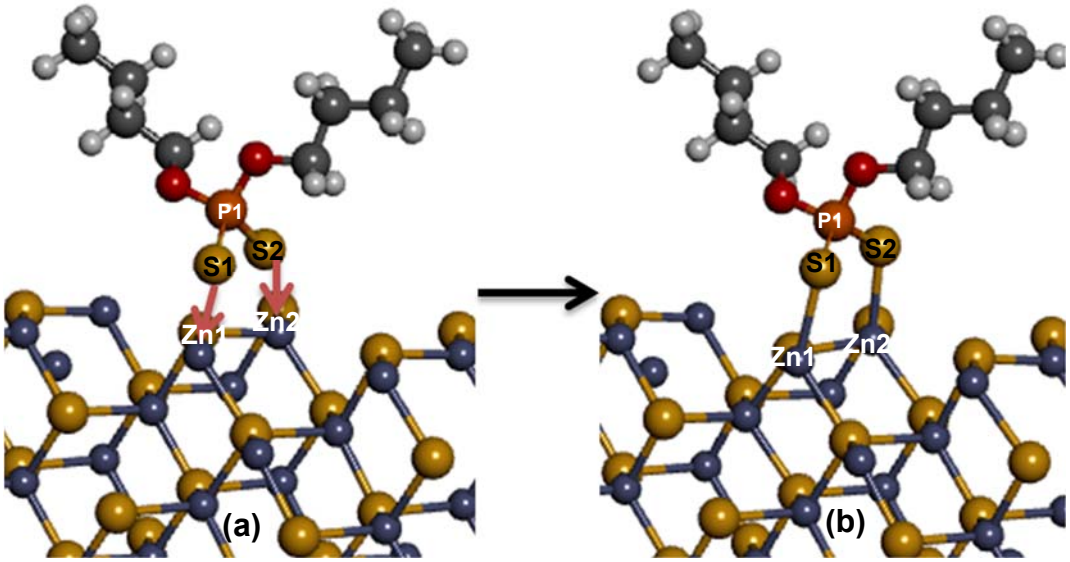

Figure 5.23: DbDTP collector adsorbed on the ZnS (110) surface: (a) before and (b) after adsorption.

The adsorption configurations DTCs on the CuFeS2/PbS/ZnS surfaces are shown in Figure 5.14 to Figure 5.23, Concerning the interacting distance, the distances between DTCs on the CuFeS2/PbS/ZnS surface for DeDTC,nbDTC and DbDTC R(Fe1–S1) 2.127, 2.138 and 2.124 and R(Fe2–S2) 2.146, 2.133 2.121 (S1−Pb1: 2.957Å, S2−Pb2: 2.853 Å) are the shortest, while for xanthate and DTC are the exactly same

suggesting that the interaction of xanthate/DTC with the galena surface are the same. The adsorption energy order for xanthate and DTC doesn't agree well with the interacting distance result. The reason may ascribe to the structural distortion during the adsorption which would consume the energy.

For dithiocarbamates (DeDTC,nbDTC and DbDTC), calculated values of C3-N bond lengths (1.355,1.358 and 1.358 Å), (1.363,1.361 and 1.365 Å) and (1.372, 1.358 and1.369 Å) for chalcopyrite, galena and sphalerite respectively, are much closer to the standard C-N double bond (1.38 Å) than to C-N single bond (1.47 Å), which indicate presence of strong double-bond character and participation of C3-N bond in electron delocalization with $-CS_2^-$ head group. All the bonds at the N centre lie in the same plane as $-CS_2^-$ group. the analysis shows that the three σ-binding orbitals of N atom in dithiocarbamates are sp2 hybridized and the lone pair has 100% p-character. Consistent with a previous study [88], C-N bond length is shorter in ENH–CS2- than in $E_2N–CS_2^-$ as N atom in $E_2NH–CS_2^-$ has a more negative charge. Hybridization of O atom in xanthate is also close to sp2; the two σ-binding orbitals are sp2.24 and sp2.26 hybridized, and one lone pair has sp1.60 hybridization. The second lone pair has 100% p-character and lies perpendicular to the molecular plane. This suggests the presence of a similar type of conjugative effects in xanthate as observed for dithiocarbamates.

Table 5.14: Calculated bond lengths (*R*, in Å), bond angles (θ, in deg.) for collectors on the (112) surface.

Bonds	DeDTC	nbDTC	DbDTC
	Fe-top		
d_o(Fe–S)	2.281	2.281	2.281
R(Fe1–S1)	2.127	2.138	2.124
R(Fe2–S2)	2.146	2.133	2.121
R(N1-C3)	1.355	1.358	1.358
R(C3-S1)	1.726	1.726	1.729
R(C3=S2)	1.730	1.719	1.733
θ(S1–P1/C3–S2)	127.47	130.28	127.85

$d_o = r_o + r_{metal}$, is the theoretical value, r_o is the radius of S for the collector; r_{metal} is the atomic radius of metal (M) for sulphide.

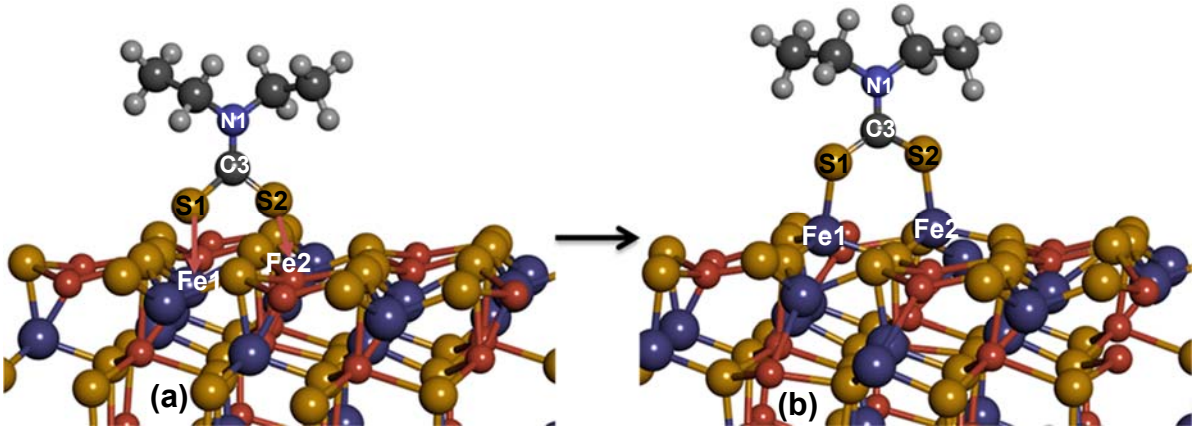

Figure 5.24: DeDTC collector adsorbed on the $CuFeS_2$ (112) surface: (a) before and (b) after adsorption.

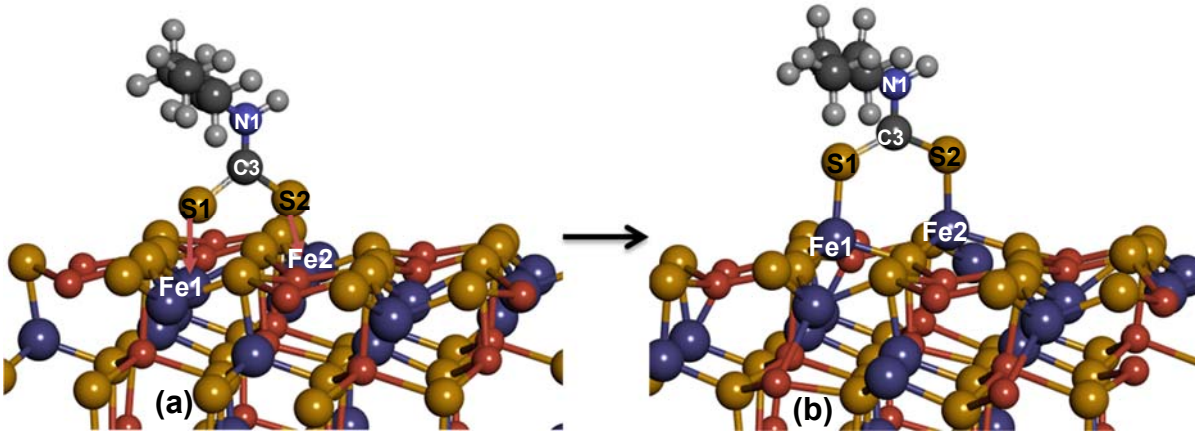

Figure 5.25: nbDTC collector adsorbed on the $CuFeS_2$ (112) surface: (a) before and (b) after adsorption.

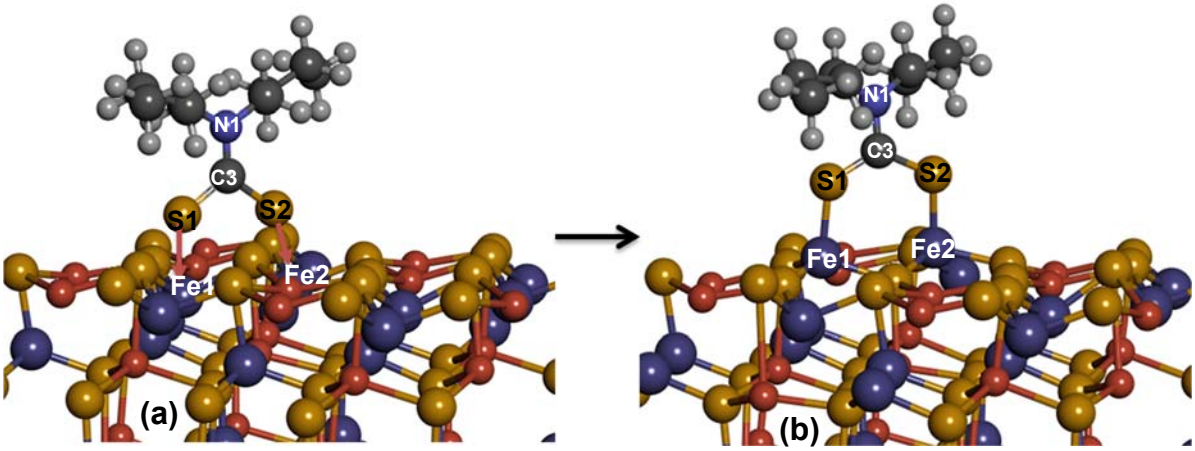

Figure 5.26: DbDTC collector adsorbed on the $CuFeS_2$ (112) surface: (a) before and (b) after adsorption.

Table 5.15: Calculated bond lengths (*R*, in Å), bond angles (θ, in deg.) for collectors on the galena (100) surface.

Bonds	DeDTC	nbDTP	DbDTC
	Pb-top		
d_o(Pb–S)	2.840	2.840	2.840
R(Pb1–S1)	2.854	2.827	2.840
R(Pb2–S2)	2.851	2.902	2.833
R(N1-C3)	1.363	1.361	1.365
R(C3-S1)	1.724	1.733	1.721
R(C3=S2)	1.724	1.701	1.726
θ(S1–P1/C3–S2)	127.31	129.51	127.29

$d_o = r_o + r_{metal}$, is the theoretical value, r_o is the radius of S for the collector; r_{metal} is the atomic radius of metal (M) for sulphide.

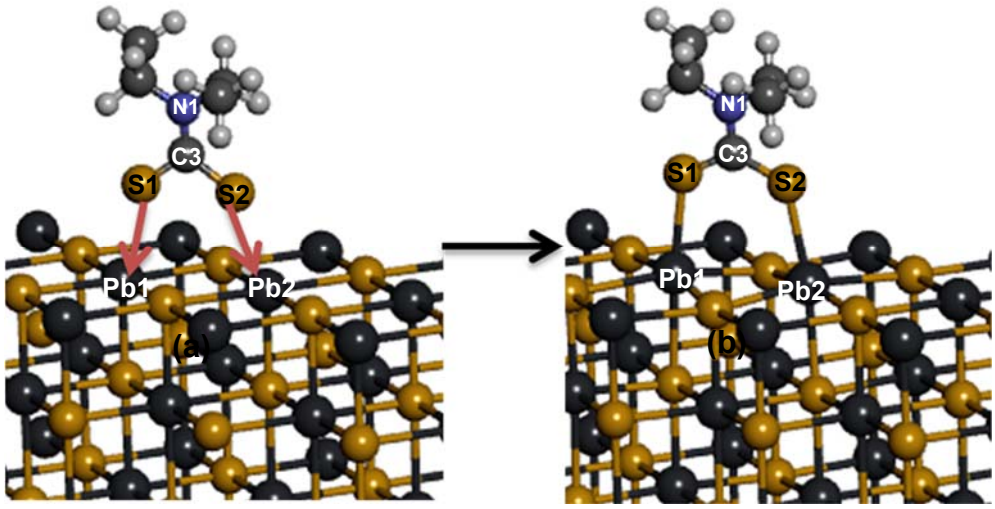

Figure 5.27: DeDTC collector adsorbed on the PbS (100) surface: (a) before and (b) after adsorption.

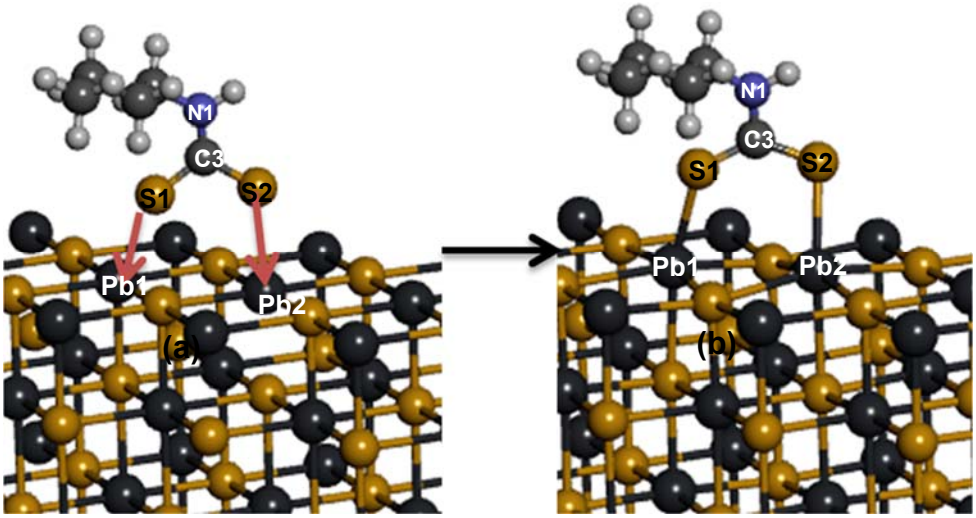

Figure 5.28: nbDTC collector adsorbed on the PbS (100) surface: (a) before and (b) after adsorption.

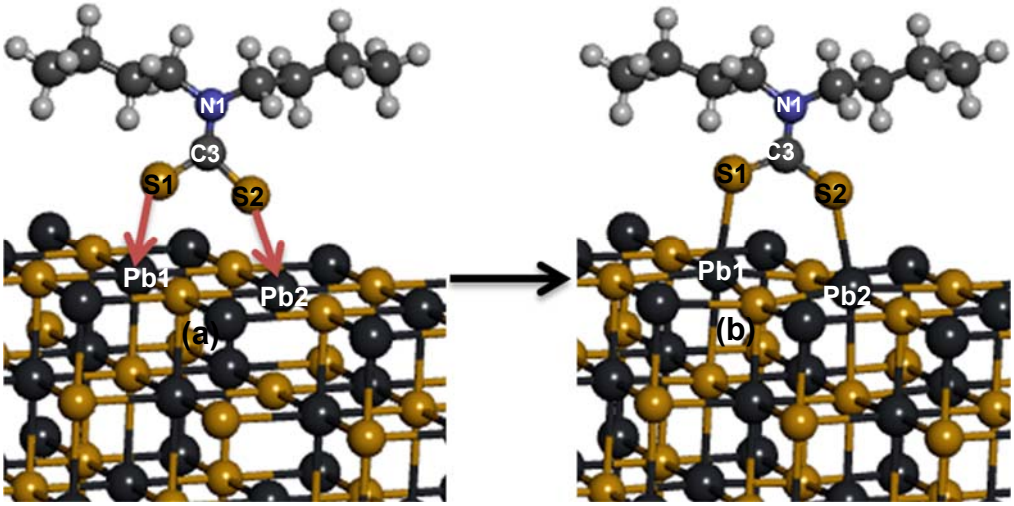

Figure 5.29: DbDTC collector adsorbed on the PbS (100) surface: (a) before and (b) after adsorption.

Table 5.16: Calculated bond lengths (*R*, in Å), bond angles (θ, in deg.) for collectors on the sphalerite (110) surface.

Bonds	DeDTC	nbDTP	DbDTC
	Zn-top		
d_o(Zn–S)	2.281	2.281	2.281
R(Zn1–S1)	2.514	2.453	2.525
R(Zn2–S2)	2.505	2.452	2.504
R(N1-C3)	1.372	1.358	1.369
R(C3-S1)	1.721	1.733	1.736
R(C3=S2)	1.721	1.713	1.715
θ(S1–P1/C3–S2)	126.76	126.00	125.40

$d_o = r_o + r_{metal}$, is the theoretical value, r_o is the radius of S for the collector; r_{metal} is the atomic radius of metal (M) for sulphide.

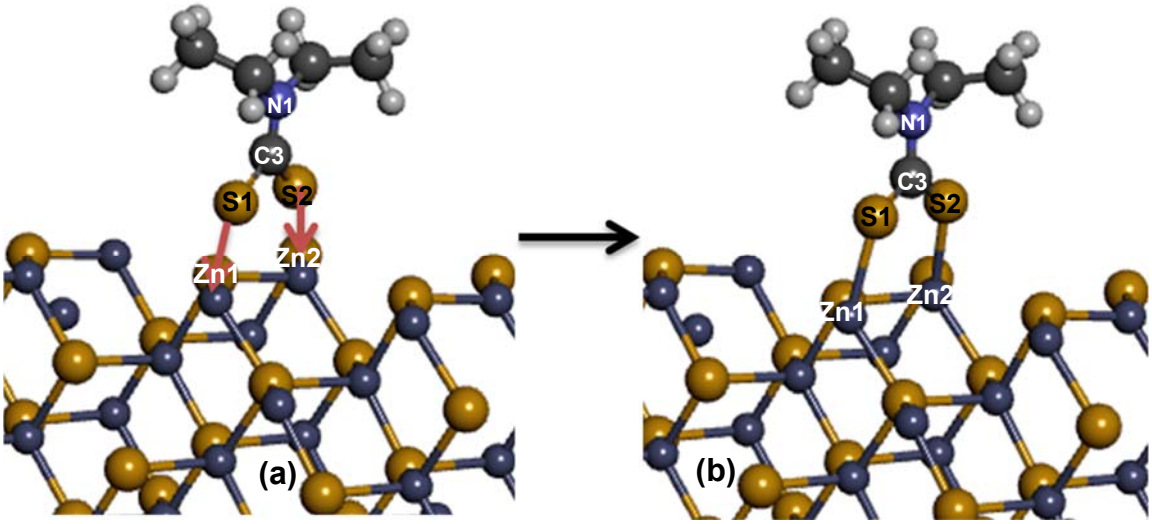

Figure 5.30: DeDTC collector adsorbed on the ZnS (110) surface: (a) before and (b) after adsorption.

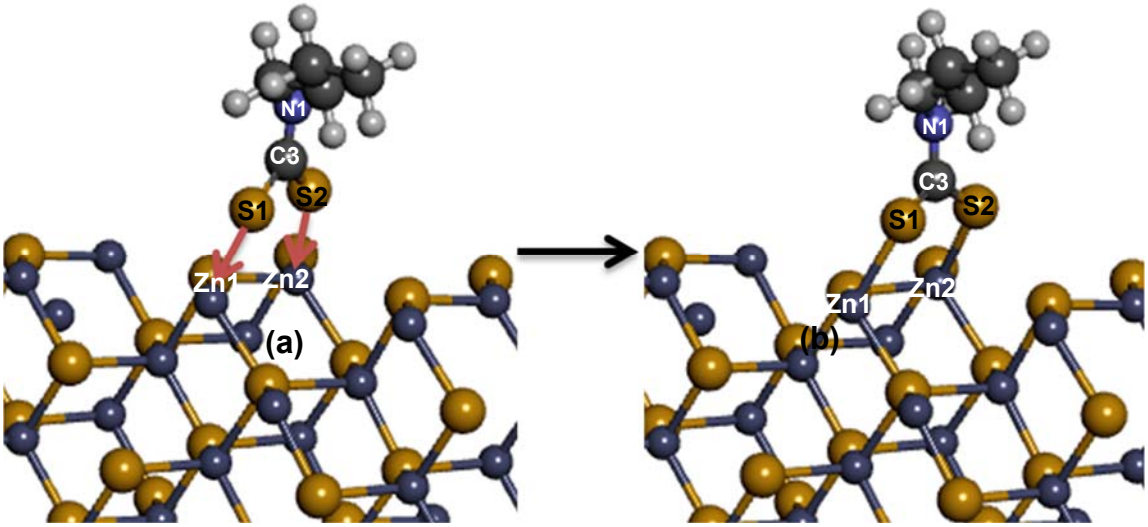

Figure 5.31: nbDTC collector adsorbed on the ZnS (110) surface: (a) before and (b) after adsorption.

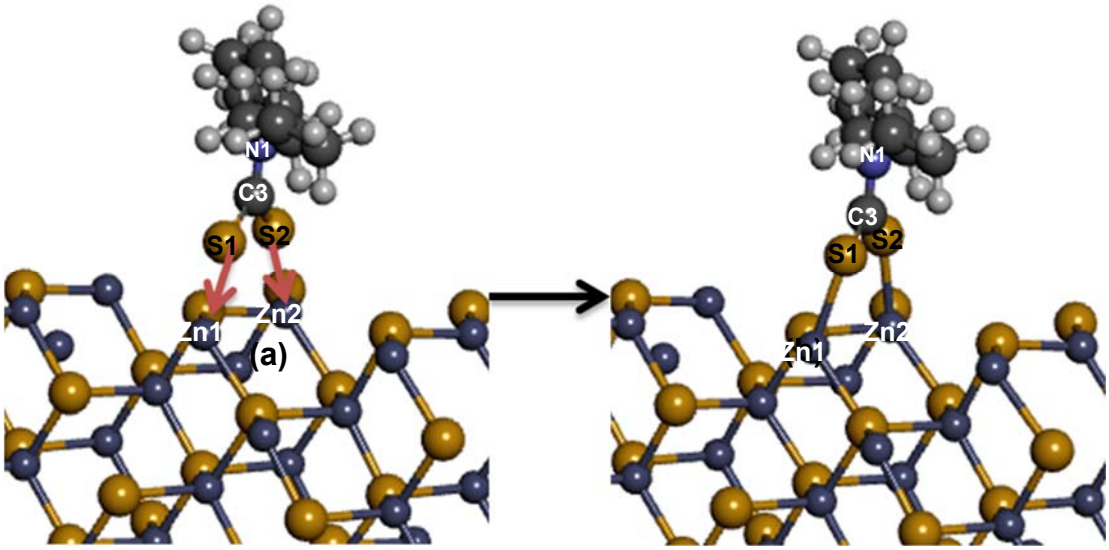

Figure 5.32: nbDTC collector adsorbed on the ZnS (110) surface: (a) before and (b) after adsorption.

Evidently, C-O bond length (1.348 Å) in xanthate lies between standard single and double C-O bond lengths of 1.43 and 1.21 Å respectively. The less double bond character of the C-O bond compared to C-N bond can be explained in terms of higher electronegativity of O atom.

Table 5.17: Calculated bond lengths (*R*, in Å), bond angles (θ, in deg.) for collectors on the (112) surface.

Bonds	eX
	Fe-top
d_o(Fe–S)	2.281
R(Fe1–S1)	2.135
R(Fe2–S2)	2.122
R(C3–S1)	1.713
R(C3=S1)	1.699
R(C3–O1)	1.341
θ(S1–P1/C3–S2)	131.83

$d_o = r_o + r_{metal}$, is the theoretical value, r_o is the radius of S for the collector; r_{metal} is the atomic radius of metal (M) for sulphide.

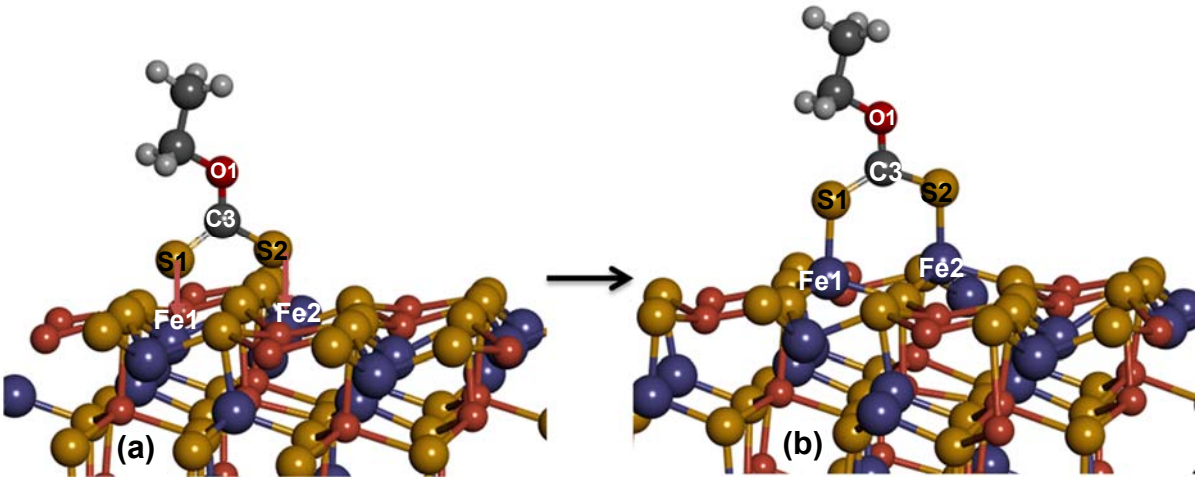

Figure 5.33: eX collector adsorbed on the $CuFeS_2$ (112) surface: (a) before and (b) after adsorption.

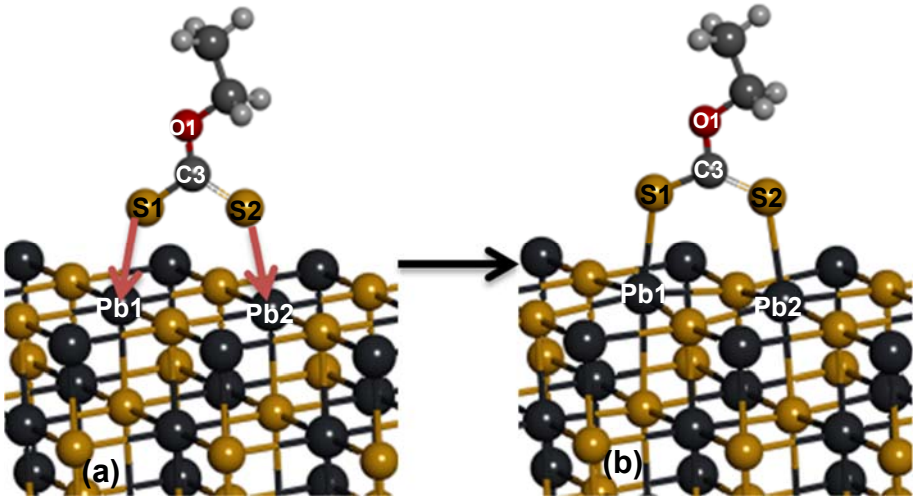

Figure 5.34: eX collector adsorbed on the PbS (100) surface: (a) before and (b) after adsorption.

Table 5.18: Calculated bond lengths (*R*, in Å), bond angles (θ, in deg.) for collectors on the Galena (100) surface.

Bonds	eX
	Pb-top
d_o(Pb–S)	2.840
R(Pb1–S1)	2.867
R(Pb2–S2)	2.876
R(C3–S1)	1.700
R(C3=S1)	1.697
R(C3–O1)	1.354
θ(S1–C3–S2)	132.57

$d_o = r_o + r_{metal}$, is the theoretical value, r_o is the radius of S for the collector; r_{metal} is the atomic radius of metal (M) for sulphide.

Table 5.19: Calculated bond lengths (*R*, in Å), bond angles (θ, in deg.) for collectors on the sphalerite (110) surface.

Bonds	eX
	Zn-top
d_o(Zn–S)	2.281
R(Zn1–S1)	2.608
R(Zn2–S2)	2.575
R(C3–S1)	1.696
R(C3=S1)	1.701
R(C3–O1)	1.356
θ(S1–P1/C3–S2)	129.7

$d_o = r_o + r_{metal}$, is the theoretical value, r_o is the radius of S for the collector; r_{metal} is atomic radius of metal (M) for sulphide.

The ligands bind to Zn atom in a manner such that two Y2M planes are perpendicular to each other, thus forming a tetrahedral or slightly distorted tetrahedral structure around the Zn atom. Tetrahedral geometry of these ligands around the Zn centre has been reported in various experimental and theoretical investigations, e.g., xanthate [89] dialkyl dithiocarbamate [90], and dialkyldithiophosphate [91].The geometrical

parameters calculated in this study match closely with those of the past investigations [91].

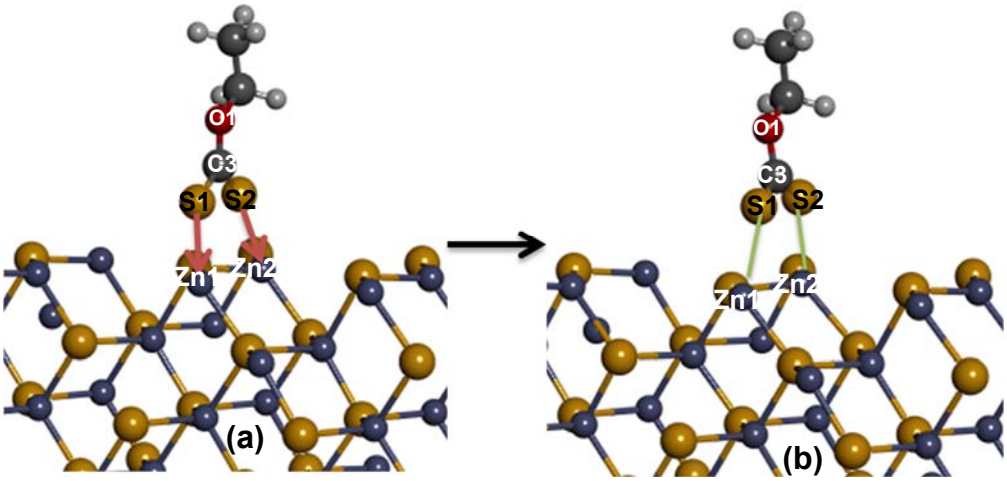

Figure 5.35: DbDTC collector adsorbed on the $CuFeS_2$ (112) surface: (a) before and (b) after adsorption.

Table 5.20: Calculated bond lengths (*R*, in Å), bond angles (θ, in deg.) for collectors on the (100) galena surface.

Bonds	DeDTP	DispDTP	DbDTP
	Fe-top		
d_o(Fe–S)	2.281	2.281	2.281
R(Fe1–S1)	2.138	2.160	2.137
R(Fe2–S2)	2.135	2.138	2.149
R(C3/P1–S1)	2.043	2.037	2.043
R(P1-O1)	1.570	1.584	1.584
R(C3/P1–S2)	2.041	2.030	2.015
R(P1-O2)	1.570	1.566	1.567
θ(S1–P1/C3–S2)	123.99	123.03	125.128

$d_o = r_o + r_{metal}$, is the theoretical value, r_o is the radius of S for the collector; r_{metal} is the atomic radius of metal (M) for sulphide.

5.2.2 Electronic shift between S atoms of thiol molecules and surface atoms of chalcopyrite, Galena and sphalerite.

High populations indicate that the bond is covalent. On the contrary, low populations suggest that the interaction between bonds is ionic. Tables 5.21, Table 5.23 and Table 2.25 summarise the Mulliken bond populations of the three sulphide minerals with DTPs collectors. The Fe–S bond on the DeDTP adsorption surface (0.55 to 0.58) was greater than that on the both DispDTP and DbDTP showing a covalence effect, while the similar trends were observed between S atom of DTPs and Pb of PbS and Zn of ZnS, the bonding between DTPs and Pb were less covalent compare to both Fe-S and Zn-S bonding. The population values of bonds for $CuFeS_2$ Fe, including (DeDTC,nbDTC and DbDTC) Fe1-S1: Fe2-S2 are (0.60:0.58, 0.58: 0.57, 0.60: 0.58), Pb1-S1: Pb2-S2 (0.15:0.15, 0.15: 0.15, and 0.14: 0.14) and Zn1-S1: Zn2-S2 0.46: 0.48, 0.51: 0.51 and 0.40: 0.51) respectively.

For chalcopyrite, The Mulliken population of the Fe–S bond shown in Table 5.21 suggests that the population of Fe–S bond on the DeDTP adsorption surface (0.55 to 0.58) was greater than that on the both DispDTP and DbDTP.

Table 5.21: Mulliken bond populations of the interaction between DeDTP, DispDTP and DbDTP chalcopyrite surface.

	Adsorbate	Bond atoms	Population	Bond
$CuFeS_2$(112)	DeDTP	S1– Fe1	0.58	2.138
		S2—Fe2	0.55	2.135
	DispDTP	S1– Fe1	0.55	2.160
		S2– Fe2	0.55	2.138
	DbDTP	S1– Fe1	0.57	2.137
		S2—Fe2	0.53	2.149

For the $CuFeS_2$ surface, the distances between R(P-S) of the adsorbed DTPs molecules increases and surface S-Fe and S-Cu atoms distance become shorter after adsorption, Similar interaction was observed for DTCs and eX indicating that the interaction between thiol collectors and the Fe atom is strengthened. Comparing DTPs, DTCs and eX interaction with the surface, we found that Fe-S bonds on average

are shorter for DTCs than DTPs and eX. The bond population for DTPs R(P1-S1) and R(P1=S2) decreases as shown in Table 5.33. In addition, the surface S-Fe population decreases while S-Cu almost remain the same as shown in Table A.8 and Table 5.33 and Table 5.34. Indicating that the addition of thiol collectors to the surface molecules enhance the covalent character of the collector while diminishing the surface population. Table A.5 and Table A.13 show that there is a stronger covalent interaction between DTCs S atoms and sulphides surfaces compared to DTPs and eX.

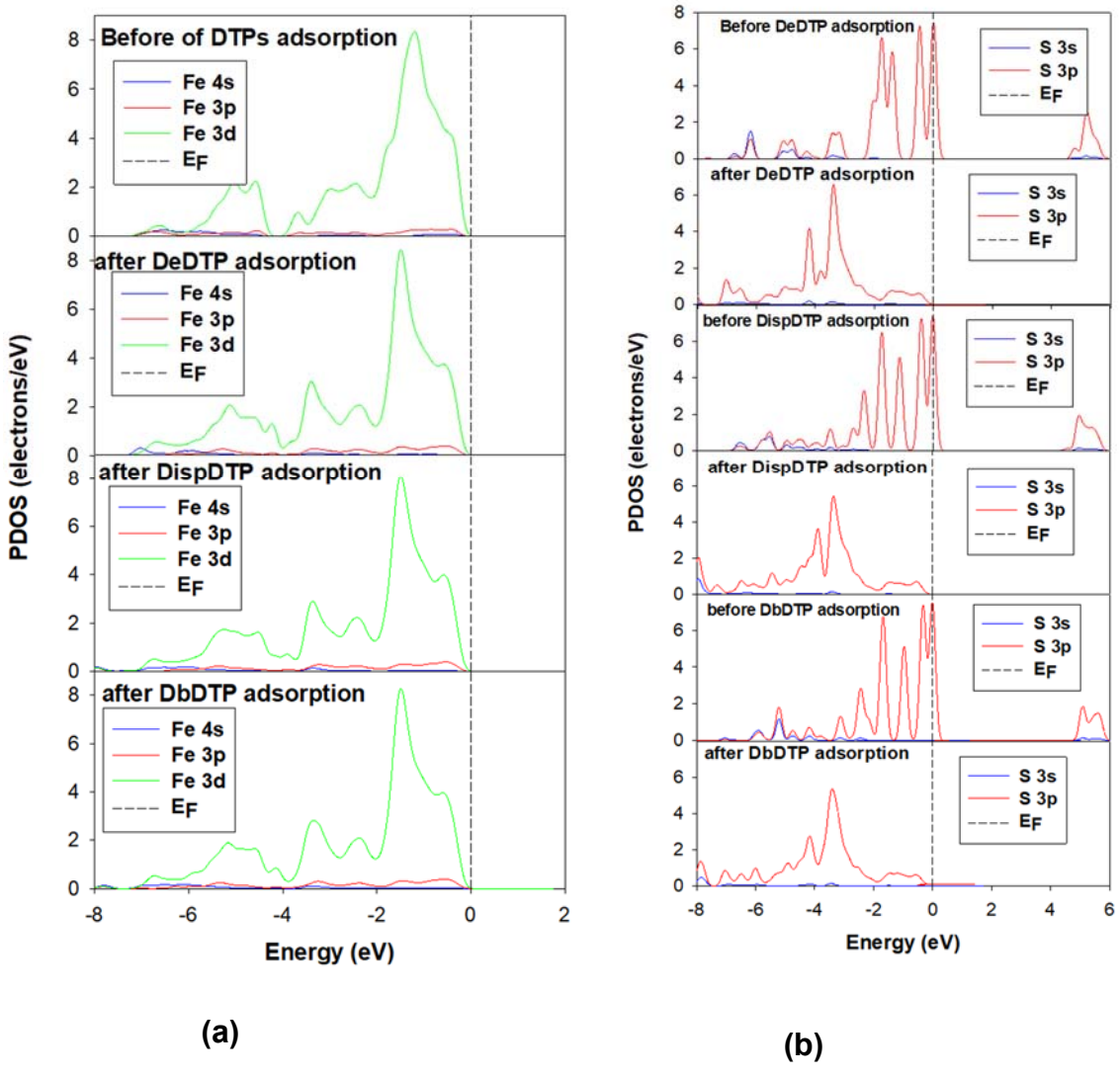

Figure 5.36: Bonding Fe–S atoms before and after DTPs adsorption on $CuFeS_2$. The zero of energy has been set at the Fermi level EF. (a) Surface Fe and (b) S of DTPs atom.

Fe 3d orbital $CuFeS_2$ surface crossed the Fermi level (as shown in the arrow in Figure 5.36) with a large bandwidth, indicating that chalcopyrite was not a conductor, which is consistent with the properties of chalcopyrite. There was little change in the

delocalization and locality of the PDOS on the chalcopyrite surface Fe after adsorption. Meanwhile, the 3d orbitals still existed in the Fe atoms on the chalcopyrite (112) surface, which indicates that the chalcopyrite (112) surface was still stable. It is clearly shown that the DOS of DTPs S atoms is changed dramatically after adsorption. Three DOS peaks of the S 3p orbital decrease greatly and shift greatly to the lower energy direction, indicating that the S 3p orbital is losing electrons. The DOS of Fe 3d near the Fermi level becomes localized. The bands from 0.0 to −7.6 eV are the bonding DOS of Fe 3d and S 3p orbitals, and hybridization DOS peaks are observed within these ranges, implying a relatively strong interaction between Fe 3d and S 3p orbitals.

Table 5.22: Mulliken charge populations of DTPs adsorption on the chalcopyrite surface (s, p and d represent s orbitals, p orbitals and d orbitals, respectively) before and after adsorption.

	Adsorbate	Adsorption status	Atom	s	p	d	total	q/e
$CuFeS_2$(112)	DeDTP	before	S1	1.9	4.48	0.00	6.38	-0.38
			S2	1.9	4.48	0.00	6.38	-0.38
		after	S1	1.86	4.46	0.00	6.32	-0.32
			S2	1.86	4.47	0.00	6.32	-0.32
		before	Fe1	0.33	0.41	6.94	7.68	0.32
			Fe2	0.33	0.41	6.94	7.69	0.31
		after	Fe1	0.33	0.53	6.96	7.81	0.19
			Fe2	0.33	0.52	6.97	7.82	0.18
	DispDTP	before	S1	1.9	4.48	0.00	6.38	-0.38
			S2	1.9	4.48	0.00	6.38	-0.38
		after	S1	1.86	4.49	0.00	6.35	-0.35
			S2	1.86	4.44	0.00	6.30	-0.30
		before	Fe1	0.33	0.41	6.94	7.68	0.32
			Fe2	0.33	0.41	6.94	7.69	0.31
		after	Fe1	0.34	0.50	6.96	7.80	0.20
			Fe2	0.33	0.53	6.97	7.82	0.18

	DbDTP	before	S1	1.85	4.18	0.00	6.03	-0.03
			S2	1.85	4.17	0.00	6.02	-0.02
		after	S1	1.85	4.49	0.00	6.34	-0.34
			S2	1.86	4.44	0.00	6.29	-0.29
		before	Fe1	0.33	0.41	6.94	7.68	0.32
			Fe2	0.33	0.41	6.94	7.69	0.31
		after	Fe1	0.32	0.51	6.96	7.8	0.20
			Fe2	0.33	0.52	6.97	7.82	0.18

According to the plot in Figure A.2, Fe 3d DOS curve of DTCs–$CuFeS_2$ is close to that of pure $CuFeS_2$ mineral near Femi level, while DTCs S 3p DOS curve of DTCs–$CuFeS_2$ shows an obvious difference compared with pure DTCs collectors. The shape of the DOS curve of S 3p changes, and peak position shifts to a lower energy level. Densitiy of state in Figure A.4 showed that Cu has little influence in the adsorption of DTCs to $CuFeS_2$.

Table 5.23: Mulliken bond populations of the interaction between DeDTP, DispDTP and DbDTP on galena surface.

	Adsorbate	**Bond atoms**	**Population**	**Bond**
PbS(100)	DeDTP	S1 – Pb1	0.14	2.936
		S2—Pb2	0.15	2.869
	DispDTP	S1—Pb1	0.15	2.910
		S2– Pb2	0.14	2.913
	DbDTP	S1—Pb1	0.13	2.873
		S2—Pb2	0.13	2.897

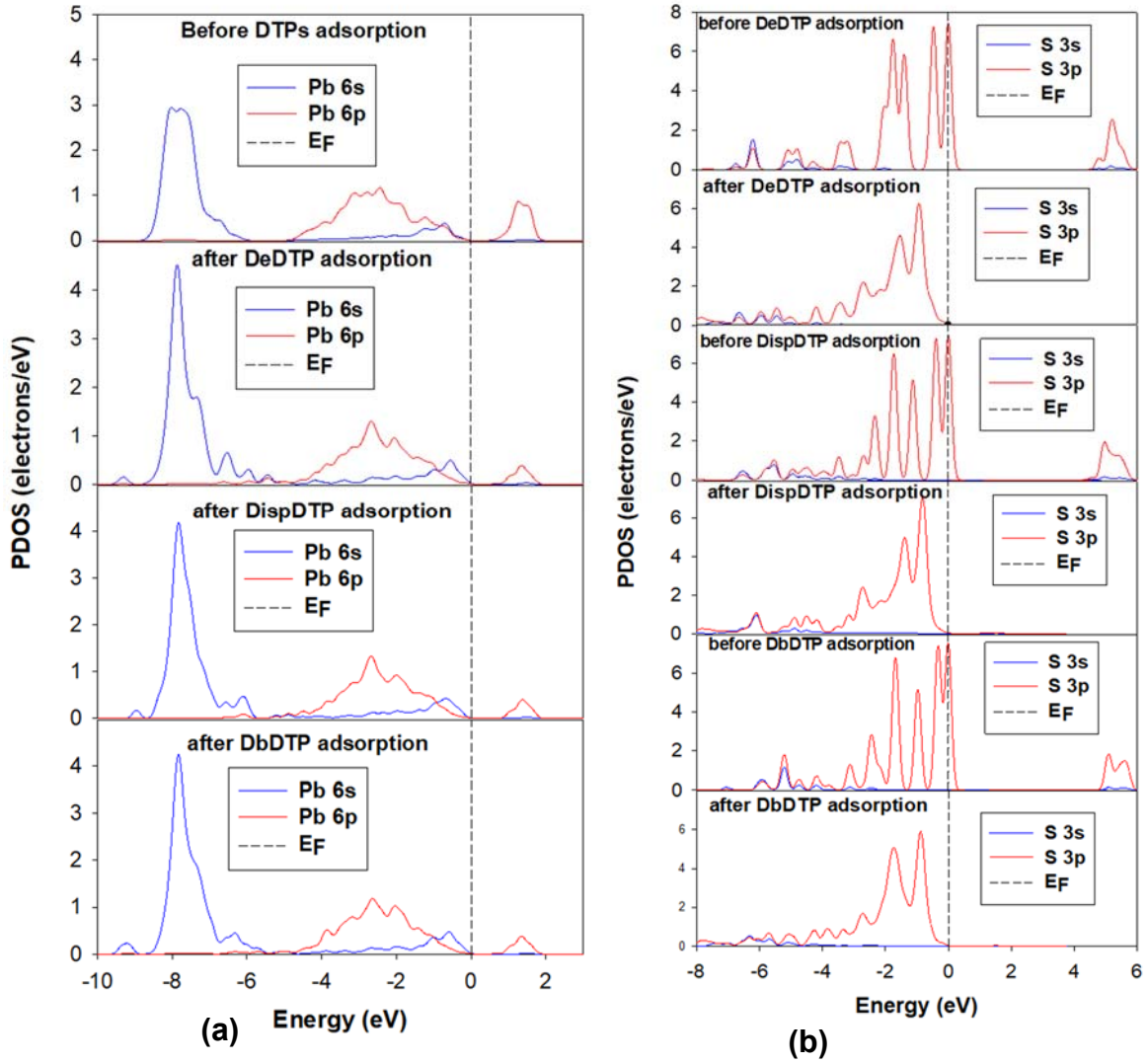

Figure 5.37: Bonding Pb–S atoms before and after DTPs adsorption on PbS. The zero of energy has been set at the Fermi level EF. (a) Surface Fe and (b) S of DTPs atom.

The partial density of states (PDOS) of Pb and S atoms with different DTPs is investigated (Figure 5.37) to give insight into the nature of the bonding mechanism. it is clearly seen that the S 3p−Pb 6s bonding DOS peak is located at −7.8 eV and -0.7 eV while the antibonding DOS peak at −5.4 eV; meanwhile, the S 3p − Pb 6p bonding DOS peak appears between −4.7 and 0 eV, and the antibonding DOS peak resonances are at 1.3−2.0 eV. Figure A.3 showed a similar effect as Figure 5.37.

Table 5.24: Mulliken charge populations of DTPs adsorption on the galena surface (s, p and d represent s orbitals, p orbitals and d orbitals, respectively) before and after adsorption.

	Adsorbate	Adsorption status	Atom	s	p	d	total	q/e
PbS(100)	DeDTP	before	S1	1.90	4.48	0.00	6.38	-0.38
			S2	1.90	4.48	0.00	6.38	-0.38
		after	S1	1.89	4.67	0.00	6.55	-0.55
			S2	1.88	4.66	0.00	6.54	-0.54
		before	Pb1	1.98	1.41	10.00	13.4	0.60
			Pb2	1.98	1.41	10.00	13.4	0.60
		after	Pb1	1.92	1.36	10.00	13.28	0.72
			Pb2	1.97	1.37	10.00	13.34	0.66
	DisDTP	before	S1	1.90	4.50	0.00	6.41	-0.41
			S2	1.90	4.49	0.00	6.39	-0.39
		after	S1	1.88	4.68	0.00	6.56	-0.56
			S2	1.89	4.64	0.00	6.53	-0.53
		before	Pb1	1.98	1.41	10.00	13.4	0.60
			Pb2	1.98	1.41	10.00	13.4	0.60
		after	Pb1	1.87	1.37	10.00	13.24	0.76
			Pb2	1.92	1.37	10.00	13.29	0.71
	DbDTP	before	S1	1.85	4.18	0.00	6.03	-0.03
			S2	1.85	4.17	0.00	6.02	-0.02
		after	S1	1.88	4.68	0.00	6.56	-0.56
			S2	1.89	4.62	0.00	6.5	-0.50
		before	Pb1	1.98	1.41	10.00	13.4	0.60
			Pb2	1.98	1.41	10.00	13.4	0.60
		after	Pb1	1.88	1.38	10.00	13.26	0.74
			Pb2	2.00	1.36	10.00	13.37	0.63

Table 5.25: Mulliken bond populations of the interaction between DeDTP, DispDTP and DbDTP and spharelite surface.

	Adsorbate	Bond atoms	Population	Bond
ZnS(110)	DeDTP	S1 – Zn1	0.45	2.520
		S2 – Zn2	0.40	2.576
	DispDTP	S1-- Zn1	0.40	2.620
		S2 – Zn2	0.37	2.664
	DbDTP	S1 – Zn1	0.39	2.597
		S2 – Zn2	0.46	2.513

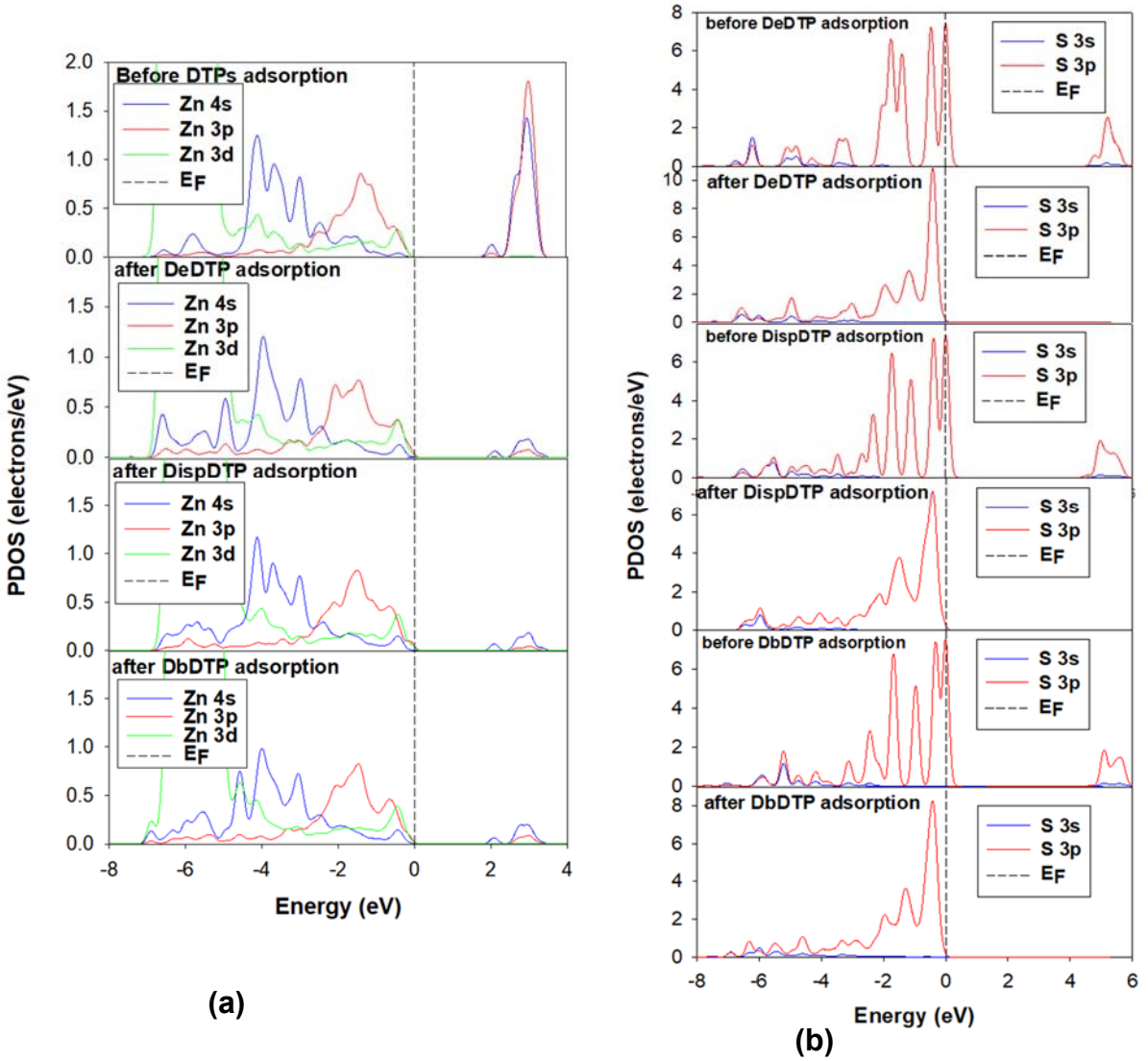

Figure 5.38: Bonding Zn–S atoms before and after DTPs adsorption on ZnS. The zero of energy has been set at the Fermi level EF. (a) Surface Fe and (b) S of DTPs atom.

Table 5.26: Mulliken charge populations of DTPs adsorption on the sphalerite surface (s, p and d represent s orbitals, p orbitals and d orbitals, respectively) before and after adsorption.

	Adsorbate	Adsorption status	Atom	s	p	d	total	q/e
ZnS(110)	DeDTP	before	S1	1.9	4.48	0.00	6.38	-0.38
			S2	1.9	4.48	0.00	6.38	-0.38
		after	S1	1.87	4.59	0.00	6.46	-0.46
			S2	1.87	4.59	0.00	6.46	-0.46
		before	Zn1	0.91	0.76	9.98	11.66	0.34
			Zn2	0.91	0.76	9.98	11.66	0.34
		after	Zn1	0.78	0.88	9.99	11.65	0.35
			Zn2	0.79	0.88	9.98	11.65	0.35
	DisDTP	before	S1	1.9	4.48	0.00	6.38	-0.38
			S2	1.9	4.48	0.00	6.38	-0.38
		after	S1	1.88	4.51	0.00	6.39	-0.39
			S2	1.88	4.54	0.00	6.42	-0.42
		before	Zn1	0.91	0.76	9.98	11.66	0.34
			Zn2	0.91	0.76	9.98	11.66	0.34
		after	Zn1	0.72	0.88	9.98	11.57	0.43
			Zn2	0.78	0.86	9.98	11.62	0.38
	DbDTP	before	S1	1.85	4.18	0.00	6.03	-0.03
			S2	1.85	4.17	0.00	6.02	-0.02
		after	S1	1.88	4.56	0.00	6.44	-0.44
			S2	1.87	4.55	0.00	6.43	-0.43
		before	Zn1	0.91	0.76	9.98	11.66	0.34
			Zn2	0.91	0.76	9.98	11.66	0.34
		after	Zn1	0.73	0.87	9.98	11.58	0.42
			Zn2	0.83	0.87	9.99	11.69	0.31

Under the same condition of parameters setting, the numerical value of Mulliken bond population can reflect the intensity information of atomic bonding. Larger numerical value means more electron clouds overlapped between two atoms and a stronger bond is formed. A negative numerical value indicates that there is no electron clouds overlap between the two atoms. Figure 5.38 shows DOS results of Zn atoms of the ZnS surface. The position of the Fermi level is 0. DOS is large at the Fermi level, which indicates that this ZnS surface is active. Hence, it is easy for the surface to react with DTPs or absorb DTPs on the surface. After DTPs absorb on the surface, the DOS curve of S shifts to a lower energy level and the electrons at Fermi level is close to zero, suggesting that S atom electronic nonlocality is enhanced and DTPs molecules become very stable. However, the shape of the DOS curve of Zn did not change much, which is in good agreement with its hydrophilicity. There is virtually no changes or small interaction for Zn 4s, 3p and 3d. Both the S 3p and Zn 4s 3p orbital peaks have partially overlapped in the energy level of −4 eV to 0 eV. Figure A.4 showed related effect.

Population values of bonds for $CuFeS_2$, including -S-S, -N-S, =O-S, and -O-S, are not present because their distances are too large to form stable bonds. The population values of Fe-S and Zn-S are much larger than those of Pb-S, indicating that the bonds of Fe-S and Zn-S tend to be more covalent than Pb-S.

Table 5.27, Table 5.29 and Table 5.31 the Mulliken population of S-Fe/Pb/Zn bond for the adsorption of eX on $CuFeS_2$ (112) surface are as high as 0.57 to 0.59, which indicated that there is a strong covalent bond between S atom Fe as compared to both or S atom Pb or Zn atoms. Such results are in good consistent with the result of other thiol collectors.

Table 5.27: Mulliken bond populations of the interaction between eX on chalcopyrite surface.

	Adsorbate	**Bond atoms**	**Population**	**Bond**
$CuFeS_2$(112)	eX	S1—Fe1	0.56	2.135
		S2 – Fe2	0.52	2.122

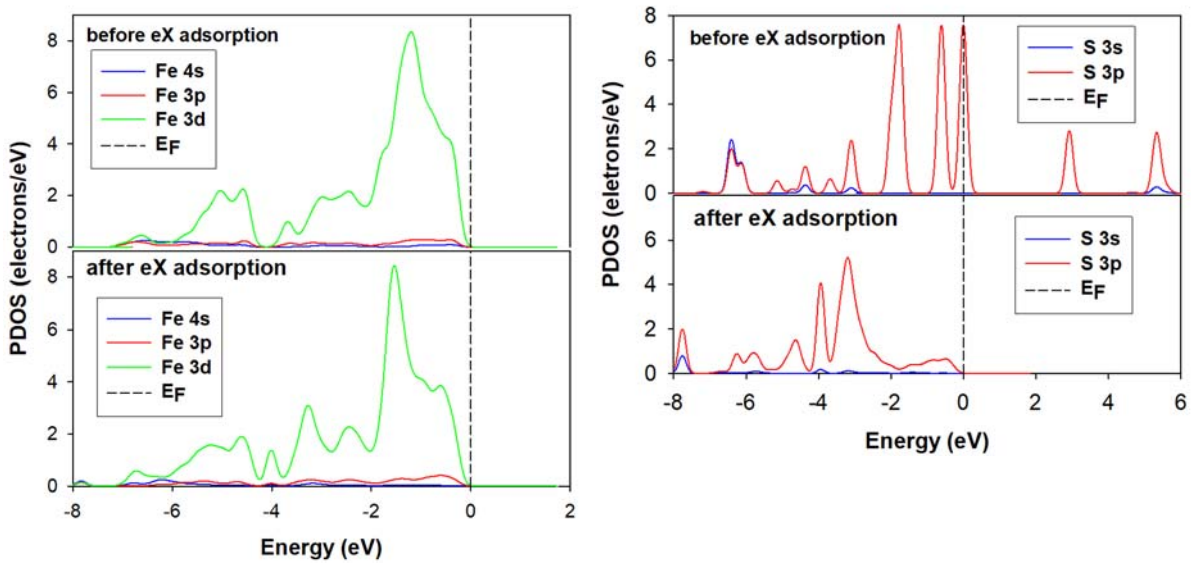

(a) **(b)**

Figure 5.39: Bonding Fe–S atoms before and after eX adsorption on $CuFeS_2$. The zero of energy has been set at the Fermi level EF. (a) Surface Fe and (b) S of eX atom.

Table 5.28: Mulliken charge populations of eX adsorption on the chalcopyrite surface (s, p and d represent s orbitals, p orbitals and d orbitals, respectively) before and after adsorption.

	Adsorbate	Adsorption status	Atom	s	p	D	total	q/e
$CuFeS_2$(112)	eX	before	S1	1,84	4,08	0.00	5,92	0,08
			S2	1,85	4,13	0.00	5,98	0,02
		after	S1	1.82	4.10	0.00	5.92	0.08
			S2	1.80	4.15	0.00	5.95	0.05
		before	Fe1	0,33	0,41	6.94	7,68	0,32
			Fe2	0,33	0,41	6.94	7,69	0,31
		after	Fe1	0.34	0.49	6.97	7.80	0.20
			Fe2	0.32	0.52	6.98	7.82	0.18

Table 5.29: Mulliken bond populations of the interaction between eX on galena surface.

	Adsorbate	Bond atoms	Population	Bond
PbS(100)	eX	S1 – Pb1	0.16	2.867
		S2 – Pb2	0.13	2.876

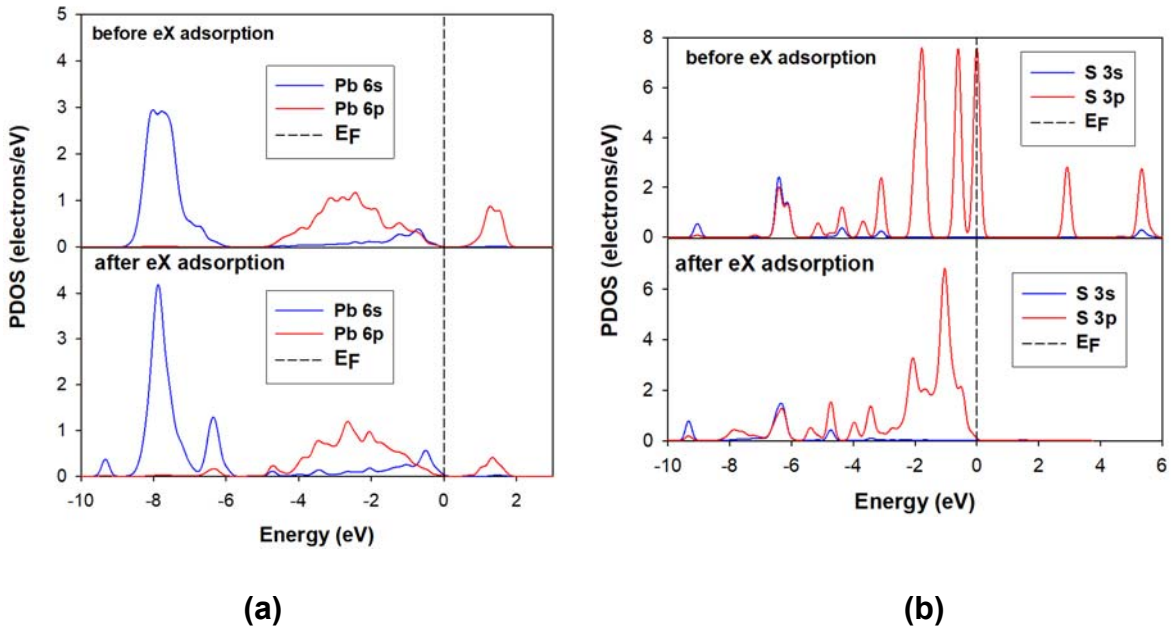

(a) **(b)**

Figure 5.40: Bonding Pb–S atoms before and after eX adsorption on PbS. The zero of energy has been set at the Fermi level EF. (a) Surface Fe and (b) S of eX atom.

DOS values of surface Zn atom after adsorption on sphalerite surface were calculated, as shown in Figure 5.40. For the convenience of comparison, DOS of Zn atom for pure ZnS mineral surface is also shown in Figure 5.40 Plots in this figure show that Zn 3d DOS of eX−ZnS surface approximates to the pure ZnS surface, while S atom DOS peaks are shifts to a lower energy level. Tables 5.28, 5.30 and 5.32 show the Mulliken charge populations of eX atoms before and after adsorption on the $CuFeS_2$, PbS and ZnS surfaces. The calculated data indicate that S atom of eX gain electrons from PbS Pb and ZnS ZnS Zn Surface, while eX S lose electrons to $CuFeS_2$ Fe.

Table 5.30: Mulliken charge populations of eX adsorption on the galena surface (s, p and d represent s orbitals, p orbitals and d orbitals, respectively) before and after adsorption.

	Adsorbate	Adsorption status	Atom	s	p	d	total	q/e
PbS(100)	eX	before	S1	1.84	4.08	0.00	5.92	0.08
			S2	1.85	4.13	0.00	5.98	0.02
		after	S1	1.83	4.3	0.00	6.13	-0.13
			S2	1.82	4.34	0.00	6.17	-0.17
		before	Pb1	1.98	1.41	10.00	13.4	0.60
			Pb2	1.98	1.41	10.00	13.4	0.60
		after	Pb1	2	1.39	10.00	13.39	0.61
			Pb2	1.9	1.39	10.00	13.29	0.71

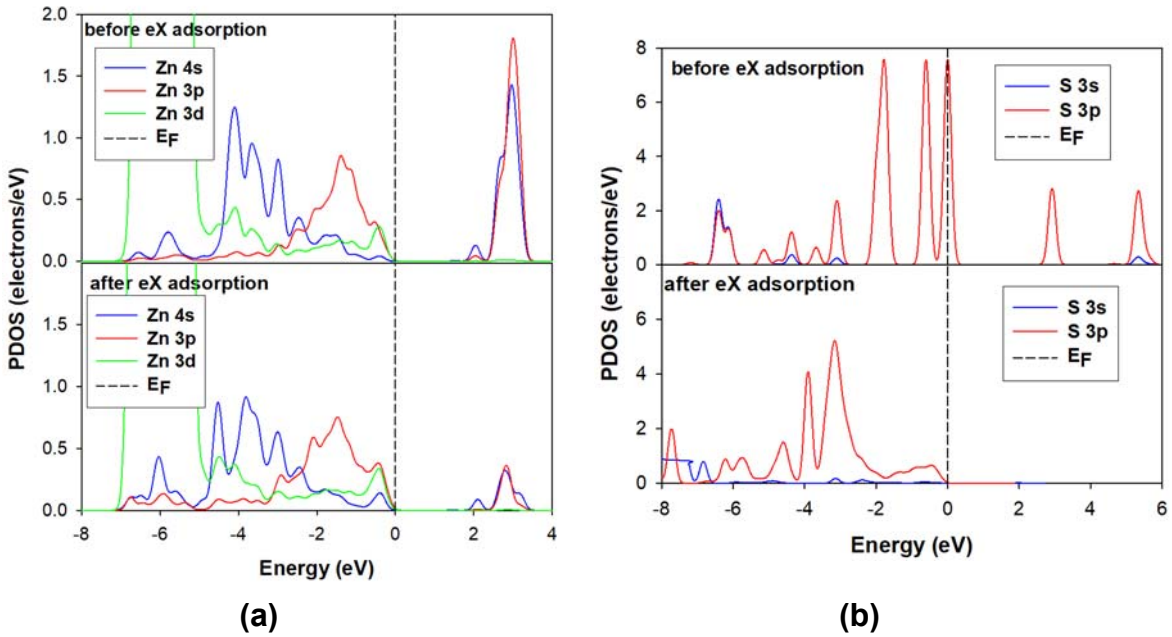

Figure 5.41: Bonding Zn–S atoms before and after eX adsorption on ZnS. The zero of energy has been set at the Fermi level EF. (a) Surface Zn and (b) S of eX atom.

Compared with the bare surfaces, the adsorptions of thiol molecules have an apparent effect on the surface structure of FeS_2 (subsection 5.1.3), $CuFeS_2$, PbS and surfaces and ZnS. it is found that on the galena surface the average value of the Pb−S bond length increases from 2.813 to 2.864 Å (see Table 1). In addition, the formation of H

bonds between surface S and H atoms results in the axial S1−Pb, S3−Pb, and S4−Pb bonds become longer (from 2.835 to 2.975, 2.879, and 2.994 Å).

Table 5.31: Mulliken bond populations of the interaction between eX on sphalerite surface

	Adsorbate	Bond atoms	Population	Bond
ZnS(110)	eX	S1 – Zn1	0.38	2.575
		S2 – Zn2	0.44	2.608

Compared with the monolayer water adsorption, it is interesting to notice that Pb−S bond length decreases from 2.864 to 2.836 Å (see Table 1). As we discussed before, the hydrogen bonding at the z direction is stronger than S−H bonding and weakens the interaction of water and the surface, which results in the smaller relaxation of the galena surface covered by multilayer water.

In the case of the FeS_2 surface, the adsorption of monolayer water causes the surface axial Fe−S bond to lengthen greatly; especially the Fe1, Fe2, and Fe3 atoms interacting with O atoms are significantly moved upward, and the average value of these Fe−S bond lengths increases from 2.120 to 2.188 Å.

Table 5.32: Mulliken charge populations of eX adsorption on the sphalerite surface (s, p and d represent s orbitals, p orbitals and d orbitals, respectively) before and after adsorption.

	Adsorbate	Adsorption status	Atom	s	p	d	total	q/e
ZnS(110)	eX	before	S1	1.84	4.08	0.00	5.92	0.08
			S2	1.85	4.13	0.00	5.98	0.02
		after	S1	1.83	4.20	0.00	6.02	-0.02
			S2	1.83	4.20	0.00	6.03	-0.03
		before	Zn1	0.91	0.76	9.98	11.66	0.34
			Zn2	0.91	0.76	9.98	11.66	0.34
		after	Zn1	0.76	0.88	9.98	11.62	0.38
			Zn2	0.88	0.86	9.98	11.72	0.28

Table 5.33: DeDTP, DispDTP and DbDTP Mulliken bonding population of atoms before and after adsorption to the Chalcopyrite surface.

	Adsorbate	Adsorption status	Bond	Population	length
$CuFeS_2$(112)	DeDTP	Before	R(P1-S1)	0.72	1.974
			R(P1=S2)	0.72	1.972
		after	R(P1-S1)	0.65	2.043
			R(P1=S2)	0.65	2.041
	DispDTP	Before	R(P1-S1)	0.74	1.969
			R(P1=S2)	0.72	1.966
		after	R(P1-S1)	0.68	2.037
			R(P1=S2)	0.68	2.030
	DbDTP	Before	R(P1-S1)	0.73	1.966
			R(P1=S2)	0.73	1.965
		after	R(P1-S1)	0.67	2.043
			R(P1=S2)	0.70	2.015

Table 5.34: chalcopyrite Mulliken bonding population of atoms before and after thiol collector adsorption to the surface DeDTP, DispDTP and DbDTP.

		Bond	Population	length
$CuFeS_2$(112)	In the absence of thiol collector	S3–Fe1	0.56	2.127
		S4–Fe2	0.56	2.127
		S3 –Cu1	0.45	2.273
		S4 –Cu2	0.45	2.272
	DeDTP	S3–Fe1	0.56	2.097
		S4–Fe2	0.58	2.102
		S3 –Cu1	0.41	2.263
		S4 –Cu2	0.42	2.264
	DispDTP	S3–Fe1	0.55	2.092

		S4–Fe2	0.57	2.104
		S3 –Cu1	0.41	2.273
		S4 –Cu2	0.41	2.254
	DbDTP	S3–Fe1	0.55	2.098
		S4–Fe2	0.57	2.101
		S3 –Cu1	0.42	2.262
		S4 –Cu2	0.41	2.263

Table 5.35: DeDTP, DispDTP and DbDTP Mulliken bonding population of atoms before and after adsorption to the galena surface.

	Adsorbate	Adsorption status	Bond	Population	length
PbS(100)	DeDTP	Before	R(P1-S1)	0.72	1.974
			R(P1=S2)	0.72	1.972
		after	R(P1-S1)	0.77	1.998
			R(P1=S2)	0.77	2.000
	DispDTP	Before	R(P1-S1)	0.74	1.969
			R(P1=S2)	0.72	1.966
		after	R(P1-S1)	0.76	2.011
			R(P1=S2)	0.77	2.001
	DbDTP	Before	R(P1-S1)	0.73	1.966
			R(P1=S2)	0.73	1.965
		after	R(P1-S1)	0.77	2.002
			R(P1=S2)	0.80	1.984

The Mulliken atomic charges and bonds populations of mineral surface layers are listed in Tables 5.22, Table 5.24 and Table 5.26, respectively. It is seen that the Mulliken atomic charges populations of $CuFeS_2$, PbS and ZnS surfaces layers are different before and after DTPs adsorption, i.e., the charges of Fe1 and Fe2, Pb1 and Pb2, and Zn1 and Zn2; S1 and S2 for DeDTP from +0.32 and +0.31 to +0.19 and 0.18e; -0.38 and -0.38 to -0.32 and -0.32, 0.60e and 0.60e to 0.72e and 0.66e;-0.38

and -0.38 to -0.55 and -0.54 and +0.34 and +0.34 to +0.35 and +0.35; -0.38 and -0.38 to -0.46 and -0.46 respectively, for from (DispDTP) from +0.32e and +0.31e to +0.20e to +0.18e; -0.38 and -0.38 to -0.35 and -0.30, +0.60 and +0.60 to +0.76 and +0.71; -0.41 and -0.39 to -0.56 and-0.53 and +0.34 and +0.34 to +0.43 and +0.38; -0.38 and -0.38 to -0.39 and-0.42 and (DbDTP) +0.32 and +0.31 to +0.20 and +0.18; -0.03 and -0.02 to -0.34 and -0.29, +0.60 and +0.60 To +0.74 and +0.63; -0.03 and -0.02 to -0.56 and -0.50, and from +0.34 and +0.34 to +0.42 and +0.31; -0.03 and -0.02 to -0.44 and -0.43 respectively. The charges of surface Fe atom reduce, the Fe atom becomes more negative and Zn and Pb became more, which indicates that the Zn and Pb atoms lost electrons to the collector while Fe gain electrons from the collector

Table 5.36: galena Mulliken bonding population of atoms before and after thiol collector adsorption to the surface DeDTP, DispDTP and DbDTP.

		Bond	**Population**	**length**
PbS(100)	In the absence of thiol collector	S3 – Pb1	0.06	2.994
		S4—Pb2	0.06	2.995
		S3—Pb2	0.06	2.995
	DeDTP	S3 – Pb1	0.11	2.885
		S4 – Pb2	0.10	2.936
		S3 – Pb2	0.11	2.898
	DispDTP	S3 – Pb1	0.14	2.847
		S4– Pb2	0.10	2.998
		S3 – Pb2	0.13	2.836
	DbDTP	S3 – Pb1	0.12	2.872
		S4 – Pb2	0.07	2.988
		S3 – Pb2	0.10	2.911

In addition, there are changes in the charges of Fe/Pb/Zn atoms on $CuFeS_2$, ZnS and PbS surface layers before and after DTCs and eX absorption, that is, the charge of Fe/Pb/Zn atom on the surface layers of $CuFeS_2$, ZnS and PbS showed the similar as DTPs.

Table 5.37: DeDTP, DispDTP and DbDTP Mulliken bonding population of atoms before and after adsorption to the sphalerite surface.

	Adsorbate	Adsorption status	Bond	Population	length
ZnS(100)	DeDTP	Before	R(P1-S1)	0.72	1.974
			R(P1=S2)	0.72	1.972
		after	R(P1-S1)	0.75	2.013
			R(P1=S2)	0.75	2.009
	DispDTP	Before	R(P1-S1)	0.74	1.969
			R(P1=S2)	0.72	1.966
		after	R(P1-S1)	0.73	2.025
			R(P1=S2)	0.81	1.996
	DbDTP	Before	R(P1-S1)	0.73	1.966
			R(P1=S2)	0.73	1.965
		after	R(P1-S1)	0.75	2.019
			R(P1=S2)	0.79	2.005

Table 5.38: sphalerite Mulliken bonding population of atoms before and after thiol collector adsorption to the surface DeDTP, DispDTP and DbDTP.

		Bond	Population	length
ZnS(100)	In the absence of thiol collector	S3 – Zn1	0.70	2.282
		S4 – Zn2	0.70	2.282
		S5 – Zn1	0.48	2.405
	DeDTP	S3 – Zn1	0.61	2.324
		S4 – Zn2	0.68	2.276
		S5 – Zn1	0.47	2.419
	DispDTP	S3 – Zn1	0.66	2.291
		S4 – Zn2	0.69	2.279
		S5 – Zn1	0.45	2.475
	DbDTP	S3 – Zn1	0.66	2.280
		S4 – Zn2	0.64	2.312
		S5 – Zn1	0.43	2.498

.

Table 5.39: eX Mulliken bonding population of atoms before and after adsorption to the Chalcopyrite surface.

	Adsorbate	Adsorption status	Bond	Population	length
$CuFeS_2$(112)	eX	Before	R(C1–O1)	0.67	1.326
			R(C1-S1)	0.73	1.674
			R(C1=S2)	0.77	1.675
		after	R(C1–O1)	0.66	1.341
			R(C1-S1)	0.76	1.713
			R(C1=S2)	0.81	1.699

Table 5.40: Chalcopyrite Mulliken bonding population of atoms before and after thiol collector adsorption to the surface eX.

	Adsorbate	Adsorption status	Bond	Population	length
$CuFeS_2$(112)	eX	Before	S3–Fe1	0.56	2.127
			S4–Fe2	0.56	2.127
			S3 –Cu1	0.45	2.273
			S4 –Cu2	0.45	2.272
		after	S3–Fe1	0.54	2.089
			S4–Fe2	0.58	2.107
			S3 –Cu1	0.41	2.247
			S4 –Cu2	0.42	2.252

Table 5.41: eX Mulliken bonding population of atoms before and after adsorption to the galena surface.

	Adsorbate	Adsorption status	Bond	Population	length
PbS(100)	eX	Before	R(C1–O1)	0.67	1.326
			R(C1-S1)	0.73	1.674
			R(C1=S2)	0.77	1.675
		after	R(C1–O1)	0.66	1.354
			R(C1-S1)	0.83	1.700
			R(C1=S2)	0.85	1.697

Table 5.42: Galena Mulliken bonding population of atoms before and after thiol collector adsorption to the surface eX.

	Adsorbate	Adsorption status	Bond	Population	length
PbS(100)	eX	Before	S3 – Pb1	0.06	2.995
			S4—Pb2	0.06	2.995
			S3—Pb2	0.06	2.995
		after	S3 – Pb1	0.10	2.912
			S4 – Pb2	0.10	2.892
			S3 – Pb2	0.10	2.892

Table 5.43: eX Mulliken bonding population of atoms before and after adsorption to the sphalerite surface.

		Adsorption status	Bond	Population	length
ZnS(100)	eX	Before	R(C1–O1)	0.67	1.326
			R(C1-S1)	0.73	1.674
			R(C1=S2)	0.77	1.675
		after	R(C1–O1)	0.68	1.356
			R(C1-S1)	0.87	1.696
			R(C1=S2)	0.85	1.701

Table 5.44: Sphalerite Mulliken bonding population of atoms before and after thiol collector adsorption to the surface eX.

		Adsorption status	Bond	Population	length
ZnS(100)	eX	Before	S3 – Zn1	0.70	2.282
			S4 – Zn2	0.70	2.282
			S5 – Zn1	0.48	2.405
		after	S3 – Zn1	0.63	2.294
			S4 – Zn2	0.66	2.294
			S5 – Zn1	0.46	2.491

5.3 Effect of ligand type on the enthalpy of adsorption

This study investigated the effect of ligand type on the performance of thiol collectors by measuring the enthalpies of adsorption on different sulphide minerals. The alkyl chain length of the collectors was fixed and only the ligand type was varied. For this purpose, the diethyldithiophosphates, ethylxanthates and diethyldithiocarbamates were used.

The effect of ligand type on the enthalpy of adsorption on the pyrite, galena, chalcopyrite and sphalerite was investigated. The enthalpies of adsorption for the interaction of DeDTP, ethyl xanthate and DeDTC with different sulphide minerals are shown in Figure 5.42.

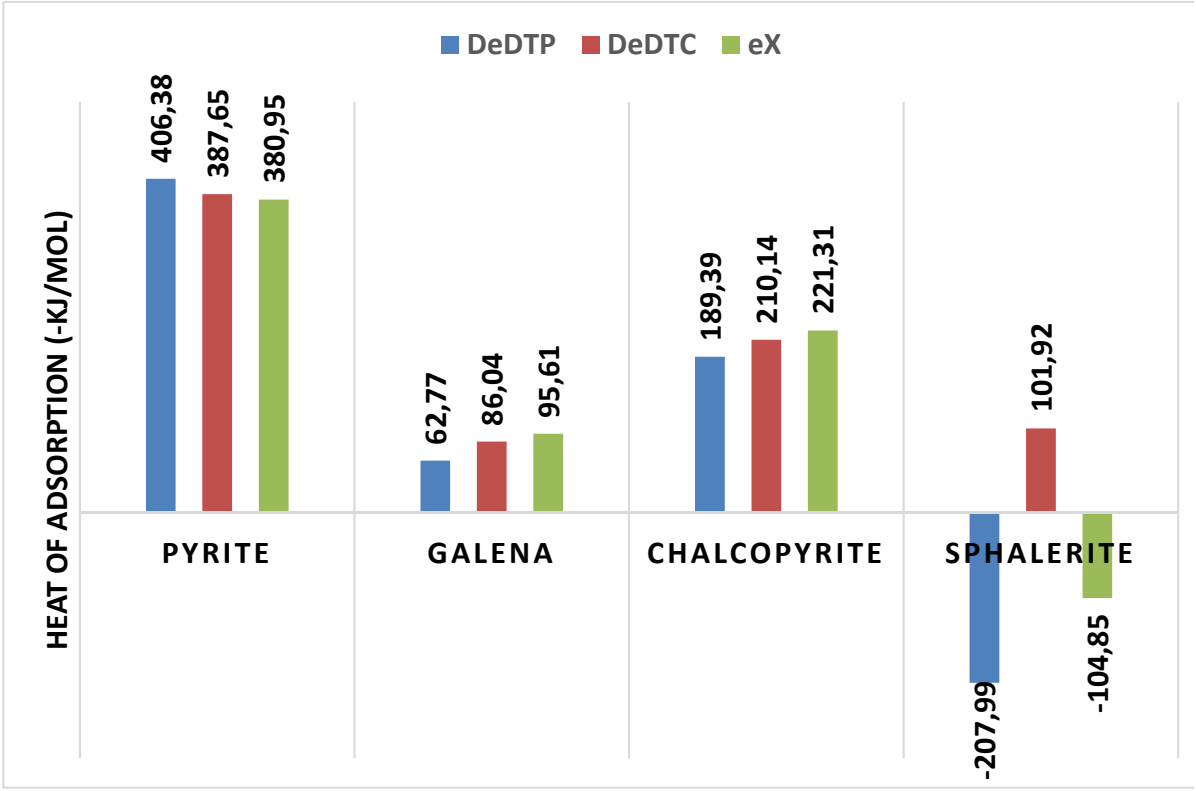

Figure 5.42: Effect of ligand type on the enthalpy of adsorption of pyrite, galena, chalcopyrite and sphalerite.

Figure 5.42 shows the variation of enthalpy of adsorption with ligand type for different sulphide minerals. The results show that there was minimal enthalpy of adsorption when DeDTP was dosed to galena, chalcopyrite and sphalerite minerals as compared to DeDTC and ethyl xanthate. On the other hand, the enthalpies of adsorption of DeDTP pyrite was very high which represented a greater exothermic reaction than for any of the DeDTC and ethyl xanthate. It should thus be noted that DeDTC and ethyl xanthate interacts more strongly with three sulphide minerals than pyrite when compared to DTP. However, in the case of sphalerite, both DeDTP and xanthates have a relatively low enthalpy of adsorption compared to the other sulphides thus indicating that this sulphide behaves quite differently to the others studied here.

The effect of the type of ligand on the enthalpy of adsorption was also investigated and results were shown in Figure 5.45. The DeDTP, DeDTC and ethyl xanthate was initially chosen for this investigation. It must be emphasised that the alkyl chain length was fixed so that only the effect of collector type could be investigated. The investigations were conducted on pyrite, galena, chalcopyrite, and sphalerite.

Our calculations showed that the ethyl xanthates produced a higher enthalpy of adsorption followed by DeDTC on galena and chalcopyrite minerals. In fact, DeDTP showed essentially less interaction with galena, chalcopyrite, and sphalerite as compared to the pyrite mineral as evidenced by the extremely low enthalpies of adsorption. It is interesting to note that the enthalpy of adsorption of the DeDTP, DeDTC and ethyl xanthate was observed on pyrite, galena and chalcopyrite, and only ethyl xanthates adsorb on the sphalerite indicating how mineral specific such interactions are.

The main difference in the enthalpy of adsorption of the collectors for a sulphide mineral is probably due to the differences in the electronegativity of the O, C, P and N atoms in the polar head group [18, 16]. The DTP is less reactive than the DeDTC because of the two RO groups which are electron-withdrawing and the more electropositive phosphorous, thus reducing electron density around the donor sulphur atoms. The electron releasing tendency of the R2N in DTC increases the electron density around the donor S atom, rendering DTC more reactive [12]. Hence, the reactivity decreases in the following order: DTC > DTP [17]. Thus, the observed trends in enthalpies of adsorption can be attributed to the differences in reactivities of DeDTC and DeDTP arising from different structure-related inductive effects.

The results agree with the fact that the pKa value of DeDTP (~0) is lower than that of DeDTC (7.5) [12]. The very low pKa value of DeDTP indicates that it is more electron-withdrawing than DeDTC, implying that DeDTP forms weaker bonds with the mineral surface.

It is reported that the reactivity decreases in the following order: DTC > X> DTP. [17] This is in keeping with the more electron-withdrawing effect of the single O atom of the xanthate compared to the electron-releasing effect of the N atom of the DTC. Thus the observed trends in enthalpies of adsorption can be attributed to the differences in reactivities of n-butyl DTC and eX arising from different structure-related inductive effects

5.4 Summary

In this section, we summarise the effect of thiol collectors' adsorption on the pyrite (100), galena (100), chalcopyrite (112) and sphalerite (110) mineral surfaces. The enthalpies of adsorption were found to increase with increasing DTPs chain on pyrite. The same observations were made for galena and sphalerite, while the chalcopyrite showed high adsorption for DpDTP collector. There is a decrease of enthalpy of adsorptions with an increase of DTCs on pyrite. observations for galena, chalcopyrite and sphalerite showed there is a decrease of adsorption energy with increasing DTCs chain. The effect of branching was mineral dependent as n-butyl DTC always produces higher energy of adsorption than DeDTP for galena, chalcopyrite and sphalerite. However, n-butyl produces lower energy for the pyrite surface. The enthalpy of adsorptions for ethyl xanthates was always greater than DeDTC and DeDTP for galena and chalcopyrite, while DeDTP was greater for pyrite and DeDTC was great for sphalerite, in fact, DeDTP and ethyl-xanthate showed no interaction with sphalerite. It is interesting to note that the adsorption energies for sphalerite showed no adsorption of eX, DbDTC and all DTPs, these imply that the was no interactions between these collectors and sphalerite, these agree well with floatation practice.

The bonding geometric behaviours of collectors were evaluated before and after geometries optimisation of the collectors on the mineral surfaces. The adsorption of collectors on the surfaces showed that the DTPs and eX favoured the formation of the conjugated π– or π*–bonding, however, this was not observed in the case of DTPs. It was also observed that the thiol collectors formed a bridge bond on all the mineral surfaces. Furthermore, the collectors preferred to bend either horizontal or at an angle on the surface, suggesting a strong interaction in bridging mode. The geometric orientation of the DTPs tends to bend towards the surface. Interestingly, we noted that the adsorption of DDTP on Fe-top site on showed collector dissociative, where the phosphorus interacted with the Fe atoms.

The is a decrease in bond length between DTPs S atoms and pyrite Fe with increasing of DTP chain length. The same observations for galena, while there is an opposite observed trend for chalcopyrite. However, the distance between DTPs S atoms with the surface atoms shows that there is a strong interaction between chalcopyrite surface with DTPs, and there is no interaction between DTPs and sphalerite as highlighted by the longest bond length between DTPs and sphalerite

surface. The DTCs showed an increase of bond length between with an increase of DTCs chain length for pyrite, which agrees well with the adsorption energies. While there is a general decrease of bond length with an increase of DTCs for galena and chalcopyrite, and for sphalerite, the values are high indicating that there is no adsorption. The shorter and longer bonds reflected strong and weak electron overlap, respectively [13].

The PDOS of DTPs, DTCs and eX functional groups were found to be similar near the E_F, which are composed of the S *3p*-orbital, indicating that the S *3p*-orbital is the centre of reactivity. In addition, there was no significant difference between the PDOS of the S atom with a single bond and that with a double bond. This may imply that the two S atoms in the thiol group have similar chemical reactivity, which may be ascribed to the conjugation effect of a pie bond.

The DOS of the thiol collectors on the surfaces showed that the S *3p*-orbitals HOMO lone-pair electrons ($2\pi_p$) hybridised with the metals *3d*-orbitals and as such reduced the states to almost zero energy. The DTPs, DTCs and eX DOS behaviour on the surface showed that the LUMO peak shifted to the VB, suggesting electron accepter from the metal surface. In order to confirm the charges transferred we analysed the Mulliken charges and populations. We found that the S atoms became less negative while the metals adopted more positive charge. This suggested that both the S atoms and the metals lose charges. It was also found that some charges resided on the internuclear region between the metals and sulphurs (M–S), in particular on the xanthate adsorption. This confirmed that the xanthates are electron donors. In contrast to xanthate, the case of DeDTP adsorption showed that the S atoms become more negative as the metals become more positive. This suggested that the S atoms gained charges as the metals lose charges and confirmed that DeDTP is an electron acceptor.

Chapter 6

Effect of water: A comparison of computational and experimental

The adsorption of the flotation reagent does not occur at the pristine mineral surface but at the water pre-adsorbed surface, therefore, the presence of water molecule would certainly affect the surface reagent adsorption. It has been reported that the adsorption of water on the sulphide mineral surface could result in the surface relaxation and the change of the density of states of the surface [92, 93]. Becker et al. [94] have observed surface proximity effects on semiconducting mineral surfaces such as galena (PbS) and pyrite (FeS_2). This showed that the chemical reaction on the surface site influences the electronic structure and reactivity of neighbouring sites on semiconducting mineral surfaces. The chemisorption or physisorption on the mineral surface will affect the electron transfer and the reactivity of nearby surface sites. Experimental validation of computational modelling can be challenging, principally due to the difficulty in relating idealised models to real-world systems. For this project, the difficulty is compounded by froth flotation process being an extremely complex, multi-component process, which no computational method could realistically model completely. Nevertheless, computational modelling can only be useful to the industry if some route exists to validate the results it obtains. For this study, two experimental techniques were chosen since they have the potential to give insight into either the fundamental binding of molecules to metal/mineral surfaces or else to relate these systems to froth flotation in a wider sense. These methods were: isothermal titration calorimetry (ITC) and The micro flotation technique.

6.1 Water and ITC-Computational adsorptions energy comparison.

In the presence of water, there is another parameter than adsorption energy such as bond length that could also represent the interaction between the single collector molecule and the mineral surface. In general, to form covalent bonding, the interacting distance of two atoms (d1) should be close to the sum of atomic radii between two atoms (d2) to cause the overlap of the electrons. Therefore, the difference between d1 and d2 (Δd) is given by $\Delta d = d1 - d2$, which represent the strength of the interaction. If the interaction distance (d1) exceeds the sum of atomic radii between the two atoms

(d2), it shows that there is poor chemical adsorption between the collector and the mineral surface and vise versa.

6.1.1 Pyrite adsorptions

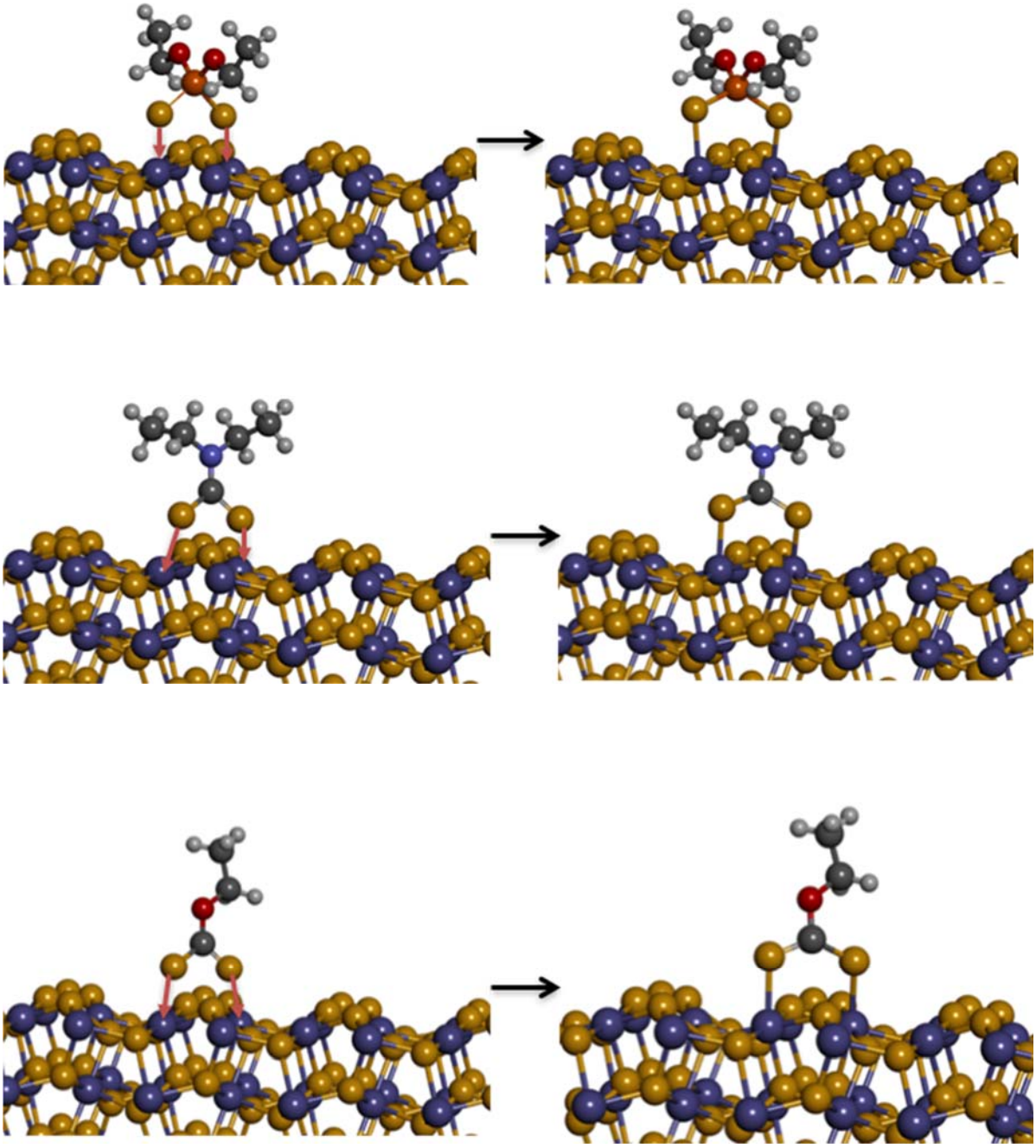

Figure 6.1: The adsorption configurations of DTP, DTC and xanthate on the pyrite (100) surfaces : (a) before and (b) after adsorption in the absence of water.

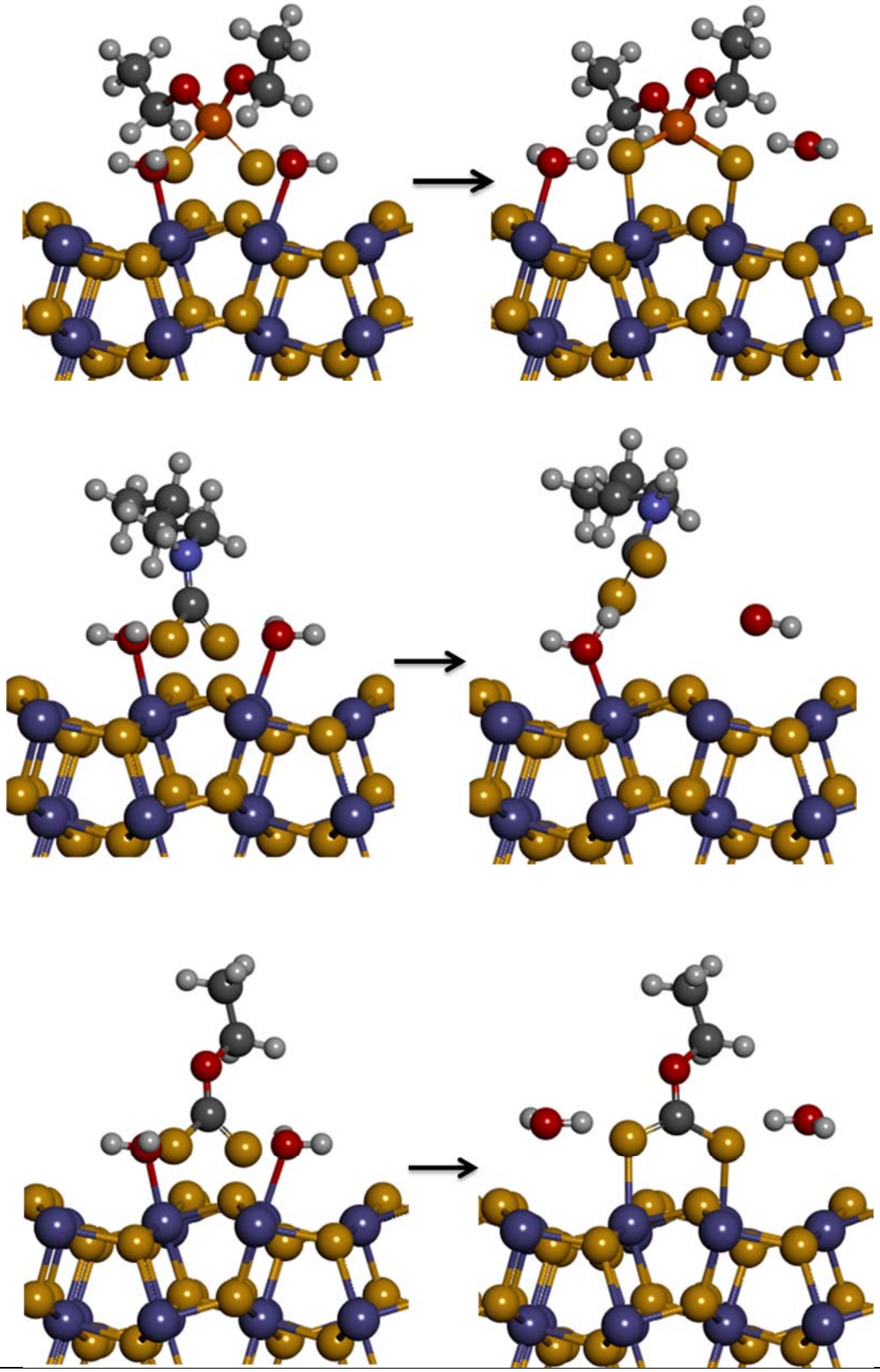

Figure 6.2: The adsorption configurations of DTP, DTC and xanthate on the pyrite (100) surfaces in the presence of water.

Since the surface free energy of FeS_2 can be expressed as a function of the Wulff-constructions facets, the obtained construction should also be related to the three-dimensional equilibrium shapes of FeS_2. The exposed surfaces are labelled accordingly. In chapter 2, Fig 3.10 the shape of the FeS_2 crystal is shown to be is a truncated octahedron, covered by the (100) and (111) surfaces. Furthermore, the (100) terminating at the apices of the octahedron has a higher surface ratio than (111) at the surface of the octahedron. There is no visible appearance of other surfaces. On this basis, the (100) and (111) terminated surface was be used as the pyrite working surface.

The adsorption configurations and energies of xanthate, DeDTP and DeDTC on the pyrite surfaces in the absence and presence of water are presented in Figure 6.1, Figure 6.2 and Table 6.1. We found that in the absence of water the distances between DTP/ DTC/ xanthate S atom and the pyrite Fe atom are in the order: DeDTP (S1−Fe1: 2.455 Å, S2−Fe2:2.411 Å) > xanthate (S1−Fe1: 2.440 Å, S2−Fe2:2.360 Å) > DeDTC (S1−Fe1: 2.349 Å, S2−Fe2:2.377 Å), which are close to the sum of atomic radius of Fe and S of 2.310 Å. This implied that there was a relatively strong interaction between these three collectors and pyrite surface. In the presence of water, it was perceived that the Δd values are much larger than the sum of the atomic radii of Fe-S (d2), which inferred that their bonds are weaker. Moreover, this indicated that the collector are able to do displace the water molecules on the surface, a required effect during flotation.

The calculated adsorption energies strength for collector adsorption on FeS_2 (100) followed the order as: DeDTP (406 kJ/mol) > eX (387.6 kJ/mol) > and DeDTC (380.9. kJ/mol), respectively (see Figure 6.3). It could be concluded from the calculated results that DeDTP, DeDTC and eX can float pyrite. We observed that the order does not follow the anticipated experimental results, after water adsorptions as shown in Figure 6.1 and 6.2, We found that the adsorption energies of DeDTP, DeDTC and eX decrease dramatically: 119.3 kJ/mol, 56.3 kJ/mol and 61.4 kJ/mol, respectively as shown in Figure 6.3. This suggested that the chemisorption occurs on the water pre-adsorbed pyrite surface and the presence of water molecule will not hinder the adsorption of the collector.

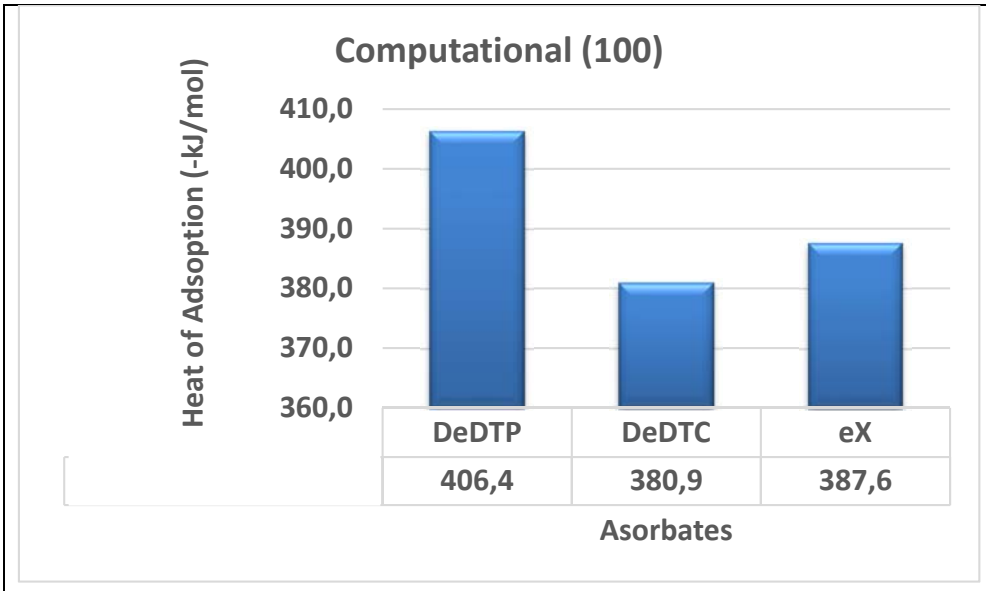

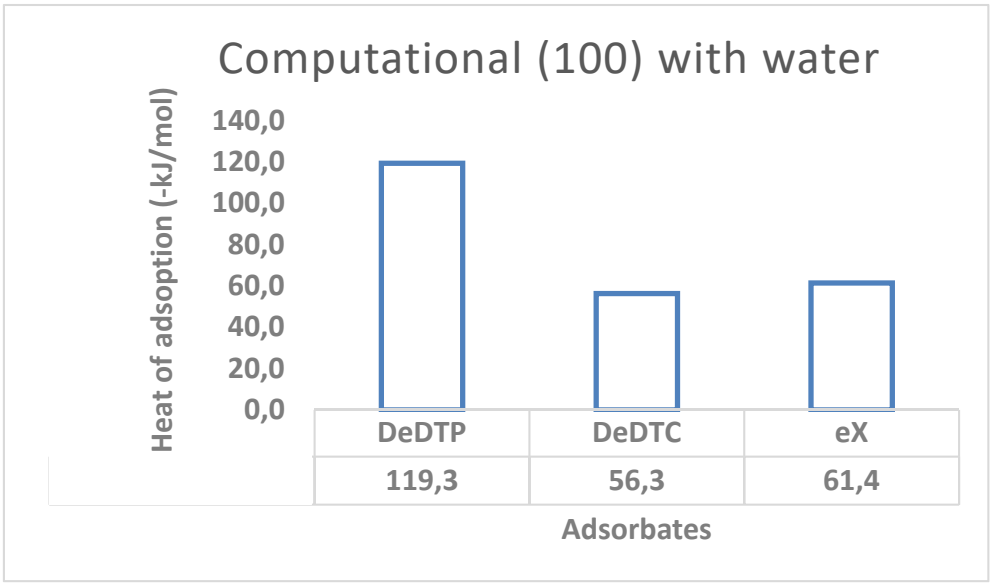

Figure 6.3:The adsorption energies of DTP, DTC and xanthate on the pyrite (100) surfaces in the absence and presence of water.

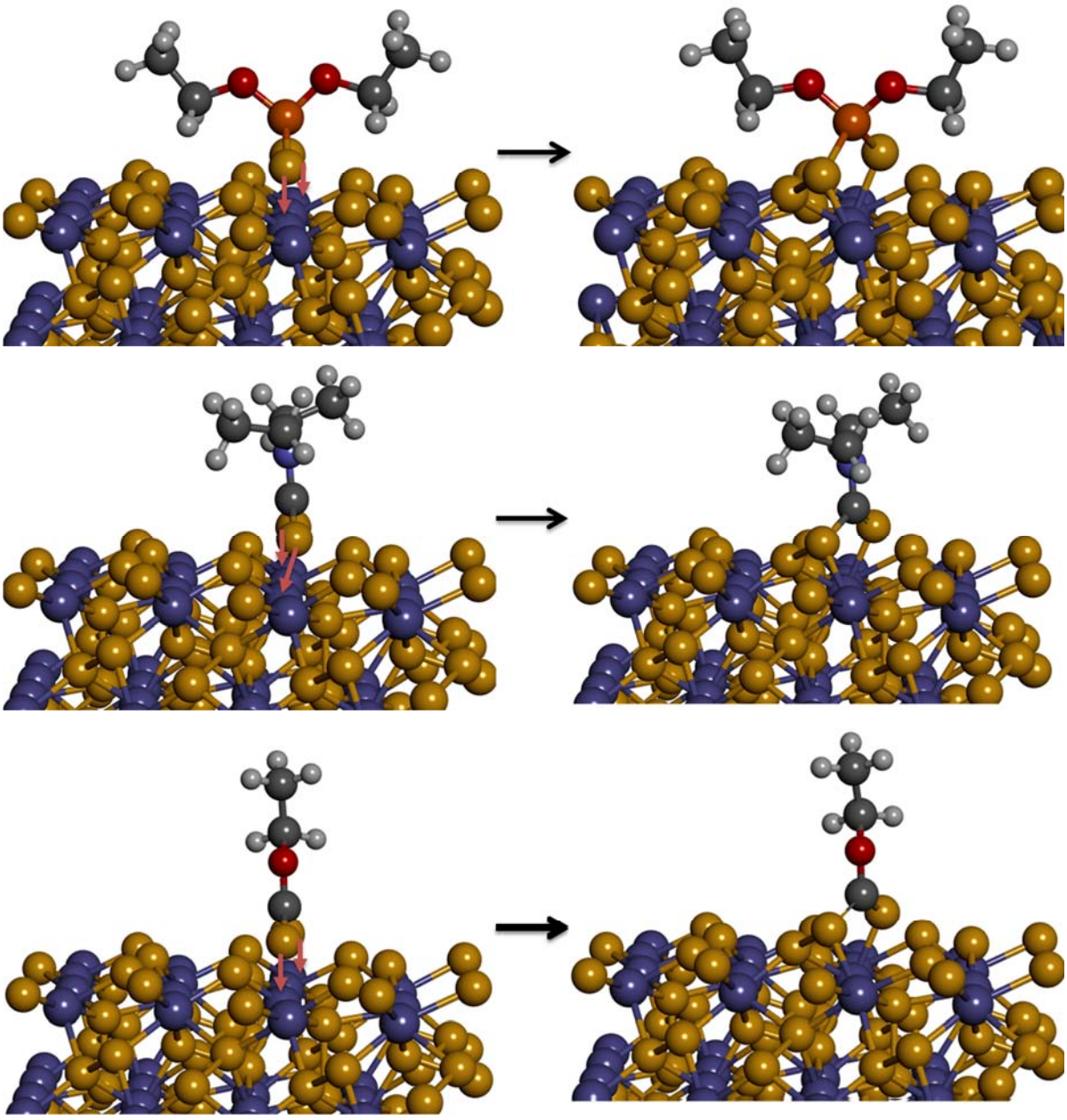

Figure 6.4: The adsorption configurations of DTP, DTC and xanthate on the pyrite (111) surfaces in the absence of water.

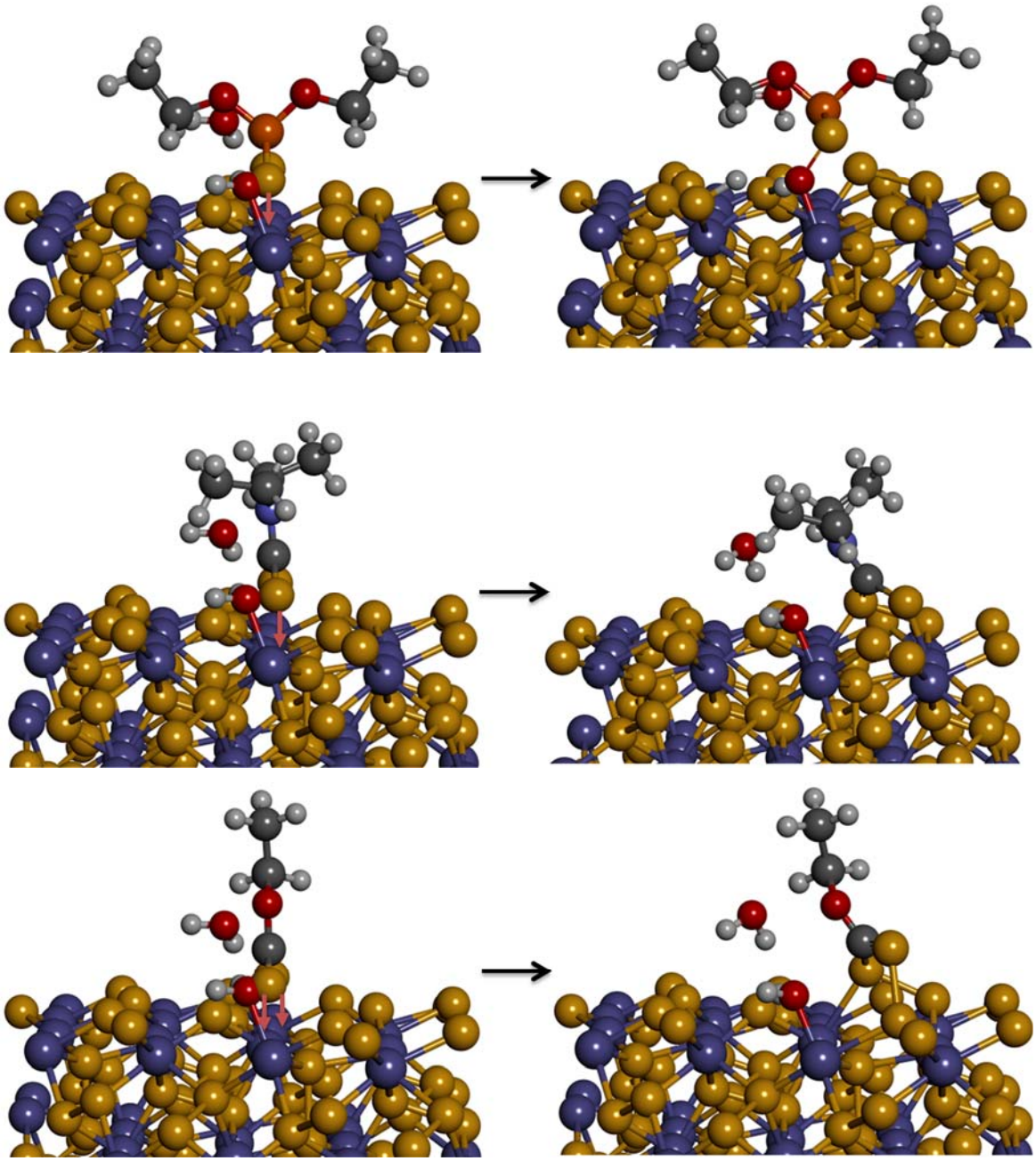

Figure 6.5: The adsorption configurations of DTP, DTC and xanthate on the pyrite (111) surfaces in the presence of water.

The FeS_2 (111) adsorptions energy strength followed the order as: DeDTC (272.6 kJ/mol) > eX (252.7 kJ/mol) > DeDTP (232.4 kJ/mol), which follows the same order of experimental heats of adsorption (DeDTC > SEX > DeDTP) as shown in Figure 6.4 and 6.5, This suggested that the FeS_2 (111) adsorption behaviour emulate those of the ITC experiments.

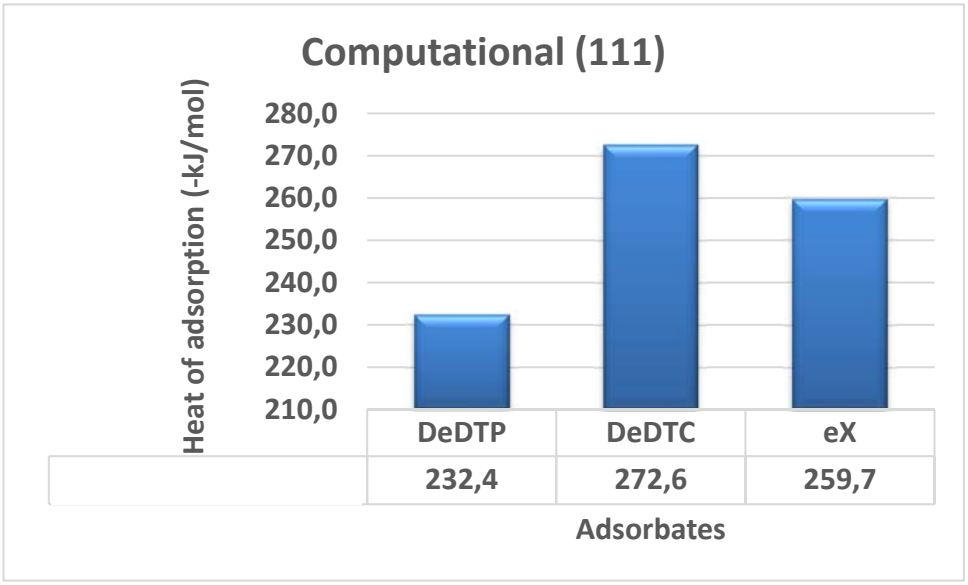

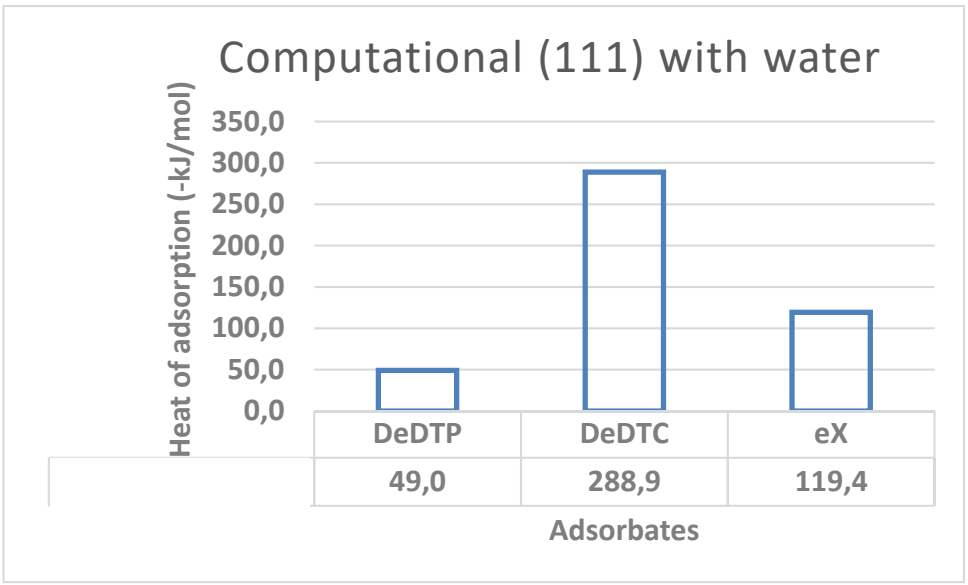

Figure 6.6: The adsorption energies of DTP, DTC and xanthate on the pyrite (111) surfaces in the absence and presence of water.

It was notable that the presence of water molecules decreased the adsorption energy for DeDTP and eX, while adsorption energy increased for DeDTC. which suggests that the water molecule could enhance the adsorption of DTC on (111) surface. suggesting that the chemisorption occurs on the water pre-adsorbed pyrite surface.

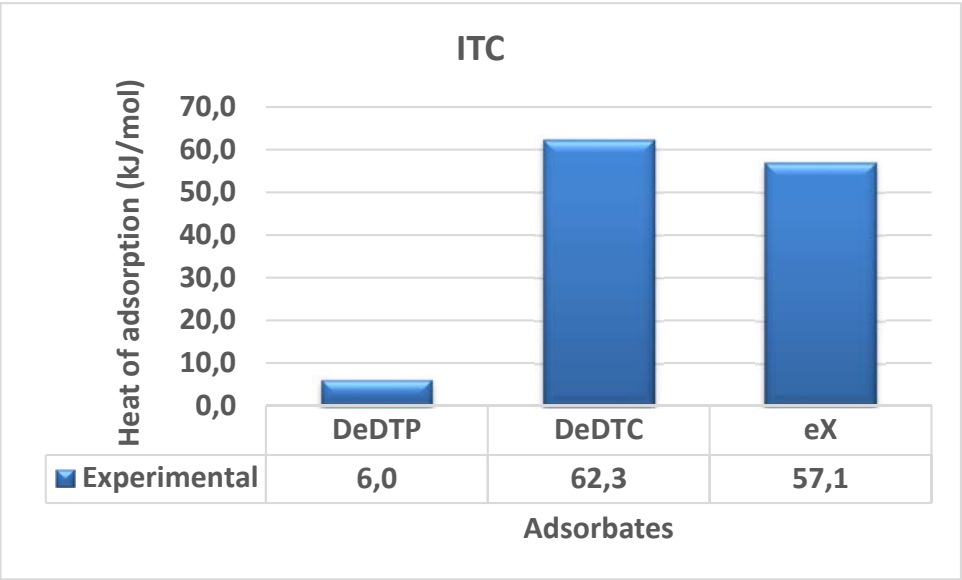

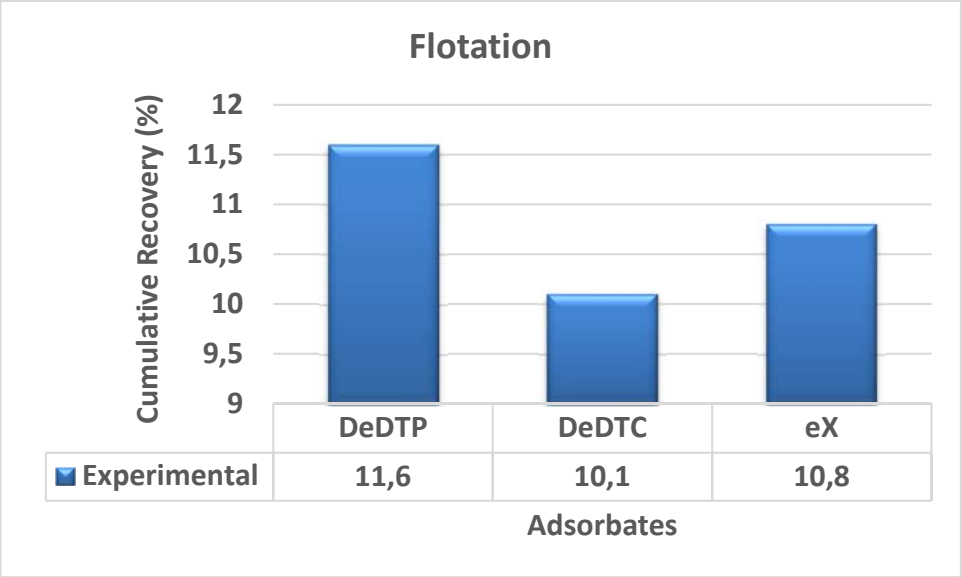

Figure 6.7: The adsorption energies of DTP, DTC and xanthate on the pyrite. Microflotation recoveries for pyrite using DeDTC, DeDTP and ethyl xanthates as collectors (pH 9.2; the relative standard error was always < ±2% hence error bars are too small to be visible on the graphs) [10].

The computational results showed that the calculated adsorption energies were more exothermic than the experimentally determined ones [10]. It must be emphasised that this study focussed more on the trends observed between the calculated and the experimental enthalpies of adsorption, and not necessarily their absolute values. The results showed that the trends in the calculated and experimental energies of

adsorption were similar only in the case of FeS_2 (111). The adsorption of water molecules was found to have little influence on the DTC adsorption on (111) surfaces.

Table 6.1: Mulliken bond populations of the interaction between DeDTP, DispDTP and DbDTP pyrite surface.

	collector	Mineral surface	Average interactive distance d_1 (Å)	Sum of the atomic radius d_2 (Å)	Strength of interaction $\Delta d = d_1 - d_2$ (Å)
In the absence of water	DTP	FeS_2 (100)	2.412	2.310	0.102
		PbS (100)	2.902	2.840	0.062
	DTC	FeS_2 (100)	2.416	2.310	0.106
		PbS (100)	2.853	2.840	0.013
	Xanthate	FeS_2 (100)	2.398	2.310	0.088
		PbS (100)	2.872	2.840	0.032
In the presence of water	DTP	FeS_2 (100)	2.429	2.310	0.119
		PbS (100)	2.955	2.840	0.115
	DTC	FeS_2 (100)	2.402	2.310	0.092
		PbS (100)	3.041	2.840	0.201
	Xanthate	FeS_2 (100)	2.393	2.310	0.083
		PbS (100)	3.069	2.840	0.229

6.1.2 Galena adsorptions

In the presence of water, the value of Δd for galena are larger than the sum of atomic radii of Pb-S (d2), indicating that these three collectors could adsorb on the galena surface in the solution, which corresponds well with the observation of flotation experiment [10]. For galena, the order of Δd was DTP < DTC < xanthate, indicating that the interaction of DTP was the strongest. The DTP is known to exhibit good selectivity when used in weak alkaline pulp, while the DTC is usually used in the high alkaline pulp.

For PbS in chapter 3, Figure 3.19 ,only (100) surface is visible. There is no visible appearance of other surfaces. On this basis, the (100) terminated surface was be used as the PbS working surface.

The adsorption energies of DTP, DTC and xanthate on the galena surfaces in the absence of water are shown in Figure 6.8. The adsorption energy strength were found to follow the order as: xanthate (95.6 kJ/mol) > DTC (86.0 kJ/mol) > DTP (62.8 kJ/mol). In the presence of water, it was observed that the adsorption energy of DeDTP was very poor as it gave a positive value as seen in Figure 6.8.

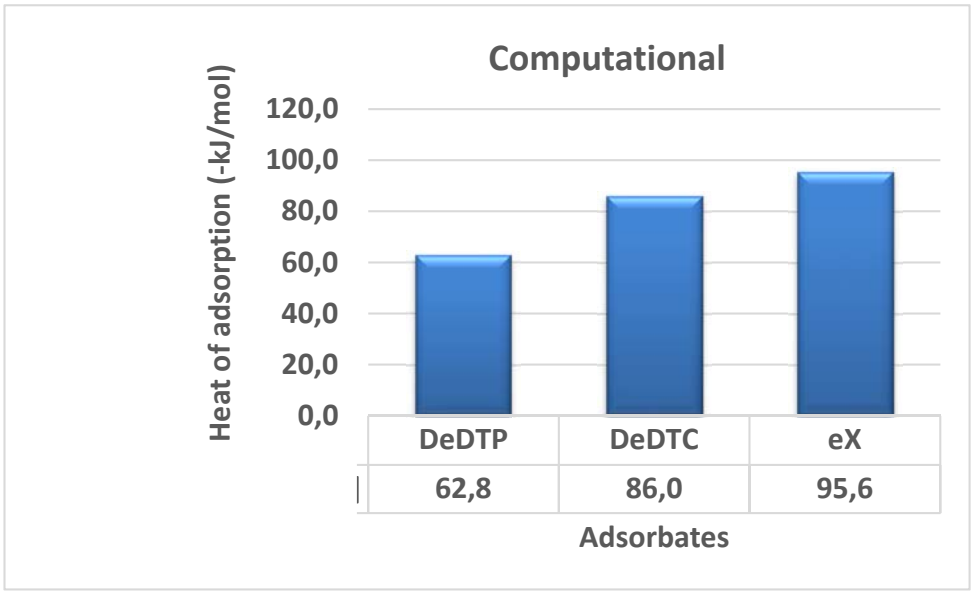

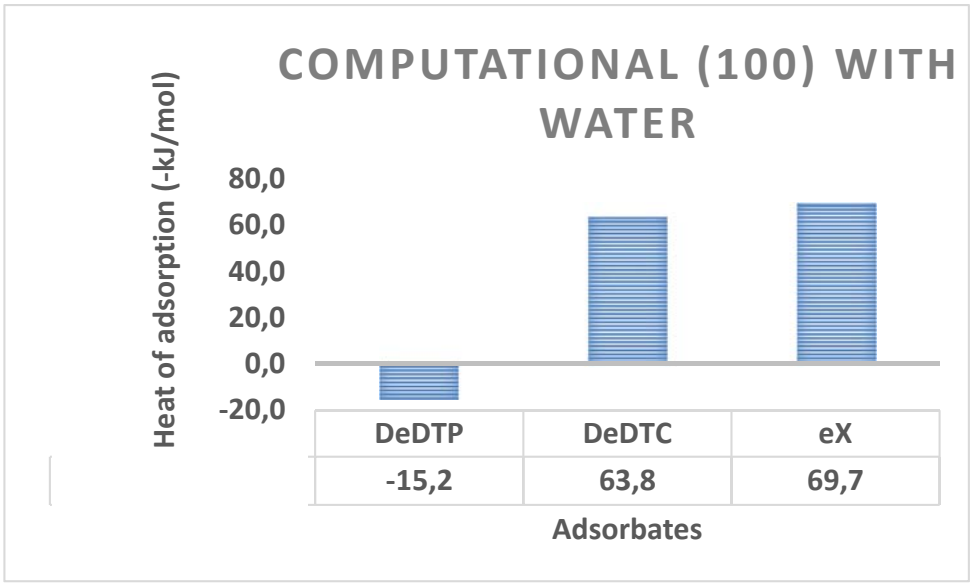

Figure 6.8: The adsorption energies of DTP, DTC and xanthate on the galena (100) surfaces in the absence and presence of water.

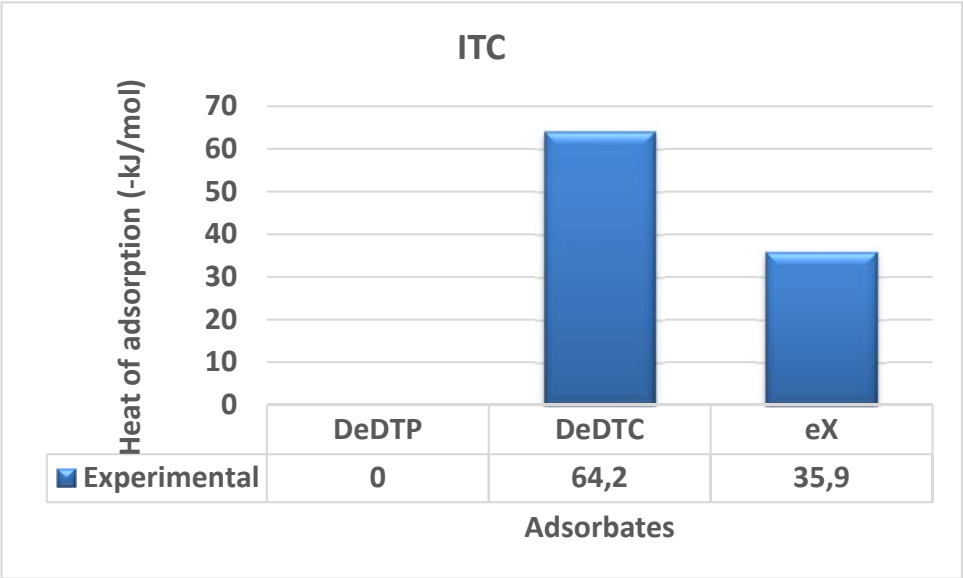

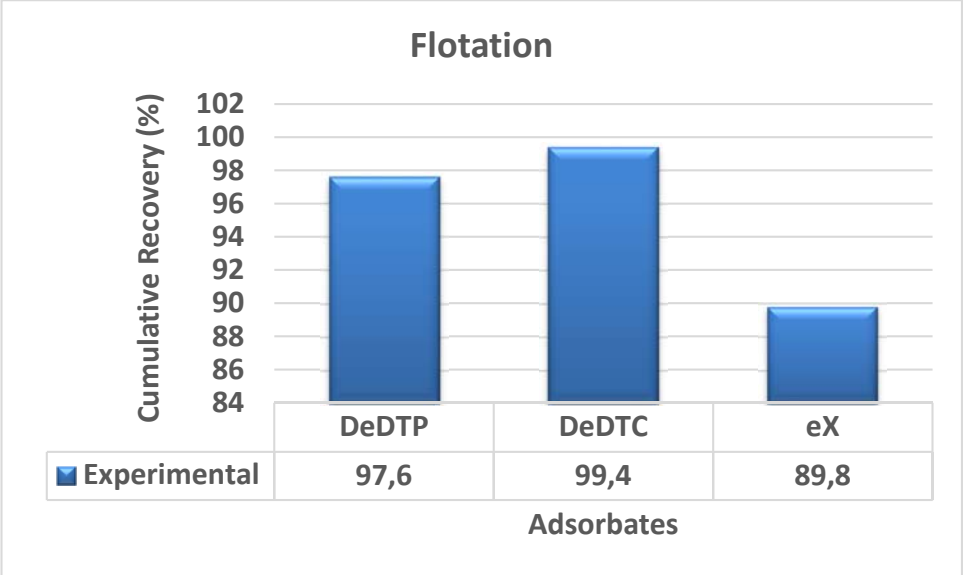

Figure 6.9: The adsorption energies of DTP, DTC and xanthate on the galena and microflotation recoveries for galena using DeDTP, DeDTC, and ethyl xanthates as collectors (pH 9.2; the relative standard error was always < ±2% hence error bars are too small to be visible on the graphs) [10].

In the case of the interacting distance between DTC and galena surface (S1−Pb1: 2.854 Å, S2−Pb2: 2.851 Å), were the shortest, while for xanthate and DTP were (2.867, 2.876) and (2.936, 2.867) respectively. This suggested that the interaction of xanthate and DTP with the galena surface was weaker compared to DTC.

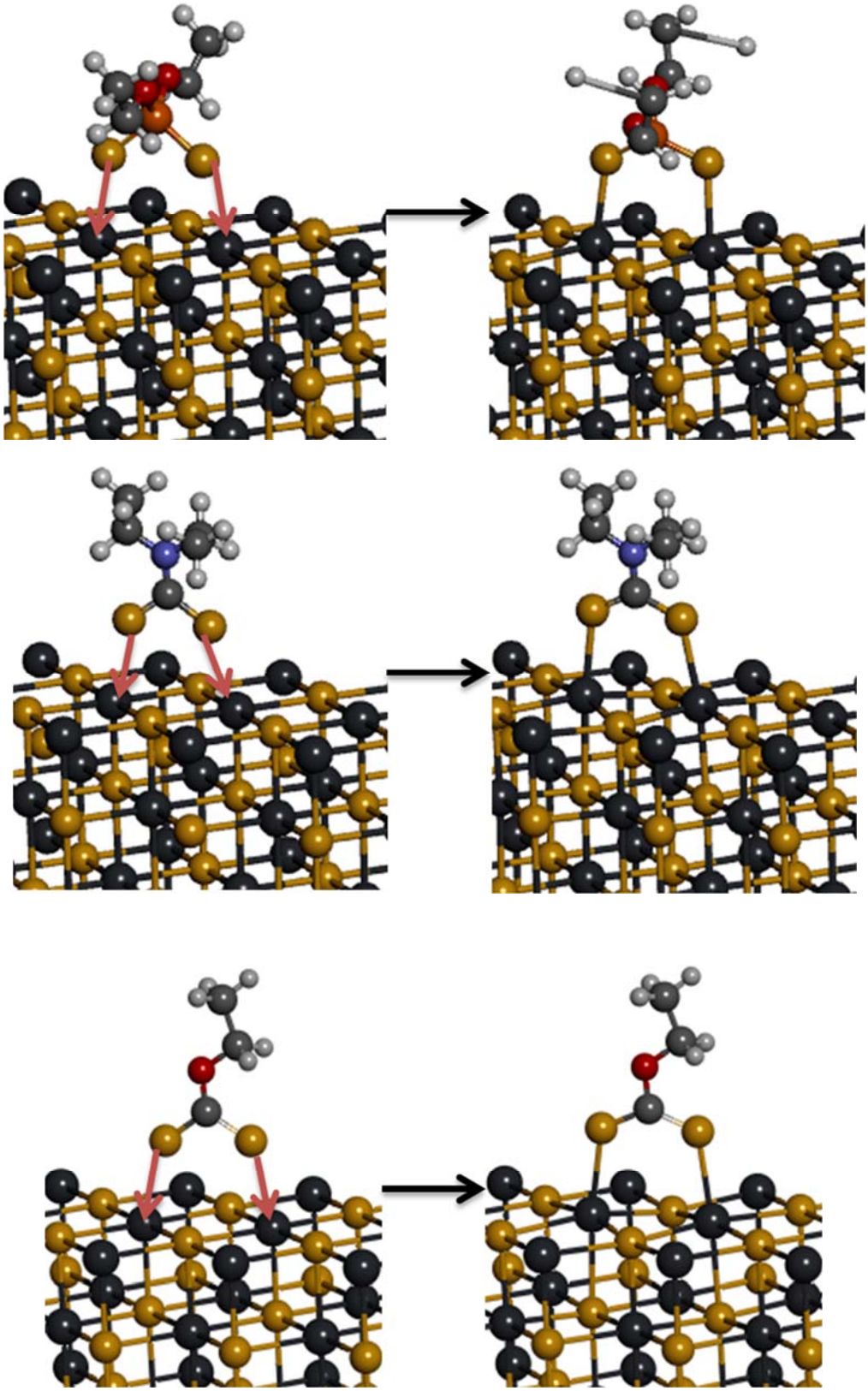

Figure 6.10: The adsorption configurations of DTP, DTC and xanthate on the galena surfaces: (a) before and (b) after adsorption in the absence of water.

The adsorption energy order for DTP, DTC and xanthate did not agree well with the interacting distance result. The reason may be ascribe to the structural distortion during the adsorption, which would consume the energy. The adsorption configurations and energies of xanthate, DTP and DTC on the galena surface in the presence of water are shown in Figure 6.11. According to the adsorption energies, the three collectors could adsorb on the water pre-adsorbed PbS (100) surface.

The adsorption of water molecules were found to weakens the interaction of DTP and had less influence on the DTC and xanthate adsorption. In comparing Figs. 7 and 8, the distance between the reagent S and surface Pb atoms become longer after water adsorption, suggesting that the presence of water will decrease the adsorption of the collectors. For the DTP, DTC and xanthate the interacting distance increased by 0.053, 0.190 and 0.97 Å, respectively. This indicated that the effect of water molecules on the xanthates adsorption was the greatest.

As defined above, the d1 is the average distance between collector S atoms and the surface Fe/Pb atoms, and d2 is the sum of atomic radii of Fe and S or Pb and S. The smaller value of Δd indicated larger electron overlap between two atoms and the stronger chemical interaction of the collector and the mineral surface. The value of d1, d2 and Δd for three collectors on the FeS_2 (100) and PbS (100) surfaces in the absence and presence of water are listed in Table 6.1. The differences in the trends observed for both the calculated and experimental enthalpies of adsorption might be attributed to flat-lying molecules on surfaces in experiments, whereas DFT calculations find the vertically adsorbed of collectors to be more stable. The introduction of water in the computational modelling framework had the effect of reducing the absolute values of the calculated adsorption energies without affecting the observed trends. The presence of water molecule had an obvious effect on the electron distribution, covalent bonding and reactivity of surface atoms and consequently influenced the interaction between the collector and mineral surface.

.

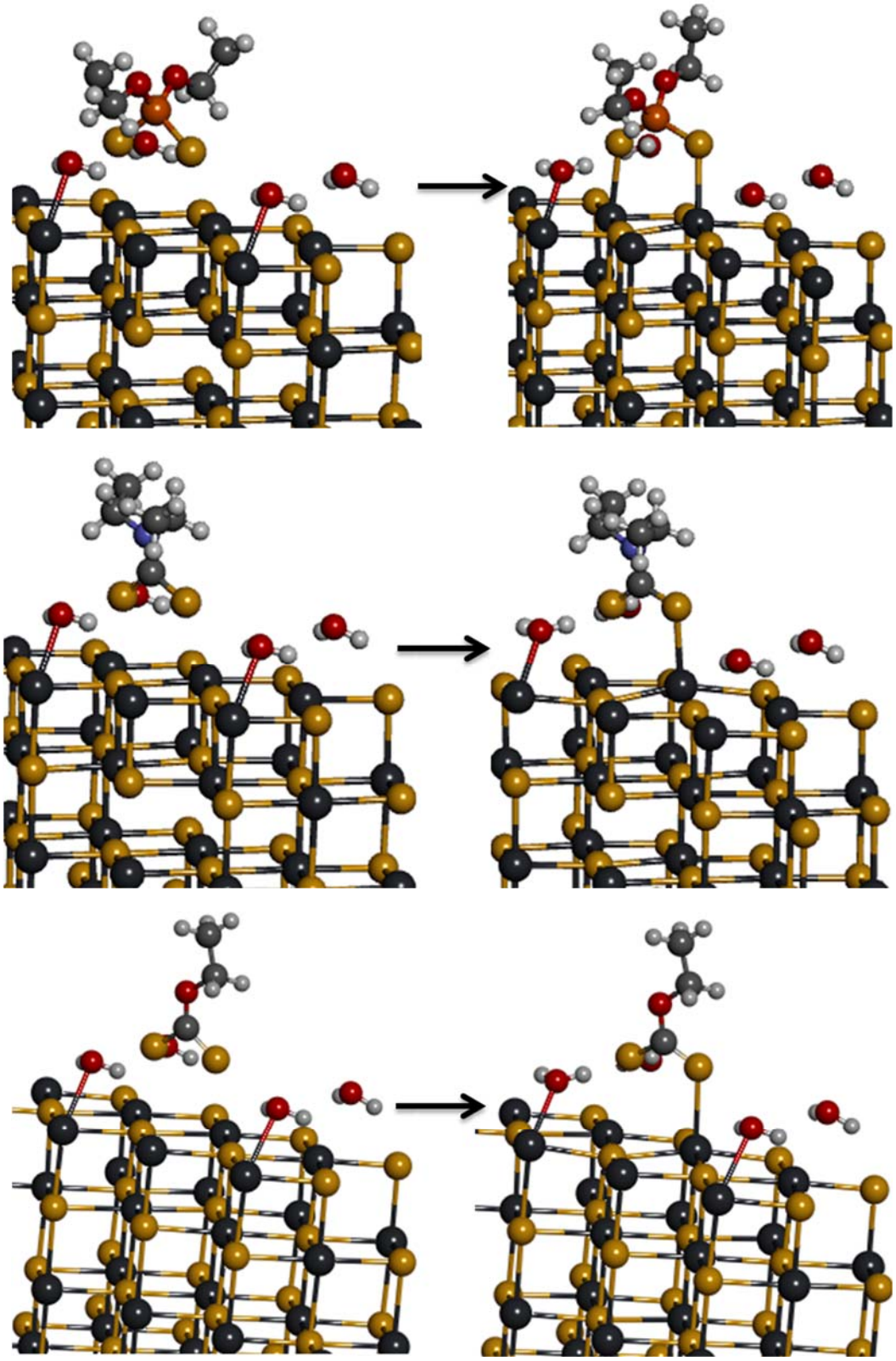

Figure 6.11: The adsorption configurations of DTP, DTC and xanthate on the galena surfaces: (a) before and (b) after adsorption in the presence of water.

6.2 Summary

Computational modelling methods isothermal titration calorimetry (ITC) comparison to investigate the interaction of pyrite and galena surface with thiol collectors was archived. Modelling work was conducted in the absence and presence of water. The microflotation technique was employed to investigate the resultant hydrophobicity of the minerals as a result of mineral-collector interactions. The ethyl xanthate (eX), diethyldithiocarbamate (DTC) and diethyl dithiophosphate (DTP) were investigated in this chapter. The calculated surface energies for FeS_2 and PbS showed that (100 and 111) and (100) were the most stable surfaces, respectively. The morphologies also indicated the appearance of the (100 and 111) only for FeS_2 and (100) surface only for PbS facets and no presence of others. When comparing different ligand types with the same alkyl chain length, the heat of adsorption of DeDTC was greater than that of ethyl xanthate and DeDTP for pyrite. The ΔH had a similar trend as the computational ΔH for (111) surface, and a different trend for (100) surfaces. Water adsorption was found to reduce the reactivity of Fe atom with respect to the interaction with thiol collectors but has little influence on FeS_2 (100) surface. In the presence of water molecule, the interaction order of three thiol collectors on PbS (100) surface and PbS (100) surface agreed well with the flotation results.

Chapter 7

Summary and conclusion

Computational modelling methods are used to search for suitable collectors in extraction of sulphides minerals. Thiol collectors continue to dominate in the base metal sulphide (BMS) and platinum group mineral (PGM) flotation industry, and those investigated in the current study are dithiophosphates of varying chain length (DeDTP, diisopropyl-DTP and Dibutyl-DTP), dithiocarbamates (DeDTC, n-butyl DTC and dibutyl-DTC) and ethyl-xanthates. The thesis gives detailed perspectives on computational modelling studies, employing density functional theory, of the thiol and xanthate collectors and their interaction with surfaces pyrite (FeS_2), galena (PbS), chalcopyrite ($CuFeS_2$) and sphalerite (ZnS), with and without water. The computational results have also been compared with experiments on interactions of some collectors and minerals, involving isothermal titration and micro calorimetry to monitor sub-monolayer reactions, and microflotation used to determine the hydrophobicity imparted onto the mineral particles due to the mineral-collector interactions. In order to study surface properties appropriately, we have determined the cut-off energies suitable to converge the total energies of the systems to be 550 eV for PbS and 450 eV for FeS_2, $CuFeS_2$ and ZnS. The k-points numbers of 7x7x7, 8x8x1, 5x5x5 and 6x6x6 for FeS_2, $CuFeS_2$, for PbS and ZnS, respectively were also found to be sufficient to converge the total energies of the bulk. Calculated lattice parameters for bulk systems are in good agreement with the experimental values and other theoretical studies.

The sulphides construction and surface structural relaxations showed that pyrite (FeS_2) possesses a cubic crystal structure and has a space group of Pa3(T). 6 h common cleavage plane is (100) face along with Fe-S bond. Each Fe atom of the surface coordinates with adjacent five S atoms, while each S atom coordinates with adjacent two Fe atoms and one S atom. Galena (PbS) also belongs to the cubic crystal structure with a space group of Fm3m. The common cleavage plane is (100) face along with Pb-S bond. Each Pb atom of the surface coordinates with adjacent five S atoms, and each S atom coordinates with five Pb atoms. Chalcopyrite crystallises in the tetragonal group (space group $I\bar{4}2d$) with four formulas ($CuFeS_2$). We focused on the (112) surface which reconstructs, to form S−S bonds. One S−S bond is formed

between sulphur atoms in the same supercell and another between sulphur atoms in different supercells. Sphalerite (ZnS) has a cubic crystal structure, whose space group is F43m with (110) surface. Each Zn atom of the surface coordinates with three S atoms, while each S atom coordinates with two Zn atoms and one S atom. The most stable surfaces were the ones with the highest surface exposure as it covered about a higher percentage of the surface area.

It was observed that the introduction of the H_2O molecule changed the structures of sulphide minerals surfaces. The surfaces of FeS_2 and ZnS relaxed significantly, while those of $CuFeS_2$ and (PbS) surfaces change slightly in the presence of H_2O molecule. Moreover, the Mulliken atomic charges and bonds populations of FeS_2, ZnS and PbS surfaces changed evidently after adsorbing H_2O, whereas those of $CuFeS_2$ surface changedssxs minimally. The adsorption of the flotation reagent at the mineral-water interface would be different from that of the mineral surface due to the changes of surface structures and electronic properties caused by H_2O molecule. Hence, the influence of the H_2O molecule on the reaction of flotation reagent with the mineral surface will attract more attention.

Our calculated results on DeDTP, DispDTP, DbDTP, eX, DeDTC, nbDTC and DbDTC classes of flotation collectors show that exploring their molecular reactivity through computational modelling methods, their interactions with sodium ion is an efficient approach to relate the molecular structure of collector reagents to their binding affinity. The trends observed in the calculated geometry correlated well with the experimental findings. This implies that reactivity and selectivity of reagents can be qualitatively extended to minerals. The calculated values of interaction energies show that all the considered collector reagents have a greater preference towards binding with Na. Reactivity of sulfhydryl collectors is mainly determined by the electron flow around the reactive S centre(s). The length of the CS bond (where S is the reactive centre) gives a fair approximation of collector's reactivity. Thus, the effect of remaining atoms or substituent groups that constitute the collector molecule on reactivity can be predicted by analysing how they affect the C-S bond length. Among the reagents studied, eX is the most efficient collector, followed by DeDTC (collectors with CS2- head group). The primary function of substituent groups in collector molecules is to impart hydrophobicity. However, these substituent groups may also alter the reactivity and binding capability of collectors' head groups if they are capable of increasing or decreasing the C-S/P-S bond length (or electron density around reactive S atom)

through inductive or resonance effect. In comparing groups, which show the only inductive effect, the groups that exhibit resonance with C-S bond have a greater significant effect on the reactivity of bonding to metal ions.

The effect of thiol collectors' adsorption on the pyrite (100), galena (110), chalcopyrite (112) and sphalerite (110) mineral surfaces was investigated. The enthalpies of adsorption were found to increase with increasing DTPs chain lengths on pyrite, galena and sphalerite, while the chalcopyrite showed high adsorption for DpDTP collector. Moreover, we noted a decrease of enthalpies of adsorption with an increase of DTCs chain lengths on pyrite, galena, chalcopyrite and sphalerite. The effect of branching was found to be mineral dependent as n-butyl DTC always produces higher energy of adsorption than DeDTP for galena, chalcopyrite and sphalerite surfaces, and lower energy for the pyrite surface. The enthalpies of adsorption for ethyl xanthates were always greater than those of DeDTC and DeDTP for galena and chalcopyrite. On the other hand, that of DeDTP was greater for pyrite and of DeDTC was greater for sphalerite. In fact, DeDTP and ethyl-xanthate showed no interaction with sphalerite. It is interesting to note that the adsorption energies for sphalerite showed no adsorption of eX, DbDTC and all DTPs, implying that there was no interactions between these collectors and sphalerite, which agrees well with floatation practice.

The bonding geometry of collectors on the mineral surfaces were evaluated before and after geometry optimisation. The adsorption of collectors on the surfaces showed that the DTPs and eX favoured the formation of the conjugated π– or π*–bonding, however, this was not observed in the case of DTPs. It was also observed that the thiol collectors formed a bridge bond on all mineral surfaces. Furthermore, the collectors preferred to bend either horizontally or at an angle on the surface, suggesting a strong interaction in the bridging mode. The geometric orientation of the DTPs tends to bend towards the surface. Interestingly, we noted that the adsorption of DDTP on Fe-top site showed collector dissociation, where the phosphorus interacted with the Fe atoms.

There is a decrease in bond length between DTPs S atoms and pyrite Fe with increasing of DTP chain length. The same was observed for galena, while the opposite trend was observed for chalcopyrite. However, the distance between DTPs S atoms with the surface atoms shows that there is a strong interaction between chalcopyrite

surfaces with DTPs, and there is no interaction between DTPs and sphalerite as highlighted by the longest bond length between DTPs and sphalerite surface. The DTCs showed an increase of bond length with an increase of chain length for pyrite, which agrees well with the adsorption energies. Moreover, there is a general decrease of bond length with an increase of DTCs for galena and chalcopyrite, and high values are observed for sphalerite indicating that there is no adsorption. The shorter and longer bonds reflected strong and weak electron overlap, respectively.

The PDOS of DTPs, DTCs and eX functional groups were found to be similar near the E_F, which are composed of the S *3p*-orbital, indicating that the S *3p*-orbital is the centre of reactivity. In addition, there was no significant difference between the PDOS of the S atom with a single bond and that with a double bond. This may imply that the two S atoms in the thiol group have similar chemical reactivity, which may be ascribed to the conjugation effect of a pie bond.

The DOS of thiol collectors on the mineral surfaces have indicated that the S *3p*-orbitals HOMO hybridises with the metals *3d*-orbitals and as such reduces states to almost zero. This suggests a transfer of electrons to the pyrite and chalcopyrite surfacess. Furthermore, as for the DOS of DEDTP on the mineral surface, we noticed that the LUMO peak moved to the VB, suggesting that it is electron acceptor. Similarly, the DTPs, DTCs and eX DOS behaviour on the surface showed that the LUMO peak shifted to the VB, suggesting electron accepter from the metal surface. In order to confirm the charges transferred we analysed the Mulliken charges and populations. We found that the S atoms became less negative while the metals gained positive charge. This suggests that both the S and the metal atoms lose electrons. It was also found that some charges resided in the internuclear region between the metals and sulphurs (M–S), particularly on xanthate adsorption. The DOS of the thiol collectors on the surfaces have shown that the S *3p*-orbital HOMO mix with the metals *3d*-orbital for pyrite and chalcopyrite, *6p*-orbital for galena and (*3d and 4s)*-orbitals for sphalerite. Collectors S *3p*-orbital reduces to zero states on surface Fe, Pb and Zn atoms. Fe-S bond population for DeDTP is lower than both DispDTP and DbDTP for pyrite. For chalcopyrite the DeDTP Fe-S population is higher than both DispDTP and DbDTP and similar trends were observed for Pb-S and Zn-S, although the Pb-S bonding was less covalent compared to Fe-S of chalcopyrite. The DTPs Fe-S bond pollution are generally higher for chalcopyrite than pyrite. The Mulliken charges analysis indicated that the DTPs S atoms lost charges and the metals gained with a decreasing DTPs

chain length for pyrite, and a similar trend was found for chalcopyrite. The DTPs S atoms gained electrons from galena and sphalerite surfaces with increasing chain length. For DTCs on pyrite and chalcopyrite, surface Fe atoms gain more electrons in the presence of DeDTP than other DTPS, while galena and sphalerite lost more electrons in the presence of DbDTC than other DTCs. As for xanthate, the Mulliken bond charges indicated that the S atoms and the metals lost charges, showing that some charges reside in the internuclear region between the metals and sulphurs (M–S). The lost electrons to the collector indicate that some charges reside within the internuclear region between the metals and sulphurs (M–S). These demonstrate that electron charge transfers are collector and mineral dependent; collector would be an electron acceptor or donor depending on the mineral makeup.

We now consider a comparison of the computational results with those of the isothermal titration calorimetry (ITC) and microfloation experiments for the interaction of DeDTP, DeDTC and eX with pyrite and galena. This should shed valuable insights on reaction mechanisms at such interfaces. The modelling work was conducted in the absence and presence of water. Generally, the results showed that calculated adsorption energies were more exothermic than the experimental findings and hydration tends reduce such differences. It must be emphasised that this study focussed more on trends rather than absolute values yielded by such techniques. Calculated DeDTP, DeDTC and eX heats of adsorption on the pyrite FeS_2 (111) surface, with and without water, are consistent. Furthermore, such calculations, with and without water, have similar trends to the ITC experimental heats of formation; with DeDTC most and DeDTP least dominant. The magnitudes of calculated heats of adsorption are reduced after hydration, and are closer to experimental values except for DeDTC. This might suggest that the FeS_2 (111) surface could possibly be a predominant exposed face of the mineral obtained after comminution in preparation for the ITC experiments. Calculated DeDTP, DeDTC and eX heats of adsorption on the FeS_2 (100) surface, with and without water, are consistent. However, such calculations do not show the same tendencies as the ITC experimental outcomes. On the other hand, they depict similar trends, with and without water, to experimental microfloation recoveries for DeDTP, DeDTC and eX collectors, with DeDTP most dominant and DeDTC least. Hence, it could be surmised that in a flotation cell or plant the predominantly exposed facet of the pyrite mineral is FeS_2 (100) and DeDTP is better attached to that facet, hence promoting mineral recovery. Calculations

pertaining to the three collectors on the galena PbS (100) surface, reflect similar tendencies with and without water. Trends for calculated DeDTP and DeDTC heats of adsorptions are consistent with ITC experimental results, especially the reduced magnitudes after hydration. However, calculations predict eX as having higher adsorption than the thiols though ITC experiments depict it as lower. Lastly, calculated DeDTP and DeDTC adsorptions on the PbS (100) are also consistent with experimental recoveries, especially the one without water. Calculations predict eX as having higher adsorption strength than the thiols, though recovery experiments depict it as lower. These results show that mineral surface orientation has a great influence on the adsorption strength of collectors and mineral recoveries The differences in the trends observed for both the calculated and experimental enthalpies of adsorption might be attributed to flat-lying molecules on surfaces in experiments, whereas DFT calculations find the vertically adsorption of collectors to be more stable. The introduction of water in the computational modelling framework effectively reduced the absolute values of the calculated adsorption energies without affecting the observed trends.

Recommendations and future work

The studies of oxidation, hydration and effect of ligand collectors on the sulphide minerals surface remain relevant in the mineral extraction and mining industries. The current findings on these three aspects have shown varying trends with regards to absorption energies and interactions. However, various properties such as electronic structure calculations are necessary to assist in interpretations of the current data, especially for the most stable surfaces. We have also observed that our results are dependent on the number of water molecules placed on the surface. Thus, there is a need for further calculations in this regard; complete oxidation and hydration of the mineral surfaces should be evaluated to gain more reliable explanation on the reaction processes.

Furthermore, the analysis on ligand collectors were mainly performed on dry surfaces; it will be of great importance to extend calculations to collectors on mineral surfaces covered with water. This will allow in-depth knowledge and understanding of mineral extraction, a factor which is of interest to Anglo platinum under SAMMRI.

The future work will focus on the following aspects:

1. Investigate the effect of thiol collectors on hydrated sulphide mineral surfaces.

2. Design of thiol collectors that can be used to extract these mineral ores better during flotation and depress some of the minerals such as pyrite.
3. Employ an atomistic simulation approach to determine and explore other different terminations on a much larger scale (using large supercell).
4. Introduce the temperature effect on the various surfaces using molecular dynamics approach.
5. The comparison isothermal calorimetric results of adsorptions energy for different PH.

Chapter 8

Works Cited

[1] Muzenda E., Afolabi A.S., Abdulkareem A.S. and Ntuli F., “Effect of pH on the recovery and grade of base metals sulphides (PGMs) by flotation,” *Proceedings of the world congress on Engineering and Computer science,* vol. 2, pp. 609-612, 2011.

[2] Fairthorne G., Fornasiero D. and Ralston J. , “Solution properties of thionocarbamate collectors,” *International Journal of Mineral Processing,* vol. 46, pp. 137-153, 1996.

[3] Urbina R.H., “Recent developments and advances in formulations and applications of chemical reagents used in froth flotation,” *Mineral Processing and Extractive Metallurgy Review,* vol. 24, pp. 139-182, 2003.

[4] Yekeler M. and Yekeler H. , “A density functional study on the efficiencies of 2-mercaptobenzoxazole and its derivatives as chelating agents in flotation processes,” *Colloids and Surfaces A: Physicochemical and Engineering Aspects,* vol. 286, pp. 121-125, 2006.

[5] Harris P.J., Reagents in Mineral Technology, New York and Basel: Marcel Dekker, 1988, pp. 371-384.

[6] Fuerstenau M.C., “Froth flotation: The first ninety years,” in *Advances in flotation technology*, Littleton, Colo., Society for Mining, Metallurgy, and Exploration, 1999, p. xi–xxxiii.

[7] Dong J. and Xu M., “Evaluation of environmentally friendly collectors for xanthate replacement,” in *Proceedings of the 43rd Annual Canadian Mineral Processors Conference.*, CIM, ottawa, ON, Canada, 2011.

[8] Ngobeni W. and Hangone G., “The effect of using sodium di-methyl-dithiocarbamate as a co-collector with xanthates in the froth flotation of

pentlandite containing ore from Nkomati mine in South Africa," *Minerals Engineering,* vol. 54, pp. 94-99, 2013.

[9] Ngobeni W. and Hangone G., "The effect of using pure thiol collectors on the froth flotation of pentlandite containing ore.," *South African Journal of Chemical Engineering,* vol. 18, pp. 41-50, 2013.

[10] Taguta J., The thermochemical behaviour of thiol collectors and collector mixtures with sulphide minerals, Msc thesis, Cape Town: South Africa: University of Cape Town, 2015.

[11] Wills B.A. and Napier-Munn T.J. , Will's Minerals Processing Technology – An introduction to the practical aspects of ore treatment and mineral recovery, Burlington: Elsevier Ltd, 2006.

[12] Raju G.B. and Forsling W. , "Adsorption of thiol collectors on chalcopyrite," *Journal of Surface Science and Technology,* vol. 13, p. 25–37, 1997.

[13] Chen J., Lan L. and Chen Y., "Computational simulation of adsorption and thermodynamic study of xanthate dithiophospate and dithiocarbamate on galena and pyrite surfaces," *Minerals Engineering,* Vols. 46-47, pp. 136-143, 2013.

[14] Wiese J., Harris P. and Bradshaw D.J. , " Investigation of the role and interactions of a dithiophosphate collector in the flotation of sulphides from the Merensky reef," *Minerals Engineering,* vol. 18, pp. 791-800 , 2005.

[15] Chen J., Lan L. and Chen Y., "computational simulation of adsorptrion and thermodynamicic study of xanthate, dithiophospahte and dithiocarbamate on galena and pyrite surfaces," *Minerals Engineering,* Vols. 46-47, pp. 136-143, 2013.

[16] Bradshaw D.J., Buswell A.M., Harris P.J. and Ekmekci Z., "Interactive effect of the type of milling media and copper sulphide addition on the flotation performance of sulphide minerals from Meresky ore part 1: pulp chemistry," *International Journal of Mineral Processing,* vol. 78, pp. 164-174, 2005a.

[17] Somasundaran P. and Nagaraj D.R., “Chemistry and applications of chelating agents in flotation and flocculation,” in *Reagents in mineral industry*, London, Institution of Mining and Metallurgy, 1984, pp. 209-219.

[18] McMurry J., Organic Chemistry Fourth Edition, Belmont, Carlifonia: Brooks Cole, 1996.

[19] Kim D.S., Kuh S.E. and Moon K.S., “Characteristics of xanthates related to hydrocarbon chain length characteristics of xanthates related to hydrocarbon chain length,” *Geosystem Engineering,* vol. 3, p. 30–34, 2012.

[20] Persson I., “Review: adsorption of ions and molecules to solid surfaces in connection with flotation of sulphide minerals,” *Journal of Coordination Chemistry,* vol. 4, p. 261–342, 1994.

[21] Larsson M.L., Holmgren A. and Forsling W., “Xanthate adsorbed on ZnS studied by polarized FTIR-ATR spectroscopy,” *Langmuir,* vol. 16, p. 8129–8133, 2000.

[22] Leppinen J.O., “FTIR and flotation investigation of the adsorption of ethyl xanthate on activated and non-activated sulphide minerals,” *International Journal of Mineral Processing,* vol. 30, p. 245–263, 1900.

[23] Larsson M.L., Fredriksson A. and Holmgren A., “Direct observation of a self-assembled monolayer of heptyl xanthate at the germanium/water interface: A polarized FTIR study,” *Journal of Colloid and Interface Science,* vol. 273, p. 345–349, 2004.

[24] Ihs A. and Liedberg B., “Infrared study of ethyl and octyl xanthate ions adsorbed on metallic and sulfidized copper and silver surfaces,” *Langmuir,* vol. 10, p. 734–740, 1994.

[25] Manyeruke T.D., The petrography and geochemistry of the platreef on the farm Townlands, near Potgiestersrus, northern Bushveld Complex, MSc Thesis, Pretoria: University of Pretoria, 2003.

[26] Cabri L.J., “The distribution of trace precious metals in minerals and minerals products: The 23rd Hallim and Lecture,” *Mineralogical Magazine,* vol. 56 , pp. 289-308, 1992.

[27] Mostert A.B., A mineralogical and Petrological investigation of the Platreef on Drenthe 778 LR, northwest of Potgietersrus, MSc thesis, Pretoria: University of Pretoria, 1982.

[28] Wei Z., Li y., Gao H., Zhu Y., Qian G. and Yao J., “New insights into the surface relaxation and oxidation of chalcopyrite exposed to O2 and H2O: A first-principles DFT study,” *Applied Surface Science,* vol. 492, pp. 89-98, 2019.

[29] Hellstrom P., Oblatt S., Fredriksson A. and Holmgren A., “A theoretical and experimental study of vibrational properties of alkyl xanthates,” *Spetrochim. Acta,* vol. 65A, pp. 887- 895, 2006.

[30] Hellstrom P., Holmgren A. and Oberg S., “An ab-initio study of ethyl xanthate adsorbed on Ge (111) surface,” *Journal of Physical Chemistry,* vol. 111, pp. 16920-16926, 2007.

[31] Hung A., Yarovsky I. and Russo S., “Density-functional theory studies of xanthate adsorption on the pyrite FeS2 (110) and (111) surfaces,” *Journal of Chemical Physics,* vol. 118 , pp. 6022-6029, 2003.

[32] Chen J., Lan L. and Chen L. , “Computational simulation of adsorption and thermodynamic study of xanthate, dithiophosphate and dithiocarbamate on galena and pyrite surfaces,” *Minerals Enginneering,* vol. 46, pp. 136-143, 2013 .

[33] Yekeler H. and Yekeler M. , “Reactivities of some thiol collectors and their interactions with Ag(+1) ion by molecular modeling,” *Applied Surface Science,* vol. 236, pp. 435-443, 2004.

[34] Bag B., Das B. and Mishra B.K., “Geometrical optimization of xanthate collectors with copper ions and their response to flotation,” *Minerals Engineering,* vol. 24, pp. 760-765, 2011.

[35] Pradip and Fuerstenau D.W., “Design and development of novel flotation reagents for the beneficiation of mountain pass rare-earth ore,” *Minerals and Metallurgical Processing,* vol. 30, pp. 1-9, 2013.

[36] Liu G., Zhong H., Xia L., Wang S. and Dai T. , “Effect of N-substituents on performance of thiourea collectors by density functional theory calculations,” *Transactions of Nonferrous Metals Society of China,* vol. 20, pp. 695-701, 2010.

[37] Stelle H., Wright K. and Hillier I. , “A quantum-mechanical study of the (110) surface of sphalerite (ZnS) and its interaction with Pb(2+) species,” *Physics and Chemistry of Minerals,* vol. 30, pp. 69-75., 2003.

[38] Li Y., Chen J., Chen Y., Zhu Y. and Liu Y., “DFT simulation on interaction of H2O molecules with ZnS and Cu-activated surfaces,” *The Journal of Physical Chemistry C,* vol. 123, pp. 3048-3057, 2019.

[39] Mkhonto P.P., Computer simulation studies of nickel-rich pentlandite (Fe4Ni5S8) surfaces, for flotation process, PhD Thesis., Polokwane: Univeristy of Limpopo, 2016.

[40] Chowdhry M., Theoretical study on reactivity of different sulfide collectors and their binding affinity toward Cu(II), Zn(II) and Pb(II) ions, PhD thesis, Edmonton, Alberta: University of Alberta, 2015.

[41] Jordaan T.I., Investigating the role of dithiophosphate in the flotation of base metal sulfides, Cape Town: University of Cape Town , 2018.

[42] Cui W., Zhang Y., Chen J., Zhao C., Li Y., Chen Y. and Lee M.H., “Comparative study on surface structure, electronic properties of sulfide and oxide minerals: A first-principles perspective,” *Minerals,* vol. 9, pp. 1-12, 2019.

[43] Bulatovi S. M., Handbook of flotation reagents chemistry volume 2, theory and practice, flotation of gold, PGM and oxide minerals, vol. 2, Amsterdam: Elsevier, 2010.

[44] Crozier R.D., “Sulphide collector mineral bonding and the mechanism of flotation,” *Mineral Engineering,* vol. 4, p. 839–858, 1991.

[45] Fuerstenau M.C., “Thiol collector adsorption processes,” *International Journal of Mineral Processing,* vol. 29, p. 89–98, 1990.

[46] Guler Z., Hicyilmaz T., Gokagac C. and Emekci G., “Adsorption of dithiophosphate and dithiophosphinate on chalcopyrite,” *Mineral Engineering,* vol. 19, p. 62–71, 2006.

[47] Vignale R.G., “DFT in magnetic fields,” *Physical Review Letter,* vol. 59, pp. 2360-2363, 1979.

[48] Hohenberg P. and Kohn W., “Inhomogeneous electron gas,” *Physical Review B,* vol. 136 , pp. 864-871, 1965.

[49] Kohn W. and Sham L.J., “Self-consistent equations including exchange and correlation effects,” *Physical Review,* vol. 140 , pp. 1133-1138, 1965.

[50] Slater J. and Verma H.C., “The Theory of Complex Spectra,” *Physical Review,* vol. 34, pp. 1293-1322, 1929.

[51] Payne M.C., Teter M.P., Allan D.C., Arias T.A. and Joannopoulos J.D., “Iterative minimization techniques for ab initio total-energy calculations: molecular dynamics and conjugate gradients,” *Review Modern Physics,* vol. 64, pp. 1045-1097, 1992.

[52] Kudoh Y. and Takeda A.H., “local density approximation for the exchange-correlation energy of an electronic system,” *Physical Chemical Mineral,* vol. 13 , pp. 233-237, 1986.

[53] Perdew J.P. and Wang Y., “Generalized gradient approximation for the exchange-correlation hole of a many-electron system,” *Physical Review B,* vol. 45, pp. 13 244-13 249, 1992.

[54] Perdew J.P. and Wang Y., “Generalized gradient approximation for the exchange-correlation hole of a many-electron system,” *Physical Review B,* vol. 33, pp. 8800-8822, 1986.

[55] Brazadova V. and Bowler D.R., “Atomistic computer simulations,” vol. 26, Germany, WILEY-VCH Verlag GmbH & Co. KGaA, 2013, pp. 127-143.

[56] Meyer B., “The Pseudopotential Plane Wave Approach,” *Computational Nanoscience,* vol. 31, pp. 71-83, 2006.

[57] Clark S.J., Segall M.D., Pickard C.J., Hasnip P.J., Probert M.J., Refson K. and Payne M.C., “First-principles methods using CASTEP,” *Zeitschrift für Kristallographie,* vol. 220, pp. 567-570, 2005.

[58] Monkhorst H.F. and Park J.D., “Special points for brillouin-zone integrations,” *Physical Review B,* vol. 13, pp. 5188-5192, 1976.

[59] Pierce F.S., Basov D.N., Volkov P., Poon S.J. and Timusk T., “Optical Conductivity of Insulating Al-Based Alloys: Comparison of Quasiperiodic and Periodic Systems,” *Physical Review Letters,* vol. 73, pp. 1865-1868, 1994.

[60] Matsuda A., Sugita S., Fujii T. and Watanabe T., “Study of Pseudogap Phenomena by STM and Other Probes,” *Journal of Physics and Chemistry Solids,* vol. 62, pp. 65-68, 2001.

[61] Meister J. and Schwarz W.H.E., “Principal Components of Ionicity,” *The Journal of Physical Chemistry,* vol. 98, p. 8245–8252, 1994.

[62] Coelho A.A., *TOPAS-Academic,* Brisbane, Australia: Coelho Software, 2007.

[63] Grano S.R., Prestidge C.A. and Ralston J., “Solution interaction of ethyl xanthate and sulphite and its effect on galena flotation and xanthate adsorption,” *International Journal of Mineral Processing,* vol. 52, p. 161–186., 1997.

[64] McFadzean B. and O'Connor C.T., "A thermochemical study of thiol collector surface reactions on galena," *Minerals Engineering,* vol. 65, p. 54–60, 2014.

[65] Bradshaw D.J. and O'Connor C.T., " Measurement of the sub-process of bubble loading in flotation," *Minerals Engineering,* vol. 9, p. 443–448, 1996.

[66] Vanderbilt D., "Soft sself-consistent pseudopotentials in generalized eigenvalue formalism," *Physical Review B,* vol. 41, pp. 7892-7894, 1990.

[67] Hamann R., Schluter M. and Chiang C., "Norm-conserving pseudopotentials," *Physical Review Letter,* vol. 43, pp. 1494-1497, 1979.

[68] Segall M. D., Shah R., Pickardk C. J. and Payne M .C., "Population analysis of plane-wave electronicstructure calculations of bulk materials," *Phys. Rev. B.,* vol. 54, p. 16317–16320, 1996.

[69] Goodenough J.B. , "Direct Cation-Cation Interactions in several oxides," *Physical Review,* vol. 117, pp. 1442-1551, 1960.

[70] Hung A., Yarovsky I. and Russo S.P., "Density functional theory studies of xanthate adsorption on the pyrite FeS2 (110) and (111) surfaces," *The Journal of Chemical Physics,* vol. 118 (13), pp. 6022-6029, 2003.

[71] Mkhonto D., Ngoepe P.E. Cooper T.G. and de Leeuw N.H., "A computer modelling study of the interaction of organic adsorbates with fluorapatite surfaces," *Physical Chemistry of Minerals,* vol. 33, pp. 314-331, 2006.

[72] Hall S.R. and Stewart J.M., "The crystal structure refinement of chalcopyrite, CuFeS2," *Acta Crystallogra Section B,* vol. 29, p. 579–585, 1973.

[73] De Lima G.F., de Oliveira C., de Abreu H.A. amd Duarte H.L.A. , "Water adsorption on the reconstructed (001) chalcopyrite surfaces," *Journal of Physical Chemistry C,* vol. 115, p. 10709–10717, 2011.

[74] Chen V. H.-Y., Mallia G., Mart´ınez-Casado R. and Harrison N. M. , “Surface morphology of CuFeS2: The stability of the polar (112)(112) surface pair,” *Physical Review B,* vol. 92, pp. 1554261-1554269, 2015.

[75] Dalven R. , “A review of the semiconductor properties of PbTe, PbSe, PbS and PbO,” *Infrared Physics,* vol. 9, pp. 141-184, 1969.

[76] Nelmes R. J., McMahon M. I., Wright N. G. and Allan D. R. , “Structural studies of II–VI semiconductors at high pressure.,” *J. Phys. Chem. Solids,* vol. 56, pp. 545-549, 1995.

[77] Balantseva E., Berlier G., Camino B., Lessio M. and Ferrari A.M., “Surface properties of ZnS nanoparticles: A Combined DFT and experimental study,” *Journal of Physical Chemistry C,* vol. 118, pp. 23853-23862, 2014.

[78] Rao S.R. , “Collector mechanism I. Thiol collectors in sulphide minerals,” in *Surface Chemistry of Froth Flotation*, Boston, Springer, 2004, pp. 479-526 .

[79] Winter G., “Inorganic xanthates,” *Reviews in Inorganic Chemistry,* vol. 2, pp. 253-342, 1980.

[80] Rao S.R., Surface Chemistry of Froth Flotation, volume 2, New York: Plenum , 2004.

[81] Haiduc I., Sowerby D.B. and Lu S.-F., “Polyhedron report number 57-stereochemical aspects of phosphor-1,1-dithiolato metal complexes (dithiophosphates, dithiophosphinates): coordiantion patterns, molecular structures and supramolecular associations-I,” *Polyhedron,* vol. 14, p. 3389–3472, 1995.

[82] Liu G., Wang Y., Yuan L., Xu Z., Lu Y., Zeng H. and Zhong H., “A DFT study on the flotation performance of thiol collectors for coper sulphide flotation,” *IMPC New Delhi, India,* pp. 02947-02958, 2012.

[83] Georgieva I. and Trendafilova N. , “Bonding analyses, formation energies, and vibrational properties of M-R2dtc complexes (M) Ag(I), Ni(II), Cu(II), or Zn(II)),” *The Journal of Physical Chemistry A,* vol. 111, p. 13075–13087, 2007.

[84] Boddu V.M., Abburi K., Talbott J.L. and Smith E.D. , “Removal of hexavalent chromium from wastewater using a new composite chitosan biosorbent,” *Environmental Science & Technology,* vol. 37, pp. 4449-4456, 2003.

[85] Shaoyi J., Dasgupta S., Blanco M., Frazier R., Yamaguchi E.S., Tang Y. and Goddard W.A., “Structures, vibrations, and force fields of dithiophosphate wear inhibitors from ab initio quantum chemistry,” *Journal of Physical Chemistry,* vol. 100, pp. 15760-15769, 1996.

[86] Chandra A.P. and Gerson A.R., “A review of the fundamental studies of the copper activation mechanisms for selective flotation of the sulfide minerals, sphalerite and pyrite,” *Advances in Colloid and Interface Science,* vol. 145, pp. 97-110, 2009.

[87] Fuerstenau M.C., Clifford K.L. and Kuhn M.C., “The role of zinc-xanthate precipitation in sphalerite flotation,” *International Journal of Mineral Processing,* vol. 1, pp. 307-318, 1974.

[88] Fu F.L. and Wang Q., “Removal of heavy metal ions from wastewaters: a review,” *Journal of Environmental Management,* vol. 92, p. 407–418 , 2011.

[89] Ikeda T. and Hagihara H., “The crystal structure of zinc ethylxanthate,” *Acta Crystallographica,* vol. 21, p. 919–927, 1966.

[90] Costa Jr A.C., Ondar G.F., Versiane O., Ramos J.M., Santos T.G., Martin A.A. and Téllez Soto C.A. , “DFT: B3LYP/6-311G (d, p) vibrational analysis of bis(diethyldithiocarbamate) zinc (II) and natural bond orbitals,” *Spectrochimica Acta Part A: Molecular and Biomolecular Spectroscopy,* vol. 105, pp. 251-258, 2013.

[91] Billes F., Holmgren A. and Mikosch H. , “A combined DFT and vibrational spectroscopy study of nickel and zinc O,O-diethyldithiophosphate complexes,” *Vibrational Spectroscopy,* vol. 53, pp. 296-306, 2010.

[92] Chen J.H., Long X.H., Zhao C.H., Kang D. and Guo J., “DFT calculation on relaxationand electronic structure of sulfide minera.s surfaces in presence of H_2O molecule,” *Journal of Central South University,* vol. 21, p. 3945–3954., 2014.

[93] Chen J.H., Long X.H. and Chen Y., “Comparison of multilayer water adsorption onthe hydrophobic galena (PbS) and hydrophilic pyrite (FeS_2) surfaces: a DFTstudy,” *Journal of Physical Chemistry C,* vol. 118, p. 11657–11665., 2014.

[94] Becker U., Rosso K.M. and Hochella M.F. Jr., “The proximity effect onsemiconducting mineral surfaces: a new aspect of mineral surface reactivityand surface complexation theory,” *Geochimica et Cosmochimica Acta,* vol. 65 , p. 2641–2649, 2001.

Appendix A: Mulliken bond population, and charge population and densities of states for eX and DTCs adsorptions

Table A.1: Mulliken bond populations of the interaction between DeDTC, nbDTC and DbDTC on pyrite surface.

	Adsorbate	Bond atoms	Population	Bond
FeS_2(100)	DeDTC	S1-Fe1	0.32	2.349
		S2- Fe2	0.38	2.377
	nbDTC	S1-Fe1	0.33	2.377
		S2- Fe2	0.36	2.490
	DbDTC	S1-Fe1	0.31	2.392
		S2- Fe2	0.39	2.367

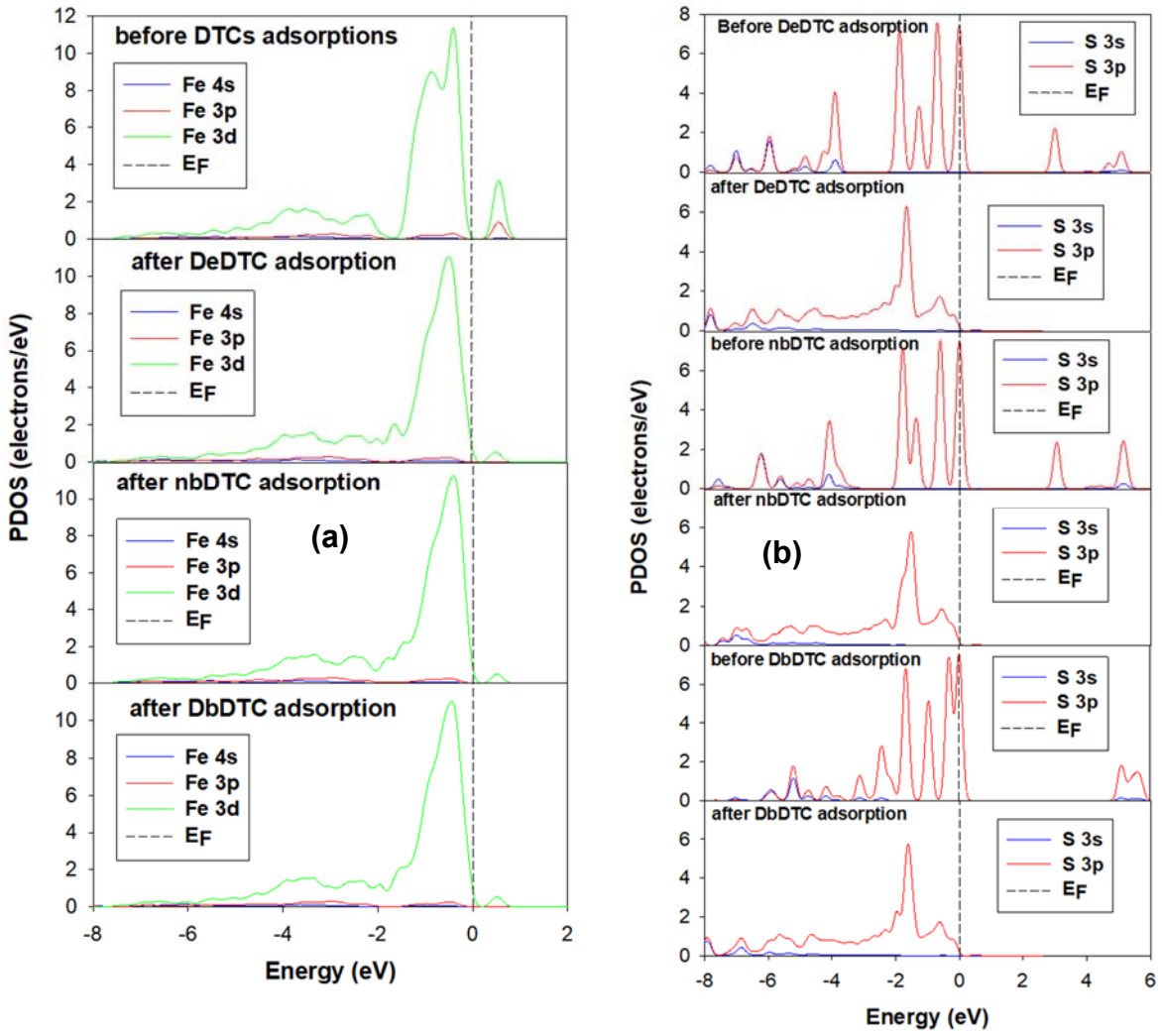

Figure A.1: Bonding Fe–S atoms before and after DTCs adsorption. The zero of energy has been set at the Fermi level EF. (a) Surface Fe and (b) S of DTCs atom.

Table A.2: Mulliken bonding population of atoms before and after thiol collector adsorption to the surface. DeDTC, nbDTC and DbDTC

		Bond	Population	length
FeS_2(100)	In the absence of thiol collector	S3 - Fe1	0.48	2.17564
		S4 – Fe1	0.51	2.21878
		S3 - Fe2	0.52	2.22089
		S5 - Fe2	0.49	2.16419
	DeDTC	S3 - Fe1	0.45	2.190
		S4 – Fe1	0.47	2.196
		S3 - Fe2	0.46	2.201
		S5 - Fe2	0.40	2.223
	nbDTC	S3 - Fe1	0.45	2.190
		S4 – Fe1	0.46	2.234
		S3 - Fe2	0.46	2.206
		S5 - Fe2	0.41	2.220
	DbDTC	S3 - Fe1	0.44	2.182
		S4 – Fe1	0.47	2.207
		S3 - Fe2	0.45	2.201
		S5 - Fe2	0.40	2.228

Table A.3: Mulliken bonding population of atoms before and after adsorption to the surface. DeDTP, DispDTC and DbDTC

		Adsorption status	Bond	Population	length
FeS_2(100)	DeDTC	Before	R(C1–N1)	0.96	1.345
			R(C1-S1)	0.72	1.691
			R(C1=S2)	0.72	1.691
		after	R(C1–N1)	0.98	1.354
			R(C1-S1)	0.81	1.757
			R(C1=S2)	0.74	1.778
	nbDTC	Before	R(C1–N1)	0.91	1.344
			R(C1-S1)	0.71	1.690
			R(C1=S2)	0.72	1.685
		after	R(C1–N1)	0.93	1.359
			R(C1-S1)	0.78	1.762
			R(C1=S2)	0.77	1.759
	DbDTC	Before	R(C1–N1)	0.96	1.349
			R(C1-S1)	0.71	1.694
			R(C1=S2)	0.72	1.692
		after	R(C1–N1)	0.98	1.364
			R(C1-S1)	0.81	1.758
			R(C1=S2)	0.75	1.772

Table A.4: Mulliken charge populations of DeDTC, nbDTC and DbDTC adsorption on the pyrite surface (s, p and d represent s orbitals, p orbitals and d orbitals, respectively) before and after adsorption.

	Adsorbate	Adsorption status	Atom	s	p	d	total	q/e
FeS_2(100)	DeDTC	Before	S1	1.85	4.17	0.00	6.02	-0.02
			S2	1.85	4.17	0.00	6.02	-0.02
		After	s1	1.83	4.23	0.00	6.06	-0.06
			s2	1.83	4.25	0.00	6.08	-0.08
		Before	Fe1	0.35	0.44	7.14	7.93	0.07
			Fe2	0.34	0.44	7.14	7.93	0.07
		After	Fe1	0.35	0.53	7.10	7.98	0.02
			Fe2	0.35	0.53	7.10	7.98	0.02
	nbDTC	Before	S1	1.85	4.16	0.00	6.00	0.00
			S2	1.85	4.16	0.00	6.01	-0.01
		After	S1	1.83	4.25	0.00	6.08	-0.08
			S2	1.83	4.26	0.00	6.09	-0.09
		Before	Fe1	0.35	0.44	7.14	7.93	0.07
			Fe2	0.34	0.44	7.14	7.93	0.07
		After	Fe1	0.36	0.53	7.10	7.98	0.02
			Fe2	0.36	0.53	7.10	7.98	0.02
	DbDTC	Before	S1	1.85	4.17	0.00	6.02	-0.02
			S2	1.85	4.17	0.00	6.02	-0.02
		After	S1	1.83	4.24	0.00	6.06	-0.06
			S2	1.82	4.26	0.00	6.07	-0.07
		Before	Fe1	0.35	0.44	7.14	7.93	0.07
			Fe2	0.34	0.44	7.14	7.93	0.07
		After	Fe2	0.35	0.53	7.10	7.99	0.01
			Fe1	0.35	0.52	7.11	7.98	0.02

Table A.5: Mulliken bond populations of the interaction between DeDTC, nbDTC and DbDTC on chalcopyrite surface.

	Adsorbate	Bond atoms	Population	Bond
CuFeS2(112)	DeDTC	S1 – Fe1	0.60	2.127
		S2—Fe2	0.58	2.146
	nbDTC	S1—Fe1	0.58	2.138
		S2—Fe2	0.57	2.133
	DbDTC	S1 – Fe1	0.60	2.124
		S2 – Fe2	0.58	2.121

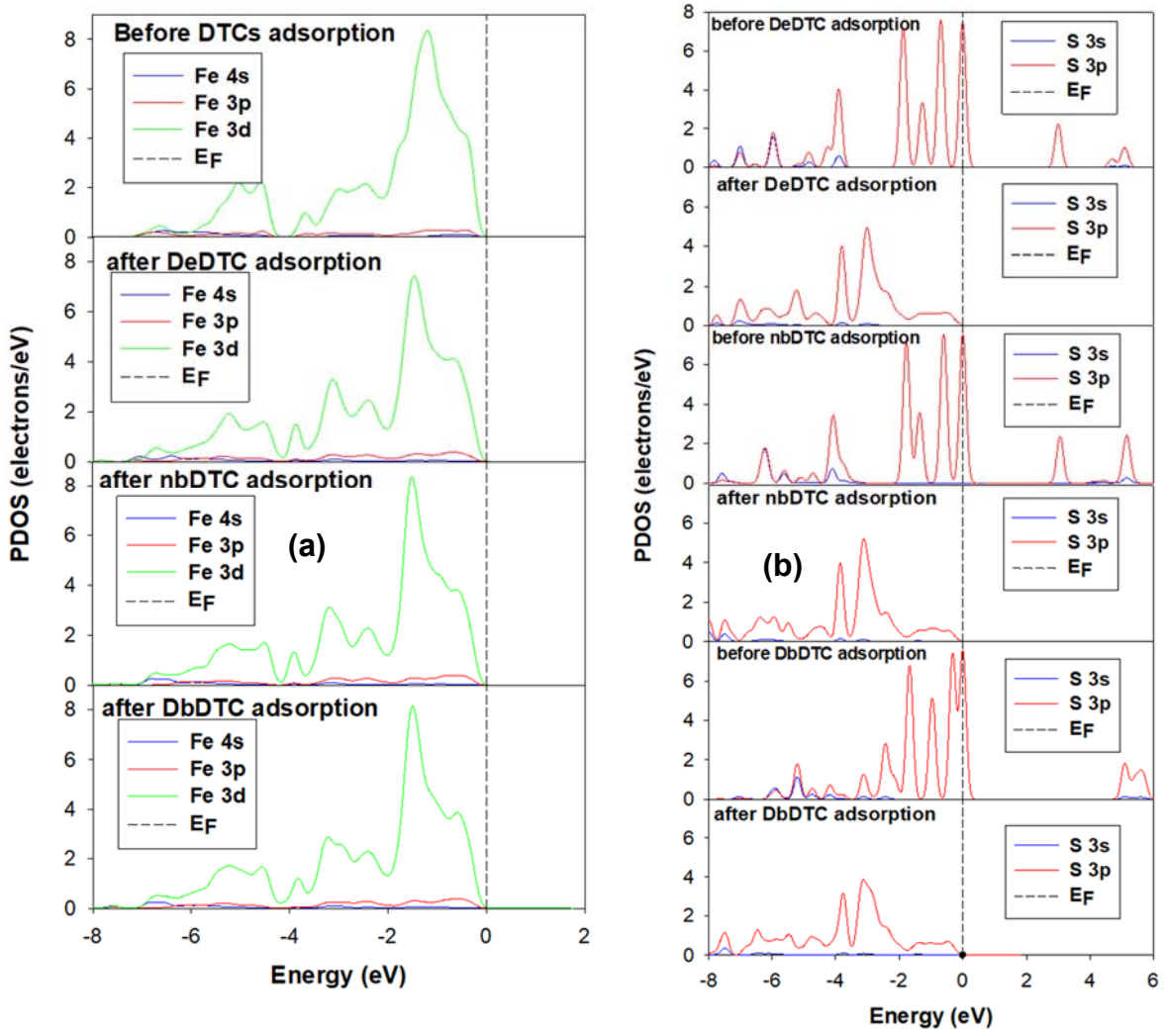

Figure A.2: Bonding Fe–S atoms before and after DTCs adsorption on $CuFeS_2$. The zero of energy has been set at the Fermi level EF. (a) Surface Fe and (b) S of DTCs atom.

Table A.6: Mulliken charge populations of DTCs adsorption on the chalcopyrite surface (s, p and d represent s orbitals, p orbitals and d orbitals, respectively) before and after adsorption.

	Adsorbate	Adsorption status	Atom	s	p	d	total	q/e
$CuFeS_2$(112)	DeDTC	before	S1	1.85	4.17	0.00	6.02	-0.02
			S2	1.85	4.17	0.00	6.02	-0.02
		after	S1	1.8	4.18	0.00	5.99	0.01
			S2	1.81	4.18	0.00	5.99	0.01
		before	Fe1	0.33	0.41	6.94	7.68	0.32
			Fe2	0.33	0.41	6.94	7.69	0.31
		after	Fe1	0.33	0.52	6.97	7.81	0.19
			Fe2	0.33	0.51	6.97	7.81	0.19
	nbDTC	before	S1	1.85	4.16	0.00	6.00	0.00
			S2	1.85	4.16	0.00	6.01	-0.01
		after	S1	1.81	4.18	0.00	5.99	0.01
			S2	1.8	4.19	0.00	5.99	0.01
		before	Fe1	0.33	0.41	6.94	7.68	0.32
			Fe2	0.33	0.41	6.94	7.69	0.31
		after	Fe1	0.33	0.48	6.97	7.78	0.22
			Fe2	0.33	0.51	6.98	7.82	0.18
	DbDTC	before	S1	1.85	4.17	0.00	6.02	-0.02
			S2	1.85	4.17	0.00	6.02	-0.02
		after	S1	1.81	4.17	0.00	5.98	0.02
			S2	1.81	4.18	0.00	5.99	0.01
		before	Fe1	0.33	0.41	6.94	7.68	0.32
			Fe2	0.33	0.41	6.94	7.69	0.31
		after	Fe1	0.33	0.49	6.97	7.79	0.21
			Fe2	0.33	0.52	6.97	7.82	0.18

Table A.7: DeDTC, nbDTC and DbDTC Mulliken bonding population of atoms before and after adsorption to the chalcopyrite surface.

	Adsorbate	Adsorption status	Bond	Population	length
$CuFeS_2$(112)	DeDTC	Before	R(C1–N1)	0.96	1.345
			R(C1-S1)	0.72	1.691
			R(C1=S2)	0.72	1.691
		after	R(C1–N1)	0.97	1.355
			R(C1-S1)	0.75	1.726
			R(C1=S2)	0.75	1.730
	nbDTC	Before	R(C1–N1)	0.91	1.344
			R(C1-S1)	0.71	1.690
			R(C1=S2)	0.72	1.685
		after	R(C1–N1)	0.91	1.358
			R(C1-S1)	0.75	1.726
			R(C1=S2)	0.77	1.719
	DbDTC	Before	R(C1–N1)	0.96	1.349
			R(C1-S1)	0.71	1.694
			R(C1=S2)	0.72	1.692
		after	R(C1–N1)	0.98	1.358
			R(C1-S1)	0.75	1.729
			R(C1=S2)	0.75	1.733

Table A.8: chalcopyrite Mulliken bonding population of atoms before and after thiol collector adsorption to the surface DeDTC, nbDTC and DbDTC.

		Bond	Population	length
$CuFeS_2$(112)	In the absence of thiol collector	S3–Fe1	0.56	2.127
		S4–Fe2	0.56	2.127
		S3 –Cu1	0.45	2.273
		S4 –Cu2	0.45	2.272
	DeDTC	S3–Fe1	0.54	2.098
		S4–Fe2	0.55	2.098
		S3 –Cu1	0.42	2.261
		S4 –Cu2	0.41	2.245
	nbDTC	S3–Fe1	0.55	2.089
		S4–Fe2	0.60	2.107
		S3 –Cu1	0.39	2.268
		S4 –Cu2	0.42	2.254
	DbDTC	S3–Fe1	0.55	2.090
		S4–Fe2	0.58	2.105
		S3 –Cu1	0.41	2.257
		S4 –Cu2	0.42	2.256

Table A.9: Mulliken bond populations of the interaction between DeDTC, nbDTC and DbDTC on galena surface.

	Adsorbate	Bond atoms	Population	Bond
PbS(100)	DeDTC	S1 – Pb1	0.15	2.854
		S2 – Pb2	0.15	2.851
	nbDTC	S1 – Pb1	0.15	2.827
		S2 – Pb2	0.15	2.902
	DbDTC	S1 – Pb1	0.14	2.840
		S2 – Pb2	0.14	2.833

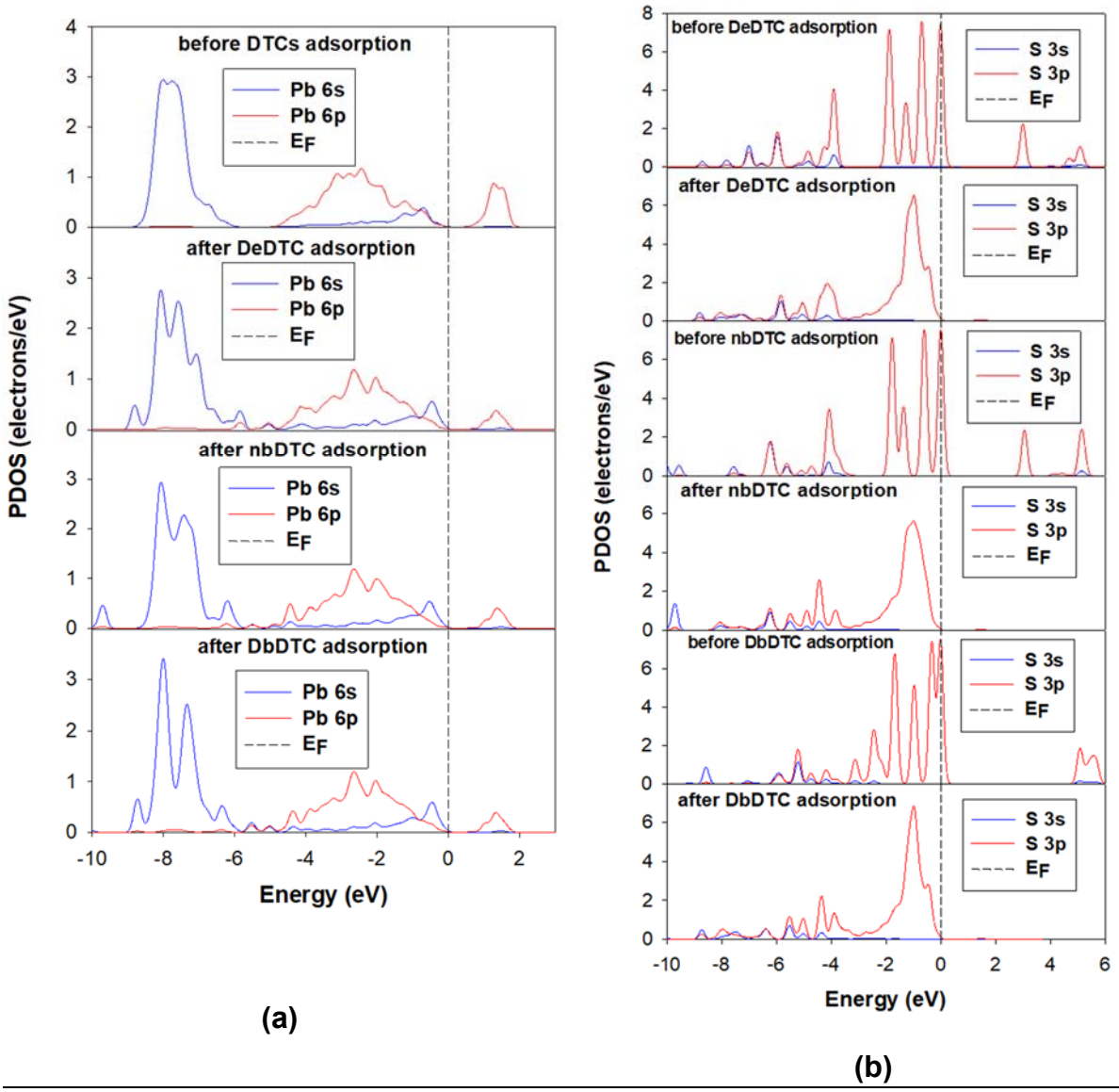

Figure A.3: Bonding Pb–S atoms before and after DTCs adsorption on PbS. The zero of energy has been set at the Fermi level EF. (a) Surface Fe and (b) S of DTCs atom.

Table A.10: Mulliken charge populations of DTCs adsorption on the galena surface (s, p and d represent s orbitals, p orbitals and d orbitals, respectively) before and after adsorption.

	Adsorbate	Adsorption status	Atom	s	p	d	total	q/e
PbS(100)	DeDTC	before	S1	1.85	4.17	0.00	6.02	-0.02
			S2	1.85	4.17	0.00	6.02	-0.02
		after	S1	1.83	4.4	0.00	6.23	-0.23
			S2	1.84	4.37	0.00	6.21	-0.21
		before	Pb1	1.98	1.41	10.00	13.4	0.60
			Pb2	1.98	1.41	10.00	13.4	0.60
		after	Pb1	1.89	1.39	10.00	13.27	0.73
			Pb2	1.89	1.39	10.00	13.28	0.72
	nbDTC	before	S1	1.85	4.16	0.00	6.00	0.00
			S2	1.85	4.16	0.00	6.01	-0.01
		after	S1	1.84	4.35	0.00	6.19	-0.19
			S2	1.82	4.39	0.00	6.21	-0.21
		before	Pb1	1.98	1.41	10.00	13.4	0.60
			Pb2	1.98	1.41	10.00	13.4	0.60
		after	Pb1	1.93	1.39	10.00	13.32	0.68
			Pb2	1.9	1.38	10.00	13.28	0.72
	DbDTC	before	S1	1.85	4.17	0.00	6.02	-0.02
			S2	1.85	4.17	0.00	6.02	-0.02
		after	S1	1.83	4.39	0.00	6.21	-0.21
			S2	1.83	4.37	0.00	6.20	-0.20
		before	Pb1	1.98	1.41	10.00	13.4	0.60
			Pb2	1.98	1.41	10.00	13.4	0.60
		after	Pb1	1.86	1.39	10.00	13.25	0.75
			Pb2	1.87	1.39	10.00	13.27	0.73

Table A.11:DeDTC, nbDTC and DbDTC Mulliken bonding population of atoms before and after adsorption to the galena surface.

	Adsorbate	Adsorption status	Bond	Population	length
PbS(100)	DeDTC	Before	R(C1–N1)	0.96	1.345
			R(C1-S1)	0.72	1.691
			R(C1=S2)	0.72	1.691
		after	R(C1–N1)	0.96	1.363
			R(C1-S1)	0.80	1.724
			R(C1=S2)	0.80	1.724
	nbDTC	Before	R(C1–N1)	0.91	1.344
			R(C1-S1)	0.71	1.690
			R(C1=S2)	0.72	1.685
		after	R(C1–N1)	0.91	1.361
			R(C1-S1)	0.76	1.733
			R(C1=S2)	0.84	1.701
	DbDTC	Before	R(C1–N1)	0.96	1.349
			R(C1-S1)	0.71	1.694
			R(C1=S2)	0.72	1.692
		after	R(C1–N1)	0.97	1.365
			R(C1-S1)	0.81	1.721
			R(C1=S2)	0.80	1.726

Table A.12: galena Mulliken bonding population of atoms before and after thiol collector adsorption to the surface DeDTC, nbDTC and DbDTC.

		Bond	Population	length
PbS(100)	In the absence of thiol collector	S3 – Pb1	0.06	2.995
		S4—Pb2	0.06	2.995
		S3—Pb2	0.06	2.995
	DeDTC	S3 – Pb1	0.11	2.894
		S4 – Pb2	0.10	2.914
		S3 – Pb2	0.10	2.919
	nbDTC	S3 – Pb1	0.11	2.880
		S4– Pb2	0.08	2.981
		S3 – Pb2	0.13	2.838
	DbDTC	S3 – Pb1	0.11	2.880
		S4 – Pb2	0.10	2.922
		S3 – Pb2	0.10	2.914

Table A.13: Mulliken bond populations of the interaction between DeDTC, nbDTC and DbDTC on sphalerite surface.

	adsorbate	Bond atoms	Population	Bond
ZnS(110)	DeDTC	S1 – Zn1	0.46	2.514
		S2 – Zn2	0.48	2.505
	nbDTC	S1 – Zn1	0.51	2.453
		S2 – Zn2	0.51	2.452
	DbDTC	S1 – Zn1	0.40	2.525
		S2 – Zn2	0.51	2.504

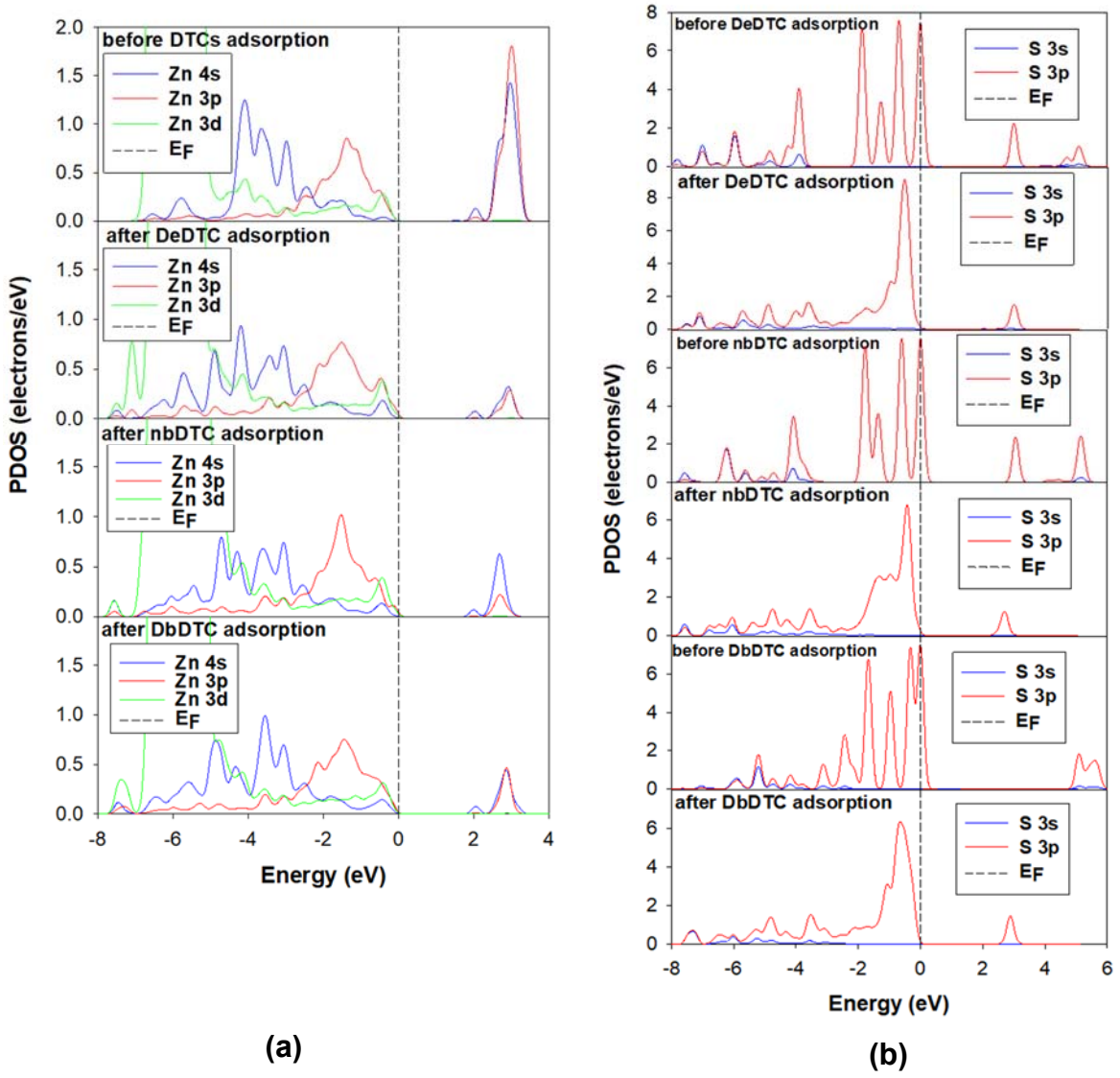

Figure A.3: Bonding Zn–S atoms before and after DTCs adsorption on ZnS. The zero of energy has been set at the Fermi level EF. (a) Surface Fe and (b) S of DTCs atom.

Table A.14: Mulliken charge populations of DTCs adsorption on the sphalerite surface (s, p and d represent s orbitals, p orbitals and d orbitals, respectively) before and after adsorption.

	Adsorbate	Adsorption status	Atom	s	p	d	total	q/e
ZnS(110)	DeDTC	before	S1	1.85	4.17	0.00	6.02	-0.02
			S2	1.85	4.17	0.00	6.02	-0.02
		after	S1	1.82	4.26	0.00	6.08	-0.08
			S2	1.82	4.27	0.00	6.09	-0.09
		before	Zn1	0.91	0.76	9.98	11.66	0.34
			Zn2	0.91	0.76	9.98	11.66	0.34
		after	Zn1	0.69	0.89	9.98	11.56	0.44
			Zn2	0.69	0.88	9.98	11.55	0.45
	nbDTC	before	S1	1.85	4.16	0.00	6.00	0.00
			S2	1.85	4.16	0.00	6.01	-0.01
		after	S1	1.83	4.25	0.00	6.08	-0.08
			S2	1.82	4.27	0.00	6.09	-0.09
		before	Zn1	0.91	0.76	9.98	11.66	0.34
			Zn2	0.91	0.76	9.98	11.66	0.34
		after	Zn1	0.78	0.90	9.98	11.66	0.34
			Zn2	0.73	0.90	9.98	11.61	0.39
	DbDTC	before	S1	1.85	4.18	0.00	6.03	-0.03
			S2	1.85	4.17	0.00	6.02	-0.02
		after	S1	1.88	4.56	0.00	6.44	-0.44
			S2	1.87	4.55	0.00	6.43	-0.43
		before	Zn1	0.91	0.76	9.98	11.66	0.34
			Zn2	0.91	0.76	9.98	11.66	0.34
		after	Zn1	0.73	0.87	9.98	11.58	0.42
			Zn2	0.83	0.87	9.99	11.69	0.31

Table A.15: DeDTC, nbDTC and DbDTC Mulliken bonding population of atoms before and after adsorption to the sphalerite surface.

	Adsorbate	Adsorption status	Bond	Population	length
ZnS(100)	DeDTC	Before	R(C1–N1)	0.96	1.345
			R(C1-S1)	0.72	1.691
			R(C1=S2)	0.72	1.691
		after	R(C1–N1)	0.97	1.372
			R(C1-S1)	0.83	1.721
			R(C1=S2)	0.83	1.721
	nbDTC	Before	R(C1–N1)	0.91	1.344
			R(C1-S1)	0.71	1.690
			R(C1=S2)	0.72	1.685
		after	R(C1–N1)	0.94	1.358
			R(C1-S1)	0.80	1.733
			R(C1=S2)	0.85	1.713
	DbDTC	Before	R(C1–N1)	0.96	1.349
			R(C1-S1)	0.71	1.694
			R(C1=S2)	0.72	1.692
		after	R(C1–N1)	1.00	1.369
			R(C1-S1)	0.86	1.715
			R(C1=S2)	0.71	1.539

Table A.16: sphalerite Mulliken bonding population of atoms before and after thiol collector adsorption to the surface DeDTC, nbDTC and DbDTC.

		Bond	Population	length
ZnS(100)	In the absence of thiol collector	S3 – Zn1	0.70	2.282
		S4 – Zn2	0.70	2.282
		S5 – Zn1	0.48	2.405
	DeDTC	S3 – Zn1	0.59	2.346
		S4 – Zn2	0.66	2.310
		S5 – Zn1	0.49	2.397
	nbDTC	S3 – Zn1	0.63	2.321
		S4 – Zn2	0.67	2.297
		S5 – Zn1	0.43	2.431
	DbDTC	S3 – Zn1	0.59	2.323
		S4 – Zn2	0.65	2.323
		S5 – Zn1	0.49	2.448

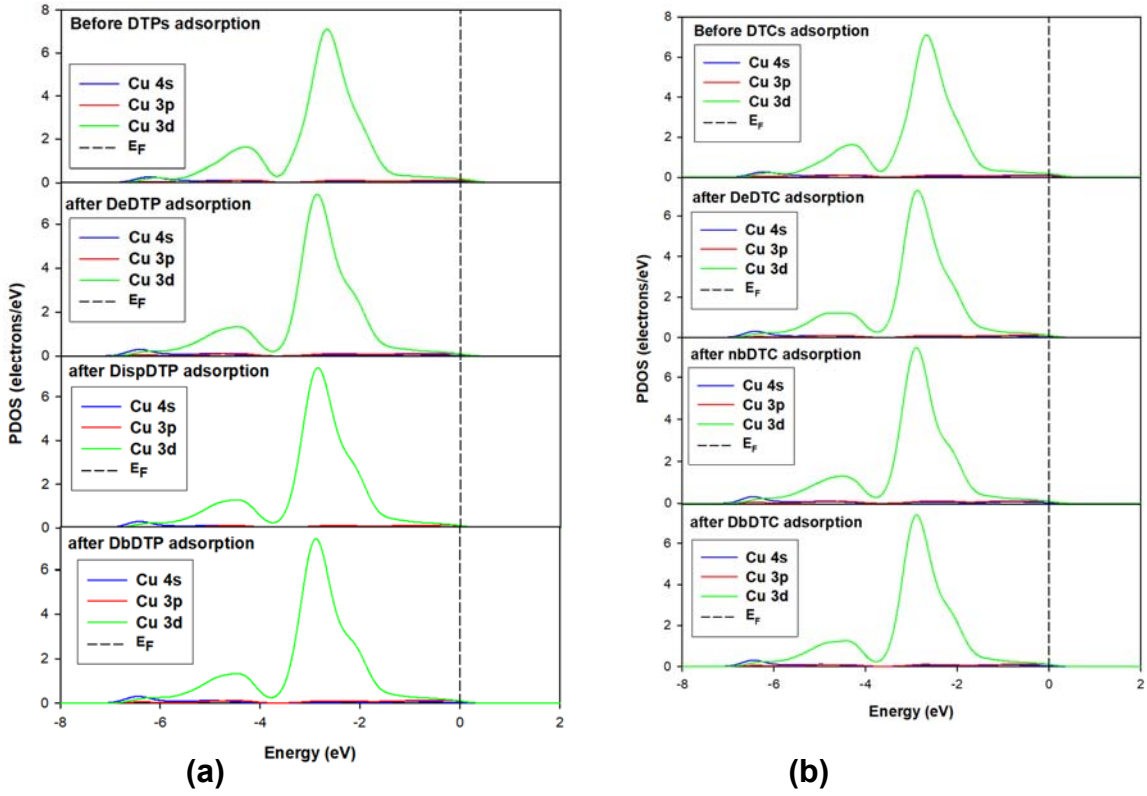

Figure A.4: The zero of energy has been set at the Fermi level (a) Cu atoms before and after DTPs adsorption on $CuFeS_2$ and (b) Cu atoms before and after DTCs adsorption on $CuFeS_2$.

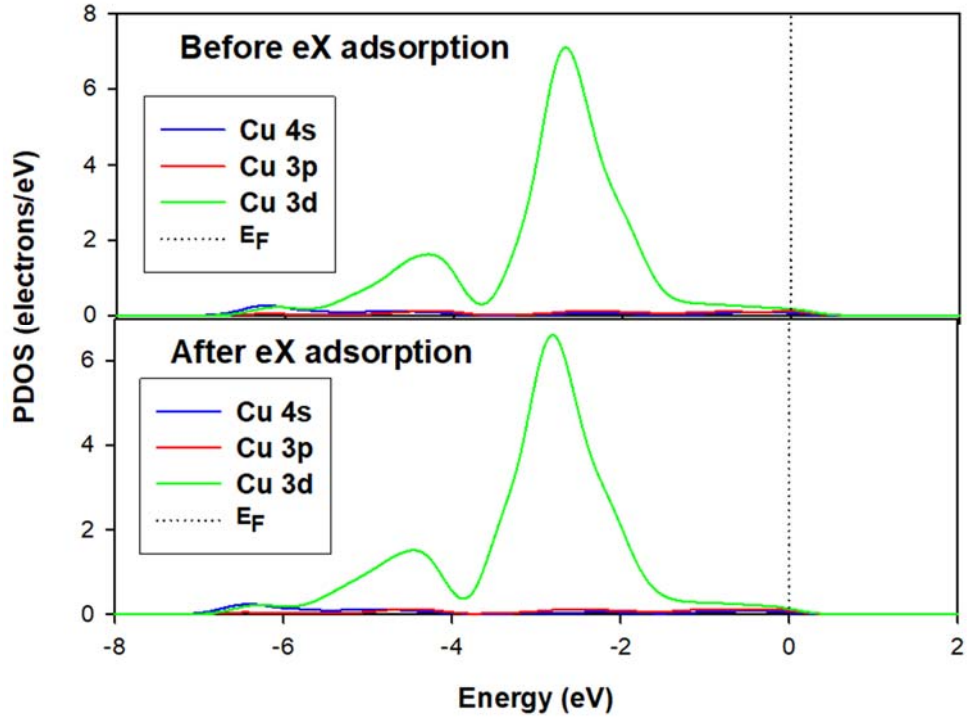

Figure A.5: Bonding Pb–S atoms before and after DTCs adsorption on PbS. The zero of energy has been set at the Fermi level EF. (a) Cu atoms before and after eX adsorption on $CuFeS_2$. .

Appendix B: Microcalorimetry and flotation

The experimental part was done by our experimental collaborators from centre for minerals research at UCT and part of the work has already been published in the Master of Science in Chemical Engineering [10].

Table B.1 Collector dosage calculations pyrite

no of ejection	Cumulative mol added	Fraction of monolayer	Specific enthalpy of adsorption		
			SEX	DiethylDTC	DiethylDTP
1	1.79E-07	0.25	58.6	62.3	5.4
2	3.59E-07	0.50	55.6	62.5	6.6
3	5.38E-07	0.75	51.4	62.4	6.0
4	7.18E-07	1.00	47.7	64.1	6.0

Table B.2 Collector dosage calculations galena

no of ejection	Cumulative mol added	Fraction of monolayer	Specific enthalpy of adsorption		
			SEX	DeDTC	DeDTP
1	1.00E-07	0.25	43.3	63.5	-1.5
2	2.01E-07	0.50	28.5	65.2	1.6
3	3.01E-07	0.75	25.8	68.0	1.1
4	4.01E-07	1.00	29.8	69.4	-4.0

Table B.3 Flotation of Pyrite using DeDTP

DeDTP	*Time(min)*	*Run 1*	*Run 2*	*Avg*	*SD*	*SE*
C0	0	0	0	0	0	0
C1	2	2.3	2.2	2.3	0.073	0.052
C2	6	4.7	4.6	4.6	0.099	0.070
C3	12	7.7	8.4	8.0	0.479	0.339
C4	20	11.6	12.3	11.9	0.496	0.351

Table B.4 Flotation of Pyrite using eX

eX	*Time(min)*	*Run 1*	*Run 2*	*Avg*	*SD*	*SE*
C0	0	0	0	0	0	0
C1	2	5.6	5.6	5.6	0.015	0.011
C2	6	7.6	7.5	7.6	0.028	0.020
C3	12	8.6	8.7	8.6	0.037	0.026
C4	20	9.8	10.0	9.9	0.184	0.130

Table B.5 Flotation of Pyrite using DeDTC

DeDTC	Time(min)	Run 1	Run 2	Avg	SD	SE
C0	0	0	0	0	0	0
C1	2	3.0	2.8	2.9	0.148	0.105
C2	6	4.9	4.8	4.9	0.128	0.090
C3	12	7.0	6.9	7.0	0.111	0.079
C4	20	10.1	10.0	10.1	0.047	0.033

Table B.6 Flotation of Galena using DeDTP

Diethy-DTP	Time(min)	Run 1	Run 2	Avg	SD	SE
C0	0	0	0	0	0	0
C1	2	6.1	6.3	6.2	0.123	0.087
C2	6	18.0	18.0	18.0	0.026	0.019
C3	12	41.6	41.7	41.7	0.025	0.017
C4	20	78.9	78.9	78.9	0.030	0.021

Table B.7 Flotation of Galena using eX

eX	Time(min)	Run 1	Run 2	Avg	SD	SE
C0	0	0	0	0	0	0
C1	2	11.0	11.0	11.0	0.025	0.017
C2	6	31.2	31.3	31.3	0.059	0.042
C3	12	59.5	59.5	59.5	0.034	0.024
C4	20	89.8	89.9	89.9	0.033	0.023

Table B.8 Flotation of Galena using DeDTC

DeDTC	Time(min)	Run 1	Run 2	Avg	SD	SE
C0	0	0	0	0	0	0
C1	2	49.6	49.6	49.6	0.006	0.004
C2	6	84.9	84.9	84.9	0.021	0.015
C3	12	97.3	97.4	97.3	0.012	0.009
C4	20	99.5	99.5	99.5	0.010	0.007

Appendix C: Papers presented at conferences

1. South African Institute of Physics (SAIP) conference hosted by the Nelson Mandela Metropolitan University and Rhodes University at Boardwalk San international (2015) "*Density functional theory calculation of surface properties of pyrite (100) and depression of pyrite using TGA*".
2. South African Minerals to Metals Research Institute (SAMMRI) meeting held at Vain Yard hotel in Cape Town (2015) "*Computational modelling studies on the role of dithiophosphate in the flotation of PGM's*".
3. Centre For High Performance Computing (CHPC) conference held at Council for Scientific industrial research (CSIR) (2015) "*Density functional theory calculation of surface properties of pyrite (100) and Depression of pyrite using TGA*".
4. South African Institute of Physics (SAIP) conference held at the University of Cape Town (2016) "*Modelling of Pyrite (FeS_2) surfaces and adsorption of dithiophosphate (DTP) onto pyrite surface*".
5. South African Minerals to Metals Research Institute (SAMMRI) meeting held at Southern Sun Hotel, main road, Newlands (2016) "*Computational simulation studies on role of dithiophosphate in floatation of sulphides".*
6. African Materials Research Society (AMRS) Conference held at Gaborone International Conference Center (GICC), Botswana (2017) "*Computational modelling study of pyrite surfaces and adsorption of xanthates, dithiophosphates and dithiophosphate onto pyrite.*".
7. South African Minerals to Metals Research Institute (SAMMRI) meeting held at Southern Sun Hotel, main road, Newlands (2017) "*Computational modelling study of pyrite surfaces and adsorption of dithiophosphates and dithiophosphate".*
8. Centre for High Performance Computing (CHPC) conference held Century City Convention (2018) "*Computational modelling study of pyrite surfaces and adsorption of xanthates, dithiophosphates and dithiophosphate onto pyrite*".

Appendix D: Publications

1. M.G Mulaudzi, J. Taguta, B. McFadzean and P.E. Ngoepe., Isothermal titration calorimetry and density functional theory comparison study of xanthate, dithiophosphate and dithiocarbamate adsorption on pyrite surfaces. Materials Modelling Centre, Department of Physics, University of Limpopo, SA. (submitted).

2. M.G Mulaudzi, J. Taguta, B. McFadzean and P.E. Ngoepe, DFT study of interactions of xanthate, dithiocarbamate and dithiophosphate on surface of pyrite, chalcopyrite, sphalerite and galena minerals, Materials Modelling Centre, Department of Physics, University of Limpopo, SA. (To be published).